Doctoral School: Science of Matter, Radiation and Environment

Laboratory: PhysicoChemistry of Combustion Processes and the Atmosphere

Discipline: Theoretical, Physical and Analytical Chemistry

Dissertation

Studying the Reactivity of Pesticides Using Molecular Simulations

Presented by

Hisham KHALIFEH AL RAWAS

Thesis submitted in partial fulfilment of the requirements for the degree of Doctor of Philosophy of the University of Lille

Defended on **September 24, 2024**

Defence Committee

Jury president	Dr. Valérie VALLET	University of Lille
Reviewer	Dr. Carine CLAVAGUERA	University of Paris-Saclay
Reviewer	Pr. Maurice MILLET	University of Strasbourg
Examiner	Pr. Henri WORTHAM	University of Aix-Marseille
Thesis director	Dr. Florent LOUIS	University of Lille
Thesis co-advisor	Dr. Sonia TAAMALLI	University of Lille

Ecole Doctorale : Science de la Matière, du Rayonnement et de l'Environnement

Laboratoire : PhysicoChimie des Processus de Combustion et de l'Atmosphère

Filière : Chimie Théorique, Physique, et analytique

Thèse de Doctorat

Étude de la Réactivité des Pesticides à l'aide de Simulations Moléculaires

Présentée par

Hisham KHALIFEH AL RAWAS

Pour obtenir le diplôme de Docteur en Philosophie de l'Université de Lille

Soutenue le **24 September, 2024**

Composition du Jury

Présidente du jury	Dr. Valérie VALLET	Université de Lille
Rapportrice	Dr. Carine CLAVAGUERA	Université de Paris-Saclay
Rapporteur	Pr. Maurice MILLET	Université de Strasbourg
Examinateur	Pr. Henri WORTHAM	Université d'Aix Marseille
Directeur de thèse	Dr. Florent LOUIS	Université de Lille
Co-encadrante	Dr. Sonia TAAMALLI	Université de Lille

Abstract

Pesticides are semi volatile organic compounds used to control pests that risks crops, animals, humans, or the environment. When applied to the soil or crops, they have the potential to accumulate not only within the crops themselves but also to be transported through air, soil, and water across long distances, posing a major source of pollution within ecosystems. Pesticides can undergo biotic and abiotic degradation pathways. In the atmosphere, abiotic degradation of pesticides occurs mainly by photolysis, and chemical reactions initiated by radicals and atmospheric oxidants. In this thesis, we theoretically studied the environmental degradation by hydroxyl radical ($HO^{\bullet}$) of three used pesticides: phosmet, chlorpyrifos (CPF), and fenpyrazamine (FPA), using DFT calculations at the M06-2X/6-311++G(3df,3pd)//M06-2X/6-31+G(d,p) level of theory. Three different reaction pathways were considered: formal hydrogen transfer (FHT), radical adduct formation (RAF), and single electron transfer (SET). The thermodynamics, mechanisms, and kinetics of the reactions, as well as the lifetime of these pesticides were examined in both gas and aqueous phases at different temperatures (*i.e.*, 253-323 K). The further oxidation of main radical products obtained from the decomposition of the pesticides were studied towards different oxidizing agents in aquatic environment such as O_2, $HO^{\bullet}$, $^{\bullet}NO$, and $^{\bullet}NO_2$ at 298 K. Finally, the ecotoxicity of these pesticides and their degradation by-products were estimated in the aquatic environment to understand their impact on aquatic species.

Keywords: pesticides, atmosphere, molecular simulations, $HO^{\bullet}$ radical, kinetics, ecotoxicity

Résumé

Les pesticides sont des composés organiques semi-volatils utilisés pour lutter contre les ravageurs qui mettent en danger les cultures, les animaux, les humains ou l'environnement. Lorsqu'ils sont appliqués sur le sol ou les cultures, ils peuvent non seulement s'accumuler dans les cultures elles-mêmes, mais également être transportés dans l'air, le sol et l'eau sur de longues distances, constituant ainsi une source majeure de pollution au sein des écosystèmes. Les pesticides peuvent subir des voies de dégradation biotiques et abiotiques. Dans l'atmosphère, la dégradation abiotique des pesticides se produit principalement par photolyse et par réactions chimiques initiées par les radicaux et les oxydants atmosphériques. Dans cette thèse, nous avons étudié théoriquement la dégradation environnementale par radical hydroxyle ($HO^{\bullet}$) de trois pesticides utilisés : le phosmet, le chlorpyrifos (CPF) et le fenpyrazamine (FPA), en utilisant des calculs DFT au M06-2X/6-311++G(3df,3pd)//M06-2X/6-31+G(d,p) niveau de théorie. Trois voies de réaction différentes ont été considérées : le transfert formel d'hydrogène (FHT), la formation de produits d'addition radicalaires (RAF) et le transfert d'électrons uniques (SET). La thermodynamique, les mécanismes et la cinétique des réactions, ainsi que la durée de vie de ces pesticides ont été examinés en phase gazeuse et aqueuse à différentes températures (253-323 K). L'oxydation ultérieure des principaux produits radicalaires issus de la décomposition des pesticides a été étudiée vis-à-vis de différents agents oxydants en milieu aquatique tels que O_2, $HO^{\bullet}$, $^{\bullet}NO$, et $^{\bullet}NO_2$ à 298 K. Enfin, l'écotoxicité de ces pesticides et leur dégradation Les sous-produits ont été estimés dans le milieu aquatique pour comprendre leur impact sur les espèces aquatiques.

Mots clés: pesticides, atmosphère, simulations moléculaires, radical $HO^{\bullet}$, cinétique, écotoxicité

Acknowledgements

Above all, I am grateful to God for granting me the opportunity, patience and self-motivation to undertake and complete this chapter of my life.

Additionally, “I wanna thank me for believing in me”, I want to thank myself for the hard work, great effort, perseverance, and dedication that I invested in this journey. The countless hours of study, research, and writing have culminated in this achievement, and I am proud of what I have accomplished.

I would like to express my deepest gratitude to my supervisors, Dr. Florent Louis and Dr. Sonia Taamalli, for their guidance, support, and encouragement throughout the course of my research. Their expertise and insightful feedback were invaluable to this thesis.

I am also grateful to my collaborators in Vietnam, Dr. Duy Quang Dao, Dr. Thi Le Anh Nguyen, Mr. Dinh Hieu Truong, whose contributions and cooperation were crucial to the success of this work.

Thanks to our “Molecular Simulations of Environmental Processes, SMPE” team members, Dr. Valérie Fevre-Nollet, Dr. Marc Ribaucour, Pr. Abderrahman El Bakali, and all PC2A laboratory members, the director Benjamin Hanoune, and the administration and technical staff.

I extend my sincere thanks to my office colleagues, Dr. Zainab Srour, Mrs. Nesrine Bekkal, Mrs. Luna Cartayrade, and Mr. Valisoa Rakotonirinjanahary, for their help and support, and for the constructive discussions and the funny moments we had together during these three years.

To my real friends around the world, thank you for your constant encouragement and for always being there when I needed a break.

Finally, I am profoundly thankful to my family for their endless love, patience, and sacrifices, which provided me with the strength and determination to pursue and complete this academic journey.

Table of Content

Table of Figures

Table of Tables

List of Abbreviations and Symbols

Abbreviation	Full Term
DFT	Density Functional Theory
PES	Potential Energy Surface
TST	Transition State Theory
ZPE	Zero-Point Energy
SMD	Solvation Model based on Density
SOC	Spin-Orbit Coupling
IRC	Intrinsic Reaction Coordinate
TS	Transition State
MCR	Molecular Complex from Reactant side
MCP	Molecular Complex from Product side
FHT	Formal Hydrogen Transfer
RAF	Radical Adduct Formation
SET	Single Electron Transfer
HOMO	Highest Occupied Molecular Orbital
LUMO	Lowest Unoccupied Molecular Orbital
ESP	Electrostatic Potential
BAF	Bioaccumulation Factor
BCF	Bioconcentration Factor
CPF	Chlorpyrifos
FPA	Fenpyrazamine
k	Rate constant
Γ	Branching ratio
τ	Lifetime
$S°_{298K}$	Standard Molar Entropy at 298 K
E_0	Vibrationally Adiabatic Energy Barrier
$\Delta_r H°_{0K}$	Standard Reaction Enthalpy at 0 K
$\Delta_r H°_{298K}$	Standard Reaction Enthalpy at 298 K
$\Delta H°^{\neq}_{298K}$	Standard Activation Enthalpy at 298 K
$\Delta_r G°_{298K}$	Standard Gibbs Free Reaction Energy at 298 K
$\Delta G°^{\neq}_{298K}$	Standard Gibbs Free Activation Energy at 298 K

General introduction

Atmospheric contaminants originate either from direct emissions from sources such as incineration, fossil fuel combustion, and industrial activities, or from diffuse emissions or re-emissions from contaminated soils or water bodies. This issue involves a wide array of molecules that come from human activities releasing volatile organic compounds with various heteroatoms, forming a significant group of emerging contaminants like pesticides, plastics, tire wear additives, and PFAS. For many of these contaminants, the primary mode of dispersion is through the atmosphere.

The main methods for removing contaminants from the atmosphere are dry or wet deposition techniques. Atmospheric oxidants (*e.g.*, O_2, O_3, $HO^{\bullet}$, $^{\bullet}NO$, and $^{\bullet}NO_2$) initiate chemical reactions that transform these contaminants. The resulting products from these reactions can be hazardous and lead to several adverse effects. The deposited atmospheric fluxes of contaminants and their degradation products pose ecological risks to marine and terrestrial hydrosystems, in addition to potential human health risks from their presence in the air.

Pesticides are considered major contaminants in the environment. They are widely used in agriculture to control pests and improve crop yields, but their extensive and persistent use leads to significant environmental pollution. Moreover, hydroxyl radical ($HO^{\bullet}$) is the most abundant radical in the atmosphere, and is considered as a key player in the atmospheric processes that regulate air quality and the removal of contaminants.

For this reason, the primary objective of this thesis is to explore the atmospheric degradation processes of three pesticides: phosmet, chlorpyrifos (CPF), and fenpyrazamine (FPA), into different organic contaminants using various theoretical approaches to identify their most favourable pathways and determine their atmospheric fate and environmental impact.

This thesis includes five chapters outlined as follows:

In **Chapter I**, the definition and history of pesticides will be mentioned, outlining their development and usage over time. The pesticides market and sales across various countries will then be explored, highlighting the economic impact and differences in usage patterns globally. The classification of pesticides will be discussed, detailing the various types and their specific applications. Furthermore, the transport routes of pesticides will be analysed, explaining how these chemicals move through the environment. The health risks associated with synthetic pesticides will also be reviewed, emphasizing the potential dangers to human health. Lastly, the issue of environmental pollution by pesticides will be addressed, discussing how these substances contaminate soil, water, and air, and the subsequent ecological consequences, by referring to case studies from France and Vietnam.

In **Chapter II**, molecular simulations will be elaborated from a theoretical chemistry background, by explaining the transition state theory, the potential energy surface, and the density functional theory. The various computational methods and the software used will be detailed to explain how the electronic structures and rate constants were calculated, and how

the ecotoxicity of the studied compounds was evaluated. Additionally, the identification of the thermochemical properties and kinetic parameters will be made, emphasizing their importance in predicting the behaviour and reactivity of the chemical species.

Chapter III will address the atmospheric degradation of phosmet insecticide by HO$^{\bullet}$ radical. The structure and electronic properties of phosmet will be examined. The oxidation mechanisms of phosmet will be explored, including formal hydrogen transfer (FHT) reactions, radical adduct formation (RAF) reactions, and single electron transfer (SET) reactions. The thermodynamics, mechanisms, and kinetics of these reactions, as well as the lifetime of phosmet, will be examined across a range of temperatures, spanning from 253 to 323 K in the gas phase, and from 283 to 323 K in the aqueous phases (relevant to environmental water and water treatment processes). Finally, the ecotoxicity of phosmet and its degradation by-products will be assessed in aquatic environments to understand their impact on aquatic organisms.

Chapter IV will investigate the HO$^{\bullet}$-induced degradation of chlorpyrifos (CPF) insecticide in both gas and aqueous phases, exploring conventional mechanisms such as H-, S-, Cl-, and CH_3-abstraction, HO$^{\bullet}$-addition, and single electron transfer. Thermodynamic and kinetic parameters of these reactions will be analysed to identify the dominant reactions and determine the branching ratio of the potential pathways. Moreover, attempts will be made to oxidize the primary radical products further using other oxidizing agents, which results in primary neutral products. Then, the acute and chronic toxicity of these products, as well as CPF itself, will be evaluated across various aquatic organisms, including fish, daphnia, and green algae. Lastly, through docking and molecular dynamics, the binding sites and inhibitory activity of CPF and its degradation products on typical neural acetylcholinesterase (AChE) and butyrylcholinesterase (BChE) enzymes will be predicted at the molecular level.

Finally, the degradation of fenpyrazamine (FPA) fungicide will be studied in **Chapter V**. In this chapter, oxidation mechanisms of FPA induced by HO$^{\bullet}$ will be considered through three distinct reaction pathways: FHT, RAF, and SET. The thermodynamics, mechanisms, kinetics of reactions, and the lifetime of FPA will be examined in the aqueous phase at various temperatures ranging from 283 to 323 K, covering the temperature range of water in environmental settings and water treatment processes. Additionally, the ecotoxicity of FPA and its degradation products will be assessed in the aquatic environment, highlighting their impact on aquatic organisms.

This PhD thesis was done at the Physico-Chimie des Processus de Combustion et de l'Atmosphère (PC2A) laboratory of the University of Lille in France (2021-2024), within the research team "Molecular Simulations of Environmental Processes, SMPE" supervised by Dr. Florent Louis and Dr. Sonia Taamalli.

The work involved was carried out in collaboration with the research group of Dr. Duy Quang Dao at Duy-Tan Computational Chemistry Laboratory (DTC2 Lab) of the Duy Tan University in Vietnam, and with Pr. Ivan Černušák at the Department of Physical and Theoretical Chemistry, Faculty of Natural Sciences of Comenius University in Bratislava, Slovakia, who helped us in theoretical computations with his great experience in the field.

This work used the HPC facility clara@uniba.sk at the Comenius University in Bratislava. This work also used the Extreme Science and Engineering Discovery Environment (XSEDE), which is supported by National Science Foundation grant number OCI-1053575.

Moreover, this thesis is a contribution to the CaPPA project (Chemical and Physical Properties of the Atmosphere), funded by the French National Research Agency (ANR) through the PIA (Programme Investissement d'Avenir) under contract ANR-11-LABX-005-01, to the Institut de Recherches Pluridisciplinaires en Sciences de l'Environnement (IRePSE Fed 4129), and a contribution to the CPER research project ECRIN, with financial support from the French Ministère de l'Enseignement Supérieur et de la Recherche, the Hauts-de-France Region and the European Regional Development Fund (ERDF). This work was supported also by the Slovak Research and Development Agency, grant agreement No. APVV-20-0127.

Chapter I. General context

I.1. Introduction

I.1.1. Pesticides definition and history

Pesticides are a diverse group of chemical or biological agents used to control or kill pests (***Figure I-1***) that risks crops, animals, humans, or the environment (Parra-Arroyo *et al.*, 2022). In the last century, pesticides have played a great role in helping the growing global population, by increasing agricultural yields through pest control (Carvalho, 2017; Morillo and Villaverde, 2017). Their use and development have increased dramatically after the Second World War (Gavrilescu, 2005).

In 1940, 140 tons of pesticides were used. At that time, organic pesticides like plant extracts and inorganic ones containing heavy metals, were the most commonly used pesticides. In the mid-1940s, there was a rapid increase in the production and application of synthetic organic pesticides. Fast forward to 1991, the US Environmental Protection Agency had registered roughly 23400 pesticide products (Frazar, 2000; Singhvi, 1994).

In 1997, 600 thousand tons of pesticides were employed, of which 77% were used in the agriculture industry, 12% used by industrial, commercial and government organizations, and 11% by the private households (Fishel, 2005; US EPA, 2000; Moerner, 2002).

Figure I-1: *pesticides application on a potatoes field in Godewaersvelde, northern France. (Photo by: Philippe Huguen).*

The European Union (EU) Pesticides Database listed in 2016 over 1378 active ingredients, with 466 being allowed to be used in the EU, while 858 have not received approval (Kalyabina *et*

al., 2021). Globally, research data show that pre-harvest crop losses would average about 40% without effective pest management. Post-harvest procedures for pest management are essential and should be mandatory, and inadequate pesticide control during these activities could pose environmental risks.

Losing crops due to infestations would accelerate the depletion of natural resources, posing challenges in meeting the needs of the global population. Alexandratos and Bruinsma predicted that by 2025, there would no longer be enough land or resources to support the worldwide population (Alexandratos and Bruinsma, 2012).

Arthropods alone are responsible for destroying approximately 18-26% of annual crops with an economic value of more than 470 billion dollars. The majority of these losses occur in the field before harvesting, disproportionately affecting developing countries more heavily (Culliney, 2014). For this reason, pesticides have been widely adopted as a fast, simple, and effective strategy to reduce the loss of crops, enhance the cosmetic appearance and improve nutritional value sometimes (Damalas and Eleftherohorinos, 2011).

I.1.2. Pesticides market and sales in different countries

Pesticide use is the base of modern agriculture, with more than 2.7 million tons of active substances applied globally in 2020 with an increase of 50% since the 1990s, resulting in an annual application rate of 1.8 kg/ha on cropland (Froger *et al.*, 2023). The market and sales of pesticides vary significantly between different countries, influenced by factors including agricultural practices, regulatory policies and frameworks, pest challenges, economic status, and technological advancements. Here is the pesticides market size in some regions (Mordor Intelligence, 2024):

Brazil plays a major role in the global pesticides market, boasting a substantial agricultural sector primarily focused on crops like soybeans, cotton, maize, and sugarcane. The estimated size of the Brazil Crop Protection Chemicals Market in 2024 is about 33.00 billion USD.

The United States comes after Brazil as one of the largest pesticides markets worldwide, due to its expansive agricultural industry and abundant crop production. The estimated size of the US Crop Protection Chemicals Market in 2024 is approximately 20.41 billion USD.

The pesticides market within the European Union is defined by rigorous regulatory measures under EU's Plant Protection Products Regulation (EC) No 1107/2009. In 2024, the estimated size of the Europe Crop Protection Chemicals Market stands at 15.20 billion USD, with projections indicating growth to 18.59 billion USD by 2029. This growth is anticipated to occur at a Compound Annual Growth Rate (CAGR) of 4.11% during the forecast period (2024-2029).

In Europe, France is the largest consumer of pesticides (FAO, 2022), and ranks seventh globally in the total pesticide consumption, reaching 65,000 tons in 2020. ***Figure I-2*** presents the consumption of pesticides in France between 2017 and 2022. Large amounts of pesticides (5.8 kg/ha) were consumed in 2018, while it was reduced to 3.8 kg/ha in 2019 during Covid epidemic. This quantity increased again to reach 4.8 kg/ha in 2022.

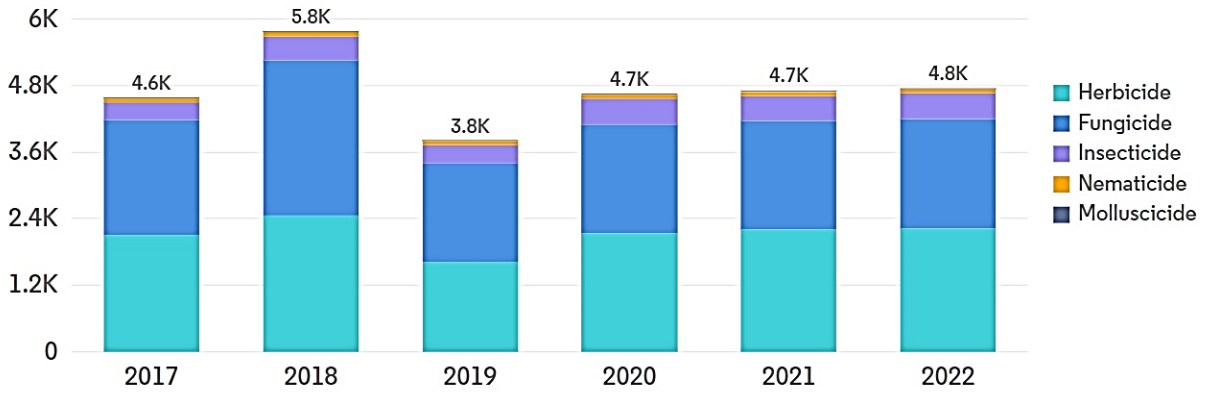

***Figure I-2**: consumption of pesticides (in g/ha) in France, 2017-2022 (Mordor Intelligence, 2024).*

There has been a movement towards decreasing pesticide usage and promoting sustainable agriculture, with initiatives such as integrated pest management (IPM) and organic farming gaining traction. For this reason, the French government authorized in 2022 the export of over 7400 tons of banned pesticides, despite the introduction of a landmark law aimed at prohibiting such actions. Furthermore, France has worked to decrease the reliance on chemical pesticides while simultaneously investing efforts in the development of biopesticides. Nowadays, France is considered as the third largest market for biopesticides in Europe, and was always one of Europe's primary agricultural centers. It owns the largest area of organic farmland in the region, totalling 2.7 million hectares in 2021. Until now, few biopesticides products are currently approved in France, despite the many years of extensive research on biological control numerous biopesticides that showed to be effective in the laboratory. The estimated size of the France Crop Protection Chemicals Market is 2.59 billion USD in 2024 (***Figure I-3***), with an expectation to increase to 3.47 billion USD by 2029, indicating a CAGR of 5.97% during the forecast period (2024-2029).

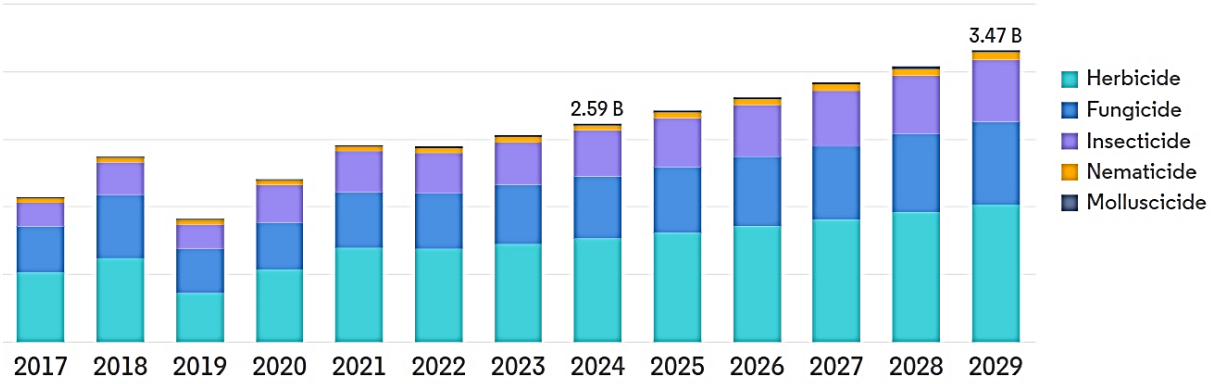

***Figure I-3**: estimated pesticides market size (in USD) in France, 2017-2029 (Mordor Intelligence, 2024).*

Many companies are dominating the French market with their products, services, and ongoing product innovations and developments, including Syngenta, Bayer CropScience, Corteva Agriscience, UPL Limited, Novozymes, and Sumitomo Chemical.

In Asia, China, and India are the largest consumers of pesticides with a market size of 5.14 and 3.13 billion USD in 2024, respectively.

In Vietnam, the Crop Protection Chemicals Market is expected to reach a size of 558.74 million USD in 2024. In 2022, the country applied an average of 1.1 kilograms of crop protection chemicals per hectare of agricultural land, with fungicides having the largest portion of the market at 38.2%. Insecticides and herbicides accounted for 32.9% and 21.5% of the Vietnamese crop protection chemicals market, respectively.

I.1.3. Pesticides classification

According to the organism or the pest they control, pesticides can be classified as (Gavrilescu, 2005):

- **Insecticide:** control or eliminate insects and other arthropods. They can be further categorized based on their mode of action, such as contact insecticides (kill pests on contact), stomach insecticides (kill pests when ingested), systemic insecticides (absorbed by plants and kill pests that feed on them), and repellents (deter pests from feeding or settling).

- **Fungicide:** Control fungal diseases in plants, including molds, mildews, and rusts. They can be applied preventively to protect plants from infection or curatively to treat existing fungal infections. Fungicides may inhibit fungal growth, disrupt fungal cell membranes, or interfere with fungal enzymes.

- **Herbicide:** Control noxious weeds and other vegetation that are growing or competing with a desired species. They can be selective (target specific types of plants) or non-selective (kill a wide range of plant species). Herbicides may act by inhibiting plant growth, disrupting photosynthesis, or interfering with metabolic processes.

- **Nematicide:** Kill nematodes, which are microscopic wormlike organisms that live in the soil and cause damage to food crops. They can be synthetic chemicals or biological agents that target nematodes at different life stages.

- **Rodenticide:** Control mice, rats, and other rodents. They may act by interfering with blood clotting, causing internal bleeding, or affecting the nervous system of rodents.

- **Miticide:** Kill mites including spider mites, rust mites, broad mites, that live on plants, livestock, and people.

- **Algaecide:** kill and prevent the growth of algae. They work by disrupting the photosynthetic process, damaging cell membranes, or inhibiting algal growth and reproduction.

- **Biopesticides:** Naturally occurring substances with pesticidal properties. They are derived from natural sources such as plants, microbes, or biochemicals.

- **Molluscicides:** Kill molluscs such as snails and slugs. They may act by poisoning molluscs or by creating physical barriers to prevent their access to plants.

- **Avicides:** Control bird populations, particularly those considered pests. They act by affecting the nervous system of birds, leading to their death.

Synthetic pesticides can be divided into either organic or inorganic according to their chemical composition (***Figure I-4***) (Parra-Arroyo *et al.*, 2022).

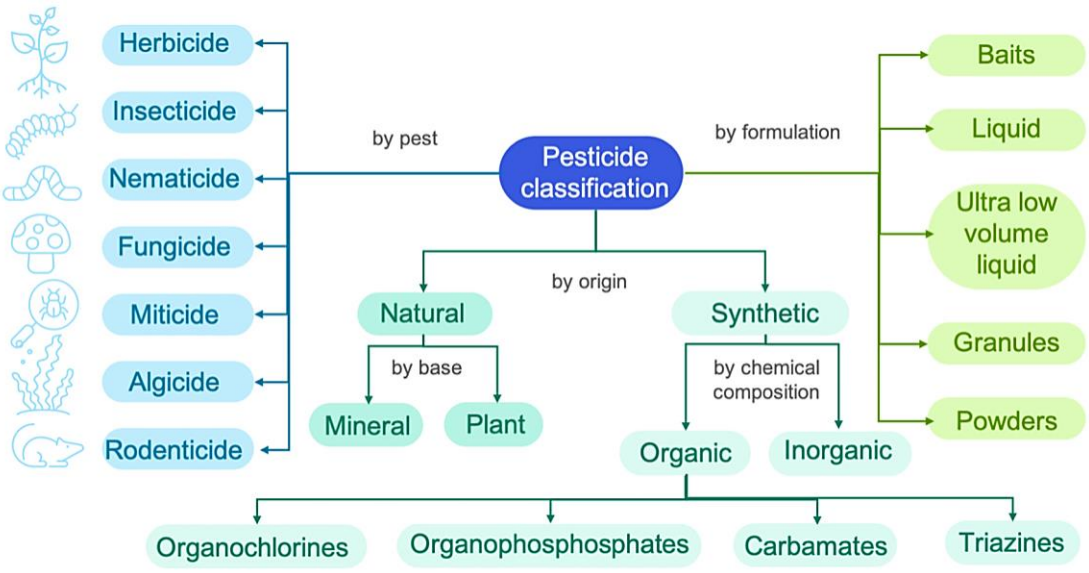

Figure I-4*: classification of pesticides (Parra-Arroyo et al., 2022).*

Organic pesticides may include different families, such as:

- **Organochlorines:** Organochlorine pesticides are characterized by their white, crystalline nature, semi-volatile, and non-polar properties. Structurally, they consist of carbon, hydrogen, and chlorine atoms. These pesticides are employed to repel a range of organisms, including insects, bacteria, fungi, and weeds (Bilal *et al.*, 2019). Their main mode of action involves disrupting the equilibrium of sodium and potassium ions

in nerves, making them incapable of transmitting impulses. These pesticides can travel long distances by volatilizing upon application and subsequently condensing in cooler climates across various regions of the world. Organochlorine pesticides have greater toxicity and persistence compared to pesticides belonging to other chemical classes. Examples of these include chlordane, heptachlor, endosulfan, and aldrin. Dichlorodiphenyltrichloroethane (DDTs) and hexachlorocyclohexane (HCHs) are commonly utilized for the eradication of termites, mosquitoes, and the tsetse fly, primarily within agricultural and healthcare sectors (Bilal *et al.*, 2019).
Despite being infrequently used and prohibited in most countries globally, organochlorine pesticides are highly persistent in the environment (Gonçalves *et al.*, 2021a).

- **Organophosphates:** Organophosphorus pesticides are the most widely and extensively used pesticides, with their widespread adoption occurring following the prohibition of organochlorines due to their toxicity and persistence. These pesticides represent 34% of global pesticide sales, with chlorpyrifos, diazinon, malathion, parathion, and phorate being among the most prevalent in the environment (Khedr *et al.*, 2019; Malakootian *et al.*, 2020). The main mode of action of organophosphorus pesticides involves the nonspecific inhibition of cholinesterase enzymes found in neuromuscular junctions, resulting in voluntary muscle spasms. These pesticides are phosphoric acid esters and can undergo hydrolysis upon exposure to air, light, and soil, producing water-soluble by-products (Bilal *et al.*, 2019). They have the potential to travel considerable distances via evaporation and condensation, and may be transported through runoff and leaching into soils.

- **Carbamates:** Carbamates are a class of preemergent herbicides designed to prevent undesired plants from sprouting. They are derived from carbamic acid, and they include carbaryl (the initial insecticide utilized in agricultural contexts), oxamyl, carbofuran, aldicarb, ethienocarb, and methomyl. Their high solubility in water enables their absorption in plant leaves and roots. Their mode of action involves the inhibition of acetylcholinesterase, resulting in muscle twitching and eventual paralysis. They may pose environmental risks, such as soil, water, and air contamination through runoff, drift, and leaching.

- **Triazines:** Triazines are a class of herbicides frequently used for weed control in diverse crops including corn, sorghum, sugarcane, and fruits. They are distinguished by their triazine ring structure, which underlies their herbicidal activity. Their mode of action involves inhibiting photosynthesis in plants, disrupting the electron transport chain within chloroplasts, and ultimately resulting in the death of the plant (Gonçalves *et al.*, 2021a). Triazine pesticides are primarily retained in plant roots, with their accumulation and movement varying depending on their level of hydrophobicity. Through runoff and leaching, triazines enter water bodies, where they can persist for extended periods, with half-lives reaching months. Their persistence in soil is influenced by factors such as soil composition, pH levels, organic matter content, and climatic conditions.

I.1.4. Pesticides transport routes

When applied to the soil or crops, pesticides have the potential to accumulate not only within the crops themselves but also to be transported through air, soil, and water across long distances, posing a major source of pollution within ecosystems (Kaushal *et al.*, 2021; Qu *et al.*, 2019). Moreover, they are capable of migrating within various environments and, ultimately, accumulate in food chains or persist as degradation products (***Figure I-5***).

The mechanisms through which pesticides may move from one environmental component to another include adsorption/desorption, volatilization, runoff, leaching, and uptake. The transport of pesticides and their fate are primarily controlled by subsurface and surface conditions, along with the agricultural practices, and are influenced by a series of physical, chemical, and biological phenomena, including infiltration, evapotranspiration, crop-root absorption, advection, dispersion, adsorption, degradation, and volatilization, and others (Gavrilescu, 2005).

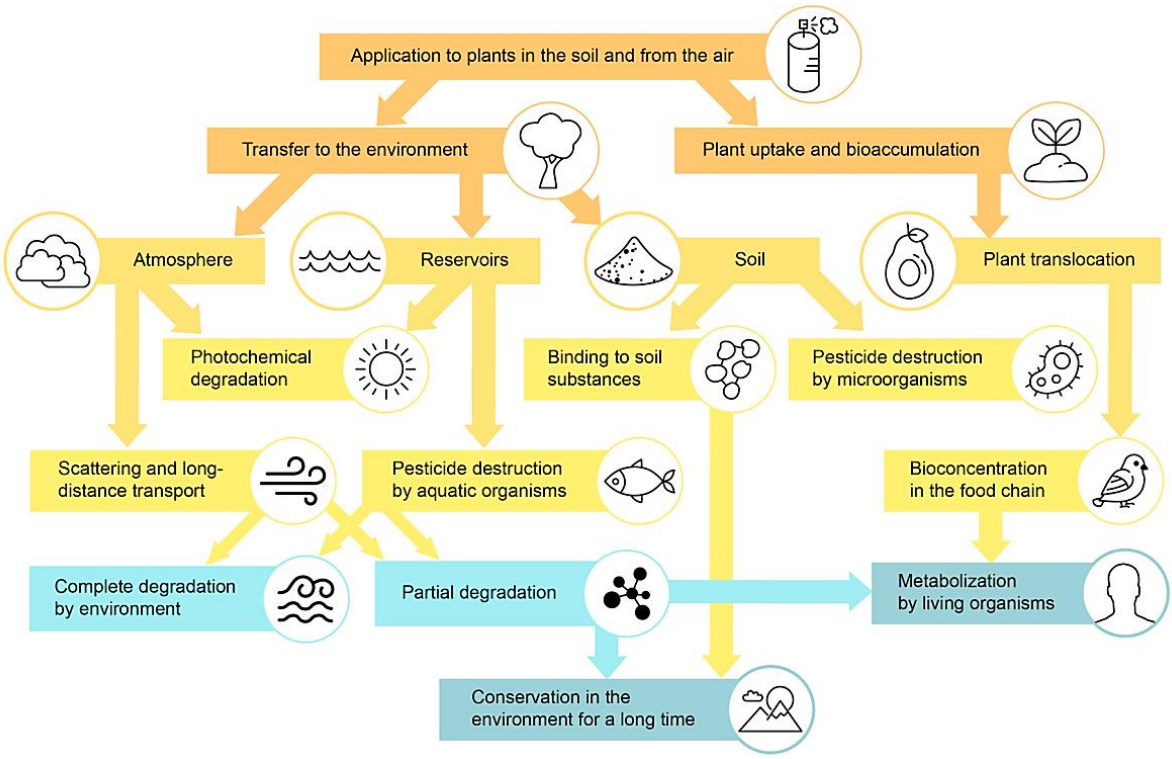

Figure I-5*: schematic representation of pesticide transport routes after application (Kalyabina et al., 2021).*

The emission of pesticides into the air from the agricultural fields, happens from either the plant canopy or the soil surface into the atmosphere. The intensity of emission (Nyer, 2000; Suthersan, 2001) is determined by factors such as vapor pressure, the heat required for

volatilization of the substance, the partition coefficient between the atmosphere and other phases, air flow mass, and the application method of the pesticide.

After application, airborne pesticides could be transported by the wind over long distances, and all over the world in the case of a stable gaseous chemical (Woodrow *et al.*, 2019). In addition, pesticides have the potential to be transported on small particles like soil or larger entities such as leaves carried by the wind. Additionally, they can volatilize from any surface to which they are applied.

In the atmosphere, pesticides may also undergo photochemical degradation. This process involves the absorption of sun's UV radiation by the pesticide molecules, which can lead to the formation of reactive intermediates such as free radicals or excited states. These intermediates then undergo a series of chemical reactions, including oxidation, isomerization, and bond cleavage, ultimately breaking down the pesticide molecule into smaller fragments or transforming it into different chemical species. Moreover, the photodegradation process depends on factors such as the pesticide's photostability, the intensity and wavelength of sunlight, atmospheric composition (e.g., presence of oxygen, ozone, water vapor), temperature, humidity, and the presence of other pollutants or reactive species in the air. In addition, pesticides can be degraded in air and water environments by their reaction with free radicals such as $HO^{\bullet}$, $SO_4^{\bullet-}$, $^{\bullet}NO$, $^{\bullet}NO_2$, as well as $^3O_2$ and O_3.

Pesticides may also be transferred to the water environment. The release of pesticides into aquatic ecosystems is influenced by various factors such as weather conditions, soil characteristics, the properties of the pesticides, and the methods used for their application (Cui *et al.*, 2020; Gramlich *et al.*, 2018; Vryzas, 2018). Pesticide residues have the potential to infiltrate the soil and migrate through underground water systems, or they may enter rivers or lakes through agricultural runoff water (Kaushal *et al.*, 2021; Ulrich *et al.*, 2022). Consequently, water bodies that are contaminated by pesticides, serve as the main source of entry into the food chain (Sutton *et al.*, 2019).

When pesticides are applied directly on the crops, they can move downwards through soil with the water flow. During this movement, they can adsorb, desorb, and break down. The properties of the pesticides and the soil, in addition to the other environmental conditions, can affect the speed of this movement (Katagi, 2013). Soil fumigation has the potential to significantly increase the leaching of pesticide into the groundwater (Huang *et al.*, 2019). Furthermore, pesticides suspended in the air can also return to the soil through precipitation (Zaller *et al.*, 2022).

The properties of pesticides play a crucial role in determining their behaviour in the environment. These properties involve: water solubility (the extent to which a pesticide dissolve in water), soil adsorption (the tendency of a pesticide to adhere to soil particles), and environmental persistence (half-life). These three criteria are typically used to tells the ability of pesticides to leach or to be carried by surface runoff following application. Pesticides that have high water solubility, low tendency to adsorb to soil particles, and long half-life, have the highest potential to move into water (Gavrilescu, 2005).

In natural environments, certain bacteria, fungi, and microalgae have the ability to fully degrade pesticides, without causing secondary environmental pollution that can occur with chemical and physical degradation. However, microbial degradation may sometimes be ineffective (Huang *et al.*, 2018). For example, metribuzin is a herbicide that undergoes microbial degradation, and as such, its decomposition is influenced by climatic factors, where slower decomposition is observed in colder conditions (Stenrød *et al.*, 2008).

I.1.5. Health risks associated with synthetic pesticides

The human exposure to pesticides occurs not only in the outdoor environments, but also in the indoor ones such as houses. A case study conducted in nine houses in Strasbourg in France revealed, from the collected dust and air samples, their contamination with several pesticides (Al-Alam *et al.*, 2022). The biomonitoring of pesticides in human specimens (urine, blood, and breast milk) leads to the detection of several types of pesticides, the currently-used and banned-persistent pesticides (Yusa *et al.*, 2015).

Because of their toxicity, some classes of pesticides, like organochlorines and organophosphates, have been banned in multiple countries (Gonçalves *et al.*, 2021b). Pesticides have many effects on human health, including mutagenic, neurotoxic, carcinogenic, and teratogenic effects (Liu *et al.*, 2019; Pereira *et al.*, 2015).

The acute risk varies greatly depending on the pesticide and may involve peripheral and central neurotoxicity, as well as reduced blood clotting capacity. Additionally, the particular formulation of the pesticide can greatly influence both exposure and toxicity levels. Short-term exposure can result in adverse harmful effects on the different body organs and systems including the liver, kidneys, blood, lungs, nervous system, immune system, and gastrointestinal tract (WHO, 2019).

Pesticides enter the human body via the mouth, nose, skin, and eyes (Kim *et al.*, 2017), leading to various acute illnesses such as stomach-aches, headaches, skin rashes, vomiting, sneezing, eye irritation, respiratory issues, convulsions, and coma (Raschke and Burger, 1997). Direct exposure to pesticides can be fatal (Dasgupta *et al.*, 2005; Page *et al.*, 2017).

Chronic or long-term exposure to highly hazardous pesticides (HHPs) can lead to impacts on the eyes, skin, liver, kidneys, cardiovascular system, nervous system, gastrointestinal tract, reproductive system, immune system, endocrine system, and blood (***Figure I-6***).

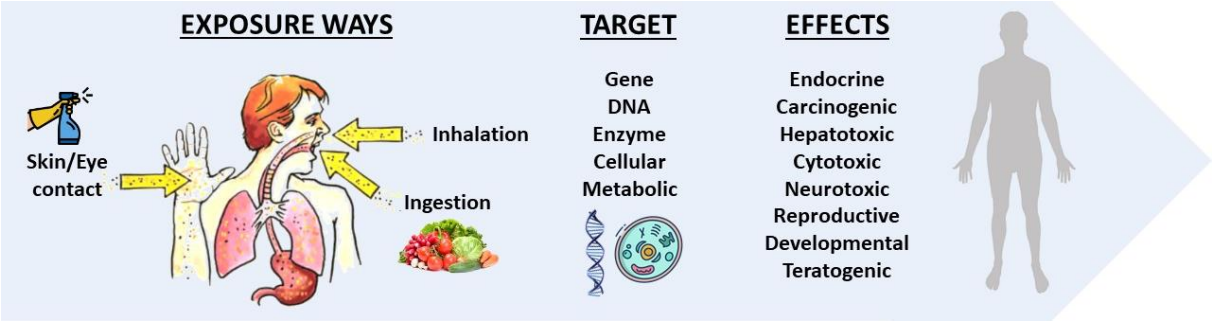

***Figure I-6**: exposure ways to pesticides and their effects on humans.*

Chronic disorders can arise from disruptions in cellular homeostasis caused by pesticides' primary effects, including ion channel, enzyme, and receptor disorders, as well as morphological alteration of mitochondria (Chen *et al.*, 2017), and the accumulation of DNA damage (Alleva *et al.*, 2018).

The toxic effects of pesticides come from their ability to initiate processes that cause molecular and cellular damage. Pesticides can change the rates of enzymatic reaction, impacting the activity of several enzymes like catalase, superoxide dismutase, and glutathione peroxidase, as well as aspartate transaminase, alanine transaminase, and alkaline phosphatase. High levels of these enzymes in cells indicate the organism's toxic response to pesticide exposure (Kalyabina *et al.*, 2021).

Some HHPs may cause cancer, including childhood cancer. Children are at a heightened risk of pesticide effects because of their smaller size, which results in higher exposure levels relative to their body weight. Additionally, their metabolism differs, and their internal organs are still developing.

***Figure I-7**: placards seen near entrance of the International Agriculture Fair at the Porte de Versailles exhibition center in Paris on February 2024. (Photo by: Ludovic Marin).*

In France, a child, named Théo Grataloup, was born with birth defects after his mother's exposure to glyphosate herbicide when she was pregnant (RFI, 2023). Théo, now aged 17, has already undergone 54 operations and is still suffering from damage in his larynx, esophagus, and respiratory system. This case is obviously a proof that pesticides in general and glyphosate in particular are harmful and dangerous (***Figure I-7***). Moreover, the World Health Organization's International Agency for Research on Cancer (IARC) in 2015, classified glyphosate as a "probable human carcinogen".

According to the World Health Organization (WHO), pesticide poisoning resulted in 193,460 unintentional fatalities in 2012, with 84% of these incidents taking place in low to middle-income countries (Parra-Arroyo *et al.*, 2022).

Approximately 385 million cases of unintentional acute pesticide poisoning are reported worldwide each year, resulting in around 11,000 deaths. With a global farming population of approximately 860 million, this suggests that roughly 44% of farmers are poisoned by pesticide annually (Boedeker *et al.*, 2020).

I.1.6. Environmental pollution by pesticides

While pesticides play a significant role in modern agriculture, their excessive and prolonged application leads to the damage of farmland, soil pollution, and deterioration of soil quality and environmental conditions. A large portion of pesticides applied in agriculture fails to reach their intended target organisms (Chawla *et al.*, 2013), however they disperse through soil, water, and air, and are detected in food intended for human consumption.

Ground or aerial spraying techniques are the primary sources of air pollution from agrochemicals. Semi-volatile pesticides, primarily absorbed onto atmospheric aerosol particles, have half-lives ranging from several days to a month in the particulate phase, and have the ability to remain stable to gas-phase reactions with hydroxyl radicals in the atmosphere (Socorro *et al.*, 2016). Oxidation and photochemical reactions can convert airborne pesticide residues into compounds that are more toxic than their original form (Woodrow *et al.*, 2019).

When directly applied to the soil, pesticides and their residues and by-products may accumulate in the soil at unacceptable high levels, resulting in soil contamination (Morillo and Villaverde, 2017) and posing potential risks to soil organisms, plants, and subsequent crop cycles. For instance, farmers in Southeast Asia who lack specialized knowledge often rely on the guidance of pesticide store clerks and end up using excessive amounts of pesticides to control pests in their fields (Schreinemachers *et al.*, 2017). Conversely, soils can act as a secondary reservoir of pollutants due to the exchange of substances between the air and soil (Pokhrel *et al.*, 2018).

Pesticides can disrupt soil microbial communities, essential for nutrient cycling, organic matter decomposition, and soil fertility. Some pesticides may inhibit the activity of beneficial soil organisms, leading to imbalances in soil microbiota and reduced soil health.

Pesticide contamination can also harm non-target organisms in soil ecosystems, including earthworms, beneficial insects, soil-dwelling microbes, and small mammals. These organisms play crucial roles in soil structure maintenance, nutrient cycling, and ecosystem functioning. Soil contamination by pesticides can disrupt soil food webs and decrease biodiversity, impacting the resilience and stability of terrestrial ecosystems.

Moreover, pesticide residues in soil may affect crop growth, yield, and quality. Some pesticides can inhibit seed germination, root development, or nutrient uptake by plants, leading to reduced crop productivity and economic losses for farmers. The contamination of soil may also result in the accumulation of pesticide residues in food crops, posing risks to human health through dietary exposure.

To add more, soil contamination by pesticides can impair ecosystem services provided by soil ecosystems, including nutrient cycling, water filtration, carbon sequestration, and regulation of greenhouse gas emissions. Disruption of these services can have far-reaching impacts on ecosystem resilience and human well-being.

In the water environments, pesticide leaching from soils leads to the contamination of subsurface water systems. Due to pesticide loading from surface runoff, erosion, and groundwater discharge to an adjacent river/stream, the related surface water system may also be polluted.

The contamination of water can have ecological impacts by harming aquatic organisms such as fish, amphibians, invertebrates, and aquatic plants. Even low concentrations of pesticides can disrupt aquatic ecosystems by affecting reproduction, growth, behaviour, and food webs, leading to biodiversity loss and ecosystem degradation. Contaminated water sources can expose humans to pesticides through drinking water, recreational activities (e.g., swimming, fishing), and consumption of contaminated aquatic organisms.

Moreover, pesticide contamination can degrade water quality, affecting its suitability for drinking, agriculture, industry, and wildlife habitat. High pesticide concentrations may exceed regulatory limits, leading to water-use restrictions, increased treatment costs, and potential ecological and economic impacts.

I.1.6.1. The case of France

France used an average of 4.8 kg of pesticides per hectare of agricultural land in 2022 (Mordor Intelligence, 2024). The extensive application of pesticides gives rise to concerns regarding their environmental destiny and their consequent effects on ecosystems.

Various types of pesticides have been detected in French water sources despite their monitoring in water bodies under the European Water Framework Directive Hering (Hering *et al.*, 2010).

In 2023, the French National Agency for Food, Environmental, and Occupational Health & Safety (ANSES) made a study by collecting samples from both surface and groundwater, focusing on 157 pesticides and their metabolites. It was found that 89 of these pesticides were

detected at least once in raw water and 77 times in treated water. Seven "emerging" compounds have resulted in surpassing the quality limit of 0.1 µg/liter, with one of these being a metabolite of chlorothalonil known as R471811. This particular metabolite is the most commonly detected pesticide by-product, present in over half of the samples. It originates from the environmental breakdown of chlorothalonil, a fungicide that has been prohibited in France since 2020.

Furthermore, metolachlor ESA was detected in over half of the samples, with fewer than 2% of them surpassing the management threshold of 0.9 µg/liter set for irrelevant metabolites (ANSES , 2023). According to the samples collected by the agency, ANSES estimates that approximately 34% of water in France may not meet regulatory standards (Thompson, 2023).

On the other hand, recent research on French agricultural soils has revealed the widespread presence of numerous pesticide residues, posing a threat to biodiversity. A study made by researchers from INRAE, in partnership with the University of Bordeaux, aimed to evaluate pesticide contamination in nearly fifty soils collected across mainland France in 2022 (Bispo, A., 2023).

The results revealed that 98% of the examined sites contained at least one compound. A total of 67 different molecules were identified, predominantly fungicides and herbicides. Glyphosate and its primary metabolite, Aminomethylphosphonic Acid (AMPA), were the most commonly detected compounds, present in 70% and 83% of the soil samples, respectively. Triazole fungicides (such as epoxiconazole) and succinate dehydrogenase inhibitors (SDHI) were also observed in over 40% of the sites, along with pyrethroid insecticides like tefluthrin. These findings pose a high risk of chronic toxicity to earthworms, in addition to other environmental issues linked to soil contamination (Pelosi *et al.*, 2022).

Researchers at the University of Orléans investigated a recent analytical study to measure the concentration of 111 pesticides in the environment across France (Froger *et al.*, 2023). They took 47 soil samples across the country, including several types of soils from arable lands, grasslands, forests ***(Figure I-8).***

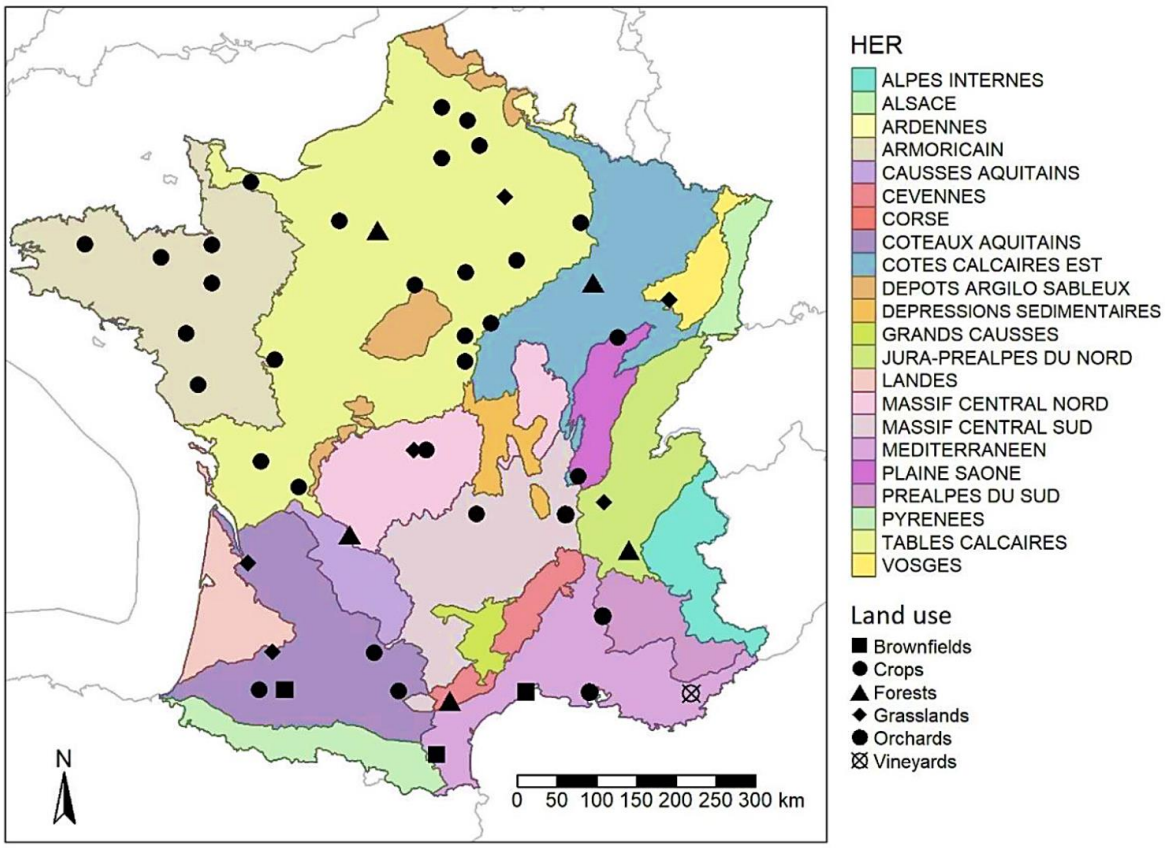

***Figure I-8**: sampling sites selected for the study displayed by land use with hydroecoregions (HER) distributions (Froger et al., 2023).*

The results indicated that a total of 67 substances were detected in nearly all of the soil samples, including both organic fields and untreated areas like forests and permanent grasslands. Many pesticides, including glyphosate, AMPA, pendimethalin, diflufenican, triazole compounds, boscalid, prochloraz, and imidacloprid, were identified as common and highly concentrated compounds. The number of pesticides found per site ranged from 1 to 33 (with a median of 9 substances), with the total cumulative concentration varied from 0.08 to 1274 ng/g.

Despite regulatory efforts, challenges remain in effectively reducing pesticide pollution in France. Agricultural intensification, pesticide resistance, inadequate enforcement of regulations, and socio-economic factors pose obstacles to achieving sustainable pest management practices. Addressing these challenges requires collaborative efforts among policymakers, farmers, industry stakeholders, scientists, and civil society to promote agroecological approaches, support innovation, and foster a transition towards more environmentally friendly agricultural practices.

I.1.6.2. The case of Vietnam

As the work involved in this thesis was done in collaboration with the research group of Dr. Duy Quang Dao at Duy Tan University in Vietnam, it is important to shed light on the pollution caused by pesticides in this country.

In Vietnam, a big quantity of chemicals has been extensively used to insure high agricultural productivity and to get rid of vector-borne illnesses over the last decades. The use of pesticide increased significantly from 100 tons per year in the 1950s to 35,000 tons in 2002, and further to approximately 105,000 tons a decade later. During the period from 2005 to 2012, pesticide imports experienced an average growth rate of 18.8% in terms of value and 10.6% in terms of quantity (Van Hoi *et al.*, 2013).

In 2002, there were over 7,000 cases (involving 7,647 individuals) of food poisoning due to pesticide residues, resulting in 277 fatalities across 37 of the 61 provinces. Fenobucarb, hexaconazole, propiconazole, and pretilachlor, are the most used pesticides in Vietnamese agriculture. In paddy rice farming, farmers prefer imidacloprid, fenitrothion, fenobucarb, and dichlorvos (Berg, 2001).

Research indicated significant concentrations of these pesticides residues in water, soils, and sediments found in fields, field ditches, and canals (Chau *et al.*, 2015; Lamers *et al.*, 2011; Toan *et al.*, 2013). Vietnam has banned the use of certain organochlorine pesticides like dichlorodiphenyltrichloroethane (DDTs), hexachlorobenzene (HCB), and hexachlorocyclohexanes (HCHs) (Sinh, N.N., 1999).

Many of these prohibited pesticides persist at relatively high concentrations in the environment across Vietnam. Some of these substances are toxic and/or persistent, posing potential risks to the environment.Carvalho *et al.* for example examined the residues of over 70 pesticides in the Mekong Delta region (Carvalho *et al.*, 2008). They discovered sediment concentrations of SDDT ranging from 0.45 to 67.5 ng/g dry weight and concentrations in the soft tissues of bivalve molluscs ranging from 5.5 to 123.0 ng/g dry weight.

In 2011, Hoai and colleagues conducted a study to evaluate the concentrations of pesticides residues in biota (vegetables and fish), and in the environment (water, soil) (Hoai *et al.*, 2011). The study was made on two sites in Northern Vietnam (Minh Dai and Hoang Liet) (***Figure I-9***), focusing on certain presently employed pesticides as well as some formerly utilized persistent organochlorine pesticides.

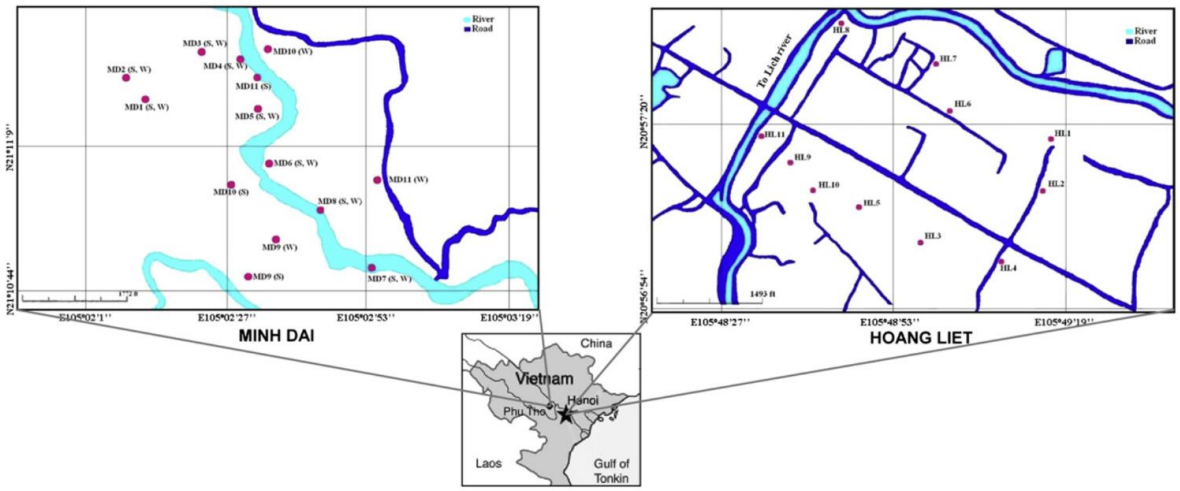

***Figure I-9**: Hoang Liet and Minh Dai sampling sites (Hoai et al., 2011).*

74 samples taken from water, soil, vegetable, tea and fish were analysed, targeting 25 pesticide compounds including some popular families like organochlorine.

The authors found that all the fish samples contained DDT, Drin and HCH pesticides with concentration up to 80 ng/g wet wt., and cypermethrin, cyfluthrin and trichlorfon with concentration up to 674 ng/g wet wt. Similarly, in the soil samples, they detected different organochlorine pesticides like DDT, DDE and DDD. Additionally, HCHs, Drins, and DDTs were the predominant compounds found in tea and vegetable samples. Moreover, fenobucarb, trichlorfon, cyfluthrin, and cypermethrin were detected across a wide range of concentrations, with cyfluthrin reaching levels as high as 62 ng/g wet wt.

Currently, management practices of farmers are not sustainable from the human and environmental health point of view. The Vietnamese government has put considerable effort into the promotion of different campaigns aiming to reduce chemical inputs in agricultural production. However, there has been no consistent improvement observed in pesticide market so far.

I.2. Research motivation and objectives

As we have known that the pesticides after application will be vaporized in the atmosphere and transferred into the soil and water environments, contaminating the crops and aquatic species, as well as risking human health (***Figure I-10***), several questions can be asked. What are the mechanisms and kinetics of the pesticide's degradation processes? Its environmental fate? Its toxicity towards the species in the ecosystems and human health?

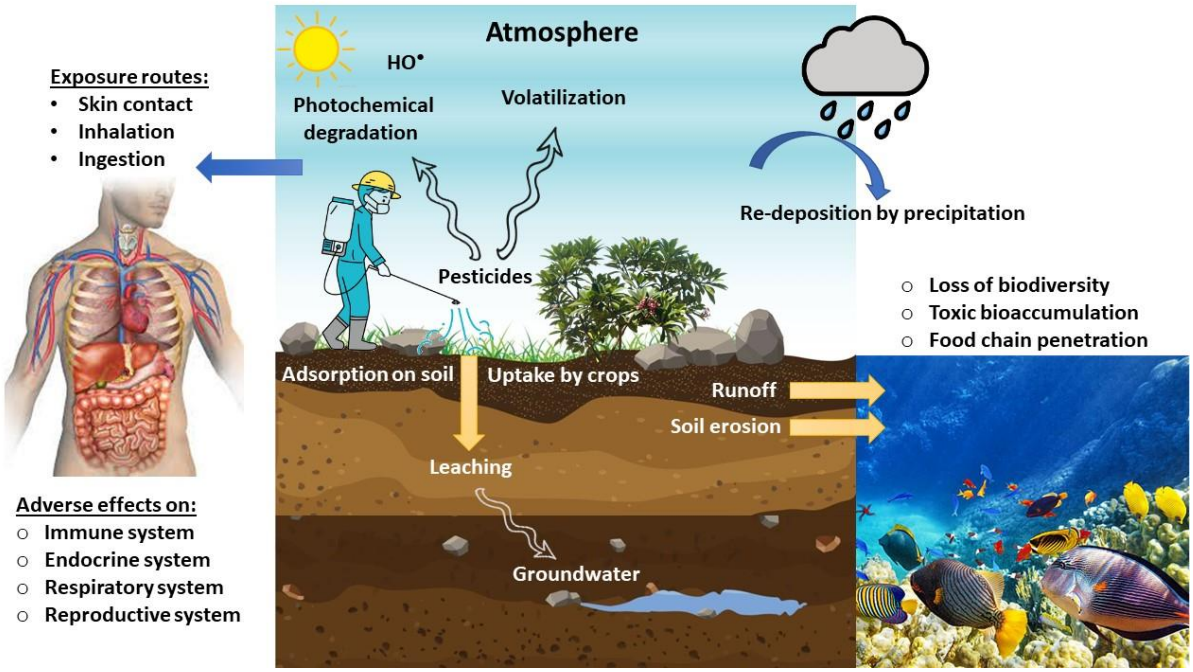

Figure I-10*: schematic illustration of the transport pathways of pesticides and their adverse effects.*

To answer these questions, we studied the environmental degradation of three used pesticides including phosmet (insecticide), chlorpyrifos (insecticide), and fenpyrazamine (fungicide), by hydroxyl radicals where no literature data exists.

Through this study, we were able to understand the decomposition of these pesticides by their oxidation reaction with $HO^{\bullet}$ under environmental conditions, by using molecular simulations and applying the DFT method. Three different reaction pathways were considered: formal hydrogen transfer (FHT), radical adduct formation (RAF), and single electron transfer (SET). The thermodynamics, mechanisms, and kinetics of the reactions, as well as the lifetime of these pesticides were examined in both gas and aqueous phases at different temperatures. Finally, the ecotoxicity of these pesticides and their degradation by-products were estimated in the aquatic environment to understand their impact on aquatic organisms.

I.3. References

Al-Alam, J., Sonnette, A., Delhomme, O., Alleman, L.Y., Coddeville, P., Millet, M., 2022. Pesticides in the Indoor Environment of Residential Houses: A Case Study in Strasbourg, France. International Journal of Environmental Research and Public Health 19, 14049. https://doi.org/10.3390/ijerph192114049

Alexandratos, N., Bruinsma, J. (Eds.), 2012. World agriculture towards 2030/2050: the 2012 revision, ESA Working Papers 12-03. https://doi.org/10.22004/ag.econ.288998

Alleva, R., Manzella, N., Gaetani, S., Bacchetti, T., Bracci, M., Ciarapica, V., Monaco, F., Borghi, B., Amati, M., Ferretti, G., Tomasetti, M., 2018. Mechanism underlying the effect of long-term exposure to low dose of pesticides on DNA integrity. Environmental Toxicology 33, 476–487. https://doi.org/10.1002/tox.22534

F. M. Fishel, Pesticide-Organism Interactions, PI-43 Document, Pesticide Information Office, Florida Cooperative Extension Service, Institute of Food and Agricultural Sciences, University of Florida, 2005. (http:// edis.ifas.ufl.edu/pdffiles/PI/PI0800.pdf)

Berg, H., 2001. Pesticide use in rice and rice–fish farms in the Mekong Delta, Vietnam. Crop Protection 20, 897–905. https://doi.org/10.1016/S0261-2194(01)00039-4

Bilal, M., Iqbal, H.M.N., Barceló, D., 2019. Persistence of pesticides-based contaminants in the environment and their effective degradation using laccase-assisted biocatalytic systems. Science of The Total Environment 695, 133896. https://doi.org/10.1016/j.scitotenv.2019.133896

Boedeker, W., Watts, M., Clausing, P., Marquez, E., 2020. The global distribution of acute unintentional pesticide poisoning: estimations based on a systematic review. BMC Public Health 20, 1875. https://doi.org/10.1186/s12889-020-09939-0

Carvalho, F.P., 2017. Pesticides, environment, and food safety. Food and Energy Security 6, 48–60. https://doi.org/10.1002/fes3.108

Carvalho, F.P., Villeneuve, J.P., Cattini, C., Tolosa, I., Thuan, D.D., Nhan, D.D., 2008. Agrochemical and polychlorobyphenyl (PCB) residues in the Mekong River delta, Vietnam. Marine Pollution Bulletin 56, 1476–1485. https://doi.org/10.1016/j.marpolbul.2008.04.042

Chau, N.D.G., Sebesvari, Z., Amelung, W., Renaud, F.G., 2015. Pesticide pollution of multiple drinking water sources in the Mekong Delta, Vietnam: evidence from two provinces. Environmental Science and Pollution Research 22, 9042–9058. https://doi.org/10.1007/s11356-014-4034-x

Chawla, N., Sunita, S., Kamlesh, K., Kumar, R., 2013. Bioremediation: An emerging technology for remediation of pesticides. Research Journal of Chemistry and Environment 17, 88–105.

Chen, T., Tan, J., Wan, Z., Zou, Y., Kessete Afewerky, H., Zhang, Z., Zhang, T., 2017. Effects of Commonly Used Pesticides in China on the Mitochondria and Ubiquitin-Proteasome System in Parkinson's Disease. International Journal of Molecular Sciences 18, 2507. https://doi.org/10.3390/ijms18122507

Cui, S., Hough, R., Yates, K., Osprey, M., Kerr, C., Cooper, P., Coull, M., Zhang, Z., 2020. Effects of season and sediment-water exchange processes on the partitioning of pesticides in the catchment environment: Implications for pesticides monitoring. Science of The Total Environment 698, 134228. https://doi.org/10.1016/j.scitotenv.2019.134228

Culliney, T.W., 2014. Crop Losses to Arthropods, in: Pimentel, D., Peshin, R. (Eds.), Integrated Pest Management: Pesticide Problems, Vol.3. Springer Netherlands, Dordrecht, pp. 201–225. https://doi.org/10.1007/978-94-007-7796-5_8

Damalas, C.A., Eleftherohorinos, I.G., 2011. Pesticide Exposure, Safety Issues, and Risk Assessment Indicators. International Journal of Environmental Research and Public Health 8, 1402–1419. https://doi.org/10.3390/ijerph8051402

Dasgupta, S., Meisner, C., Huq, M., 2005. Health Effects And Pesticide Perception As Determinants Of Pesticide Use: Evidence From Bangladesh, Policy Research Working Papers. The World Bank. https://doi.org/10.1596/1813-9450-3776

WHO (2019). Exposure to highly hazardous pesticides: a major public health concern. (https://iris.who.int/bitstream/handle/10665/329501/WHO-CED-PHE-EPE-19.4.6-eng.pdf?ua=1)

Pesticides Industry Sales and Usage: 1996 and 1997 Market Estimates, US EPA, Office of Pesticide Programs, June 13, 2000. (www.epa.gov/ oppbead1/pestsales/97pestsales/table3.htm).

FAO, 2022. Pesticides use, pesticides trade and pesticides indicators – Global, regional and country trends, 1990–2020. FAOSTAT Analytical Briefs, no. 46. Rome. https://doi.org/10.4060/cc0918en.

C. Frazar, The Bioremediation and Phytoremediation of Pesticide- Contaminated Sites, National Network of Environmental Studies (NNEMS) Fellow, Washington DC 2000.

RFI, 2023. French child compensated for birth defects caused by glyphosate. URL https://www.rfi.fr/en/france/20231012-french-minor-compensated-for-birth-defects-caused-by-glyphosate (accessed 5.16.24).

Froger, C., Jolivet, C., Budzinski, H., Pierdet, M., Caria, G., Saby, N.P.A., Arrouays, D., Bispo, A., 2023. Pesticide Residues in French Soils: Occurrence, Risks, and Persistence. Environmental Science & Technology 57, 7818–7827. https://doi.org/10.1021/acs.est.2c09591

Gavrilescu, M., 2005. Fate of Pesticides in the Environment and its Bioremediation. Engineering in Life Sciences 5, 497–526. https://doi.org/10.1002/elsc.200520098

Gonçalves, A.M.M., Rocha, C.P., Marques, J.C., Gonçalves, F.J.M., 2021a. Fatty acids as suitable biomarkers to assess pesticide impacts in freshwater biological scales – A review. Ecological Indicators 122, 107299. https://doi.org/10.1016/j.ecolind.2020.107299

Gonçalves, A.M.M., Rocha, C.P., Marques, J.C., Gonçalves, F.J.M., 2021b. Enzymes as useful biomarkers to assess the response of freshwater communities to pesticide exposure – A review. Ecological Indicators 122, 107303. https://doi.org/10.1016/j.ecolind.2020.107303

Gramlich, A., Stoll, S., Stamm, C., Walter, T., Prasuhn, V., 2018. Effects of artificial land drainage on hydrology, nutrient and pesticide fluxes from agricultural fields – A review. Agriculture, Ecosystems & Environment 266, 84–99. https://doi.org/10.1016/j.agee.2018.04.005

Hering, D., Borja, A., Carstensen, J., Carvalho, L., Elliott, M., Feld, C.K., Heiskanen, A.-S., Johnson, R.K., Moe, J., Pont, D., Solheim, A.L., de Bund, W. van, 2010. The European Water Framework Directive at the age of 10: A critical review of the achievements with recommendations for the future. Science of The Total Environment 408, 4007–4019. https://doi.org/10.1016/j.scitotenv.2010.05.031

Hoai, P.M., Sebesvari, Z., Minh, T.B., Viet, P.H., Renaud, F.G., 2011. Pesticide pollution in agricultural areas of Northern Vietnam: Case study in Hoang Liet and Minh Dai communes. Environmental Pollution 159, 3344–3350. https://doi.org/10.1016/j.envpol.2011.08.044

Huang, B., Yan, D., Wang, Xiaoning, Wang, Xianli, Fang, W., Zhang, D., Ouyang, C., Wang, Q., Cao, A., 2019. Soil fumigation alters adsorption and degradation behavior of

pesticides in soil. Environmental Pollution 246, 264–273. https://doi.org/10.1016/j.envpol.2018.12.003
Huang, Y., Xiao, L., Li, F., Xiao, M., Lin, D., Long, X., Wu, Z., 2018. Microbial Degradation of Pesticide Residues and an Emphasis on the Degradation of Cypermethrin and 3-phenoxy Benzoic Acid: A Review. Molecules 23, 2313. https://doi.org/10.3390/molecules23092313
Kalyabina, V.P., Esimbekova, E.N., Kopylova, K.V., Kratasyuk, V.A., 2021. Pesticides: formulants, distribution pathways and effects on human health – a review. Toxicology Reports 8, 1179–1192. https://doi.org/10.1016/j.toxrep.2021.06.004
Katagi, T., 2013. Soil Column Leaching of Pesticides, in: Whitacre, D.M. (Ed.), Reviews of Environmental Contamination and Toxicology Volume 221. Springer, New York, NY, pp. 1–105. https://doi.org/10.1007/978-1-4614-4448-0_1
Kaushal, J., Khatri, M., Arya, S.K., 2021. A treatise on Organophosphate pesticide pollution: Current strategies and advancements in their environmental degradation and elimination. Ecotoxicology and Environmental Safety 207, 111483. https://doi.org/10.1016/j.ecoenv.2020.111483
Khedr, T., Hammad, A.A., Elmarsafy, A.M., Halawa, E., Soliman, M., 2019. Degradation of some organophosphorus pesticides in aqueous solution by gamma irradiation. Journal of Hazardous Materials 373, 23–28. https://doi.org/10.1016/j.jhazmat.2019.03.011
Kim, K.-H., Kabir, E., Jahan, S.A., 2017. Exposure to pesticides and the associated human health effects. Science of The Total Environment 575, 525–535. https://doi.org/10.1016/j.scitotenv.2016.09.009
Lamers, M., Anyusheva, M., La, N., Nguyen, V.V., Streck, T., 2011. Pesticide Pollution in Surface- and Groundwater by Paddy Rice Cultivation: A Case Study from Northern Vietnam. CLEAN – Soil, Air, Water 39, 356–361. https://doi.org/10.1002/clen.201000268
Liu, L., Bilal, M., Duan, X., Iqbal, H.M.N., 2019. Mitigation of environmental pollution by genetically engineered bacteria — Current challenges and future perspectives. Science of The Total Environment 667, 444–454. https://doi.org/10.1016/j.scitotenv.2019.02.390
Malakootian, M., Shahesmaeili, A., Faraji, M., Amiri, H., Silva Martinez, S., 2020. Advanced oxidation processes for the removal of organophosphorus pesticides in aqueous matrices: A systematic review and meta-analysis. Process Safety and Environmental Protection 134, 292–307. https://doi.org/10.1016/j.psep.2019.12.004
Mordor Intelligence provides Market Research - Consulting, Reports, Advisory, Sizing; Consulting - Client Research, Market Analysis, Competitive Landscape Analysis, Global Strategic Business Reports and Custom Market Research. Contact Us Now for any kind of report, 2024. URL https://www.mordorintelligence.com/market-analysis (accessed 5.13.24).
Morillo, E., Villaverde, J., 2017. Advanced technologies for the remediation of pesticide-contaminated soils. Science of The Total Environment 586, 576–597. https://doi.org/10.1016/j.scitotenv.2017.02.020
Nyer, E.K. (Ed.), 2000. In Situ Treatment Technology, 2nd ed. CRC Press, Boca Raton. https://doi.org/10.1201/9781420032642
Page, A., Liu, S., Gunnell, D., Astell-Burt, T., Feng, X., Wang, L., Zhou, M., 2017. Suicide by pesticide poisoning remains a priority for suicide prevention in China: Analysis of national mortality trends 2006–2013. Journal of Affective Disorders 208, 418–423. https://doi.org/10.1016/j.jad.2016.10.047
Parra-Arroyo, L., González-González, R.B., Castillo-Zacarías, C., Melchor Martínez, E.M., Sosa-Hernández, J.E., Bilal, M., Iqbal, H.M.N., Barceló, D., Parra-Saldívar, R., 2022.

Highly hazardous pesticides and related pollutants: Toxicological, regulatory, and analytical aspects. Science of the Total Environment 807, 151879. https://doi.org/10.1016/j.scitotenv.2021.151879

Pelosi, C., Bertrand, C., Bretagnolle, V., Coeurdassier, M., Delhomme, O., Deschamps, M., Gaba, S., Millet, M., Nélieu, S., Fritsch, C., 2022. Glyphosate, AMPA and glufosinate in soils and earthworms in a French arable landscape. Chemosphere 301, 134672. https://doi.org/10.1016/j.chemosphere.2022.134672

Pereira, L.C., de Souza, A.O., Bernardes, M.F.F., Pazin, M., Tasso, M.J., Pereira, P.H., Dorta, D.J., 2015. A perspective on the potential risks of emerging contaminants to human and environmental health.Environmental Science and Pollution Research 22, 13800–13823. https://doi.org/10.1007/s11356-015-4896-6

Bispo, A., 2023. Persistence of pesticide residues in soils: the benefits of national monitoring. University of Bordeaux. URL https://www.u-bordeaux.fr/en/news/persistence-of-pesticide-residues-in-soils-the-benefits-of-national-monitoring (accessed 5.14.24).

Pokhrel, B., Gong, P., Wang, X., Chen, M., Wang, C., Gao, S., 2018. Distribution, sources, and air–soil exchange of OCPs, PCBs and PAHs in urban soils of Nepal. Chemosphere 200, 532–541. https://doi.org/10.1016/j.chemosphere.2018.01.119

ANSES, 2023. Polluants émergents dans l'eau potable : le point sur les principaux résultats de la dernière campagne nationale. URL https://www.anses.fr/fr/content/polluants-emergents-dans-leau-potable-le-point-sur-les-principaux-resultats-de-la-derniere-2 (accessed 5.14.24).

Qu, C., Albanese, S., Lima, A., Hope, D., Pond, P., Fortelli, A., Romano, N., Cerino, P., Pizzolante, A., De Vivo, B., 2019. The occurrence of OCPs, PCBs, and PAHs in the soil, air, and bulk deposition of the Naples metropolitan area, southern Italy: Implications for sources and environmental processes. Environment International 124, 89–97. https://doi.org/10.1016/j.envint.2018.12.031

Raschke, A.M., Burger, A.E.C., 1997. Risk Assessment as a Management Tool Used to Assess the Effect of Pesticide Use in an Irrigation System, Situated in a Semi-Desert Region. Archives of Environmental Contamination and Toxicology 32, 42–49. https://doi.org/10.1007/s002449900153

J. Moerner, R. Bos, M. Fredrix, Reducing and eliminating the use of persistent organic pesticides, in Guidance on Alternative Strategies for Sustainable Pest and Vector Management, United Nations Environment Programme (UNEP), Geneva 2002.

Schreinemachers, P., Chen, H., Nguyen, T.T.L., Buntong, B., Bouapao, L., Gautam, S., Le, N.T., Pinn, T., Vilaysone, P., Srinivasan, R., 2017. Too much to handle? Pesticide dependence of smallholder vegetable farmers in Southeast Asia. Science of The Total Environment 593–594, 470–477. https://doi.org/10.1016/j.scitotenv.2017.03.181

Sinh, N.N., Thuy, L.T.B., Kinh, N.K., Thang, L.B., 1999. The persistent organic pollutants and their management in Vietnam. In: Proceedings of the Regional Workshop on the Management of Persistent Organic Pollutant, POPs, United Nations Environment Programme, March 16e19, 1999, Hanoi, Vietnam, 385e406.

Socorro, J., Durand, A., Temime-Roussel, B., Gligorovski, S., Wortham, H., Quivet, E., 2016. The persistence of pesticides in atmospheric particulate phase: An emerging air quality issue. Scientific Reports 6, 33456. https://doi.org/10.1038/srep33456

Stenrød, M., Perceval, J., Benoit, P., Almvik, M., Bolli, R.I., Eklo, O.M., Sveistrup, T.E., Kværner, J., 2008. Cold climatic conditions: Effects on bioavailability and leaching of the mobile pesticide metribuzin in a silt loam soil in Norway. Cold Regions Science and Technology, Fifth International Conference on Contaminants in Freezing Ground 53, 4–15. https://doi.org/10.1016/j.coldregions.2007.06.007

Suthersan, S.S., 2001. Natural and Enhanced Remediation Systems. CRC Press, Boca Raton. https://doi.org/10.1201/9781420033069

Sutton, R., Xie, Y., Moran, K.D., Teerlink, J., 2019. Occurrence and Sources of Pesticides to Urban Wastewater and the Environment, in: Pesticides in Surface Water: Monitoring, Modeling, Risk Assessment, and Management, ACS Symposium Series. American Chemical Society, pp. 63–88. https://doi.org/10.1021/bk-2019-1308.ch005

R. Singhvi, R.N. Koustas, M. Mohn, Contaminants and Remediation Options at Pesticide Sites, EPA/600/R-94/202, US EPA Office of Research and Development, Risk Reduction Engineering Laboratory, Cincinnati 1994.

Thompson, H., 2023. Traces of banned pesticide found in French tap water. URL https://www.connexionfrance.com/news/traces-of-banned-pesticide-found-in-french-tap-water/170700 (accessed 5.14.24).

Toan, P.V., Sebesvari, Z., Bläsing, M., Rosendahl, I., Renaud, F.G., 2013. Pesticide management and their residues in sediments and surface and drinking water in the Mekong Delta, Vietnam. Science of The Total Environment 452–453, 28–39. https://doi.org/10.1016/j.scitotenv.2013.02.026

Ulrich, U., Lorenz, S., Hörmann, G., Stähler, M., Neubauer, L., Fohrer, N., 2022. Multiple pesticides in lentic small water bodies: Exposure, ecotoxicological risk, and contamination origin. Science of The Total Environment 816, 151504. https://doi.org/10.1016/j.scitotenv.2021.151504

Van Hoi, P., Mol, A., Oosterveer, P., 2013. State governance of pesticide use and trade in Vietnam. NJAS - Wageningen Journal of Life Sciences 67, 19–26. https://doi.org/10.1016/j.njas.2013.09.001

Vryzas, Z., 2018. Pesticide fate in soil-sediment-water environment in relation to contamination preventing actions. Current Opinion in Environmental Science & Health, Pesticides in agriculture: environmental and health risks 4, 5–9. https://doi.org/10.1016/j.coesh.2018.03.001

Woodrow, J.E., Gibson, K.A., Seiber, J.N., 2019. Pesticides and Related Toxicants in the Atmosphere, in: de Voogt, P. (Ed.), Reviews of Environmental Contamination and Toxicology Volume 247. Springer International Publishing, Cham, pp. 147–196. https://doi.org/10.1007/398_2018_19

Yusa, V., Millet, M., Coscolla, C., Roca, M., 2015. Analytical methods for human biomonitoring of pesticides. A review. Analytica Chimica Acta 891, 15–31. https://doi.org/10.1016/j.aca.2015.05.032

Zaller, J.G., Kruse-Plaß, M., Schlechtriemen, U., Gruber, E., Peer, M., Nadeem, I., Formayer, H., Hutter, H.-P., Landler, L., 2022. Pesticides in ambient air, influenced by surrounding land use and weather, pose a potential threat to biodiversity and humans. Science of The Total Environment 838, 156012. https://doi.org/10.1016/j.scitotenv.2022.156012

Chapter II. Molecular simulations

II.1. Theoretical chemistry background

The inception of theoretical chemistry dates back to the 1930s when it began employing mathematical and physical principles to delve into foundational aspects of chemistry. Substantial expansion occurred in the late 1960s with the introduction of advanced computational tools, leading to significant growth in theoretical chemistry. This field primarily focuses on scrutinizing the electron behaviour within molecules, unravelling crucial structural characteristics like geometries and vibrational frequencies. Additionally, it aims to analyse the energetic aspects of chemical entities participating in a reaction, encompassing reagents, transition states, products, and molecular complexes. Schrödinger equation and Born-Oppenheimer approximation are the basics of this field.

- The Schrödinger equation

Erwin Schrödinger introduced the Schrödinger equation in 1926 through his paper titled "An undulatory theory of the mechanics of atoms and molecules" (Schrödinger, 1996).

This differential equation serves as a crucial element in quantum physics, illustrating the evolution of the wave-function that characterizes the state of a particle over time. As a time-dependent equation, it stands as a fundamental principle governing all phenomena in the microscopic world.

The Schrödinger equation is written as:

$$i\hbar\frac{d\Psi}{dt} = \widehat{H}\Psi \qquad \textbf{\textit{Eq. II-1}}$$

A mathematical function, denoted as Ψ and referred to as a wave function, is employed to characterize a system comprising N particles. The likelihood of finding these particles within a specified volume at a particular moment is dictated by the magnitude squared of the wave function, denoted as $|\Psi|^2$. In the Schrödinger equation, $\hbar$ represents the reduced Planck constant, t signifies time, and $\widehat{H}$ denotes the Hamiltonian operator. Assuming the time independence of $\widehat{H}$, ***Eq. II-1*** can be expressed as follows:

$$\widehat{H}\Psi = E\Psi \qquad \textbf{\textit{Eq. II-2}}$$

where E is the system energy.

The Hamiltonian operator can be written as follows:

$$\widehat{H} = \widehat{\mathrm{T}}_{\mathrm{n}} + \widehat{\mathrm{T}}_{\mathrm{e}} + \widehat{\mathrm{V}}_{\mathrm{ee}} + \widehat{\mathrm{V}}_{\mathrm{en}} + \widehat{\mathrm{V}}_{\mathrm{nn}} \qquad \textbf{\textit{Eq. II-3}}$$

In Equation ***Eq. II-3***, $\widehat{\mathrm{T}}_{\mathrm{n}}$ represents the operator linked to the kinetic energy of nuclei, $\widehat{\mathrm{T}}_{\mathrm{e}}$ is the operator associated with the kinetic energy of electrons, $\widehat{\mathrm{V}}_{\mathrm{ee}}$ accounts for the potential energy arising from electron-electron interactions, $\widehat{\mathrm{V}}_{\mathrm{en}}$ corresponds to the potential energy stemming from electron-nucleus interactions, and $\widehat{\mathrm{V}}_{\mathrm{nn}}$ signifies the potential energy arising from nucleus-nucleus interactions.

Solving this equation proves challenging in the majority of cases due to its nature as a second-order partial differential equation with a considerable number of variables. As a result, resorting to approximations becomes necessary to facilitate its resolution.

- Born-Oppenheimer approximation

The Born-Oppenheimer approximation is essential for simplifying the treatment of complex quantum systems, particularly those involving the motion of atomic nuclei and electrons in molecules. The key idea behind the Born-Oppenheimer approximation is to separate the motion of electrons and nuclei in a molecule. This separation exploits the significant difference in mass between electrons and nuclei. It simplifies the calculation of wave functions and energy levels of a molecule. The hypothesis proposed by Born and Oppenheimer states that it's feasible to separate the motion of electrons from that of nuclei, presuming that nuclei move at a significantly slower pace compared to electrons. In this regard, nuclei are treated as stationary entities when analysing the movement of electrons within the molecule. Consequently, internuclear distances are regarded as parameters in the analysis (Born and Oppenheimer, 1927).

The Hamiltonian operator associated with the nuclei's kinetic energy is consequently neglected.

$$\hat{T}_n = 0 \qquad \textbf{\textit{Eq. II-4}}$$

II.1.1. Potential energy surface (PES)

The potential energy surface (PES) for chemical reactions was initially introduced by the French physicist René Marcelin in 1913. Subsequently, the first computation of a PES was conducted by Eyring and Polanyi in 1931, utilizing a combination of experimental data and theoretical methods.

The potential energy surface is a fundamental concept in chemistry, illustrating the correlation between the energy and geometric structure of a molecule or system. This concept stems from the big mass difference between nuclei and electrons, and it can be comprehended by envisioning the nucleus as immobile relative to the electrons. Typically depicted as a three-dimensional plot, the PES represents the energy in relation to the positions of atoms or molecules within the system (Kwon *et al.*, 2021). This tool is useful for predicting the behaviour of molecules during chemical reactions by providing insights into potential energy barriers and the pathways of the reactions.

In the field of quantum mechanics, the Born-Oppenheimer approximation is frequently utilized to model chemical reactions through the application of the PES.

The foundational aspect of quantum chemistry investigations lies in the molecular structure, which serves as the primary unit of analysis. However, it is appropriate not only to examine a

specific structure but to encompass all potential structures within a compound family. Each of these structures is distinguished by a corresponding potential energy, and the PES represents a hypersurface encapsulating the potential energies associated with every possible atomic arrangement. The dimensions of the PES stems from the three-dimensional nature of the Cartesian space (3N coordinates describe the structure of a molecule with N atoms).

In a structure composed of N atoms, there exist:

- 3N-5 degrees of freedom for linear species (where the exclusion of the five degrees of freedom pertains to the translational movements of the entire molecular system along the x, y, and z axes, as well as rotations around the x and y axes).
- 3N-6 degrees of freedom for nonlinear species (where the elimination of the six degrees of freedom corresponds to the translational and rotational motions of the molecular system along the x, y, and z axes) (Truhlar, 2003).

II.1.2. Characterisation of stationary points

Characterising stationary points on a PES is an essential step in understanding the behaviour of a molecular system. To find the configuration where the potential energy is at a minimum or a stationary point on the PES, geometry optimization of the molecular structure should be done using computational methods.

The process starts with the potential energy calculation of the system for the given molecular geometry, followed by the gradient calculation of the potential energy with respect to the atomic coordinates. The gradient provides information on how the potential energy changes as the atoms are displaced.

The optimized geometries of the reactants, products, and molecular complexes are represented as points on the potential energy surface. These points are called stationary points, represented as local and global minima corresponding to an optimal molecular structure, and saddle points known as transition states (***Figure II-1***).

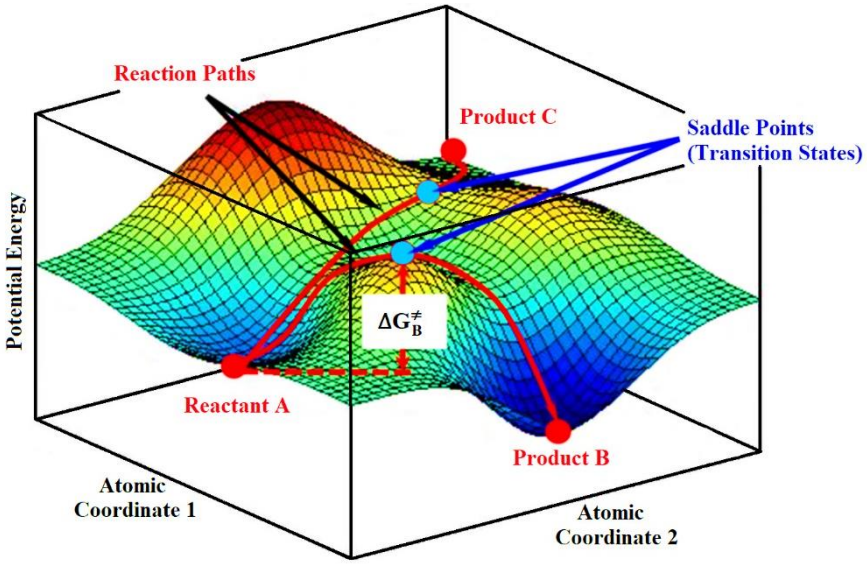

***Figure II-1**: schematic representation of the PES (Shi et al.).*

The PES's concave or convex features identify the stationary point, influencing the characteristics of molecular structures corresponding to these points on the PES. The Hessian matrix dictates the curvature direction of the PES. It possesses dimensions of (3N-6) × (3N-6), with its elements representing the second derivatives of the potential energy at a specific point on the surface.

Upon diagonalizing this matrix, the eigenvalues acquired provide insights into the nature of the stationary point. Specifically, on the PES, the stationary point corresponds to:

- A minimum on the PES when no negative eigenvalue is obtained.
- A saddle point of order 1 in case a negative eigenvalue is obtained.
- A saddle point of order n (where n > 1) if multiple negative eigenvalues are obtained.

The transition state point (saddle point of order 1) corresponds to the lowest energy barrier on the path that links the two minima (reactants and products). It represents a maximum along the direction of the IRC (Intrinsic Reaction Coordinate), and a minimum along the direction of the other coordinates (Gonzalez and Schlegel, 1989, 1990).

This stationary point is mathematically defined as the one having a first derivative of the potential energy equal to zero with respect to the molecular coordinates. Moreover, the level of theory used for the calculations affects the accuracy of these points on the PES.

II.1.3. Vibrational frequencies and zero-point energies

Vibrational frequencies refer to the specific frequencies at which atoms within a molecule oscillate about their equilibrium positions. In molecular systems, these vibrations are associated with changes in bond lengths, bond angles, and dihedral angles. The vibrational frequencies are

modelled by the harmonic oscillator, which necessitates 3N coordinates for specifying the positions of N atoms within a molecule. Within these coordinates, three are allocated for pinpointing the molecule's center of mass or detailing its collective translational motion.

The remaining (3N-3) coordinates, representing the degrees of freedom, pertain to the internal motion of the molecule. In the case of a non-linear molecule, it features three independent rotations, each corresponding to one of the three axes in a coordinate system fixed at its center of mass. Conversely, a linear molecule exhibits only two distinct rotations, aligning with the two axes perpendicular to its molecular (z) axis. Alternatively, the count of independent rotations can be conceptualized as the number of angles needed to express the molecule's orientation concerning the coordinate system at its center of mass. The rest of the degrees of freedom are allocated to molecular vibrations. As a result, a non-linear molecule possesses (3N-6) unique vibrations, while a linear molecule has (3N-5).

According to quantum mechanics, vibrational energy levels are quantized. The vibrational frequencies are proportional to the square root of the force constant divided by the reduced mass of the vibrating atoms according to the following formula:

$$\omega = \frac{1}{2\pi c} \times \sqrt{\frac{k}{\mu}} \qquad \textbf{\textit{Eq. II-5}}$$

with c the velocity of light in vacuum ($c = 3 \times 10^8$ m s^{-1}), μ the reduced mass of the compound in kg and k the force constant in kg s^{-2}. Force constants provide information about the relative stiffness of bonds. In the case of a molecule, these force constants are derived through the diagonalization of the mass-weighted Hessian matrix. The majority of effort in calculating vibrational frequencies is dedicated to constructing the Hessian. From a mathematical perspective, a Hessian matrix is employed to identify points representing local maxima or minima.

Zero-point energy (ZPE) is the lowest possible energy that a quantum mechanical physical system may have. It is the energy associated with the ground state of a system, where particles are in their lowest energy states, and all possible motions are minimized as much as allowed by the uncertainty principle. The ZPE is calculated according to the value of the vibrational frequencies using the following equation:

$$ZPE = 1/2 \sum_i^N hc\omega_i \qquad \textbf{\textit{Eq. II-6}}$$

where h is Planck's constant ($h = 6.626 \times 10^{-34}$ J s). In classical mechanics, it was traditionally assumed that particles at absolute zero temperature (0 K) would have no motion, but quantum mechanics introduces the concept of zero-point energy due to the uncertainty principle, such as Heisenberg uncertainty principle. This principle asserts that there exists a constraint on the accuracy with which specific pairs of a particle's properties, like its position and momentum, can be concurrently determined. The greater the precision in measuring one property, the lesser the precision in determining the other.

II.2. Computational methods

II.2.1. Software used

II.2.1.1. Electronic structure and rate constant calculations

The utilization of the computational method comes highly recommended and has proven effective in accurately calculating radical reactions (Galano and Alvarez-Idaboy, 2014) involved in the degradation/oxidation of harmful organic molecules such as o-anisidine, prosulfocarb, permethrin, and diclofenac (Abdel-Rahman *et al.*, 2021a; Bo *et al.*, 2020; Huo *et al.*, 2021; Qiu *et al.*, 2020), respectively.

The pesticide's structure underwent conformational analysis using MSTor software (Bao *et al.*, 2017). MS-T method is the multi-structural approximation with torsional anharmonicity, where it is designed to facilitate the handling of molecules possessing numerous conformational structures resulting from internal rotations, commonly known as torsions. The most stable conformation obtained was selected for examining the potential energy surfaces of the pesticide towards $HO^{\bullet}$ radicals.

The Gaussian 16 Rev. C.01 software (Frisch *et al.*, 2016) was employed for optimizing the molecular geometries and performing the harmonic vibrational frequency calculations using the density functional theory (DFT), and to find the transition states.

Molden software and GaussView 6 program, by Gaussian, were used to visualize molecular structures and analyse vibrational modes and frequencies obtained from the Gaussian output file.

The Gaussian Post Processor (GPOP) software (Miyoshi, 2022) was utilized to compute all rate constants across a specific temperature range.

To know more about the electronic properties of the studied pesticides molecules, their Fukui indices, HOMO, LUMO, and ESP maps were investigated. The Highest Occupied Molecular Orbital (HOMO) refers to the highest energy orbital in a molecule that contains electrons. The Lowest Unoccupied Molecular Orbital (LUMO) refers to the lowest energy orbital in a molecule that does not contain electrons but is available to accept them.

The Electrostatic Potential (ESP) maps was also investigated. It provides information about the distribution of positive and negative charges within the molecule, helping to understand the reactivity and interaction of the molecule with its environment. Typically, ESP maps are used to identify regions of high electron density (negative potential) and low electron density (positive potential) within a molecule.

Additionally, Fukui indices (Parr and Yang, 1984) were calculated to identify the primary reactive sites of the pesticide molecule towards $HO^{\bullet}$ radical attack. The Fukui function, developed by the Japanese chemist Kenichi Fukui, is a concept in computational chemistry used to predict the reactivity of atoms within a molecule, where it measures the sensitivity of the electronic density of a molecule to changes in the number of electrons caused by the addition

or removal of an electron. It helps identify the most reactive sites within a molecule, indicating where electrophilic or nucleophilic attacks are likely to occur.

II.2.1.2. Ecotoxicity evaluation

The toxicity of the pesticide compound and its degradation products in the environment and their impact on the aquatic organisms, was studied using the quantitative structure-activity relationships (QSAR) method. The estimation of the acute and chronic toxicities in fish, daphnia, and green algae, was carried out using the Ecological Structure-Activity Relationships (ECOSAR version 2.2) software (US EPA, 2015a). The ECOSAR method has commonly been employed for toxicity tests in aquatic organisms (Bo *et al.*, 2020; Dao *et al.*, 2023; Huo *et al.*, 2021; Yao *et al.*, 2022). Acute and chronic toxicities applied to three aquatic organisms, including fish, daphnia, and green algae, are employed to estimate the potential aquatic toxicity of the pesticides. The median lethal concentration (LC50) and the median effect concentration (EC50) values were used to evaluate the acute toxicity in fish (96h of exposure), daphnia (48h of exposure) and green algae (96h of exposure), in addition to the chronic toxicity (ChV) values.

The acute and chronic toxicity classification were done based on European Union (EU, 1967) and Chinese criteria (MEE, 2004) (***Table II-1)***.

Table II-1*: acute and chronic toxicity classification based on European Union and Chinese criteria (mg* L^{-1}*).*

Classification	Acute toxicity[1]	Chronic toxicity[2]
Not harmful	$LC_{50} > 100$ or $EC_{50} > 100$	$ChV > 10$
Harmful	$10 < LC_{50} < 100$ or $10 < EC_{50} < 100$	$1 < ChV < 10$
Toxic	$1 < LC_{50} < 10$ or $1 < EC_{50} < 10$	$0.1 < ChV < 1$
Very toxic	$LC_{50} < 1$ or $EC_{50} < 1$	$ChV < 0.1$

[1] Criteria set by the European Union (described in Annex VI of Directive 67/548/EEC).

[2]Criteria set by the Chinese hazard evaluation guidelines for new chemical substances (HJ/T 154–2004).

The EPI Suite software (EPI Suite 4.1) (US EPA, 2015b) was used to calculate the bioaccumulation factor (BAF) and bioconcentration factor (BCF). The bioaccumulation factor (BAF) and bioconcentration factor (BCF) are two related measures used in environmental toxicology to assess the potential accumulation of a chemical in living organisms. The BCF is the ratio of a chemical's concentration in an organism to its concentration in the surrounding environment. It is typically used to assess the potential uptake of chemicals by aquatic organisms such as fish (Meylan, 1999) and measure the ability of the organism to accumulate a chemical from its environment.

BAF is typically expressed as the ratio of the concentration of a chemical in the tissues of an organism to its concentration in the organism's diet or food. A chemical is classified as bioaccumulative when the BAF or BCF in aquatic organisms is above 2000 L/kg wet-wt and

very bioaccumulative when it is above 5000 L/kg wet-wt according to REACH Annex XIII (2011) and the Canadian Environmental Protection Act (CEPA) (Arnot and Gobas, 2006).

Finally, Toxicity Estimation Software Tool (T.E.S.T version 5.1) (US EPA, 2015c) was used to predict the developmental toxicity and mutagenicity of the pesticide and its degradation products. Developmental toxicity is the potential of a chemical compound to cause adverse effects on the development and growth of living organisms. The compounds are classified as developmental toxicants (> 0.5) and developmental non-toxicants (< 0.5), according to whether or not this chemical can cause developmental toxicity effects. In addition, a compound is mutagenicity positive (> 0.5) if it can cause mutations in the genetic material of the organisms; otherwise, it is mutagenicity negative (< 0.5).

II.2.2. The Density Functional Theory M06-2X

Density functional theory (DFT) is a quantum-mechanical most widely used electronic structure method in chemistry and physics to calculate the electronic structure of atoms, molecules, and solids (Van Mourik *et al.,* 2014). It focuses on the electron density instead of describing the electronic system in terms of individual electron wavefunctions. Moreover, its goal is to reduce the total electronic energy of a system. DFT involves various families of functionals designed for specific types of problems. The main families of DFT functionals include:

- Local Density Approximation (LDA):

This is the simplest form of DFT, where the exchange-correlation energy is a function of the local electron density. Examples: Vosko-Wilk-Nusair (VWN), and Perdew-Zunger (PZ81).

- Generalized Gradient Approximation (GGA):

GGAs include the gradient of the electron density in addition to the density itself, providing a better approximation than LDA. Examples: Perdew-Burke-Ernzerhof (PBE), Becke-88 (B88), and Lee-Yang-Parr (LYP).

- Meta-Generalized Gradient Approximation (meta-GGA):

These functionals incorporate the second derivative of the electron density (the Laplacian) or the kinetic energy density. Examples: Tao-Perdew-Staroverov-Scuseria (TPSS), and Minnesota Functionals (e.g., M06-L).

- Hybrid Functionals:

These combine a portion of exact Hartree-Fock exchange with GGA or meta-GGA exchange-correlation functionals. Examples: B3LYP (Becke, 3-parameter, Lee-Yang-Parr), PBE0 (also known as PBE1PBE), and HSE (Heyd-Scuseria-Ernzerhof).

- Range-Separated Hybrid Functionals:

These functionals split the exchange interaction into short-range and long-range components, treating them with different methods (e.g., DFT for short-range and Hartree-Fock for long-

range). Examples: HSE06 (Heyd-Scuseria-Ernzerhof 2006), and CAM-B3LYP (Coulomb-attenuating method B3LYP).

- Double-Hybrid Functionals:

These include a mixture of GGA or meta-GGA exchange-correlation, Hartree-Fock exchange, and second-order perturbation theory (MP2) correlation. Examples: B2PLYP (Becke, 2-parameter, Lee-Yang-Parr), and PWPB95.

- Van der Waals Functionals:

These functionals incorporate long-range dispersion interactions, which are important for accurately modelling weakly bound systems. Examples: vdW-DF (Van der Waals Density Functional), and DFT-D (Dispersion-Corrected DFT, e.g., DFT-D3).

- Strongly Correlated Electron Systems Functionals:

These are designed to handle systems with strong electron-electron correlations that standard DFT struggles with. Examples: DFT+U (DFT with an added Hubbard U term), and Dynamical Mean-Field Theory (DMFT) combined with DFT.

- Special Purpose Functionals:

These are tailored for specific classes of problems, such as excited states or specific types of reactions. Examples: Time-Dependent DFT (TD-DFT) for excited states, and Constrained DFT (CDFT) for charge transfer processes.

Various methods and levels of theory can be employed for electronic structure calculations using the DFT method. In this work, all the calculations were done using the M06-2X method in conjunction with the 6-31+G(d,p) Pople-style basis set. The M06-2X functional is a meta-generalized gradient approximation (meta-GGA) hybrid functional developed by the Minnesota group, specifically designed for thermochemistry, thermochemical kinetics, and noncovalent interactions. This functional was recommended by Zhao and Truhlar (Zhao and Truhlar, 2008), because it is characterized by high nonlocality, featuring twice the amount of nonlocal exchange (2X), and it is specifically parameterized for non-metals. The M06-2X functional includes 54% Hartree-Fock (HF) exchange, which is higher than many other hybrid functionals. This characteristic makes it particularly useful for accurately modelling systems with significant non-local exchange interactions, such as those involving reaction barriers and noncovalent interactions. The wave numbers and zero-point energies calculated at the M06-2X/6-31+G(d,p) level of theory, are adjusted using the appropriate scaling factor of 0.952 (NIST CCCBDB).

Additional single-point electronic energy calculations, at all the stationary points of the reaction profile, were carried out based on the optimized geometries with a larger basis set namely 6-311++G(3df,3pd). The single-point energy calculations are executed to examine the impact of the basis set on the vibrationally adiabatic barrier, representing the transition state's position relative to the reactants. This assessment provides insights into the sensitivity of the barrier to variations in the chosen basis set, aiding in the understanding of its influence on the overall reaction energetics.

The notation of 6-311++G(3df,3pd) basis set stands for:

- **6**: Indicates the number of primitive Gaussian functions used to describe the core (innermost) electron orbitals.
- **311++G**: Describes the valence (outermost) electron orbitals and includes several components. "**3**" represents the number of primitive Gaussian functions used for s-type orbitals in valence shells, and "**1**" represents that used for p-type orbitals. The "**++**" indicates that diffuse functions are added to all atoms (heavy atoms and hydrogen).
- **(3df, 3pd)**: Corresponds to polarization functions on heavy atoms and hydrogen. It represents 3 sets of d functions and 1 set of f functions on heavy atoms, and 3 sets of p functions and 1 set of d functions on hydrogen atoms.

II.2.3. Solvation Model based on Density (SMD)

The computations conducted in water utilized the universal continuum Solvation Model based on Density (SMD) (Marenich et al., 2009), which is designed to account for the effects of solvent (solvation) on molecular properties, especially in the context of electronic structure calculations. This model is called continuum because the solvent is represented implicitly as a dielectric medium with surface tension at the solute-solvent boundary. Moreover, it is termed universal because it can be applied to any uncharged or charged solute in any liquid medium or solvent where certain key descriptors are known. These descriptors include refractive index, dielectric constant, acidity and basicity parameters, and bulk surface tension

Additionally, the SMD model divides the observable solvation free energy into two primary components. The first component is the bulk electrostatic contribution, which results from a self-consistent reaction field approach involving the solution of the nonhomogeneous Poisson equation for electrostatics, based on the integral-equation-formalism polarizable continuum model (IEF-PCM). The second component, known as the cavity-dispersion-solvent-structure term, accounts for the short-range interactions between the solvent molecules and solute in the first solvation shell.

II.2.4. Stability of the wave function

The stability of the wave function refers to the convergence of the calculation to an energetically favourable and physically meaningful electronic state. The stability of the wave function at each stationary point is determined using the Berny Optimization Algorithm (Schlegel, 1982) implemented in the Gaussian16 software. This algorithm incorporates a constraint on the wave function, and if the wave function corresponds to a minimum, it reverts to its original state, indicating that the wave function is stable.

On the other hand, the instability of a wave function typically indicates that the electronic structure calculation has not converged to a reliable solution. According to Gaussian, the instability of a wave function is due to mixing of electronic states (for example singlet and triplet), which change drastically the potential energy and exhibit large spin contamination. This

electronic instability can manifest as oscillations or divergences in the wave function. Moreover, a non-stable wave function may also indicate that the calculated electronic state does not correspond to a physically meaningful configuration, and this could be due to incorrect choice of method.

In our studied molecular systems, no instabilities of wave function have been found.

II.2.5. Spin-Orbit Coupling (SOC)

Spin-orbit coupling (SOC) is a fundamental interaction in quantum mechanics that arises from the interaction between the intrinsic spin angular momentum of electrons and their orbital angular momentum as they move in the electric field of an atomic nucleus. It is a relativistic effect and plays a crucial role in determining the electronic structure and properties of atoms, molecules, and solids.

In the case of the HO$^{\bullet}$ radical, spin-orbit coupling emerges due to the interaction between the electron spin and its orbital motion around the oxygen atom.

Although the SOC magnitude within the HO$^{\bullet}$ radical is relatively weak due to its light mass and small spin-orbit interaction, advanced experimental methods such as laser and magnetic resonance spectroscopy enable its detection and measurement. According to research findings, the SOC value is reported as -0.836 kJ mol^{-1} (Hess *et al.*, 1982a; Huber and Herzberg, 1979) or -0.833 kJ mol^{-1} as given in the NIST-JANAF thermochemical database (Chase, 1998) Chase, M.W., 1998. NIST-JANAF Thermochemical Tables, 4th Edition. Journal of Physical Chemistry Monograph No. 9.

In this work, the SOC values for all species of interest are considered negligible, except those where the HO$^{\bullet}$ radical appears in the structure as detached (*i.e.*, MCR and TS), with a value of -0.836 kJ mol^{-1}.

II.2.6. Splitting and the electronic partition function

In molecular systems, splitting refers to the splitting of energy levels due to various interactions such as spin-orbit coupling, crystal field effects, or Jahn-Teller distortions. This splitting can significantly impact the electronic partition function, which is a measure of the distribution of molecules across different electronic states at a given temperature.

When electronic energy levels are split into sub-levels, the electronic partition function needs to account for these additional levels. Each split level can have its own population based on its energy and degeneracy. At higher temperatures, more split levels may be thermally accessible, which increases the electronic partition function. The changes in the electronic partition function due to splitting affect various thermodynamic properties, such as entropy, heat capacity, and free energy.

SOC is a common cause of splitting in molecules and atoms, where the interaction between an electron's spin and its orbital motion around the nucleus splits degenerate electronic states into multiple sub-levels. This interaction leads to a splitting of the energy levels within the $^2\Pi$ ground state of the HO$^\bullet$ radical by 139.21 cm^{-1}, and that of $^\bullet$NO by 119.8 cm^{-1} (Huber and Herzberg, 1979) which can be observed in spectroscopic experiments. For this reason, we considered correcting the electronic state for these two species.

II.2.7. Identification of the Transition State (TS)

A transition state is a high energy state that occurs during a chemical reaction in which the products are formed by the partially transformation of reactants. Within this state, the molecules are highly reactive and unstable, and characterized by the presence of partial bonds and varying degrees of bond strain. The highest point on the reaction energy profile corresponds to the transition state. The rate of the reaction is determined by the activation energy required to reach the transition state, where higher energy barrier correlates with a slower reaction rate.

The imaginary frequency of a transition state, denoted by $\omega_i^{\neq}$, refers to a specific vibrational frequency associated with the transition state. It offers significant insights into the characteristics of the transition state and the reaction mechanism. In contrast to real frequencies, which signify stable vibrational modes, an imaginary frequency signifies that the transition state represents a saddle point on the reaction energy surface. In another way, the presence of an imaginary frequency indicates that the transition state represents a peak along certain directions and a minimum along others, and that the reaction can proceed in the direction corresponding to the imaginary frequency. Furthermore, a high value (in magnitude) of the imaginary frequency indicates a steep curvature of the potential energy surface along the reaction coordinate at the transition state. This suggests that the energy barrier for the reaction is sharply defined.

II.2.8. Intrinsic Reaction Coordinate (IRC)

The IRC calculations were made in order to confirm whether the imaginary frequency corresponds to the appropriate motion along the reaction coordinates. The initial step in investigating a chemical reaction involves identifying the positions of the reactant, product, and transition state geometries on the potential energy surface. Upon acquiring the TS geometry, an Intrinsic Reaction Coordinate analysis can be conducted (Fukui, 1970).

This analysis aids in tracing the path of minimum energy back to the reactants and forward to the products. It serves to confirm that the identified TS genuinely links the molecular complexes from both the reactants and products sides of the reaction, known as MCR and MCP, respectively.

A molecular complex is a temporary species resulting from the interaction between two or more species (molecules or radicals) during a reaction. This complex is stabilized through intermolecular forces like hydrogen bonding, van der Waals forces, or electrostatic interactions. Molecular complexes serve a crucial function in chemical reactions by stabilizing transition states.

The IRC path is the most direct route in mass-weighted Cartesian coordinates. As the reaction system progresses from the transition state to either the reactant or product on the potential energy surface at an infinitesimal velocity, it follows the IRC path in both forward and reverse directions. The computations for IRC analysis are conducted utilizing the Gaussian 16 software, using the Hessian-based Predictor-Corrector (HPC) algorithm (Hratchian and Schlegel, 2004).

II.3. Thermochemical properties and kinetic parameters

II.3.1. Thermochemical parameters

For a molecule (or a radical), the total partition function q_{tot} is mathematically defined by the following equation:

$$q_{tot} = q_{trans} \times q_{rot} \times q_{vib} \times q_{elec} \qquad \textbf{Eq. II-7}$$

where q_{trans}, q_{rot}, q_{vib}, and q_{elec} are respectively the functions of electronic partition, translation, rotation, and vibration.

The translational partition function can be expressed as:

$$q_{trans} = \left(\frac{2\pi M k_B T}{h^2}\right)^{3/2} V \qquad \textbf{Eq. II-8}$$

where V is the volume and M is the molar mass, T is the temperature (K), and k_B is the Boltzmann's constant ($k_B = 1.38 \times 10^{-23}$ J K^{-1}).

The rotational partition function for linear and non-linear species is given by the following relation, respectively:

$$q_{rot} = \frac{(k_B T)(2\pi I)}{\sigma h^3} \qquad \textbf{Eq. II-9}$$

$$q_{rot} = \frac{8\pi^2 (2\pi\, k_B T)^{3/2} (I_x I_y I_z)^{1/2}}{\sigma h^3} \qquad \textbf{Eq. II-10}$$

where I_x, I_y, I_z are the moments of inertia of the molecule along the x, y and z axes. σ is the number of symmetries, and it is determined by the rotational symmetry of the molecule. The linear molecule has two rotational degrees of freedom, while the non-linear one has three.

The vibrational partition function is written as:

$$q_{vib} = \prod_i \frac{1}{1-exp\left(-\frac{hc\,\overline{\omega_I}}{k_B T}\right)} \qquad \textbf{Eq. II-11}$$

with ω_i the vibrational frequency of the normal mode i.

The electronic partition function is calculated using the following formula:

$$q_{elec} = g_{ground\ state} + \sum g_{excited\ state}\, exp(-\Delta\varepsilon_{excited\ state}/k_B T) \qquad \textbf{Eq. II-12}$$

with $\Delta\varepsilon_{excited\ state}$ represents the energy difference between the excited state and the ground state, and g the corresponding degeneration energy.

In minima, the vibrational partition function consists of 3N-6 terms for non-linear molecules and 3N-5 terms for linear molecules. For transition states, this function comprises 3N-7 terms for non-linear molecules and 3N-6 terms for linear molecules.

Employing statistical thermodynamics enables the computation of translational, rotational, vibrational, and electronic contributions to the desired thermodynamic properties (Irikura, 1998).

a. Translational contributions

The following equation represents the translational enthalpy contribution at a temperature T:

$$[H(T) - H(0\ K)]_{trans} = \frac{5}{2}RT \qquad \textbf{Eq. II-13}$$

with R the ideal gas constant.

The translational contribution to the standard molar entropy at temperature T ($S°_{trans}$) is defined by the following relation:

$$S°_{trans} = R\left[\left(\frac{3}{2}\right) ln\left(\frac{2\pi M}{h^2}\right) + \left(\frac{5}{2}\right)\ln(k_B T) - \ln(p°) + \frac{5}{2}\right] \qquad \textbf{Eq. II-14}$$

where p° is the standard pressure.

The translational contribution to the heat capacity at constant pressure at temperature T ($C_{p,trans}$) is given by the equation:

$$C_{p,trans} = \frac{5}{2}R \qquad \textbf{Eq. II-15}$$

b. Rotational contributions

The below equations represent the rotational enthalpy contribution at a temperature T for linear and non-linear molecules respectively:

$$[H(T) - H(0\ K)]_{rot} = RT \qquad \textbf{Eq. II-16}$$

$$[H(T) - H(0\ K)]_{rot} = \frac{3}{2}RT \qquad \textbf{Eq. II-17}$$

The external rotation involves the entire structure of the molecule. This rotational contribution to the absolute standard entropy is determined by the external symmetry number depending on the symmetry group of the species. The value of σ is equal to the number of rotational operations of the group plus the identity operation.

The rotational contribution to the standard molar entropy at temperature T ($S°_{rot}$), for a linear and non-linear species, is given by these equations:

$$S°_{rot}^{linear} = R\left[ln\left(\frac{8\pi^2 I k_B T}{\sigma h^2}\right) + 1\right] \qquad \textbf{Eq. II-18}$$

$$S°_{rot}^{non\ linear} = R\left[ln\left(\frac{8\pi^2}{\sigma}\right) + \left(\frac{3}{2}\right) ln\left(\frac{2\pi k_B T}{h^2}\right) + \left(\frac{3}{2}\right)\ln(I_A I_B I_C) + \frac{3}{2}\right] \qquad \textbf{Eq. II-19}$$

with I_A, I_B, and I_C the moments of inertia of the molecule. A, B, and C represent the three directions of space in the chosen reference frame.

The rotational contribution to the heat capacity at constant pressure at temperature T ($C_{p,rot}$), for a linear and non-linear species, is given by these equations:

$$C_{p,rot}^{linear} = R \qquad \textbf{Eq. II-20}$$

$$C_{p,rot}^{non\ linear} = \frac{3}{2}R \qquad \textbf{Eq. II-21}$$

c. Vibrational contribution

The below equation defines the vibrational enthalpy contribution at temperature T:

$$[H(T) - H(0\ K)]_{vib} = RT\sum_i \frac{h\omega_i}{k_B T}\frac{exp\left(-\frac{h\omega_i}{k_B T}\right)}{\left(1-exp\left(-\frac{h\omega_i}{k_B T}\right)\right)} \qquad \textbf{Eq. II-22}$$

The vibrational contribution to the standard molar entropy at temperature T ($S°_{vib}$) is written by the equation:

$$S°_{vib} = -R\sum_i \ln\left(1 - exp\left(-\frac{h\omega_i}{k_B T}\right)\right) + R\sum_i \frac{h\omega_i}{k_B T}\frac{exp\left(-\frac{h\omega_i}{k_B T}\right)}{\left(1-exp\left(-\frac{h\omega_i}{k_B T}\right)\right)} \qquad \textbf{Eq. II-23}$$

The vibrational contribution to the heat capacity at constant pressure at temperature T ($C_{p,vib}$) is given by equation:

$$C_{p,vib} = R\sum_i \left(\frac{h\omega_i}{k_B T}\right)^2 \frac{exp\left(-\frac{h\omega_i}{k_B T}\right)}{\left(1-exp\left(-\frac{h\omega_i}{k_B T}\right)\right)^2} \qquad \textbf{Eq. II-24}$$

d. Electronic contributions

The below equation defines the electronic enthalpy contribution at temperature T:

$$[H(T) - H(0\ K)]_{elec} = RT\frac{\sum_i g_i\left(\frac{\varepsilon_i}{k_B T}\right)exp\left(-\frac{\varepsilon_i}{k_B T}\right)}{\left(\sum_i g_i exp\left(-\frac{\varepsilon_i}{k_B T}\right)\right)} \qquad \textbf{Eq. II-25}$$

where g_i and ε_i represent the degeneracy and energy of the energy level i (this corresponds to the excited states). They are written as g_0 and ε_0 for the ground state case.

The electronic contribution to the standard molar entropy at temperature T ($S°_{elec}$) is given by the equation:

$$S°_{elec} = Rln\left(\sum_i g_i exp\left(-\frac{\varepsilon_i}{k_B T}\right)\right) + R\frac{\sum_i g_i\left(\frac{\varepsilon_i}{k_B T}\right)exp\left(-\frac{\varepsilon_i}{k_B T}\right)}{\left(\sum_i g_i exp\left(-\frac{\varepsilon_i}{k_B T}\right)\right)} \qquad \textbf{Eq. II-26}$$

The following equation represents the electronic contribution to the heat capacity at constant pressure at temperature T ($C_{p,elec}$):

$$C_{p,elec} = R\left(\frac{\sum g_i\left(\frac{\varepsilon_i}{k_B T}\right)^2 exp\left(-\frac{\varepsilon_i}{k_B T}\right)}{\left(\sum g_i exp\left(-\frac{\varepsilon_i}{k_B T}\right)\right)}\right) - R\left(\frac{\sum g_i\left(\frac{\varepsilon_i}{k_B T}\right)exp\left(-\frac{\varepsilon_i}{k_B T}\right)}{\left(\sum g_i exp\left(-\frac{\varepsilon_i}{k_B T}\right)\right)}\right)^2 \qquad \textbf{Eq. II-27}$$

II.3.2. Kinetic parameters

II.3.2.1. Transition State Theory (TST)

Transition State Theory (TST) serves as a theoretical framework employed for predicting reaction rates and understanding the transitional state in a chemical reaction. It revolves around the idea of a high-energy transition state, that molecules must traverse through to form products from reactants. The theory was formulated by Henry Eyring (Eyring, 1935) and Michael Polanyi in the 1935, to explain bimolecular reactions based on the relationship between kinetics

and thermodynamics, assuming that the reaction rates can be calculated absolutely (Ptáček et al., 2018).

For explaining the TST, Eyring mentioned that the atoms and molecules have the potential to collide and unite, forming an unstable, high-energy complex. Upon exiting this high-energy state, they may transform into new and distinct molecules or return to their original states. The energy necessary to attain the activated state must be present for molecules to undergo such transformations (Dambrowitz and Kuznicki, 2010).

Nowadays, the TST stands as the prevailing paradigm for explaining the rates of chemical processes and how these rates vary with temperature, environment, structure, and other factors (Arnaut, 2006).

The classical TST directly relies on the minimum energy profile derived from the IRC calculation. According to this theory, the transition state is positioned at the top of the minimum energy path. The determination of the rate constant follows the formulation introduced by Eyring (Eyring, 1935).

$$k_{TST} = \left(\frac{k_B T}{h}\right) \times \frac{q_{TS}}{\prod q_{R(s)}} \times e^{-E_0/RT} \qquad \textbf{Eq. II-28}$$

where $q_{R(s)}$ and q_{TS} refer to the functions of total reagent partition and transition state, and E_0 corresponds to the adiabatic vibration barrier including all energy corrections (ZPE and SOC corrections). Its formula is given below:

$$E_0 = \Delta E^{\neq} + \Delta E_{ZPE} + \Delta E_{SOC} \qquad \textbf{Eq. II-29}$$

For a bimolecular reaction:

$$\Delta \mathrm{E}_{ZPE} = ZPE_{TS} - ZPE_{Reactant1} - ZPE_{Reactant2} \qquad \textbf{Eq. II-30}$$

$$\Delta \mathrm{E}_{SOC} = SOC_{TS} - SOC_{Reactant1} - SOC_{Reactant2} \qquad \textbf{Eq. II-31}$$

$$\Delta E^{\neq} = E^{\neq}_{TS} - E^{\neq}_{Reactant1} - E^{\neq}_{Reactant2} \qquad \textbf{Eq. II-32}$$

where $E^{\neq}$ is the electronic energy obtained from the frequency calculations without any correction. Its unit is Hartree (a Hartree is equal to 2625.5 kJ mol^{-1}).

II.3.2.2. Rate constant calculations

The reaction occurs in the following path:

- MCR Formation: The reactants, HO$^{\bullet}$ and pesticide, gradually approach each other, initiating the formation of the MCR.
- TS Formation: At the transition state, the reactants undergo partial conversion into products, requiring an input of energy associated with the activation energy barrier.
- MCP Formation: Following the transition state, the system may generate a temporary molecular complex, or an adduct (in the case of HO$^{\bullet}$-addition)

- Product Species Formation: The molecular complex may dissociate, releasing the final product of the reaction. This product could undergo further modifications or reactions, or it might be isolated and purified for alternative applications.

The kinetics for the abstraction and the addition reactions between the pesticide and HO• radical was studied using the pre-reactive complexes scheme proposed by Singleton and Cvetanovic (Singleton and Cvetanovic, 1976).

Briefly, a two-step mechanism is considered:

$$\text{Pesticide} + \text{HO}^{\bullet} \xrightarrow{k_a} \text{MCR} \quad \text{(R1)}$$

$$\text{MCR} \xrightarrow{k_b} \text{Pesticide} + \text{HO}^{\bullet} \quad \text{(R2)}$$

$$\text{MCR} \xrightarrow{k_c} \text{TS} \quad \text{(R3)}$$

This scheme involved a fast pre-equilibrium between the reactants and the pre-reactive complex (MCR), leading to the hydrogen abstraction/radical addition followed by post-reactive complexes and products. The effective rate *r* applied to reactions (R1-R2) for steady-state conditions (the concentration of the intermediates is constant, *i.e.*, the effective rate of product formation is constant and do not depends on time) is defined as follows (***Eq. II-33***):

$$r = r_c = k\,[\text{HO}^{\bullet}]\,[\text{Pesticide}] \qquad \textbf{\textit{Eq. II-33}}$$

where *k* is the rate constant for each pathway, and it is calculated by the following equation (***Eq. II-34***):

$$k = \frac{k_c k_a}{k_b + k_c} \qquad \textbf{\textit{Eq. II-34}}$$

The changes in entropy in the reverse reaction (R2) are much more significant than in the reaction (R3). Thus, k_b is expected to be larger than k_c, and *k* can be written as (***Eq. II-35***):

$$k = \frac{k_c k_a}{k_b} = k_c K_{a,b} \qquad \textbf{\textit{Eq. II-35}}$$

where $K_{a,b}$ is the equilibrium constant for the separated reactants versus the pre-reactive complex (MCR). The equilibrium constant ($K_{a,b}$) of the first step is computed based on basic statistical thermodynamics principles, while k_c is calculated by the classical TST formula (Evans and Polanyi, 1935) (***Eq. II-36***) (***Eq. II-37***).

$$K_{a,b}(T) = \frac{q_{MCR}(T)}{q_{HO\bullet}(T)\,q_{Pesticide}(T)}\, exp\left(\frac{E_{Pesticide} + E_{HO\bullet} - E_{MCR}}{k_B T}\right) \qquad \textbf{\textit{Eq. II-3}}6$$

$$k_c(T) = \kappa(T) \times \frac{k_B T}{h} \times \frac{q_{TS}(T)}{q_{MCR}(T)} \times exp\left(-\frac{E_{TS} - E_{MCR}}{k_B T}\right) \qquad \textbf{\textit{Eq. II-3}}7$$

The terms $q_{HO^{\bullet}}(T)$, $q_{Pesticide}(T)$, $q_{MCR}(T)$, and $q_{TS}(T)$ are the total partition functions of the reactants (HO• and pesticide), MCR, and TS at the temperature T (K), respectively. $E_{HO^{\bullet}}$, $E_{Pesticide}$, E_{MCR}, and E_{TS} are the total potential energies at 0 K (including the zero-point energy and SOC corrections) of the HO• radical, pesticide, MCR, and TS, respectively. The κ(T) is the transmission coefficient used for the tunnelling correction estimated by the Eckart method (Eckart, 1930) at the temperature T.

Tunnelling is a phenomenon where particles (*i.e.*, electrons) described by wave functions can "tunnel" through the potential energy barrier even if they lack sufficient energy, according to quantum mechanics. Whereas in classical mechanics, only particles with enough energy can overcome the potential energy barrier's height and form the products. ***Figure II-2*** shows a schematic representation of the tunnelling effect.

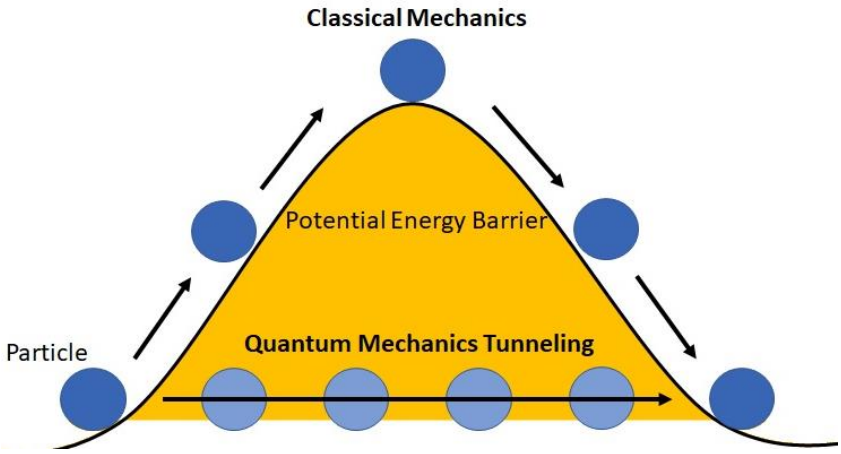

Figure II-2*: schematic representation of the tunnelling effect.*

Eckart correction is suitable for systems with asymmetric potential energy barriers, such as those encountered in many chemical reactions. The Eckart potential function is a frequently employed tool for estimating corrections related to quantum mechanical tunnelling in theoretically derived rate constants (Eckart, 1930). This correction improves the accuracy of reaction rate predictions, particularly at low temperatures where quantum tunnelling becomes significant. Throughout the studied molecular systems, the values of the Eckart correction were higher at low temperature (*i.e.*, 253 K) than that at high temperature (*i.e.*, 323 K). Moreover, much higher Eckart correction values were observed for the H-abstraction reaction in comparison to the HO$^{\bullet}$-addition reactions.

For the SET (single electron transfer) reaction, the reaction barrier was calculated by Marcus' theory (Marcus, 1956, 1957a, 1957b) as follows (***Eq. II-38***):

$$\Delta G^{\circ\neq}_{\mathrm{SET}} = \frac{\lambda}{4}\left(1 + \frac{\Delta_r G^{\circ}_{\mathrm{SET}}}{\lambda}\right)^2 \qquad \textbf{Eq. II-38}$$

$\Delta_r G°_{SET}$ is the standard Gibbs free reaction energy calculated from the energy difference between reactants and products. The λ is the nuclear reorganization energy, which is calculated by the below equation (***Eq. II-39***):

$$\lambda = \Delta_r H°_{\mathrm{SET}} - \Delta_r G°_{\mathrm{SET}} \qquad \textbf{Eq. II-39}$$

where the $\Delta_r H°_{SET}$ is the non-adiabatic energy between the reactants and products.

In the aqueous phase, the apparent rate constant (k_{app}) is typically including a diffusion limit, especially for the reaction with HO$^{\bullet}$ radical that has the rate constant close to the diffusion limit of the solution. The k_{app} was calculated based on the Collins-Kimball (Collins and Kimball, 1949) as follows (***Eq. II-40***):

$$k_{app} = \frac{k_D k}{k_D + k} \qquad \textbf{\textit{Eq. II-40}}$$

where k is the thermal rate constant, and k_D is the steady-state Smoluchowski (Smoluchowski, 1918) rate constant for an irreversible bimolecular diffusion-controlled reaction (***Eq. II-41***):

$$k_D = 4\pi R_{AB} D_{AB} N_A \qquad \textbf{\textit{Eq. II-41}}$$

where R_{AB} is the reaction distance, N_A is the Avogadro number, and D_{AB} is the mutual diffusion coefficient of reactants, and it can be estimated from D_A and D_B according to Truhlar (Truhlar, 1985). The D_A and D_B values were calculated from the Stokes-Einstein approach (Einstein, 1905; Stokes, 2009) (***Eq. II-42***):

$$D_{A\ or\ B} = \frac{k_B T}{6\pi\eta a_{A\ or\ B}} \qquad \textbf{\textit{Eq. II-42}}$$

where η denotes the solvent's viscosity varied as a function of temperature, and a is the radius of solute.

The rate constants were calculated with the GPOP software (Miyoshi, 2022). The total rate constant (k_{total}) of each reaction mechanism was derived by adding up the rate constant (k_i) of all individual reactions. The overall rate constant ($k_{overall}$) was obtained by summing up the total rate constant of the three mechanisms (*i.e.*, $k_{overall} = k_{FHT} + k_{RAF} + k_{SET}$). k_{FHT} is the total rate constant of the H-abstraction reactions (formal hydrogen transfer), k_{RAF} is the total rate constant of the HO$^{\bullet}$-addition reactions (radical adduct formation), and k_{SET} is the is the total rate constant of the charge transfer reactions (single electron transfer).

The branching ratios for each reaction are determined by dividing their respective apparent rate constants (k_i) by the overall rate constant ($k_{overall}$).

II.3.3. Lifetime calculation of the pesticide in the presence of HO$^{\bullet}$ radicals

In order to determine the residence time of the pesticide in the environment when exposed to HO$^{\bullet}$ radicals, its lifetime (τ) is calculated at a temperature range of 283-323 K (or more) in the aqueous phase and 287 K in the gas phase. In the gas phase, the following formula (***Eq. II-43)*** (Sun *et al.*, 2020) was used for calculating the atmospheric lifetime (τ_{gas}) of the pesticide, using the overall rate constant of the reactions (k) in the gas phase, and by adopting 1.09×10^6 radicals cm^{-3} as an average concentration of HO$^{\bullet}$ radical in the troposphere (Li et al., 2018). The calculation is done at 287 K, corresponding to the mean air temperature at the ground (Stein and published, 2022), where the pesticide is applied.

$$\tau_{gas} = \frac{1}{k[\mathrm{HO}^{\bullet}]} \qquad \textbf{\textit{Eq. II-43}}$$

In the aqueous phase, the calculations were done based on the diffusion-corrected overall rate constant of the reactions (k_{app}), and the concentration of $HO^{\bullet}$ radicals in the environment. According to previous studies, the concentrations of $HO^{\bullet}$ radicals in wastewater were reported to be from 10^{-9} to 10^{-10} mol L^{-1}, and in groundwater, from 10^{-15} to 10^{-18} mol L^{-1} (Brezonik and Fulkerson-Brekken, 1998) (J. M. Burns *et al.*, 2012) (Haag and Hoigné, 1985).

II.4. References

Abdel-Rahman, M.A., Shibl, M.F., El-Nahas, A.M., Abdel-Azeim, S., El-demerdash, S.H., Al-Hashimi, N., 2021. Mechanistic insights of the degradation of an O-anisidine carcinogenic pollutant initiated by OH radical attack: theoretical investigations. New Journal of Chemistry 45, 5907–5924. https://doi.org/10.1039/D0NJ06248K

Arnot, J.A., Gobas, F.A., 2006. A review of bioconcentration factor (BCF) and bioaccumulation factor (BAF) assessments for organic chemicals in aquatic organisms. Environmental Reviews 14, 257–297. https://doi.org/10.1139/a06-005

Bao, J.L., Xing, L., Truhlar, D.G., 2017. Dual-Level Method for Estimating Multistructural Partition Functions with Torsional Anharmonicity. Journal of Chemical Theory and Computation 13, 2511–2522. https://doi.org/10.1021/acs.jctc.7b00232

Bo, X., Sun, J., Mei, Q., Wei, B., An, Z., Han, D., Li, Z., Xie, J., Zhan, J., He, M., 2020. Degradation of prosulfocarb by hydroxyl radicals in gas and aqueous phase: Mechanisms, kinetics and toxicity. Ecotoxicology and Environmental Safety 191, 110175. https://doi.org/10.1016/j.ecoenv.2020.110175

Born, M., Oppenheimer, R., 1927. Zur Quantentheorie der Molekeln. Annalen der Physik 389, 457–484. https://doi.org/10.1002/andp.19273892002

Brezonik, P.L., Fulkerson-Brekken, J., 1998. Nitrate-Induced Photolysis in Natural Waters: Controls on Concentrations of Hydroxyl Radical Photo-Intermediates by Natural Scavenging Agents. Environmenal Science and Technology 32, 3004–3010. https://doi.org/10.1021/es9802908

NIST CCCBDB (Computational Chemistry Comparison and Benchmark Database). NIST Standard Reference Database Number 101. Release 22, May 2022, Editor: Russell D. Johnson III. http://cccbdb.nist.gov/ . DOI:10.18434/T47C7Z (accessed 2.20.24).

Chemical Kinetics: From Molecular Structure to Chemical Reactivity, 2019. Focus on Catalysts 2019, 7. https://doi.org/10.1016/j.focat.2019.05.048

Collins, F.C., Kimball, G.E., 1949. Diffusion-controlled reaction rates. Journal of Colloid Science 4, 425–437. https://doi.org/10.1016/0095-8522(49)90023-9

Dambrowitz, K.A., Kuznicki, S.M., 2010. Henry Eyring: A Model Life. Bull. Hist. Chem. 35.

Dao, D.Q., Taamalli, S., Louis, F., Kdouh, D., Srour, Z., Ngo, T.C., Truong, D.H., Fèvre-Nollet, V., Ribaucour, M., El Bakali, A., Černušák, I., 2023. Hydroxyl radical-initiated decomposition of metazachlor herbicide in the gaseous and aqueous phases: Mechanism, kinetics, and toxicity evaluation. Chemosphere 312, 137234. https://doi.org/10.1016/j.chemosphere.2022.137234

Eckart, C., 1930. The Penetration of a Potential Barrier by Electrons. Physical Reviews 35, 1303–1309. https://doi.org/10.1103/PhysRev.35.1303

Einstein, A., 1905. Zur Elektrodynamik bewegter Körper. Annalen der Physik 322, 891–921. https://doi.org/10.1002/andp.19053221004

EU, 1967. General classification and labeling requirements for dangerous substances and preparations. Annex VI of Directive 67/548/EEC. URL

https://ec.europa.eu/environment/archives/dansub/pdfs/annex6_en.pdf (accessed 6.26.24).
Evans, M.G., Polanyi, M., 1935. Some applications of the transition state method to the calculation of reaction velocities, especially in solution. Journal of the Chemical Society, Faraday Transactions 31, 875–894. https://doi.org/10.1039/TF9353100875
Eyring, H., 1935. The Activated Complex in Chemical Reactions. The Journal of Chemical Physics 3, 107–115. https://doi.org/10.1063/1.1749604
Frisch, M.J., Trucks, G.W., Schlegel, H.B., Scuseria, G.E., Robb, M.A., Cheeseman, J.R., Scalmani, G., Barone, V., Petersson, G.A., Nakatsuji, H., Li, X., Caricato, M., Marenich, A.V., Bloino, J., Janesko, B.G., Gomperts, R., Mennucci, B., Hratchian, H.P., Ortiz, J.V., Izmaylov, A.F., Sonnenberg, J.L., Williams, Ding, F., Lipparini, F., Egidi, F., Goings, J., Peng, B., Petrone, A., Henderson, T., Ranasinghe, D., Zakrzewski, V.G., Gao, J., Rega, N., Zheng, G., Liang, W., Hada, M., Ehara, M., Toyota, K., Fukuda, R., Hasegawa, J., Ishida, M., Nakajima, T., Honda, Y., Kitao, O., Nakai, H., Vreven, T., Throssell, K., Montgomery Jr., J.A., Peralta, J.E., Ogliaro, F., Bearpark, M.J., Heyd, J.J., Brothers, E.N., Kudin, K.N., Staroverov, V.N., Keith, T.A., Kobayashi, R., Normand, J., Raghavachari, K., Rendell, A.P., Burant, J.C., Iyengar, S.S., Tomasi, J., Cossi, M., Millam, J.M., Klene, M., Adamo, C., Cammi, R., Ochterski, J.W., Martin, R.L., Morokuma, K., Farkas, O., Foresman, J.B., Fox, D.J., n.d. Gaussian 16 Rev. C.01 [WWW Document].
Fukui, K., 1970. Formulation of the reaction coordinate. Journal Physical Chemistry 74, 4161–4163. https://doi.org/10.1021/j100717a029
Galano, A., Alvarez-Idaboy, J.R., 2014. Kinetics of radical-molecule reactions in aqueous solution: A benchmark study of the performance of density functional methods. Journal of Computational Chemistry 35, 2019–2026. https://doi.org/10.1002/jcc.23715
Gonzalez, C., Schlegel, H.B., 1989. An improved algorithm for reaction path following. The Journal of Chemical Physics 90, 2154–2161. https://doi.org/10.1063/1.456010
Gonzalez, Carlos., Schlegel, H.Bernhard., 1990. Reaction path following in mass-weighted internal coordinates. Journal Physical Chemistry 94, 5523–5527. https://doi.org/10.1021/j100377a021
Haag, W.R., Hoigné, J., 1985. Photo-sensitized oxidation in natural water via OH radicals. Chemosphere 14, 1659–1671. https://doi.org/10.1016/0045-6535(85)90107-9
Hess, B.A., Buenker, R.J., Marian, C.M., Peyerimhoff, S.D., 1982. Investigation of electron correlation on the theoretical prediction of zero-field splittings of 2Π molecular states. Chemical Physics Letters 89, 459–462. https://doi.org/10.1016/0009-2614(82)83046-7
Hratchian, H.P., Schlegel, H.B., 2004. Accurate reaction paths using a Hessian based predictor–corrector integrator. The Journal of Chemical Physics 120, 9918–9924. https://doi.org/10.1063/1.1724823
Huber, K.P., Herzberg, G., 1979. Molecular Spectra and Molecular Structure. Springer US, Boston, MA. https://doi.org/10.1007/978-1-4757-0961-2
Huo, Y., Li, M., An, Z., Sun, J., Mei, Q., Wei, B., Qiu, Z., Xie, J., He, M., 2021. Ozonolysis of Permethrin in the Atmosphere: Mechanism, Kinetics, and Evaluation of Toxicity. Journal Physical Chemistry A 125, 7705–7715. https://doi.org/10.1021/acs.jpca.1c04812
Irikura, K.K., 1998. Appendix B, in: Computational Thermochemistry, ACS Symposium Series. American Chemical Society, pp. 402–418. https://doi.org/10.1021/bk-1998-0677.ch022
J. M. Burns, W. J. Cooper, J. L. Ferry, D. W. King, B. P. DiMento, K. McNeill, C. J. Miller, W. L. Miller, B. M. Peake, S. A. Rusak, A. L. Rose, T. D. Waite, 2012. Methods for

reactive oxygen species (ROS) detection in aqueous environments. Aquatic Sciences 74, 683–734. https://doi.org/10.1007/s00027-012-0251-x

Kwon, H.-Y., Morrow, Z., Kelley, C.T., Jakubikova, E., 2021. Interpolation Methods for Molecular Potential Energy Surface Construction. Journal Physical Chemistry A 125, 9725–9735. https://doi.org/10.1021/acs.jpca.1c06812

Li, M., Karu, E., Brenninkmeijer, C., Fischer, H., Lelieveld, J., Williams, J., 2018. Tropospheric OH and stratospheric OH and Cl concentrations determined from CH_4, CH_3Cl, and SF_6 measurements. npj Climate and Atmospheric Science 1, 1–7. https://doi.org/10.1038/s41612-018-0041-9

Library [WWW Document], n.d. URL https://library.naist.jp/opac/en/book/19856 (accessed 2.20.24).

Marcus, R.A., 1957a. On the Theory of Oxidation-Reduction Reactions Involving Electron Transfer. II. Applications to Data on the Rates of Isotopic Exchange Reactions. The Journal of Chemical Physics 26, 867–871. https://doi.org/10.1063/1.1743423

Marcus, R.A., 1957b. On the Theory of Oxidation-Reduction Reactions Involving Electron Transfer. III. Applications to Data on the Rates of Organic Redox Reactions. The Journal of Chemical Physics 26, 872–877. https://doi.org/10.1063/1.1743424

Marcus, R.A., 1956. On the Theory of Oxidation-Reduction Reactions Involving Electron Transfer. I. The Journal of Chemical Physics 24, 966–978. https://doi.org/10.1063/1.1742723

Marenich, A.V., Cramer, C.J., Truhlar, D.G., 2009. Universal Solvation Model Based on Solute Electron Density and on a Continuum Model of the Solvent Defined by the Bulk Dielectric Constant and Atomic Surface Tensions. Journal Physical Chemistry B 113, 6378–6396. https://doi.org/10.1021/jp810292n

MEE, 2004. Chinese hazard evaluation guldeline for the hazard evaluation of new chemical substances (HJ/T 154–2004). Ministry of Ecology and Environment. https://english.mee.gov.cn/special_reports/chemical_regulation/newchemicals/200712/t20071217_115157.shtml (accessed 6.26.24).

Meylan, W.M., Howard, P.H., Boethling, R.S., Aronson, D., Printup, H., Gouchie, S., 1999. Improved method for estimating bioconcentration/bioaccumulation factor from octanol/water partition coefficient. Environmental Toxicology and Chemistry. https://setac.onlinelibrary.wiley.com/doi/abs/10.1002/etc.5620180412

Miyoshi, A, n.d. GPOP software. Revision 2022.01.20m1. http://akrmys.com/gpop/

Parr, R.G., Yang, W., 1984. Density functional approach to the frontier-electron theory of chemical reactivity. Journal of the American Chemical Society 106, 4049–4050. https://doi.org/10.1021/ja00326a036

Ptáček, P., Šoukal, F., Opravil, T., Ptáček, P., Šoukal, F., Opravil, T., 2018. Introduction to the Transition State Theory, in: Introducing the Effective Mass of Activated Complex and the Discussion on the Wave Function of This Instanton. IntechOpen. https://doi.org/10.5772/intechopen.78705

Qiu, Z., Sun, J., Han, D., Wei, F., Mei, Q., Wei, B., Wang, X., An, Z., Bo, X., Li, M., Xie, J., He, M., 2020. Ozonation of diclofenac in the aqueous solution: Mechanism, kinetics and ecotoxicity assessment. Environmental Research 188, 109713. https://doi.org/10.1016/j.envres.2020.109713

Schlegel, H.B., 1982. Optimization of equilibrium geometries and transition structures. Journal of Computational Chemistry 3, 214–218. https://doi.org/10.1002/jcc.540030212

Schrödinger, E., 1996. An Undulatory Theory of the Mechanics of Atoms and Molecules. https://doi.org/10.1103/PhysRev.28.1049

Singleton, D.L., Cvetanovic, R.J., 1976. Temperature dependence of the reaction of oxygen atoms with olefins. Journal of the American Chemical Society 98, 6812–6819. https://doi.org/10.1021/ja00438a006

Smoluchowski, M. v, 1918. Versuch einer mathematischen Theorie der Koagulationskinetik kolloider Lösungen. Zeitschrift für Physikalische Chemie 92U, 129–168. https://doi.org/10.1515/zpch-1918-9209

Shi, G., Shouliang, W., Qiuyue, W., and John, S. W. Standing on the Shoulders of Giants Hammond's Postulate. WuXi Biology. https://wuxibiology.com/standing-on-the-shoulders-of-giants-hammonds-postulate/ (accessed 5.23.24).

Stein, V., published, T.S., 2022. What Is Earth's Average Temperature? Available on: https://www.space.com/17816-earth-temperature.html

Stokes, G.G., 2009. Mathematical and Physical Papers. Cambridge Core. https://doi.org/10.1017/CBO9780511702297

Sun, Y., Chen, X., Xu, F., Wang, X., 2020. Quantum chemical calculations on the mechanism and kinetics of ozone-initiated removal of p-coumaryl alcohol in the atmosphere. Chemosphere 253, 126744. https://doi.org/10.1016/j.chemosphere.2020.126744

Truhlar, D.G., 2003. Potential Energy Surfaces, in: Meyers, R.A. (Ed.), Encyclopedia of Physical Science and Technology (Third Edition). Academic Press, New York, pp. 9–17. https://doi.org/10.1016/B0-12-227410-5/00606-2

Truhlar, D.G., 1985. Nearly encounter-controlled reactions: The equivalence of the steady-state and diffusional viewpoints. Journal of Chemical Education 62, 104–106. https://doi.org/10.1021/ed062p104

US EPA, 2015a. Ecological Structure Activity Relationships (ECOSAR) Predictive Model. https://www.epa.gov/tsca-screening-tools/ecological-structure-activity-relationships-ecosar-predictive-mode

US EPA, 2015b. EPI Suite^{TM}-Estimation Program Interface. https://www.epa.gov/tsca-screening-tools/epi-suitetm-estimation-program-interface

US EPA, 2015c. Toxicity Estimation Software Tool (TEST). https://www.epa.gov/chemical-research/toxicity-estimation-software-tool-test (accessed 6.9.23).

Van Mourik, T., Bühl, M., Gaigeot, M.-P., 2014. Density functional theory across chemistry, physics and biology. Philosophical Transactions of the Royal Society A: Mathematical, Physical and Engineering Sciences 372, 20120488. https://doi.org/10.1098/rsta.2012.0488

Yao, J., Tang, Y., Zhang, Y., Ruan, M., Wu, W., Sun, J., 2022. New theoretical investigation of mechanism, kinetics, and toxicity in the degradation of dimetridazole and ornidazole by hydroxyl radicals in aqueous phase. Journal of Hazardous Materials 422, 126930. https://doi.org/10.1016/j.jhazmat.2021.126930

Zhao, Y., Truhlar, D.G., 2008. The M06 suite of density functionals for main group thermochemistry, thermochemical kinetics, noncovalent interactions, excited states, and transition elements: two new functionals and systematic testing of four M06-class functionals and 12 other functionals. Theor Chem Account 120, 215–241. https://doi.org/10.1007/s00214-007-0310-x

Chapter III. Phosmet

III.1. Introduction

The use of pesticides in agriculture has significantly risen due to population growth and urbanization, as well as the increasing demand for crops. Pesticides, which encompass insecticides, herbicides, rodenticides, and fungicides (US EPA, 2013), are employed to protect plants from pests, weeds, and diseases. However, exposure to these chemicals poses various health risks to humans and animals, including acute effects like nausea, dizziness, and diarrhea, as well as chronic conditions such as Parkinson's, neurological disorders, infertility, and cancer (Sabarwal *et al.*, 2018). Moreover, the excessive application of pesticides has resulted in significant environmental pollution issues, adversely impacting biodiversity and ecosystem functions in aquatic environments (R. Münze *et al.*, 2015).

Organophosphate compounds stand out as the most extensively utilized group of pesticides globally, constituting 45% of the worldwide market (H. Mali *et al.*, 2023). Phosmet, also known as O,O-dimethyl S-phthalimidomethyl phosphorodithioate or 2-(dimethoxyphosphorylsulfanylmethyl) isoindole-1,3-dione, represents a typical organophosphorus insecticide that was initially approved for use in 1966 (***Figure III-1***). It finds application in agricultural practices, including colza fields, apple trees, and apricots (US EPA), targeting various insects such as aphids, caterpillars, fruit flies, leafhoppers, and spider mites.

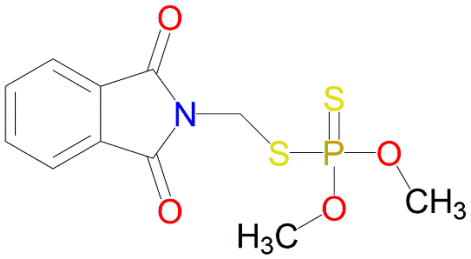

Figure III-1*: structure of phosmet.*

However, there have been reports detailing the adverse impacts of phosmet on the environment and ecosystems. Its acute exposure has been found to be highly toxic to freshwater fish and invertebrates, with chronic effects on freshwater fish include reductions in length and survival rates (Echeverria *et al.*). Consequently, on January 24th, 2022, the European Union announced regulation 94/2022, which evaluates the non-renewal of approval for phosmet and subsequently mandates the withdrawal of authorization for plant production products containing this active ingredient starting from May 1st, 2022 (LAB, 2022). There is considerable research interest in the atmospheric degradation and fate of phosmet.

Generally, the degradation of phosmet in the atmosphere generally depends on the reactive nature of the environment and specific conditions such as temperature, pH, presence of catalysts, and the oxidizing agent involved. In soil environments, phosmet exhibits low persistence, lasting approximately 19 days (Wauchope et al., 1992), and can undergo decomposition through hydrolysis and microbial activity (Camazano and Sanchez Martin,

1983). In aqueous environments, the reactivity of phosmet varies depending on the pH; it remains stable in acidic conditions but undergoes hydrolysis in the basic conditions.

The half-life of phosmet decreases progressively from 13 days (pH = 4.5) to 12 hours (pH = 7.0) and further down to 4 hours (pH = 8.3) (Zweig, 2013). In basic environments, various decomposition products are detected in hydrolysis reactions with hydroxyl anions (HO^-), including phthalamic acid, phthalic acid, and O,O-dimethyl phosphorodithionate. This suggests that the reaction at the phthalimido carbonyl group is more favourable than at phosphorous. When subjected to UV light in a diethyl ether solvent, photolysis tends to yield two primary products: N-methylphthalimide and N-methoxymethylphthalimide, alongside several minor products that remain undetected (Tanabe *et al.*, 1974).

In model solvents like cyclohexane and cyclohexene, phthalimide, N-hydroxymethylphthalimide, and N-methoxymethylphthalimide are identified as the photoproducts of phosmet (Sinderhauf and Schwack, 2003). This observation extends to fatty acid methyl esters, specifically methyl stearate (Sinderhauf and Schwack, 2004). Additionally, depending on the solvent utilized, further degradation products such as N-isopropoxy- and N-methylphthalimide are also observed, with 2-propanol and cyclohexene promoting their formation, respectively (Sinderhauf and Schwack, 2003).

Phosmet is released into the atmosphere through both gas and particulate phases due to spray drift from treatments and post-application emissions (C. Liu *et al.*, 2011). With vapor pressures ranging between 10^{-3} and 10^{-4} Pa at room temperature, phosmet can be present in both gaseous and particle forms in the atmosphere (Tomlin, 1994). Consequently, numerous studies in the literature have explored the heterogeneous transformation of phosmet on particulate surfaces under atmospheric conditions. Liu *et al.* conducted experimental investigations into the heterogeneous reaction of phosmet absorbed on azelaic acid particles with $NO_3^\bullet$ radicals. This resulted in the identification of nitrophosmet-oxon ($C_{11}H_{11}N_2O_7PS$) and nitrophthalimidomethyl-dimethoxyphosphinyl disulfide ($C_{11}H_{11}N_2O_7PS_2$) as the major products of UV photo-oxidation. The average apparent rate was found to be $(1.92 \pm 0.09)\times10^{-12}$ cm^3 $molecule^{-1}$ s^{-1}, with the corresponding atmospheric lifetime towards $NO_3^\bullet$ estimated to be approximately 0.3 hours (C. Liu *et al.*, 2011).

Employing comparable experimental methods, Liu *et al.* have additionally calculated effective rate constants and reactive uptake coefficients, that represent a crucial kinetic parameters for its heterogeneous reactions (Liu et al., 2015). As a result, the reactive uptake coefficients for $NO_3^\bullet$ on phosmet and the average effective rate constants for the heterogeneous reactions of particulate phosmet were determined to be (0.12 ± 0.03) and $(2.80 \pm 0.16) \times10^{-12}$ cm^3 $molecule^{-1}$ s^{-1}, respectively.

Recent studies have also focused on the removal of phosmet from contaminated environments, such as through adsorption by metal oxides. For instance, Nagpal and Kakkar (Nagpal and Kakkar, 2020) investigated the adsorptive removal of phosmet using hierarchically porous calcium oxide (Hr-CaO) and applying the precipitation method with glycerol/water as the solvent. Additionally, Kanan *et al.* (Kanan *et al.*, 2007) reported on the photodecomposition of phosmet under UV light using silver nanoclusters doped in mordenite zeolite, while Eren and

Gürkan (Eren and Gürkan, 2021) explored its decomposition using an aqueous TiO_2 suspension. Other studies have utilized materials such as montmorillonite clay (Sánchez Camazano and Sánchez Martín, 1983) and biochar and charcoal (Taha *et al.*, 2014) as adsorbents for phosmet removal.

Among the methods utilized for removing pollutants in water treatment, Advanced Oxidation Processes (AOPs) have been widely used due to their high removal efficiencies (Al-Anazi *et al.*, 2018; Klavarioti *et al.*, 2009). These processes involve the generation of highly reactive free radicals such as hydroxyl radicals ($HO^{\bullet}$), singlet oxygen ($^1O_2$), oxygen radical anion ($O_2^{\bullet-}$), and sulfate radical anions ($SO_4^{\bullet-}$), which can partially or completely transform harmful contaminants in water. Hydroxyl radicals are particularly reactive primary oxidants capable of initiating oxidation reactions by abstracting hydrogen atoms or adding to double bonds in organic molecules. As far as we are aware, there have been no dedicated studies in the literature on the oxidation of phosmet by reactive radicals, particularly by $HO^{\bullet}$ radicals, under environmental conditions.

Quantum mechanical methods using the DFT calculations have proven effective in examining the thermodynamics and kinetics of environmental oxidation processes involving various organic compounds by reactive radicals. For example, Abdel-Rahman *et al.* did a theoretical investigation into the degradation mechanism of O-anisidine initiated by a $HO^{\bullet}$ radical attack to explain the reaction kinetics and its impacts in the tropospheric region (Abdel-Rahman *et al.*, 2021b). Almeida and Kurtén shed light on the reaction mechanism of the imine derivative of piperazine oxidation by $HO^{\bullet}$ radicals using quantum chemistry and theoretical kinetics methods (Almeida and Kurtén, 2022). Bo *et al.* also studied the photochemical degradation process of tyrosol in wastewater by $HO^{\bullet}$ and $SO_4^{\bullet-}$ radicals (X. Bo *et al.*, 2021). Similarly, Xu *et al.* explored the degradation reaction of N, N-diethyl-m-toluamide (DEET) induced by $HO^{\bullet}$ and $SO_4^{\bullet-}$ radicals in water environments through DFT simulations (Mengmeng Xu, *et al.*, 2022). Additionally, Dao *et al.* conducted theoretical examinations of the oxidation process of metazachlor herbicide by $HO^{\bullet}$ radicals in both gas and aqueous phases using DFT, aiming to assess the mechanism and kinetics of these reactions (Dao *et al.*, 2023). Similarly, Ngo *et al.* conducted analogous investigations into the $HO^{\bullet}$-initiated oxidation of quinmerac herbicide in the aqueous phase under varying temperatures and pH conditions (Ngo *et al.*, 2023).

Understanding the decomposition and oxidation pathways of phosmet insecticides under environmental conditions is crucial for a more comprehensive assessment of their toxicity and their impact on human health and the environment. Therefore, this study aims to investigate the degradation mechanisms of phosmet initiated by $HO^{\bullet}$ through three distinct reaction pathways: formal hydrogen transfer (FHT), radical adduct formation (RAF), and single electron transfer (SET). The thermodynamics, mechanisms, and kinetics of these reactions, as well as the lifetime of phosmet, will be examined across a range of temperatures, spanning from 253 to 323 K in the gas phase, and from 283 to 323 K in the aqueous phases (relevant to environmental water and water treatment processes). Finally, the ecotoxicity of phosmet and its degradation by-products will be assessed in aquatic environments to understand their impact on aquatic organisms.

III.2. Results and discussion

III.2.1. Structure and electronic properties of phosmet

The conformational analysis of the phosmet structure was performed using MSTor software. ConfGen module generates Gaussian input files for a set of conformational structures by rotating around user-specified bonds in an input structure. 5 torsions with 4 initial dihedral angle values lead to 866 structures. Geometry optimizations at the M06-2X/6-31+G(d,p) level of theory found 44 conformers, where the most stable conformation was chosen to study the potential energy surfaces (PES) of phosmet towards HO• radicals. The optimized geometry of the most stable conformer in both the gas and aqueous phases is shown in ***Figure III-2***. A slight difference in the geometric structure is observed: specifically, the dihedral angle of N8-C10-S11-P12 is 25° and -66° for the most stable conformer in the gas and aqueous phases, respectively. The distributions of the highest occupied molecular orbital, the lowest unoccupied molecular orbital, and the electrostatic potential maps, are shown in ***Figure III-3*** and ***Figure III-4***.

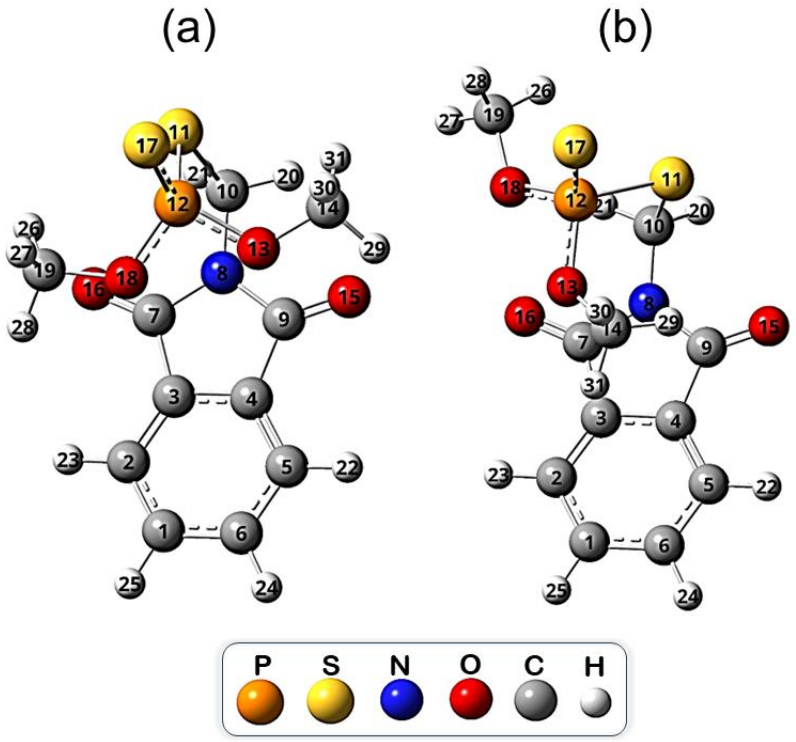

Figure III-2*: optimized structures of the most stable conformer of phosmet in (a) the gas phase and (b) aqueous phase.*

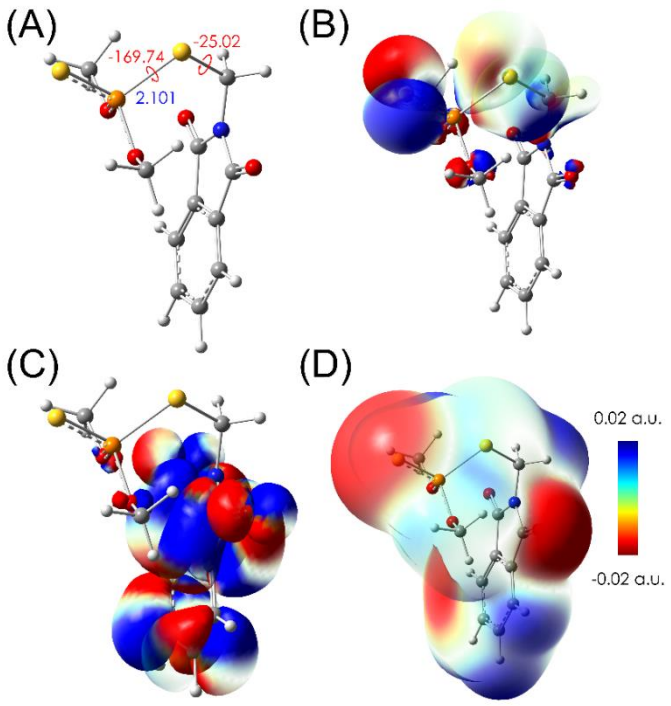

***Figure III-3**: (A) optimized structure, (B) HOMO, (C) LUMO distributions and (D) electrostatic potential (ESP) maps of phosmet in gas phase (Red represents regions of high negative potential and blue represents regions of high positive potential).*

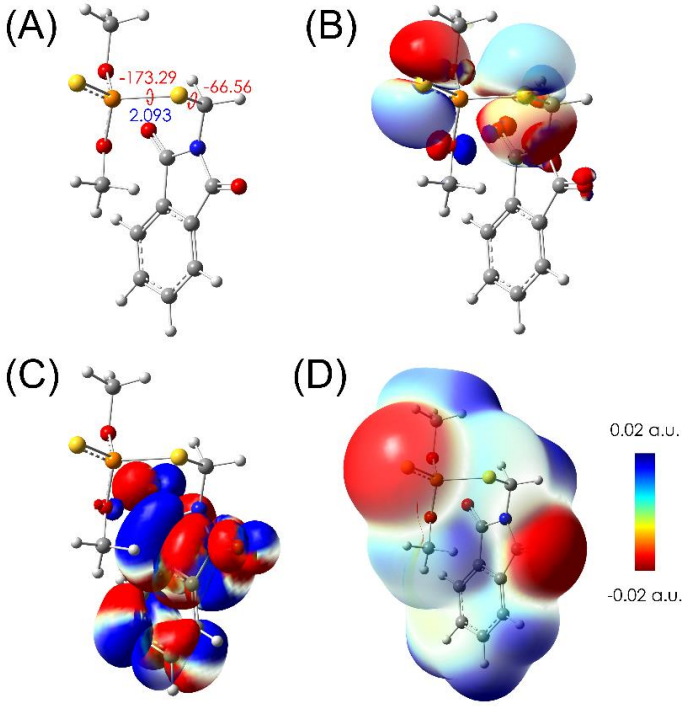

***Figure III-4**: (A) optimized structure, (B) HOMO, (C) LUMO distributions and (D) electrostatic potential (ESP) maps of phosmet in aqueous phase (Red represents regions of high negative potential and blue represents regions of high positive potential).*

It is observed that the HOMO is predominantly situated within the P=S group, while the LUMO is primarily located in the aromatic rings. The ESP maps illustrate that negatively charged regions (shown in red) are present in the C=O group and the O atom, whereas positively charged regions (shown in blue) are situated in the rings. This information enables the prediction of molecular regions with a high tendency to donate electrons and those tend to accept them in single electron transfer reactions with external radicals.

The results of the calculated Fukui indices show that the P=S group and the C atoms of the aromatic rings may be favourable (***Figure III-5***).

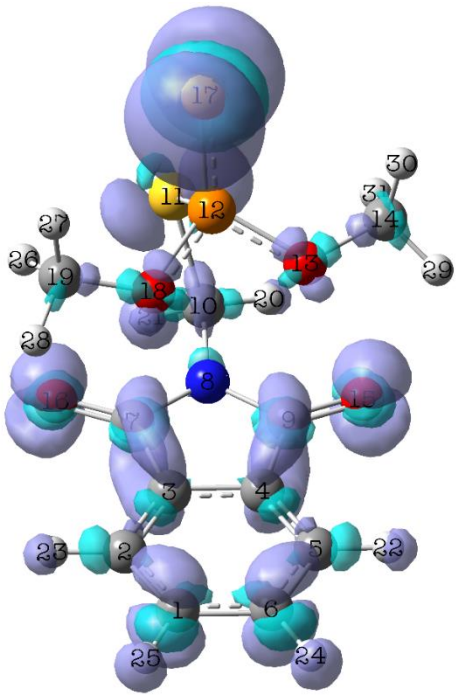

Figure III-5*: plot of Fukui function for radical attack (f^0) describing the possible main reactive sites of phosmet calculating in the gas phase.*

III.2.2. Oxidation mechanisms of phosmet

The oxidation mechanisms of phosmet initiated by HO$^\bullet$ occurs through three distinct reaction pathways: H-abstraction (FHT), HO$^\bullet$-addition (RAF), and single electron transfer (SET). Calculations were done as described in **Chapter II**.

III.2.2.1. Formal hydrogen transfer (FHT) reactions

The formal hydrogen transfer reaction involves the transfer of a hydrogen atom (H$^\bullet$) from the phosmet molecule to the HO$^\bullet$ radical acceptor, resulting in the formation of a new radical intermediate along with a water molecule.

Twelve H-abstractions from phosmet molecule by HO$^{\bullet}$ radical in the FHT reaction, will be considered in the gas and aqueous phases. These reactions will take place at the H20/H21 positions (methylene group) of the C10 carbon atom, H22/H23/H24/H25 positions of the benzyl ring, H26/H27/H28 positions (methyl group) of the C19 carbon atom, and H29/H30/H31 positions of the C14 carbon.

In ***Figure III-6***, you'll find representations of all abstraction pathways, showing the standard Gibbs free reaction energies ($\Delta_r G°_g$, $\Delta_r G°_{aq}$) and standard Gibbs free activation energies ($\Delta G°^{\neq}_g$, $\Delta G°^{\neq}_{aq}$) across both the gas and aqueous phases. Furthermore, ***Table III-1*** and ***Table III-2*** details the thermodynamic parameters, including standard reaction enthalpy at 0 K ($\Delta_r H°_{0K}$), standard reaction enthalpy at 298 K ($\Delta_r H°_{298K}$), standard Gibbs free reaction energy at 298 K ($\Delta_r G°_{298K}$), standard activation enthalpy at 298 K ($\Delta H°^{\neq}_{298K}$), and standard Gibbs free activation energy at 298 K ($\Delta G°^{\neq}_{298K}$) for all H-abstraction reactions.

In both the gas and aqueous phases, all FHT reactions are exergonic and spontaneous, as evidenced by the obtained negative $\Delta_r G°$ values at 298 K ranging from -102.16 kJ mol^{-1} (at H20 position) to -17.88 kJ mol^{-1} (at H22) in the gas phase, and from -100.78 kJ mol^{-1} (at H20) to -27.07 kJ mol^{-1} (at H22) in the aqueous phase. In addition, the standard Gibbs free activation energy ($\Delta G°^{\neq}$) values vary from 28.58 kJ mol-1 (at H21) to 52.95 kJ mol^{-1} (at H24) in the gas phase, and from 38.85 kJ mol^{-1} (at H31) to 59.65 kJ mol^{-1} (at H23) in the aqueous phase under standard conditions at 298 K.

Moreover, all FHT reactions in both the gas and aqueous phases exhibit exothermic behaviour, as indicated by negative values of the standard reaction enthalpy at 0 K ($\Delta_r H°_{0K}$). These values range from -24.45 kJ mol^{-1} (at H22 of the benzyl ring) to -99.31 kJ mol^{-1} (at H20 of the methylene group at the C10 atom) in the aqueous phase, and from -16.60 kJ mol^{-1} (at H22) to -101. kJ mol^{-1} (at H20 and H21 positions) in the gas phase. It is noteworthy that FHT reactions are more favourable in the aqueous phase than in the gas phase.

The low standard Gibbs free activation energy values detected at the methylene group (H20/H21) and the two methyl groups (H26/H27 and H30/H31) suggest that these pathways are the most favourable sites for H-abstraction. This finding will be validated later in the section of kinetic calculations.

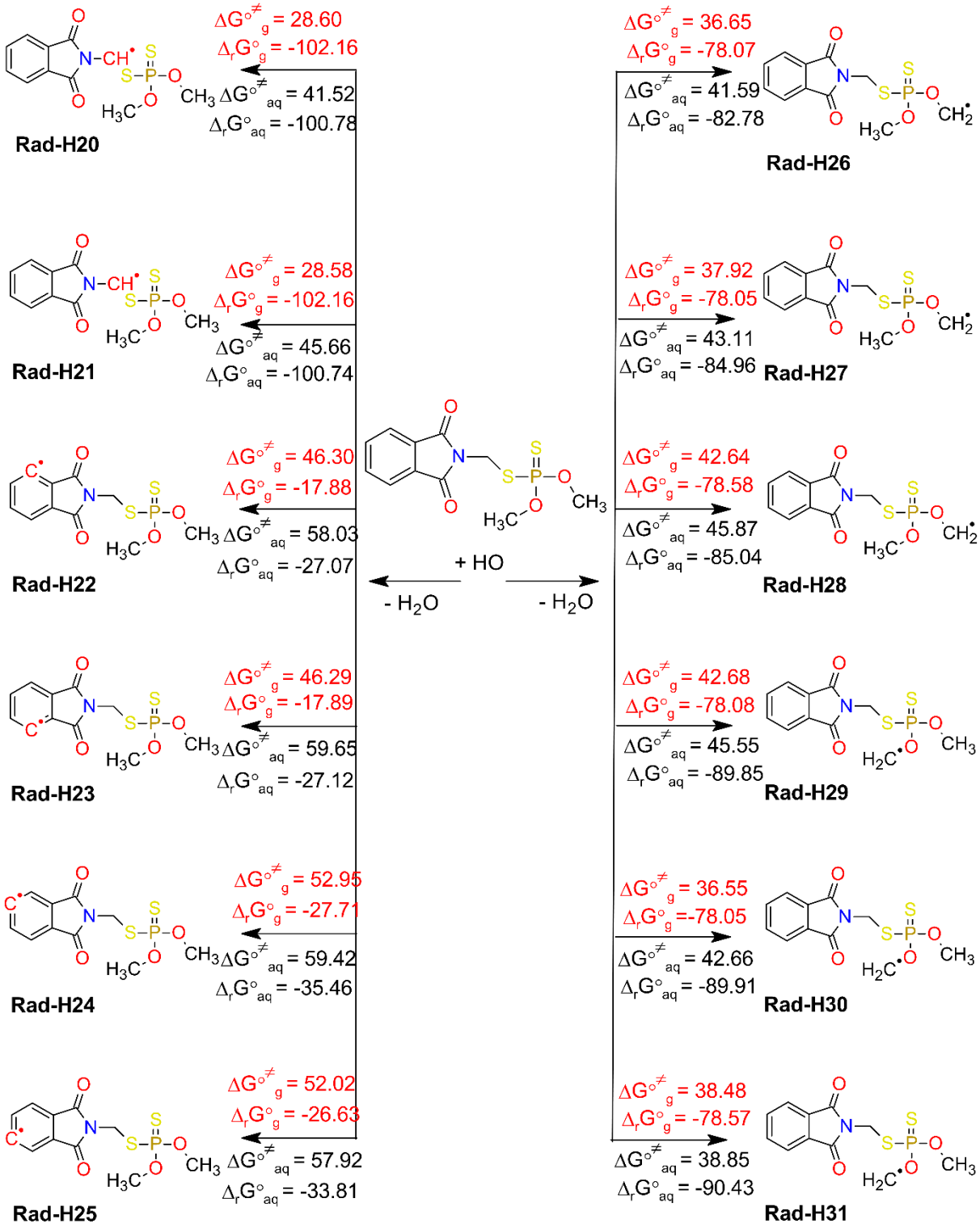

***Figure III-6**: formal hydrogen transfer reaction pathways of phosmet by HO• radical, including standard Gibbs free reaction energies ($\Delta_rG°_g$, $\Delta_rG°_{aq}$) and Gibbs free activation energies ($\Delta G°^{\neq}_g$, $\Delta G°^{\neq}_{aq}$), in the gas (g) and aqueous (aq) phases, at 298 K. Units are in kJ mol-1.*

***Table III-1**: relative standard enthalpy ($\Delta H°_{0K}$) for MCR and MCP, adiabatic energy barrier (E_0) for TS, and standard reaction enthalpy ($\Delta_r H°_{0K}$) for products (P) at 0 K of the FHT reactions in (a) the gas phase, and (b) the aqueous phase using the M06-2X/6-311++G(3df,3pd)// M06-2X/6-31+G(d,p) level of theory. Units are in kJ mol^{-1}.*

a) Gas phase:

Positions	MCR	TS	MCP	P
H20	-30.35	-9.80	-121.25	-101.36
H21	-30.35	-9.80	-121.27	-101.36
H22	-29.25	7.87	-42.52	-16.60
H23	-24.32	7.86	-42.52	-16.60
H24	-27.34	19.63	-33.36	-24.55
H25	-27.35	18.98	-33.33	-24.51
H26	-30.35	-2.29	-102.26	-78.82
H27	-21.84	-1.40	-95.70	-78.81
H28	-27.35	5.95	-102.27	-78.82
H29	-27.35	5.96	-102.24	-78.83
H30	-21.20	-1.22	-93.22	-78.81
H31	-24.32	-1.73	-102.26	-78.81

b) Aqueous phase:

Positions	MCR	TS	MCP	P
H20	-15.29	6.83	-110.58	-99.31
H21	-17.17	6.78	-104.75	-99.30
H22	-11.21	22.11	-34.79	-24.45
H23	-15.03	22.35	-37.42	-24.77
H24	-10.03	24.09	-34.69	-31.80
H25	-9.93	23.39	-35.34	-31.65
H26	-11.07	7.60	-92.42	-80.93
H27	-8.92	9.08	-91.67	-82.33
H28	-17.21	6.79	-95.18	-82.35
H29	-12.32	8.88	-100.33	-86.86
H30	-11.08	5.05	-98.94	-86.88
H31	-10.58	7.10	-95.81	-86.09

***Table III-2**: calculated standard reaction enthalpy ($\Delta_r H°_{298K}$) and standard Gibbs free reaction energy ($\Delta_r G°_{298K}$), standard activation enthalpy ($\Delta H°^{\neq}_{298K}$) and standard Gibbs free activation energy ($\Delta G°^{\neq}_{298K}$) at 298 K for FHT reactions in (a) the gas phase, and (b) the aqueous phase using the M06-2X/6-311++G(3df,3pd)// M06-2X/6-31+G(d,p) level of theory. Units are in kJ mol^{-1}.*

a) Gas phase:

Positions	$\Delta_r H°_{298K}$	$\Delta_r G°_{298K}$	$\Delta H°^{\neq}_{298K}$	$\Delta G°^{\neq}_{298K}$
H20	-100.40	-102.16	-13.87	28.60
H21	-100.40	-102.16	-13.87	28.58
H22	-16.20	-17.88	4.21	46.30
H23	-16.20	-17.89	4.21	46.29
H24	-23.79	-27.71	17.49	52.95
H25	-23.88	-26.63	17.01	52.02
H26	-78.33	-78.07	-6.56	36.65
H27	-78.32	-78.05	-5.29	37.92
H28	-78.33	-78.58	2.24	42.64
H29	-78.33	-78.08	2.24	42.68
H30	-78.32	-78.05	-5.50	36.55
H31	-78.32	-78.57	-6.35	38.48

b) Aqueous phase:

Positions	$\Delta_r H°_{298K}$	$\Delta_r G°_{298K}$	$\Delta H°^{\neq}_{298K}$	$\Delta G°^{\neq}_{298K}$
H20	-98.21	-100.78	3.74	41.52
H21	-98.21	-100.74	2.85	45.66
H22	-24.08	-27.07	18.87	58.03
H23	-24.10	-27.12	18.82	59.65
H24	-31.03	-35.46	21.29	59.42
H25	-30.99	-33.81	21.00	57.92
H26	-79.95	-82.78	4.13	41.59
H27	-81.39	-84.96	5.64	43.11
H28	-81.40	-85.04	1.93	45.87
H29	-85.57	-89.85	4.97	45.55
H30	-85.57	-89.91	1.15	42.66
H31	-84.03	-90.43	4.15	38.85

III.2.2.2. Radical adduct formation (RAF) reactions

RAF reactions depends on the molecular structure having double bonds or pi bonds. It involves the HO$^{\bullet}$ radical adding onto the double bonds of the phosmet molecule, forming a covalent bond and yielding a product referred to as a radical adduct. This reaction often competes with the FHT reaction, depending on the specific chemical configuration.

RAF reactions take place at the atoms involved in unsaturated bonds within the phosmet molecule, including the carbon atoms of the benzyl group (C1 to C6), C=O group (C7 and C9), a sulfur atom (S17), and the phosphorus atom (P12). *Ipso*-addition was performed at each carbon atom of the benzyl group. ***Figure III-7*** presents all addition pathways, including ($\Delta_r G°_g$, $\Delta_r G°_{aq}$) and ($\Delta G°^{\neq}_g$, $\Delta G°^{\neq}_{aq}$), in both the gas and aqueous phases at a temperature of 298 K.

It is important to note that, in the gas phase, all RAF reactions, except those at C7, C9, and S17 sites, are exergonic and spontaneous, as indicated by negative values of standard Gibbs free reaction energies at 298 K ($\Delta_r G°_g$), ranging from -163.99 kJ mol^{-1} (at P12) to -21.77 kJ mol^{-1} (at C3 and C4). The standard Gibbs free activation energy at 298 K ($\Delta G°^{\neq}_g$) vary from 24.73 kJ mol^{-1} (at P12) to 86.37 kJ mol^{-1} (at C7). This suggests that the most favourable HO$^{\bullet}$-addition pathway is located at the phosphorus P12-site, characterized by the lowest $\Delta G°^{\neq}_g$ value. Conversely, RAF reactions are less likely to occur at the carbonyl group and the sulfur atom, where reactions are non-spontaneous and have higher free energy barriers (approximately 86.37 kJ mol^{-1} at C7 and C9, and 72.39 kJ mol^{-1} at S17) in the gas phase.

In the aqueous phase, the HO$^{\bullet}$-addition reactions are comparatively less favourable than in the gas phase. The values of the standard Gibbs free activation energy at 298 K range from 27.70 kJ mol^{-1} (at P12) to 94.13 kJ mol^{-1} (at C7). Furthermore, the standard Gibbs free reaction energies at 298 K ($\Delta_r G°_{aq}$) vary between -149.59 kJ mol^{-1} and 39.87 kJ mol^{-1}, suggesting spontaneous reactions across most sites except at C7 (39.87 kJ mol^{-1}) and C9 (24.31 kJ mol^{-1}) (***Table III-4***).

In addition, all RAF reactions in both the gas and aqueous phases are exothermic, as indicated by the negative values of the standard reaction enthalpies ($\Delta_r H°_{0K}$) at 0 K. In the gas phase, these values range from -198.15 kJ mol^{-1} (at P12) to -20.67 kJ mol^{-1} (at C7), while in the aqueous phase, they range from -180.69 kJ mol^{-1} (at P12) to -14.56 kJ mol^{-1} (at C9). Notably, there is an exception to this trend, with the reaction at S17 being endothermic, showing a positive standard reaction enthalpy of 27.13 kJ mol^{-1} (***Table III-3***).

Upon comparing the adiabatic energy barrier (E_0) of the transition states at 0 K, it becomes apparent that the FHT reactions are more dominant than the RAF reactions in both the gas and aqueous phases. However, there is an exception observed in the aqueous phase, where the RAF reaction at P12 exhibits a lower energy of activation (-10.17 kJ mol^{-1}) compared to that at H30 (5.05 kJ mol^{-1}).

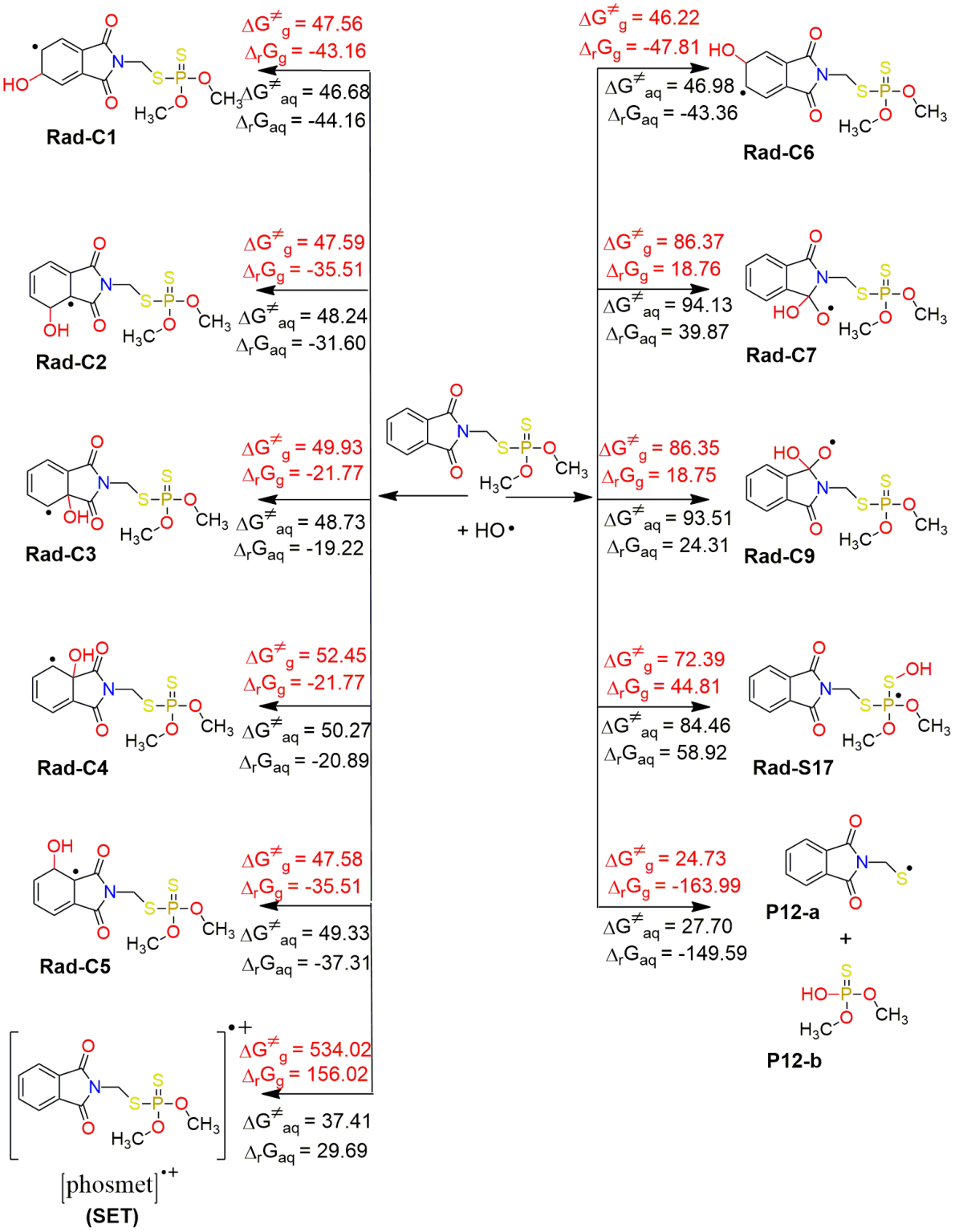

***Figure III-7**: radical adduct formation and single electron transfer (SET) reaction pathways of phosmet by HO• radical, including standard Gibbs free reaction energies ($\Delta_rG°_g$, $\Delta_rG°_{aq}$) and Gibbs free activation energies ($\Delta G^{\neq}{}°_g$, $\Delta G^{\neq}{}°_{aq}$), in the gas (g) and aqueous (aq) phases, at a temperature of 298 K. Units are in kJ mol^{-1}.*

***Table III-3**: relative standard enthalpy ($\Delta H°_{0K}$) for MCR, adiabatic energy barrier (E_0) for TS, and standard reaction enthalpy ($\Delta_r H°_{0K}$) for products (P) at 0 K of the RAF reactions in (a) the gas phase, and (b) the aqueous phase using the M06-2X/6-311++G(3df,3pd)// M06-2X/6-31+G(d,p) level of theory. Units are in kJ mol^{-1}.*

a) Gas phase:

Positions	MCR	TS	P
C1	-12.39	11.79	-82.11
C2	-27.31	5.59	-79.06
C3	-15.78	13.60	-63.35
C4	-15.67	13.57	-63.35
C5	-27.33	5.59	-79.06
C6	-27.73	10.10	-82.44
C7	-30.34	46.17	-20.67
C9	-30.35	46.16	-20.67
S17	-21.50	38.08	12.42
P12	-21.69	-13.84	-198.15

b) Aqueous phase:

Positions	MCR	TS	P
C1	-9.45	11.26	-81.80
C2	-16.59	11.54	-71.89
C3	-11.51	12.71	-60.65
C4	-11.10	12.88	-61.87
C5	-11.19	12.79	-74.36
C6	-11.88	9.82	-82.00
C7	-8.01	56.22	0.91
C9	-8.24	55.39	-14.56
S17	-11.31	48.75	27.13
P12	-18.57	-10.17	-180.69

***Table III-4**: calculated standard reaction enthalpy ($\Delta_r H°_{298K}$) and standard Gibbs free reaction energy ($\Delta_r G°_{298K}$), standard activation enthalpy ($\Delta H^{°\neq}_{298K}$) and standard Gibbs free activation energy ($\Delta G^{°\neq}_{298K}$) at 298 K for RAF reactions in (a) the gas phase, and (b) the aqueous phase using the M06-2X/6-311++G(3df,3pd)// M06-2X/6-31+G(d,p) level of theory. Units are in kJ mol^{-1}.*

a) Gas phase:

Positions	$\Delta_r H°_{298K}$	$\Delta_r G°_{298K}$	$\Delta H^{°\neq}_{298K}$	$\Delta G^{°\neq}_{298K}$
C1	-86.66	-43.16	8.43	47.56
C2	-84.56	-35.51	0.52	47.59
C3	-68.12	-21.77	9.86	49.93
C4	-68.12	-21.77	9.85	52.45
C5	-84.56	-35.51	0.52	47.58
C6	-86.77	-47.81	6.39	46.22
C7	-25.47	18.76	41.40	86.37
C9	-25.47	18.75	41.40	86.35
S17	10.76	44.81	35.17	72.39
P12	-200.58	-163.99	-18.04	24.73

b) Aqueous phase:

Positions	$\Delta_r H°_{298K}$	$\Delta_r G°_{298K}$	$\Delta H^{°\neq}_{298K}$	$\Delta G^{°\neq}_{298K}$
C1	-86.16	-44.16	7.83	46.68
C2	-76.41	-31.60	7.91	48.24
C3	-65.60	-19.22	9.54	48.73
C4	-66.50	-20.89	9.51	50.27
C5	-78.53	-37.31	9.10	49.33
C6	-86.65	-43.36	6.21	46.98
C7	-3.80	39.87	51.44	94.13
C9	-19.33	24.31	50.61	93.51
S17	25.72	58.92	45.53	84.46
P12	-182.58	-149.59	-15.13	27.70

III.2.2.3. Single electron transfer (SET) reaction

The SET process involves the transfer of an electron from the phosmet molecule to the $HO^{\bullet}$ radical. The rate of this reaction is influenced by various factors, including the energy disparity and the bond strength between the electron donor and acceptor, as well as the solvent environment in which the reaction occurs, with a preference for the aqueous phase over the gas phase. As expected, high values of $\Delta_r G°$ and $\Delta G°^{\neq}$ for the SET reaction in the gas phase at 298 K were observed (*i.e.*, 156.02 and 534.02 kJ mol^{-1}, respectively). Meanwhile, notably lower values (*i.e.*, 29.69 and 37.41 kJ mol^{-1}, respectively) were found in the aqueous phase.

This indicates that the SET reactions are non-spontaneous and insignificant (negligible) in the gas phase, but notably more significant in the aqueous phase. This observation aligns with the expectation that the SET process involves the transfer of a charged particle (*i.e.*, an electron), which is more favourable in a polar environment such as water. Additionally, it's worth noting that the SET reaction with the $HO^{\bullet}$ radical is less prevalent compared to reactions involving other radicals such as $SO4^{\bullet-}$ and $CO^{\bullet-}$, as reported in the literature (Xu et al., 2023).

III.2.3. Kinetic calculations of phosmet oxidation

In order to gain deeper insights into the oxidation mechanism of phosmet by $HO^{\bullet}$ radicals, the kinetics of the FHT, RAF, and SET reactions were studied by computing their rate constants across a temperature span of 253-323 K in the gas phase and 283-323 K in the aqueous phase. ***Figure III-8*** and ***9***, and ***Table III-5*** and ***6*** illustrate the variations in the rate constant (*k*) and the branching ratio (*Γ*) values for both abstraction (FHT) and addition (RAF) reactions in both phases as temperature changes.

In the gas phase, the rate constants of the FHT reactions obtained at 298 K varied from 9.25×10^{5} (at H24) to 6.02×10^{9} M^{-1} s^{-1} (at H21), while those of the RAF reactions varied from 1.72×10^{-1} (at C7) to 7.42×10^{9} M^{-1} s^{-1} (at P12). The total rate constant of the FHT reactions at 298 K is equal to 1.31×10^{10} M^{-1} s^{-1}, which is more significant than that of RAF reactions being 7.43×10^{9} M^{-1} s^{-1}, indicating that the FHT reactions are more favourable than the RAF ones in the gas phase.

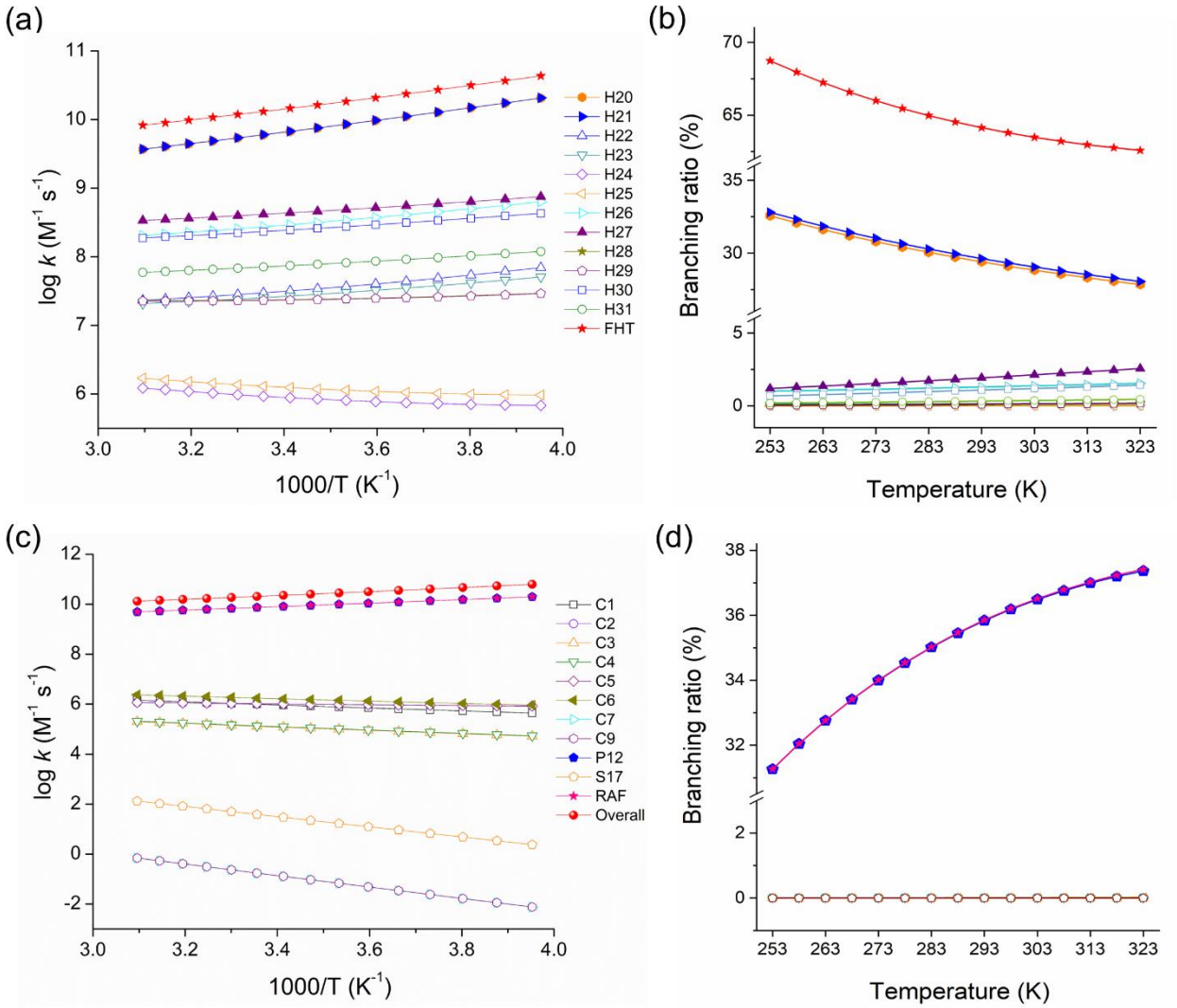

***Figure III-8**: rate constants (k) and branching ratio (Γ, %) for the formal hydrogen transfer (FHT) reactions (a, b) and the radical adduct formation (RAF) reactions (c, d), between phosmet and HO• radical in the gas phase.*

On the other hand, in the aqueous phase at 298 K, the rate constants of the FHT reactions obtained ranged from 4.82×10^{4} (at H24) to 7.09×10^{7} M^{-1} s^{-1} (at H31), while those of the RAF reactions varied from 4.82×10^{-3} (at C7) to 1.17×10^{9} M^{-1} s^{-1} (at P12). The total rate constant of the FHT reactions at 298 K being 1.86×10^{8}, less than that of RAF reactions being 1.17×10^{9} M^{-1} s^{-1}, indicates that the RAF reactions are more favourable than the FHT ones in the aqueous phase.

In contrast, the SET reaction is negligible in the gas phase, and its rate constant measured at 298 K in the aqueous phase was also minimal, at 5.57×10^{-14} M^{-1} s^{-1}. This value is considered negligible when compared to those of FHT and RAF reactions; hence, our further research focused solely on FHT and RAF reactions to explore the impact of temperature.

Furthermore, the overall rate constant (including all three reactions: FHT, RAF, and SET) at 298 K in the aqueous phase (1.36×10^{9} M^{-1} s^{-1}) is lower than that in the gas phase (2.05×10^{10} M^{-1} s^{-1}), mainly due to the diffusion limit inherent in the aqueous phase.

Remarkably, the overall rate constant at 298 K in the aqueous phase (*i.e.*, 1.36×10^{9} M^{-1} s^{-1}) is very close to the one obtained by "*py*SiRC"- python Simulator of Rate Constant of the radical-based oxidation processes of aqueous organic contaminants (*i.e.*, k_{app} = 1.56×10^{9} M^{-1} s^{-1}) (Sanches-Neto *et al.*, 2021) (Sanches-Neto et al., 2022). The latter value was obtained using the XGBoost machine learning algorithm combined with a molecular access system (MACCS) fingerprint model, showing 54.29% similarity for the phosmet molecule within the applicability domain.

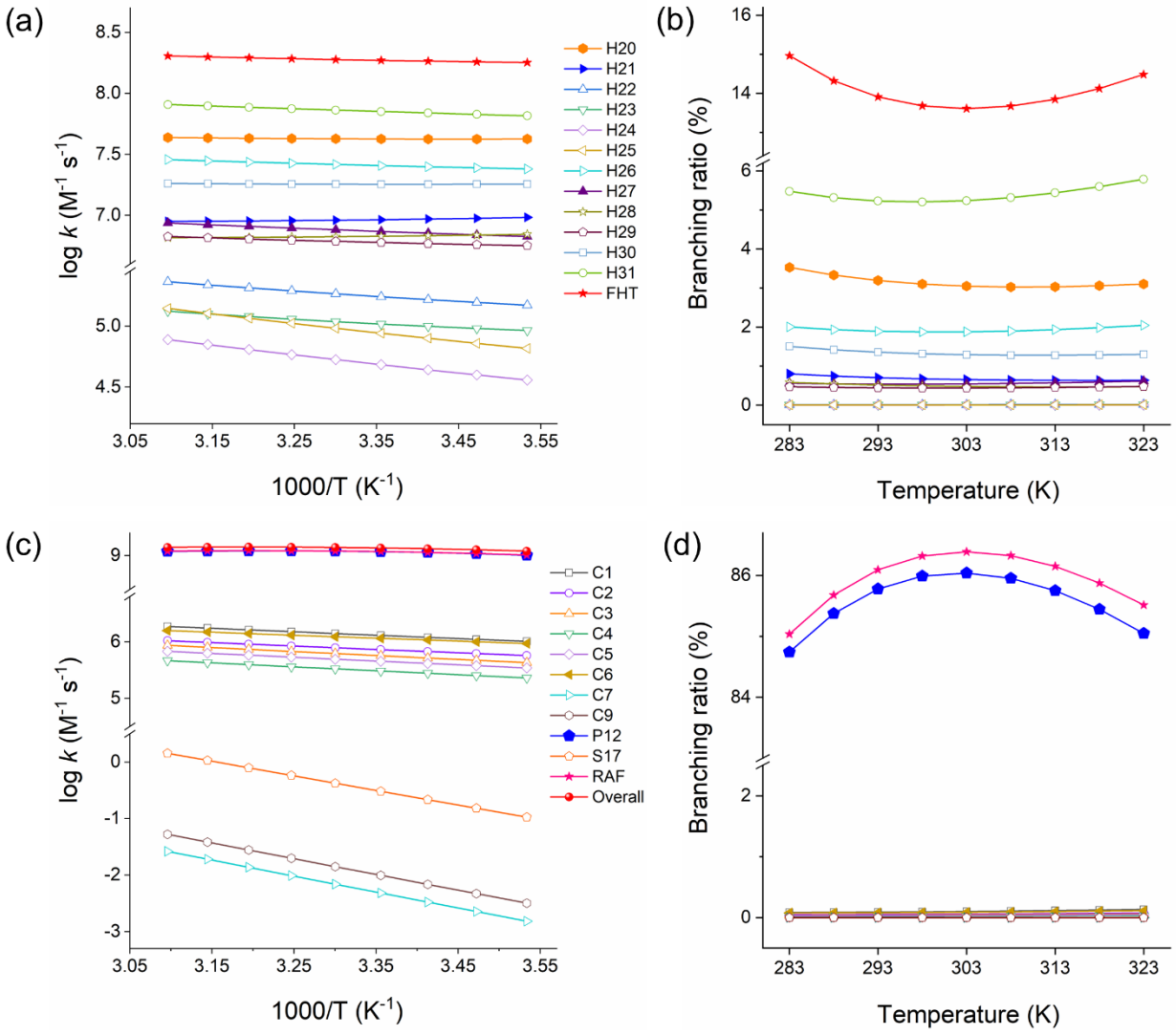

***Figure III-9**: apparent rate constants (k_{app}) and branching ratio (Γ, %) for the formal hydrogen transfer (FHT) reactions (a, b), and the radical adduct formation (RAF) reactions (c, d) between phosmet and HO$^{\bullet}$ radical in the aqueous phase.*

The calculated total branching ratio (Γ) of the FHT reactions in the gas phase gradually decreased from 68.7 to 62.6%, and that of the RAF ones increased from 31.3 to 37.4% as the temperature increase from 253 to 323 K range (***Figure III-8b*** and ***8d***).

The highest branching ratios are noted with the FHT reactions at positions H20 (ranging from 32.6 to 27.8%) and H21 (ranging from 32.8 to 28.0%), while the one at P12 atom (ranging from 31.3 to 37.4%) is the most essential branching ratio of RAF reactions. These reactions are considered the most predominant in the gas phase.

In the aqueous phase, the temperature-dependent kinetic trends exhibit slight variations. The total branching ratio values for FHT decreased as the temperature rose from 283 K to 303 K, after which they began to rise again with further increases in temperature up to 323 K. For instance, at the methyl group's H31 position, the highest Γ values for FHT decreased from 5.5% at 283 K to 5.2% at 303 K, and then slightly increased to 5.8% at 323 K. Similarly, the Γ values for the FHT reaction at the methylene group's H20 position decreased from 3.5% at 283 K to 3.0% at 303 K, and then remained stable at 3.1% at 323 K within the studied temperature range (***Figure III-9b***). In contrast, the most significant Γ value for the RAF reactions was observed at the phosphorus P12-atom, which increased from 84.7% at 283 K to 86.0% at 303 K, and then slightly decreased to 85.0% at 323 K (***Figure III-9d***).

The decreasing trends observed in FHT reactions as a function of temperature in both phases can be explained by the fact that the destabilization of pre-reactive complexes becomes more remarkable as temperature increases. Additionally, the increasing trend of the addition reaction at P12 within a relatively lower temperature range arises from the favourable impact of these low temperatures on adduct formation. Nevertheless, at higher temperatures, the thermalized HO-adducts revert to separated reactants, leading to increased competition between FHT and RAF processes compared to that at lower temperatures.

This observation has been validated both through experimental (Perry *et al.*, 1977) and computational studies (Dao *et al.*, 2023; Uc *et al.*, 2008) documented in the literature. Moreover, P12 emerges as the preferred site for HO$^{\bullet}$-addition on the phosmet molecule due to its electrophilic nature and possession of an unpaired electron in its partially filled *d*-orbital, making it more attractive to electron-rich species such as the HO$^{\bullet}$ radical.

***Table III-5**: rate constant and branching ratio values of FHT reactions in the (a) gas phase and (b) aqueous phase. (the most favourable pathways are in bold).*

a) Gas phase:

k **(M^{-1} s^{-1})**													
T (K)	**H20-abs**	**H21-abs**	**H22-abs**	**H23-abs**	**H24-abs**	**H25-abs**	**H26-abs**	**H27-abs**	**H28-abs**	**H29-abs**	**H30-abs**	**H31-abs**	**FHT**
253	**2.05×10^{10}**	**2.06×10^{10}**	6.93×10^{7}	5.07×10^{7}	6.80×10^{5}	9.63×10^{5}	6.31×10^{8}	7.50×10^{8}	2.95×10^{7}	2.91×10^{7}	4.29×10^{8}	1.19×10^{8}	4.32×10^{10}
258	**1.73×10^{10}**	**1.75×10^{10}**	6.10×10^{7}	4.57×10^{7}	6.89×10^{5}	9.75×10^{5}	5.60×10^{8}	6.89×10^{8}	2.82×10^{7}	2.78×10^{7}	3.94×10^{8}	1.11×10^{8}	3.67×10^{10}
263	**1.48×10^{10}**	**1.49×10^{10}**	5.42×10^{7}	4.14×10^{7}	7.03×10^{5}	9.95×10^{5}	5.01×10^{8}	6.37×10^{8}	2.72×10^{7}	2.68×10^{7}	3.63×10^{8}	1.03×10^{8}	3.15×10^{10}
268	**1.27×10^{10}**	**1.28×10^{10}**	4.86×10^{7}	3.79×10^{7}	7.22×10^{5}	1.02×10^{6}	4.51×10^{8}	5.92×10^{8}	2.63×10^{7}	2.59×10^{7}	3.36×10^{8}	9.70×10^{8}	2.72×10^{10}
273	**1.10×10^{10}**	**1.11×10^{10}**	4.39×10^{7}	3.49×10^{7}	7.45×10^{5}	1.05×10^{6}	4.09×10^{8}	5.52×10^{8}	2.56×10^{7}	2.52×10^{7}	3.13×10^{8}	9.12×10^{7}	2.37×10^{10}
278	**9.65×10^{9}**	**9.72×10^{9}**	4.01×10^{7}	3.23×10^{7}	7.73×10^{5}	1.09×10^{6}	3.73×10^{8}	5.18×10^{8}	2.50×10^{7}	2.46×10^{7}	2.93×10^{8}	8.62×10^{7}	2.08×10^{10}
283	**8.48×10^{9}**	**8.54×10^{9}**	3.68×10^{7}	3.02×10^{7}	8.05×10^{5}	1.13×10^{6}	3.43×10^{8}	4.87×10^{8}	2.45×10^{7}	2.41×10^{7}	2.75×10^{8}	8.17×10^{7}	1.83×10^{10}
288	**7.50×10^{9}**	**7.56×10^{9}**	3.41×10^{7}	2.83×10^{7}	8.41×10^{5}	1.18×10^{6}	3.16×10^{8}	4.60×10^{8}	2.41×10^{7}	2.37×10^{7}	2.59×10^{8}	7.77×10^{7}	1.63×10^{10}
293	**6.67×10^{9}**	**6.72×10^{9}**	3.18×10^{7}	2.67×10^{7}	8.81×10^{5}	1.24×10^{6}	2.93×10^{8}	4.36×10^{8}	2.37×10^{7}	2.34×10^{7}	2.45×10^{8}	7.42×10^{7}	1.46×10^{10}
298	**5.97×10^{9}**	**6.02×10^{9}**	2.98×10^{7}	2.54×10^{7}	9.25×10^{5}	1.30×10^{6}	2.73×10^{8}	4.15×10^{8}	2.35×10^{7}	2.31×10^{7}	2.33×10^{8}	7.10×10^{7}	1.31×10^{10}
303	**5.37×10^{9}**	**5.41×10^{9}**	2.81×10^{7}	2.42×10^{7}	9.74×10^{5}	1.37×10^{6}	2.56×10^{8}	3.96×10^{8}	2.33×10^{7}	2.29×10^{7}	2.22×10^{8}	6.81×10^{7}	1.18×10^{10}
308	**4.85×10^{9}**	**4.89×10^{9}**	2.66×10^{7}	2.31×10^{7}	1.03×10^{6}	1.44×10^{6}	2.40×10^{8}	3.79×10^{8}	2.31×10^{7}	2.28×10^{7}	2.12×10^{8}	6.55×10^{7}	1.07×10^{10}
313	**4.40×10^{9}**	**4.44×10^{9}**	2.53×10^{7}	2.22×10^{7}	1.09×10^{6}	1.52×10^{6}	2.26×10^{8}	3.64×10^{8}	2.30×10^{7}	2.27×10^{7}	2.03×10^{8}	6.31×10^{7}	9.79×10^{9}
318	**4.02×10^{9}**	**4.05×10^{9}**	2.42×10^{7}	2.14×10^{7}	1.15×10^{6}	1.60×10^{6}	2.14×10^{8}	3.50×10^{8}	2.30×10^{7}	2.26×10^{7}	1.95×10^{8}	6.10×10^{7}	8.98×10^{9}
323	**3.68×10^{9}**	**3.70×10^{9}**	2.33×10^{7}	2.07×10^{7}	1.22×10^{6}	1.70×10^{6}	2.03×10^{8}	3.38×10^{8}	2.29×10^{7}	2.26×10^{7}	1.87×10^{8}	5.90×10^{7}	8.26×10^{9}
Branching ratio (*Γ*, %)													
T (K)	**H20-abs**	**H21-abs**	**H22-abs**	**H23-abs**	**H24-abs**	**H25-abs**	**H26-abs**	**H27-abs**	**H28-abs**	**H29-abs**	**H30-abs**	**H31-abs**	**FHT**
253	**32.57**	**32.81**	0.11	0.08	0.00	0.00	1.00	1.19	0.05	0.05	0.68	0.19	68.73
258	**32.08**	**32.32**	0.11	0.08	0.00	0.00	1.04	1.28	0.05	0.05	0.73	0.21	67.95
263	**31.63**	**31.86**	0.12	0.09	0.00	0.00	1.07	1.36	0.06	0.06	0.78	0.22	67.24
268	**31.20**	**31.43**	0.12	0.09	0.00	0.00	1.11	1.45	0.06	0.06	0.82	0.24	66.59
273	**30.80**	**31.02**	0.12	0.10	0.00	0.00	1.14	1.54	0.07	0.07	0.87	0.25	65.99
278	**30.42**	**30.64**	0.13	0.10	0.00	0.00	1.18	1.63	0.08	0.08	0.92	0.27	65.46
283	**30.06**	**30.29**	0.13	0.11	0.00	0.00	1.21	1.73	0.09	0.09	0.97	0.29	64.97
288	**29.73**	**29.95**	0.14	0.11	0.00	0.00	1.25	1.82	0.10	0.09	1.03	0.31	64.53
293	**29.41**	**29.63**	0.14	0.12	0.00	0.01	1.29	1.92	0.10	0.10	1.08	0.33	64.14
298	**29.12**	**29.33**	0.15	0.12	0.00	0.01	1.33	2.02	0.11	0.11	1.13	0.35	63.79
303	**28.83**	**29.05**	0.15	0.13	0.01	0.01	1.37	2.13	0.12	0.12	1.19	0.37	63.48
308	**28.57**	**28.78**	0.16	0.14	0.01	0.01	1.41	2.23	0.14	0.13	1.25	0.39	63.21
313	**28.32**	**28.53**	0.16	0.14	0.01	0.01	1.45	2.34	0.15	0.15	1.30	0.41	62.97
318	**28.08**	**28.29**	0.17	0.15	0.01	0.01	1.50	2.45	0.16	0.16	1.36	0.43	62.76
323	**27.85**	**28.06**	0.18	0.16	0.01	0.01	1.54	2.56	0.17	0.17	1.42	0.45	62.58

b) Aqueous phase:

k (M^{-1} s^{-1})													
T (K)	**H20-abs**	**H21-abs**	**H22-abs**	**H23-abs**	**H24-abs**	**H25-abs**	**H26-abs**	**H27-abs**	**H28-abs**	**H29-abs**	**H30-abs**	**H31-abs**	**FHT**
253	**4.33×10^{7}**	1.13×10^{7}	1.16×10^{5}	7.90×10^{4}	2.04×10^{4}	3.73×10^{4}	**2.13×10^{7}**	5.61×10^{6}	8.10×10^{6}	5.17×10^{6}	1.87×10^{7}	**5.47×10^{7}**	1.69×10^{8}
258	**4.32×10^{7}**	1.09×10^{7}	1.20×10^{5}	8.01×10^{4}	2.24×10^{4}	4.09×10^{4}	**2.17×10^{7}**	5.77×10^{6}	7.84×10^{6}	5.22×10^{6}	1.86×10^{7}	**5.67×10^{7}**	1.70×10^{8}
263	**4.29×10^{7}**	1.06×10^{7}	1.24×10^{5}	8.17×10^{4}	2.46×10^{4}	4.49×10^{4}	**2.22×10^{7}**	5.94×10^{6}	7.62×10^{6}	5.29×10^{6}	1.84×10^{7}	**5.85×10^{7}**	1.72×10^{8}
268	**4.27×10^{7}**	1.03×10^{7}	1.29×10^{5}	8.37×10^{4}	2.70×10^{4}	4.93×10^{4}	**2.26×10^{7}**	6.11×10^{6}	7.42×10^{6}	5.36×10^{6}	1.83×10^{7}	**6.03×10^{7}**	1.73×10^{8}
273	**4.25×10^{7}**	1.00×10^{7}	1.35×10^{5}	8.60×10^{4}	2.98×10^{4}	5.42×10^{4}	**2.30×10^{7}**	6.30×10^{6}	7.25×10^{6}	5.45×10^{6}	1.82×10^{7}	**6.20×10^{7}**	1.75×10^{8}
278	**4.23×10^{7}**	9.80×10^{6}	1.41×10^{5}	8.88×10^{4}	3.28×10^{4}	5.96×10^{4}	**2.35×10^{7}**	6.49×10^{6}	7.11×10^{6}	5.54×10^{6}	1.81×10^{7}	**6.37×10^{7}**	1.77×10^{8}
283	**4.22×10^{7}**	9.60×10^{6}	1.49×10^{5}	9.20×10^{4}	3.61×10^{4}	6.56×10^{4}	**2.40×10^{7}**	6.69×10^{6}	6.99×10^{6}	5.64×10^{6}	1.80×10^{7}	**6.55×10^{7}**	1.79×10^{8}
288	**4.21×10^{7}**	9.44×10^{6}	1.56×10^{5}	9.55×10^{4}	3.97×10^{4}	7.21×10^{4}	**2.45×10^{7}**	6.90×10^{6}	6.88×10^{6}	5.74×10^{6}	1.80×10^{7}	**6.72×10^{7}**	1.81×10^{8}
293	**4.22×10^{7}**	9.30×10^{6}	1.65×10^{5}	9.95×10^{4}	4.38×10^{4}	7.94×10^{4}	**2.50×10^{7}**	7.12×10^{6}	6.80×10^{6}	5.86×10^{6}	1.79×10^{7}	**6.90×10^{7}**	1.84×10^{8}
298	**4.22×10^{7}**	9.19×10^{6}	1.74×10^{5}	1.04×10^{5}	4.82×10^{4}	8.73×10^{4}	**2.55×10^{7}**	7.35×10^{6}	6.72×10^{6}	5.98×10^{6}	1.79×10^{7}	**7.09×10^{7}**	1.86×10^{8}
303	**4.23×10^{7}**	9.10×10^{6}	1.84×10^{5}	1.09×10^{5}	5.31×10^{4}	9.60×10^{4}	**2.61×10^{7}**	7.59×10^{6}	6.67×10^{6}	6.11×10^{6}	1.80×10^{7}	**7.28×10^{7}**	1.89×10^{8}
308	**4.25×10^{7}**	9.03×10^{6}	1.94×10^{5}	1.14×10^{5}	5.84×10^{4}	1.06×10^{5}	**2.67×10^{7}**	7.84×10^{6}	6.62×10^{6}	6.24×10^{6}	1.80×10^{7}	**7.47×10^{7}**	1.92×10^{8}
313	**4.28×10^{7}**	8.98×10^{6}	2.06×10^{5}	1.20×10^{5}	6.42×10^{4}	1.16×10^{5}	**2.73×10^{7}**	8.10×10^{6}	6.59×10^{6}	6.38×10^{6}	1.80×10^{7}	**7.67×10^{7}**	1.95×10^{8}
318	**4.30×10^{7}**	8.94×10^{6}	2.18×10^{5}	1.26×10^{5}	7.06×10^{4}	1.27×10^{5}	**2.79×10^{7}**	8.36×10^{6}	6.56×10^{6}	6.53×10^{6}	1.81×10^{7}	**7.88×10^{7}**	1.99×10^{8}
323	**4.34×10^{7}**	8.92×10^{6}	2.31×10^{5}	1.33×10^{5}	7.75×10^{4}	1.40×10^{5}	**2.86×10^{7}**	8.64×10^{6}	6.55×10^{6}	6.69×10^{6}	1.82×10^{7}	**8.09×10^{7}**	2.02×10^{8}
Branching ratio (Γ, %)													
T (K)	**H20-abs**	**H21-abs**	**H22-abs**	**H23-abs**	**H24-abs**	**H25-abs**	**H26-abs**	**H27-abs**	**H28-abs**	**H29-abs**	**H30-abs**	**H31-abs**	**FHT**
253	**7.05**	1.84	0.02	0.01	0.00	0.01	**3.47**	0.91	1.32	0.84	3.05	**8.90**	27.41
258	**6.04**	1.53	0.02	0.01	0.00	0.01	**3.05**	0.81	1.10	0.73	2.60	**7.94**	23.83
263	**5.25**	1.30	0.02	0.01	0.00	0.01	**2.71**	0.73	0.93	0.65	2.25	**7.16**	21.01
268	**4.63**	1.12	0.01	0.01	0.00	0.01	**2.45**	0.66	0.81	0.58	1.99	**6.55**	18.82
273	**4.16**	0.98	0.01	0.01	0.00	0.01	**2.25**	0.62	0.71	0.53	1.78	**6.07**	17.14
278	**3.80**	0.88	0.01	0.01	0.00	0.01	**2.11**	0.58	0.64	0.50	1.62	**5.72**	15.88
283	**3.53**	0.80	0.01	0.01	0.00	0.01	**2.00**	0.56	0.58	0.47	1.51	**5.48**	14.96
288	**3.33**	0.75	0.01	0.01	0.00	0.01	**1.93**	0.55	0.54	0.45	1.42	**5.32**	14.32
293	**3.19**	0.70	0.01	0.01	0.00	0.01	**1.89**	0.54	0.51	0.44	1.36	**5.23**	13.91
298	**3.10**	0.68	0.01	0.01	0.00	0.01	**1.88**	0.54	0.49	0.44	1.32	**5.21**	13.68
303	**3.05**	0.66	0.01	0.01	0.00	0.01	**1.88**	0.55	0.48	0.44	1.29	**5.24**	13.61
308	**3.03**	0.64	0.01	0.01	0.00	0.01	**1.90**	0.56	0.47	0.44	1.28	**5.32**	13.67
313	**3.03**	0.64	0.01	0.01	0.00	0.01	**1.94**	0.57	0.47	0.45	1.28	**5.44**	13.85
318	**3.06**	0.64	0.02	0.01	0.01	0.01	**1.99**	0.59	0.47	0.46	1.29	**5.60**	14.12
323	**3.10**	0.64	0.02	0.01	0.01	0.01	**2.05**	0.62	0.47	0.48	1.30	**5.79**	14.49

***Table III-6**: rate constant and branching ratio values of RAF reactions in the (a) gas phase and (b) aqueous phase. (the most favourable pathways are in bold).*

a) Gas phase:

k (M^{-1} s^{-1})													
T (K)	**C1-add**	**C2-add**	**C3-add**	**C4-add**	**C5-add**	**C6-add**	**C7-add**	**C9-add**	**P12-add**	**S17-add**	**RAF**	**SET**	**Overall**
253	4.40×10^{5}	8.34×10^{5}	5.23×10^{4}	5.40×10^{4}	8.38×10^{5}	9.11×10^{5}	7.50×10^{-3}	7.58×10^{-3}	**1.97×10^{10}**	2.38×10	1.97×10^{10}	0.00	6.29×10^{10}
258	4.86×10^{5}	8.55×10^{5}	5.86×10^{4}	6.05×10^{4}	8.58×10^{5}	9.86×10^{5}	1.12×10^{-2}	1.13×10^{-2}	**1.73×10^{10}**	3.40×10	1.73×10^{10}	0.00	5.40×10^{10}
263	5.35×10^{5}	8.76×10^{5}	6.55×10^{4}	6.76×10^{4}	8.80×10^{5}	1.07×10^{6}	1.64×10^{-2}	1.65×10^{-2}	**1.53×10^{10}**	4.78×10	1.53×10^{10}	0.00	4.68×10^{10}
268	5.88×10^{5}	8.97×10^{5}	7.29×10^{4}	7.52×10^{4}	9.01×10^{5}	1.15×10^{6}	2.37×10^{-2}	2.40×10^{-2}	**1.36×10^{10}**	6.64×10	1.36×10^{10}	0.00	4.08×10^{10}
273	6.45×10^{5}	9.19×10^{5}	8.09×10^{4}	8.35×10^{4}	9.23×10^{5}	1.24×10^{6}	3.39×10^{-2}	3.43×10^{-2}	**1.22×10^{10}**	9.12×10	1.22×10^{10}	0.00	3.59×10^{10}
278	7.05×10^{5}	9.42×10^{5}	8.95×10^{4}	9.24×10^{4}	9.46×10^{5}	1.33×10^{6}	4.79×10^{-2}	4.84×10^{-2}	**1.09×10^{10}**	1.24×10^{1}	1.10×10^{10}	0.00	3.17×10^{10}
283	7.70×10^{5}	9.65×10^{5}	9.88×10^{4}	1.02×10^{5}	9.69×10^{5}	1.42×10^{6}	6.70×10^{-2}	6.76×10^{-2}	**9.88×10^{9}**	1.67×10^{1}	9.88×10^{9}	0.00	2.82×10^{10}
288	8.38×10^{5}	9.88×10^{5}	1.09×10^{5}	1.12×10^{5}	9.93×10^{5}	1.53×10^{6}	9.26×10^{-2}	9.35×10^{-2}	**8.94×10^{9}**	2.22×10^{1}	8.95×10^{9}	0.00	2.52×10^{10}
293	9.10×10^{5}	1.01×10^{6}	1.19×10^{5}	1.23×10^{5}	1.02×10^{6}	1.63×10^{6}	1.27×10^{-1}	1.28×10^{-1}	**8.13×10^{9}**	2.94×10^{1}	8.14×10^{9}	0.00	2.27×10^{10}
298	9.86×10^{5}	1.04×10^{6}	1.31×10^{5}	1.35×10^{5}	1.04×10^{6}	1.74×10^{6}	1.72×10^{-1}	1.73×10^{-1}	**7.42×10^{9}**	3.85×10^{1}	7.43×10^{9}	0.00	2.05×10^{10}
303	1.07×10^{6}	1.06×10^{6}	1.43×10^{5}	1.48×10^{5}	1.07×10^{6}	1.86×10^{6}	2.30×10^{-1}	2.33×10^{-1}	**6.80×10^{9}**	5.00×10^{1}	6.80×10^{9}	0.00	1.86×10^{10}
308	1.15×10^{6}	1.09×10^{6}	1.56×10^{5}	1.61×10^{5}	1.09×10^{6}	1.98×10^{6}	3.07×10^{-1}	3.10×10^{-1}	**6.24×10^{9}**	6.44×10^{1}	6.25×10^{9}	0.00	1.70×10^{10}
313	1.24×10^{6}	1.11×10^{6}	1.70×10^{5}	1.75×10^{5}	1.12×10^{6}	2.10×10^{6}	4.04×10^{-1}	4.08×10^{-1}	**5.75×10^{9}**	8.23×10^{1}	5.76×10^{9}	0.00	1.56×10^{10}
318	1.34×10^{6}	1.14×10^{6}	1.84×10^{5}	1.90×10^{5}	1.14×10^{6}	2.23×10^{6}	5.29×10^{-1}	5.34×10^{-1}	**5.32×10^{9}**	1.05×10^{2}	5.33×10^{9}	0.00	1.43×10^{10}
323	1.44×10^{6}	1.17×10^{6}	2.00×10^{5}	2.06×10^{5}	1.17×10^{6}	2.37×10^{6}	6.87×10^{-1}	6.94×10^{-1}	**4.93×10^{9}**	1.32×10^{2}	4.94×10^{9}	0.00	1.32×10^{10}
Branching ratio (Γ, %)													
T (K)	**C1-add**	**C2-add**	**C3-add**	**C4-add**	**C5-add**	**C6-add**	**C7-add**	**C9-add**	**P12-add**	**S17-add**	**RAF**	**SET**	**Overall**
253	0.00	0.00	0.00	0.00	0.00	0.00	0.00	0.00	**31.26**	0.00	31.27	0.00	100.00
258	0.00	0.00	0.00	0.00	0.00	0.00	0.00	0.00	**32.04**	0.00	32.05	0.00	100.00
263	0.00	0.00	0.00	0.00	0.00	0.00	0.00	0.00	**32.75**	0.00	32.76	0.00	100.00
268	0.00	0.00	0.00	0.00	0.00	0.00	0.00	0.00	**33.40**	0.00	33.41	0.00	100.00
273	0.00	0.00	0.00	0.00	0.00	0.00	0.00	0.00	**33.99**	0.00	34.01	0.00	100.00
278	0.00	0.00	0.00	0.00	0.00	0.00	0.00	0.00	**34.53**	0.00	34.54	0.00	100.00
283	0.00	0.00	0.00	0.00	0.00	0.01	0.00	0.00	**35.01**	0.00	35.03	0.00	100.00
288	0.00	0.00	0.00	0.00	0.00	0.01	0.00	0.00	**35.45**	0.00	35.47	0.00	100.00
293	0.00	0.00	0.00	0.00	0.00	0.01	0.00	0.00	**35.84**	0.00	35.86	0.00	100.00
298	0.00	0.01	0.00	0.00	0.01	0.01	0.00	0.00	**36.18**	0.00	36.21	0.00	100.00
303	0.01	0.01	0.00	0.00	0.01	0.01	0.00	0.00	**36.49**	0.00	36.52	0.00	100.00
308	0.01	0.01	0.00	0.00	0.01	0.01	0.00	0.00	**36.76**	0.00	36.79	0.00	100.00
313	0.01	0.01	0.00	0.00	0.01	0.01	0.00	0.00	**36.99**	0.00	37.03	0.00	100.00
318	0.01	0.01	0.00	0.00	0.01	0.02	0.00	0.00	**37.19**	0.00	37.24	0.00	100.00
323	0.01	0.01	0.00	0.00	0.01	0.02	0.00	0.00	**37.37**	0.00	37.42	0.00	100.00

b) Aqueous phase:

k (M^{-1} s^{-1})													
T (K)	**C1-add**	**C2-add**	**C3-add**	**C4-add**	**C5-add**	**C6-add**	**C7-add**	**C9-add**	**P12-add**	**S17-add**	**RAF**	**SET**	**Overall**
253	5.84×10^{5}	3.32×10^{5}	2.26×10^{5}	1.21×10^{5}	1.87×10^{5}	5.81×10^{5}	1.04×10^{-4}	2.26×10^{-4}	$\mathbf{4.44\times10^{8}}$	9.06×10^{-3}	4.46×10^{8}	5.30×10^{-19}	6.15×10^{8}
258	6.45×10^{5}	3.66×10^{5}	2.53×10^{5}	1.36×10^{5}	2.09×10^{5}	6.32×10^{5}	1.69×10^{-4}	3.65×10^{-4}	$\mathbf{5.42\times10^{8}}$	1.42×10^{-2}	5.44×10^{8}	2.33×10^{-18}	7.14×10^{8}
263	7.10×10^{5}	4.02×10^{5}	2.83×10^{5}	1.52×10^{5}	2.32×10^{5}	6.86×10^{5}	2.70×10^{-4}	5.80×10^{-4}	$\mathbf{6.43\times10^{8}}$	2.18×10^{-2}	6.46×10^{8}	9.69×10^{-18}	8.17×10^{8}
268	7.80×10^{5}	4.40×10^{5}	3.15×10^{5}	1.69×10^{5}	2.57×10^{5}	7.44×10^{5}	4.26×10^{-4}	9.08×10^{-4}	$\mathbf{7.45\times10^{8}}$	3.31×10^{-2}	7.48×10^{8}	3.83×10^{-17}	9.21×10^{8}
273	8.54×10^{5}	4.81×10^{5}	3.50×10^{5}	1.88×10^{5}	2.85×10^{5}	8.04×10^{5}	6.61×10^{-4}	1.40×10^{-3}	$\mathbf{8.43\times10^{8}}$	4.94×10^{-2}	8.46×10^{8}	1.44×10^{-16}	1.02×10^{9}
278	9.33×10^{5}	5.25×10^{5}	3.87×10^{5}	2.08×10^{5}	3.14×10^{5}	8.67×10^{5}	1.01×10^{-3}	2.12×10^{-3}	$\mathbf{9.33\times10^{8}}$	7.28×10^{-2}	9.37×10^{8}	5.15×10^{-16}	1.11×10^{9}
283	1.02×10^{6}	5.71×10^{5}	4.28×10^{5}	2.30×10^{5}	3.45×10^{5}	9.33×10^{5}	1.52×10^{-3}	3.18×10^{-3}	$\mathbf{1.01\times10^{9}}$	1.06×10^{-1}	1.02×10^{9}	1.77×10^{-15}	1.20×10^{9}
288	1.11×10^{6}	6.20×10^{5}	4.71×10^{5}	2.53×10^{5}	3.79×10^{5}	1.00×10^{6}	2.26×10^{-3}	4.70×10^{-3}	$\mathbf{1.08\times10^{9}}$	1.52×10^{-1}	1.08×10^{9}	5.80×10^{-15}	1.26×10^{9}
293	1.20×10^{6}	6.72×10^{5}	5.17×10^{5}	2.78×10^{5}	4.14×10^{5}	1.08×10^{6}	3.32×10^{-3}	6.86×10^{-3}	$\mathbf{1.13\times10^{9}}$	2.16×10^{-1}	1.14×10^{9}	1.83×10^{-14}	1.32×10^{9}
298	1.30×10^{6}	7.27×10^{5}	5.66×10^{5}	3.04×10^{5}	4.52×10^{5}	1.15×10^{6}	4.82×10^{-3}	9.89×10^{-3}	$\mathbf{1.17\times10^{9}}$	3.04×10^{-1}	1.17×10^{9}	5.57×10^{-14}	1.36×10^{9}
303	1.40×10^{6}	7.84×10^{5}	6.19×10^{5}	3.32×10^{5}	4.93×10^{5}	1.23×10^{6}	6.91×10^{-3}	1.41×10^{-2}	$\mathbf{1.20\times10^{9}}$	4.23×10^{-1}	1.20×10^{9}	1.63×10^{-13}	1.39×10^{9}
308	1.51×10^{6}	8.45×10^{5}	6.75×10^{5}	3.62×10^{5}	5.35×10^{5}	1.31×10^{6}	9.80×10^{-3}	1.99×10^{-2}	$\mathbf{1.21\times10^{9}}$	5.81×10^{-1}	1.21×10^{9}	4.63×10^{-13}	1.41×10^{9}
313	1.63×10^{6}	9.09×10^{5}	7.35×10^{5}	3.94×10^{5}	5.81×10^{5}	1.40×10^{6}	1.37×10^{-2}	2.78×10^{-2}	$\mathbf{1.21\times10^{9}}$	7.92×10^{-1}	1.22×10^{9}	1.27×10^{-12}	1.41×10^{9}
318	1.75×10^{6}	9.75×10^{5}	7.98×10^{5}	4.28×10^{5}	6.28×10^{5}	1.49×10^{6}	1.91×10^{-2}	3.84×10^{-2}	$\mathbf{1.20\times10^{9}}$	1.07×10^{0}	1.21×10^{9}	3.37×10^{-12}	1.41×10^{9}
323	1.88×10^{6}	1.05×10^{6}	8.65×10^{5}	4.64×10^{5}	6.79×10^{5}	1.58×10^{6}	2.63×10^{-2}	5.26×10^{-2}	$\mathbf{1.19\times10^{9}}$	1.43×10^{0}	1.20×10^{9}	8.70×10^{-12}	1.40×10^{9}

Branching ratio (Γ, %)													
T (K)	**C1-add**	**C2-add**	**C3-add**	**C4-add**	**C5-add**	**C6-add**	**C7-add**	**C9-add**	**P12-add**	**S17-add**	**RAF**	**SET**	**Overall**
253	0.09	0.05	0.04	0.02	0.03	0.09	0.00	0.00	**72.26**	0.00	72.59	0.00	100.00
258	0.09	0.05	0.04	0.02	0.03	0.09	0.00	0.00	**75.85**	0.00	76.17	0.00	100.00
263	0.09	0.05	0.03	0.02	0.03	0.08	0.00	0.00	**78.69**	0.00	78.99	0.00	100.00
268	0.08	0.05	0.03	0.02	0.03	0.08	0.00	0.00	**80.89**	0.00	81.18	0.00	100.00
273	0.08	0.05	0.03	0.02	0.03	0.08	0.00	0.00	**82.57**	0.00	82.86	0.00	100.00
278	0.08	0.05	0.03	0.02	0.03	0.08	0.00	0.00	**83.83**	0.00	84.12	0.00	100.00
283	0.09	0.05	0.04	0.02	0.03	0.08	0.00	0.00	**84.74**	0.00	85.04	0.00	100.00
288	0.09	0.05	0.04	0.02	0.03	0.08	0.00	0.00	**85.38**	0.00	85.68	0.00	100.00
293	0.09	0.05	0.04	0.02	0.03	0.08	0.00	0.00	**85.78**	0.00	86.09	0.00	100.00
298	0.10	0.05	0.04	0.02	0.03	0.08	0.00	0.00	**85.99**	0.00	86.32	0.00	100.00
303	0.10	0.06	0.04	0.02	0.04	0.09	0.00	0.00	**86.04**	0.00	86.39	0.00	100.00
308	0.11	0.06	0.05	0.03	0.04	0.09	0.00	0.00	**85.95**	0.00	86.33	0.00	100.00
313	0.12	0.06	0.05	0.03	0.04	0.10	0.00	0.00	**85.75**	0.00	86.15	0.00	100.00
318	0.12	0.07	0.06	0.03	0.04	0.11	0.00	0.00	**85.44**	0.00	85.88	0.00	100.00
323	0.13	0.07	0.06	0.03	0.05	0.11	0.00	0.00	**85.05**	0.00	85.51	0.00	100.00

III.2.4. Lifetime of phosmet in the presence of HO• radicals

To ascertain how long phosmet persists in the environment when subjected to HO• radicals, its lifespan (τ) was computed across temperatures ranging from 283 K to 323 K in the aqueous phase and at 287 K in the gas phase. In the aqueous phase, the computations relied on the diffusion-corrected overall rate constant of reactions (k_{app}) and the concentration of HO• radicals in the environment, using the formula below (Sun et al., 2020):

$$\tau_{aq} = \frac{1}{k_{app}[\mathrm{HO}\bullet]} \qquad \textit{Eq. III-1}$$

According to previous studies, the concentrations of HO• radicals in wastewater were reported to be from 10^{-9} to 10^{-10} mol L^{-1}, and in groundwater, from 10^{-15} to 10^{-18} mol L^{-1} (Brezonik and Fulkerson-Brekken, 1998) (J. M. Burns *et al.*, 2012) (Haag and Hoigné, 1985). For this reason, we calculated the lifetime by considered the [HO•] from 10^{-9} to 10^{-18}, and the results are presented in ***Table III-7***.

The results indicate that under high HO• concentration (*i.e.*, 10^{-9} mol L^{-1}), the lifetimes of phosmet were notably short, decreasing from 0.84 to 0.7 s as the temperature escalated from 283 to 323 K, respectively. Conversely, as the [HO•] decreased to 10^{-18} mol L^{-1} at 283 K, the τ values started to increase from 0.84 s, eventually reaching 8.4×10^{8} s (equivalent to 26.52 years). Briefly, the degradation of phosmet increases in the presence of high concentrations of HO• radicals and higher temperatures, while it last longer under low [HO•] and lower temperatures.

Table III-7*: the lifetime (τ_{aq}, s) of phosmet calculated at a temperature range of 283-323 K, based on [HO•] concentration in the aqueous phase.*

	[HO•] / mol L^{-1}	1×10^{-9}	1×10^{-10}	1×10^{-11}	1×10^{-12}	1×10^{-13}	1×10^{-14}	1×10^{-15}	1×10^{-16}	1×10^{-17}	1×10^{-18}
T /K	k_{app}	**Lifetime (τ_{aq}, s)**									
283	1.2×10^{9}	8.4×10^{-1}	8.4	84	8.4×10^{2}	8.4×10^{3}	8.4×10^{4}	8.4×10^{5}	8.4×10^{6}	8.4×10^{7}	8.4×10^{8}
288	1.3×10^{9}	7.9×10^{-1}	7.9	79	7.9×10^{2}	7.9×10^{3}	7.9×10^{4}	7.9×10^{5}	7.9×10^{6}	7.9×10^{7}	7.9×10^{8}
293	1.3×10^{9}	7.6×10^{-1}	7.6	76	7.6×10^{2}	7.6×10^{3}	7.6×10^{4}	7.6×10^{5}	7.6×10^{6}	7.6×10^{7}	7.6×10^{8}
298	1.4×10^{9}	7.3×10^{-1}	7.3	73	7.3×10^{2}	7.3×10^{3}	7.3×10^{4}	7.3×10^{5}	7.3×10^{6}	7.3×10^{7}	7.3×10^{8}
303	1.4×10^{9}	7.2×10^{-1}	7.2	72	7.2×10^{2}	7.2×10^{3}	7.2×10^{4}	7.2×10^{5}	7.2×10^{6}	7.2×10^{7}	7.2×10^{8}
308	1.4×10^{9}	7.1×10^{-1}	7.1	71	7.1×10^{2}	7.1×10^{3}	7.1×10^{4}	7.1×10^{5}	7.1×10^{6}	7.1×10^{7}	7.1×10^{8}
313	1.4×10^{9}	7.1×10^{-1}	7.1	71	7.1×10^{2}	7.1×10^{3}	7.1×10^{4}	7.1×10^{5}	7.1×10^{6}	7.1×10^{7}	7.1×10^{8}
318	1.4×10^{9}	7.1×10^{-1}	7.1	71	7.1×10^{2}	7.1×10^{3}	7.1×10^{4}	7.1×10^{5}	7.1×10^{6}	7.1×10^{7}	7.1×10^{8}
323	1.4×10^{9}	7.2×10^{-1}	7.2	72	7.2×10^{2}	7.2×10^{3}	7.2×10^{4}	7.2×10^{5}	7.2×10^{6}	7.2×10^{7}	7.2×10^{8}

In the gas phase, the same formula was applied to determine the atmospheric lifetime (τ_{gas}) of phosmet, utilizing the overall rate constant of reactions (*k*) in the gas phase, and by adopting 1.09×10^{6} radicals cm^{-3} as an average concentration of HO• radical in the troposphere (Li et al.,

2018). The calculation was done at 287 K, which corresponds to the typical ground-level air temperature (Stein and published, 2022) where phosmet is commonly applied.

The obtained atmospheric lifetime (τ_{gas}) of phosmet is about 2.2×10^4 s (about 6 hours) at 287 K.

III.2.5. Further oxidation reactions of Rad-H31

The H-abstraction reaction targeting the methyl group (–CH_3) on the C14 atom yields the most stable radical intermediate (*i.e.*, Rad-H31) with branching ratios ranging from 36.6% to 40.0% of the total abstraction reactions in the aqueous phase, at the temperature from 283 to 323 K. ***Figure III-10*** summarizes different reaction pathways of possible further oxidation reaction of Rad-H31 radical by other radical species which may be available in the aqueous environment.

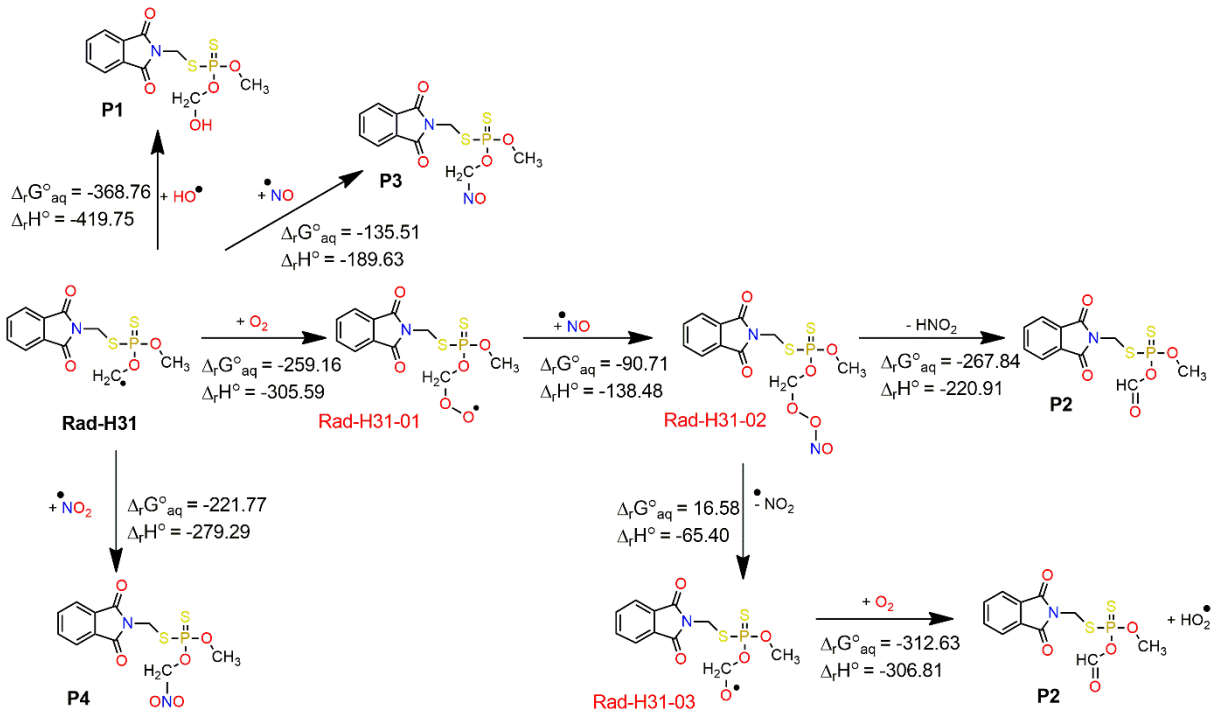

Figure III-10*: schematic presentation of further oxidation reactions of Rad-H31 with $^1O_2$, HO•, •NO, and •NO_2 in the aqueous phase at 298 K. Units are in kJ mol^{-1}.*

Notably, the direct HO•-addition to the C14 atom of the –CH_2 group will generate an adduct **P1** with the standard Gibbs free reaction energy $\Delta_rG°$ value of -368.76 kJ mol^{-1}. Furthermore, the Rad-H31 radical may react with the singlet O_2 molecule at the C14 position to form the Rad-H31-01 intermediate. The Rad-H31-01 will recombine with •NO at the O position to produce the Rad-H31-02 compound. The O–O bond of Rad-H31-02 radical can be cleaved to form •NO_2 and Rad-H31-03 radical. The process may continue with H-abstraction at–CH_2 group of C14 by a singlet O_2 molecule, resulting in the formation of the HO_2• radical and the **P2** product with

$\Delta_r G°$ value of -312.63 kJ.mol^{-1}. Alternatively, **P2** product could be directly generated by an intermolecular H-atom shift from C14 to O-atom of the Rad-H31-02 intermediate, forming HNO_2 ($\Delta_r G°$ = -267.84 kJ mol^{-1}). Moreover, the direct addition of $^{\bullet}NO$ and $^{\bullet}NO_2$ to the $–CH_2$ group at C14 may generate the **P3** and **P4** products, with $\Delta_r G°$ being -135.51 and -221.77 kJ mol^{-1}, respectively.

Similarly, the possible further oxidation reactions of P12-a radical, the most favourable product of the addition reaction of HO$^{\bullet}$ radical on P12-atom, was also studied (***Figure III-11***).

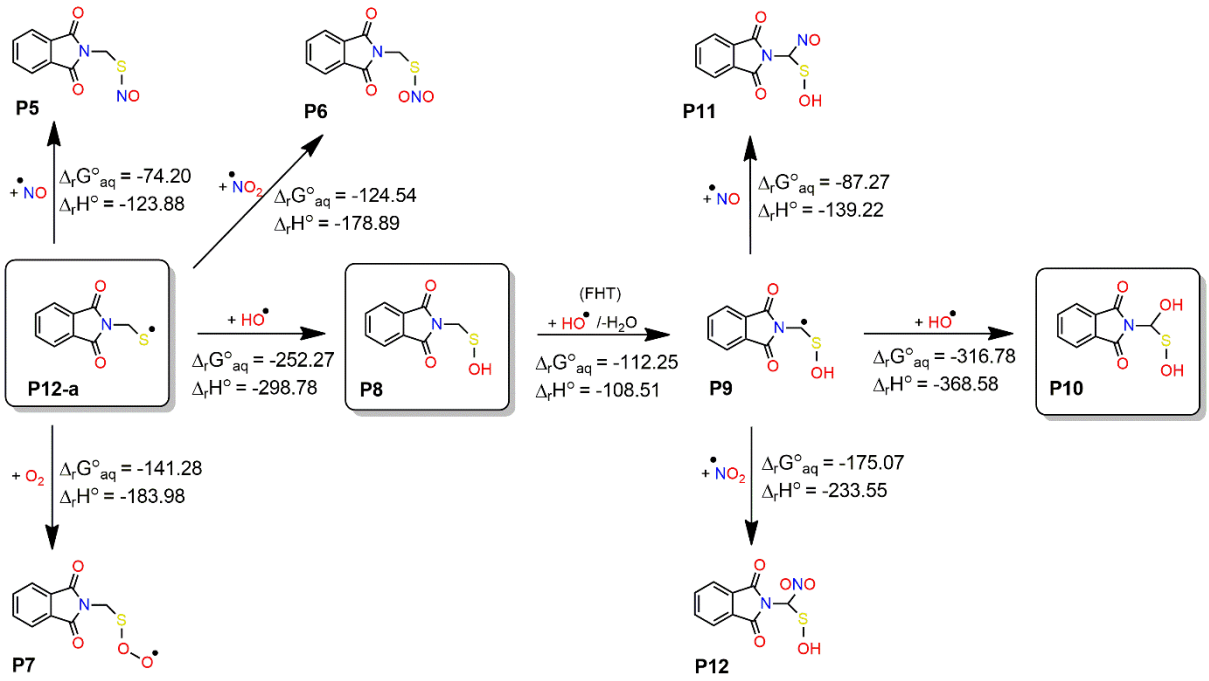

Figure III-11*: schematic presentation of further oxidation reactions of the product P12-a with* $^1O_2$, HO$^{\bullet}$, $^{\bullet}NO$, *and* $^{\bullet}NO_2$ *in the aqueous phase at 298 K. Units are in kJ mol*$^{-1}$.

Directly adding HO$^{\bullet}$ to P12-a shows more feasibility over $^{\bullet}NO$, $^{\bullet}NO_2$, and $^1O_2$ at the S atom, where a neutral **P8** product is generated with $\Delta_r G°$ being -252.27 kJ mol^{-1}. The reaction may continue with an H-abstraction by HO$^{\bullet}$ at the C10-atom of **P8** leading to the formation of P9 radical. Subsequently, this radical might undergo further attack by HO$^{\bullet}$ to produce a neutral product **P10** with $\Delta_r G°$ value of -316.78 kJ.mol^{-1}.

Thus, further reactions of the Rad-H31 intermediate can yield four stable products, **P1, P2, P3, and P4**, while the P12-a tends to form the stable products **P8** and **P10**. Therefore, studying the toxicity influence of these products accompanying the phosmet compound enables us to predict their effects on the ecosystem and the aquatic environment.

III.2.6. Risk predictions

More details about this part can be found in **Chapter II**.

Acute and chronic toxicities are employed on three aquatic organisms such as fish, daphnia, and green algae, to estimate the potential aquatic toxicity of phosmet and its degradation products: **P1**, **P2**, **P3**, and **P4**. These products are derived from the subsequent reactions of the Rad-H31 radical and the two adduct products resulting from HO•-addition on the phosphorus P12 atom, designated as P12-a and P12-b.

III.2.6.1. The aquatic toxicities of phosmet and its degradation products

The obtained aquatic toxicity data for phosmet and its derivatives towards fish, daphnia, and green algae are presented in ***Table III-8***. The calculated acute toxicities of phosmet were determined to be 13.5, 24.2, and 1.8 mg/L for fish, daphnia, and green algae, respectively. These findings indicate that phosmet was harmful to fish and daphnia, but very toxic to green algae.

Table III-8*: acute toxicity (LC50 and EC50) and chronic toxicity (ChV) of phosmet and the possible degradation products towards fish, daphnia, and green algae in the aqueous phase.*

		Concentration (mg/L)								
	Organism	**Phosmet**	**P1**	**P2**	**P3**	**P4**	**P12-a**	**P12-b**	**P8**	**P10**
Acute Toxicity	Fish	13.5	52.2	53.4	37.5	33.3	3284.1	10.8	52	434
	Daphnia	24.2	153.4	158.7	95.8	80.3	1607.6	21.6	31	237
	Green Algae	1.8	6.4	6.5	4.7	4.2	648.4	1.4	29	151
Chronic Toxicity	Fish	5.1	58.0	60.8	30.6	23.9	269.5	5.2	5	41
	Daphnia	8.5	88.4	92.5	47.9	37.7	103.7	8.4	4	21
	Green Algae	0.1	0.3	0.3	0.2	0.2	122	0.1	9	36

Not harmful Harmful Toxic Very toxic

The chronic toxicity data for phosmet revealed concentration values of 5.1, 8.5, and 0.1 mg/L for fish, daphnia, and green algae, respectively. These concentrations were found to be harmful to fish and daphnia, while proving highly toxic to green algae. Therefore, phosmet exhibits detrimental effects on these aquatic species, posing harm or toxicity.

Regarding the degradation products of phosmet, the acute toxicity and the chronic toxicity values of **P1**, **P2**, **P3**, and **P4** were also harmful to fish and daphnia and toxic to green algae. However, their concentrations were much higher than those of phosmet, which means they were less dangerous and toxic to aquatic organisms. Concerning the two adduct products resulting from HO•-addition on P12-a, both acute and chronic toxicity values of P12-a are determined to be non-harmful to fish, daphnia, and green algae. However, its possible degradation products (*i.e.*, **P8** and **P10**) are found to be harmful to all three species. Acute toxicity assessments of P12-b indicate harm to fish and daphnia, with toxicity observed in green algae. In terms of

chronic toxicity, P12-b was found to be harmful to fish and daphnia, but very toxic to green algae.

Therefore, the resulting values of the acute and chronic toxicity of the degradation products of phosmet can clearly explain how the formation of new products from the initial compound can have different influences on the aquatic organisms.

III.2.6.2. Bioaccumulation, developmental toxicity, and mutagenicity

BAF, BCF, developmental toxicity, and mutagenicity of phosmet and its degradation products are presented in the following table (***Table III-9***).

Table III-9*: BCF, BAF, developmental toxicity and mutagenicity for phosmet and its possible degradation products in the aqueous phase.*

	Phosmet	**P1**	**P2**	**P3**	**P4**	**P12-a**	**P12-b**	**P8**	**P10**
BCF (L/kg wet-wt)	6.83	3.162	3.16	3.16	3.16	3.16	4.22	23.4	2.9
BAF (L/kg wet-wt)	6.83	1.07	1.06	1.38	1.63	1.07	3.69	6.5	1.6
Developmental Toxicity	0.50	0.63	0.63	0.78	0.58	0.48	1.11	0.72	0.01
Mutagenicity	0.24	0.46	0.46	N/A	N/A	1.83	0.17	0.08	0.15

BAF and BCF values of phosmet (6.83 L/kg wet-wt) and all its products (BCF ranging from 2.9 to 23.4, and BAF ranging from 1.06 to 6.5 L/kg wet-wt) are lower than 570 L/kg wet-wt, indicating that these compounds are non-bioaccumulative in the aquatic organisms. Besides, the results suggest that bioaccumulation of phosmet is relatively higher than its degradation products but still negligible.

Phosmet and all its products are classified as developmental toxicants, with developmental toxicity values spanning from 0.50 to 1.11, except for P12-a and its derivative **P10**, which are developmental non-toxicants (0.48 and 0.01, respectively). However, phosmet and all its products are mutagenicity-negative substances with mutagenicity values ranging from 0.24 to 0.46 (lower than 0.50), meaning they do not have mutagenic toxicity, except for the P12-a, which is a mutagenicity-positive substance (1.83).

III.3. Conclusion

Phosmet, an organophosphorus insecticide widely used in agriculture to control various insects, faced a ban from the European Union in 2022 due to its toxic environmental impacts. To understand its degradation process, we investigated its oxidation through $HO^{\bullet}$ radicals in both gas and aqueous phases using the DFT method. This study aimed to unravel the mechanisms and kinetics of three reaction pathways: FHT, RAF, and SET.

At 298 K, FHT reactions were dominant in the gas phase with a total rate constant of 1.31×10^{10} M^{-1} s^{-1}, whereas the RAF ones were dominant in the aqueous phase with a total rate constant of 1.17×10^{9} M^{-1} s^{-1}, while the SET reaction is negligible.

The most favourable H-abstraction sites in the aqueous phase were observed at the H31 hydrogen atom, followed by the H26 of the methyl groups and the H20 of the methylene group.

In addition, reactions at the H20/H21 positions were the most favoured in the gas phase. Both in the gas and aqueous phases, the P12 phosphorus atom of the dithiophosphate group appears as the preferred site for HO$^{\bullet}$ addition, having the highest branching ratio ranging from 84.7 to 85.05% in the aqueous phase at temperatures of 283-323 K, and from 31.26 to 37.37% in the gas phase within the 253-323 K range.

The reactions in the aqueous phase occurred within the diffusion-controlled rate constant limit, where the overall rate constant values increased from 1.2×10^{9} to 1.40×10^{9} M^{-1} s^{-1} with the increase in temperature from 283 to 323 K. Moreover, the overall rate constant values in the gas phase decreased from 6.29×10^{10} to 1.32×10^{10} M^{-1} s^{-1} as a function of temperature.

At 287 K, phosmet has an atmospheric lifetime of approximately 6 hours. On the other hand, its lifetime in aqueous environments is very short, ranging from 0.84 to 0.7 s as temperatures rise from 283 to 323 K, respectively, particularly at high concentrations HO$^{\bullet}$ (*i.e.*, 10^{-9} mol L^{-1}). However, under low HO$^{\bullet}$ concentrations (*i.e.*, 10^{-18} mol L^{-1}), the lifetime of phosmet can reach 26.52 years. Thus, the degradation of phosmet is accelerated in environments with high concentrations of HO$^{\bullet}$ radicals and high temperatures.

The ecotoxicity evaluation illustrated that phosmet and its degradation products **P1**, **P2**, **P3**, **P4** were harmful to fish and daphnia, either toxic or very toxic to green algae, except for P12-a product that was not harmful. Meanwhile the degradation products from P12-a, *i.e.*, **P8** and **P10**, are harmful to the studied aquatic species. Nevertheless, these degradation products are less dangerous and toxic than phosmet. Moreover, phosmet and all its products are non-bioaccumulative, developmental toxicants and mutagenicity-negative compounds, except for P12-a, which represents a developmental non-toxicant and mutagenicity-positive compound.

III.4. References

A. Al-Anazi, W. H. Abdelraheem, C. Han, M. N. Nadagouda, L. Sygellou, M. K. Arfanis, P. Falaras, V. K. Sharma, D. D. Dionysiou, 2018. Cobalt ferrite nanoparticles with controlled composition-peroxymonosulfate mediated degradation of 2-phenylbenzimidazole-5-sulfonic acid. Applied Catalysis B: Environmental 221, 266–279. https://doi.org/10.1016/j.apcatb.2017.08.054

Abdel-Rahman, M.A., Shibl, M.F., El-Nahas, A.M., Abdel-Azeim, S., El-demerdash, S.H., Al-Hashimi, N., 2021. Mechanistic insights of the degradation of an O-anisidine carcinogenic pollutant initiated by OH radical attack: theoretical investigations. New Journal of Chemistry 45, 5907–5924. https://doi.org/10.1039/D0NJ06248K

Almeida, T.G., Kurtén, T., 2022. Atmospheric Oxidation of Imine Derivative of Piperazine Initiated by OH Radical. ACS Earth and Space Chemistry 6, 2453–2464. https://doi.org/10.1021/acsearthspacechem.2c00170

Brezonik, P.L., Fulkerson-Brekken, J., 1998. Nitrate-Induced Photolysis in Natural Waters: Controls on Concentrations of Hydroxyl Radical Photo-Intermediates by Natural Scavenging Agents. Environmental Science and Technology 32, 3004–3010. https://doi.org/10.1021/es9802908

C. Liu, J. Gan, Y. Zhang, M. Liang, X. Shu, J. Shu, B. Yang, 2011. Heterogeneous Reaction of Suspended Phosmet Particles with NO_3 Radicals. Journal of Physical Chemistry A 115, 10744–10748. https://doi.org/10.1021/jp205175p

Camazano, M.S., Sanchez Martin, M.J., 1983. Montmorillonite-catalized hydrolysis of phosmet. Soil Science 136, 89.

Dao, D.Q., Taamalli, S., Louis, F., Kdouh, D., Srour, Z., Ngo, T.C., Truong, D.H., Fèvre-Nollet, V., Ribaucour, M., El Bakali, A., Černušák, I., 2023. Hydroxyl radical-initiated decomposition of metazachlor herbicide in the gaseous and aqueous phases: Mechanism, kinetics, and toxicity evaluation. Chemosphere 312, 137234. https://doi.org/10.1016/j.chemosphere.2022.137234

Echeverria, M., Panger, M., Behl, E. Chuck Peck, Environmental Engineer Catherine Aubee, Biologist.

Eren, B., Gürkan, Y.Y., 2021. Theoretical and experimental photodegradation of Phosmet via oxidation techniques in the presence of aqueous TiO_2 suspension. https://doi.org/10.34049/bcc.53.4.T002

EU bans Phosmet, active ingredient used as insecticide, 2022. L.A.B. https://www.lab-sl.com/en/eu-bans-fosmet-active-ingredient-used-as-insecticide/ (accessed 6.9.23).

H. Mali, C. Shah, B. Raghunandan, A. Prajapati, D. Patel, U. Trivedi, R. Subramanian, 2023. Organophosphate pesticides an emerging environmental contaminant: Pollution, toxicity, bioremediation progress, and remaining challenges. Journal of Environmental Sciences 127, 234–250. https://doi.org/10.1016/j.jes.2022.04.023

Haag, W.R., Hoigné, J., 1985. Photo-sensitized oxidation in natural water via OH radicals. Chemosphere 14, 1659–1671. https://doi.org/10.1016/0045-6535(85)90107-9

J. M. Burns, W. J. Cooper, J. L. Ferry, D. W. King, B. P. DiMento, K. McNeill, C. J. Miller, W. L. Miller, B. M. Peake, S. A. Rusak, A. L. Rose, T. D. Waite, 2012. Methods for reactive oxygen species (ROS) detection in aqueous environments. Aquatic Sciences 74, 683–734. https://doi.org/10.1007/s00027-012-0251-x

Kanan, S.M., Yousef, I.A.A., Abdo, N.M., 2007. The photodecomposition of phosmet over UV irradiated silver nanoclusters doped in mordenite zeolite. Applied Catalysis B: Environmental 74, 130–136. https://doi.org/10.1016/j.apcatb.2007.02.004

Klavarioti, M., Mantzavinos, D., Kassinos, D., 2009. Removal of residual pharmaceuticals from aqueous systems by advanced oxidation processes. Environment International 35, 402–417. https://doi.org/10.1016/j.envint.2008.07.009

Li, M., Karu, E., Brenninkmeijer, C., Fischer, H., Lelieveld, J., Williams, J., 2018. Tropospheric OH and stratospheric OH and Cl concentrations determined from CH_4, CH_3Cl, and SF_6 measurements. npj Climate and Atmospheric Science 1, 1–7. https://doi.org/10.1038/s41612-018-0041-9

Liu, C., Yang, B., Zeng, C., 2015. Kinetic studies of heterogeneous reactions of particulate phosmet and parathion with NO_3 radicals. Chemosphere 119, 1276–1280. https://doi.org/10.1016/j.chemosphere.2014.09.049

Mengmeng Xu, Suding Yan, Simei Sun, Zhiran Ni, Wenzhong Wu, Jingyu Sun, 2022. N, N -diethyl-m-toluamide (DEET) degradation by •OH and SO4•−-assisted AOPs in wastewater treatment: Theoretical studies into mechanisms, kinetics and toxicity.

Journal of Environmental Chemical Engineering 10, 108435. https://doi.org/10.1016/j.jece.2022.108435
Nagpal, M., Kakkar, R., 2020. Adsorptive Degradation of Phosmet Using Hierarchically Porous Calcium Oxide: An Experimental and Theoretical Study. ChemistrySelect 5, 1235–1246. https://doi.org/10.1002/slct.201904740
Perry, R.A., Atkinson, R., Pitts, J.N.Jr., 1977. Kinetics and mechanism of the gas phase reaction of hydroxyl radicals with aromatic hydrocarbons over the temperature range 296-473 K. Journal of Physical Chemistry 81, 296–304. https://doi.org/10.1021/j100519a004
Phosmet Fact Sheet | Pesticides | US EPA, Available on: https://archive.epa.gov/pesticides/reregistration/web/html/phosmet_fs.html (accessed 6.9.23).
R. Münze, P. Orlinskiy, R. Gunold, A. Paschke, O. Kaske, M. Beketov, M. Hundt, C. Bauer, G. Schüürmann, M. Möder, M. Liess, 2015. Pesticide impact on aquatic invertebrates identified with Chemcatcher® passive samplers and the SPEAR pesticides index. Science of The Total Environment 537, 69–80. https://doi.org/10.1016/j.scitotenv.2015.07.012
Sabarwal, A., Kumar, K., Singh, R.P., 2018. Hazardous effects of chemical pesticides on human health-Cancer and other associated disorders. Environmental Toxicology and Pharmacology 63, 103–114. https://doi.org/10.1016/j.etap.2018.08.018
Sanches-Neto, F.O., Dias-Silva, J.R., de Oliveira, V.M., Aquilanti, V., Carvalho-Silva, V.H., 2022. Evaluating and elucidating the reactivity of OH radicals with atmospheric organic pollutants: Reaction kinetics and mechanisms by machine learning. Atmospheric Environment 275, 119019. https://doi.org/10.1016/j.atmosenv.2022.119019
Sanches-Neto, F.O., Dias-Silva, J.R., Keng Queiroz Junior, L.H., Carvalho-Silva, V.H., 2021. "pySiRC": Machine Learning Combined with Molecular Fingerprints to Predict the Reaction Rate Constant of the Radical-Based Oxidation Processes of Aqueous Organic Contaminants. Environmental Science and Technology 55, 12437–12448. https://doi.org/10.1021/acs.est.1c04326
Sánchez Camazano, M., Sánchez Martín, M.J., 1983. Factors influencing interactions of organophosphorus pesticides with montmorillonite. Geoderma 29, 107–118. https://doi.org/10.1016/0016-7061(83)90035-6
Sinderhauf, K., Schwack, W., 2004. Photodegradation Chemistry of the Insecticide Phosmet in Lipid Models and in the Presence of Wool Wax, Employing a 15N-Labeled Compound. Journal of Agricultural and Food Chemistry 52, 8046–8052. https://doi.org/10.1021/jf048537+
Sinderhauf, K., Schwack, W., 2003. Photolysis Experiments on Phosmet, an Organophosphorus Insecticide. Journal of Agricultural and Food Chemistry 51, 5990–5995. https://doi.org/10.1021/jf034253y
Stein, V., published, T.S., 2022. What Is Earth's Average Temperature? Available on: https://www.space.com/17816-earth-temperature.html
Sun, Y., Chen, X., Xu, F., Wang, X., 2020. Quantum chemical calculations on the mechanism and kinetics of ozone-initiated removal of p-coumaryl alcohol in the atmosphere. Chemosphere 253, 126744. https://doi.org/10.1016/j.chemosphere.2020.126744
T. C. Ngo, S. Taamalli, Z. Srour, V. Fèvre-Nollet, A. El Bakali, F. Louis, I. Černušák, D. Q. Dao, 2023. Theoretical insights into the oxidation of quinmerac herbicide initiated by HO• radical in aqueous media: Mechanism, kinetics, and ecotoxicity. Journal of Environmental Chemical Engineering 11, 109941. https://doi.org/10.1016/j.jece.2023.109941
Taha, S.M., Amer, M.E., Elmarsafy, A.E., Elkady, M.Y., 2014. Adsorption of 15 different pesticides on untreated and phosphoric acid treated biochar and charcoal from water.

Journal of Environmental Chemical Engineering 2, 2013–2025. https://doi.org/10.1016/j.jece.2014.09.001
Tanabe, Masato., Dehn, R.L., Bramhall, R.R., 1974. Photochemistry of imidan in diethyl ether. Journal of Agricultural and Food Chemistry 22, 54–56. https://doi.org/10.1021/jf60191a020
Tomlin, C., 1994. The Pesticide manual: a world compendium : incorporating the agrochemicals handbook, 10th ed. ed. British Crop Protection Council ; Royal Society of Chemistry, Information Sciences, Farnham, Surrey, Cambridge.
Uc, V.H., Alvarez-Idaboy, J.R., Galano, A., Vivier-Bunge, A., 2008. Theoretical Explanation of Nonexponential OH Decay in Reactions with Benzene and Toluene under Pseudo-First-Order Conditions. Journal of Physical Chemistry A 112, 7608–7615. https://doi.org/10.1021/jp8026258
US EPA, 2013. Types of Pesticide Ingredients [Online]. https://www.epa.gov/ingredients-used-pesticide-products/types-pesticide-ingredients (accessed 6.9.23).
Wauchope, R.D., Buttler, T.M., Hornsby, A.G., Augustijn-Beckers, P.W., Burt, J.P., 1992. The SCS/ARS/CES pesticide properties database for environmental decision-making. Reviews of Environmental Contamination and Toxicology 123, 1–155.
X. Bo, J. Sun, Q. Mei, B. Wei, Z. An, Z. Qiu, D. Han, J. Xie, and M. He, 2021. Theoretical insights into the degradation of tyrosol stimulated by hydroxyl and sulfate radicals in wastewater and ecotoxicity evaluation. Journal of Cleaner Production 293, 126161. https://doi.org/10.1016/j.jclepro.2021.126161
Xu, M., Yan, S., Liu, X., Sun, S., Khan, Z.U.H., Wu, W., Sun, J., 2023. Theoretical investigation on the degradation of sulfadiazine in water environments: Oxidation of •OH, SO4•−and CO3•− and reactivity of (TiO2)n clusters (n = 1–6). Journal of Environmental Chemical Engineering 11, 109994. https://doi.org/10.1016/j.jece.2023.109994
Zweig, G., 2013. Additional Principles and Methods of Analysis: Analytical Methods for Pesticides, Plant Growth Regulators, and Food Additives, Vol. 5. Elsevier.

Chapter IV. Chlorpyrifos

IV.1. Introduction

Chlorpyrifos (CPF), also known as O,O-diethyl O-(3,5,6-trichloro-2-pyridyl) phosphorothioate, is one of the primary organothiophosphate pesticides used in agricultural and domestic applications (Giesy *et al.*, 2014). The extensive use of this pesticide is widely spread in many countries including both developed and agricultural countries. However, a significant proportion of the chemical, estimated at only 0.1%, reaches its intended targets, with the remainder dispersing to unintended locations in soil, air, and water, leading to environmental contamination. The exposure to excessive amounts of CPF for long times poses toxicity risks to mammals, aquatic ecosystems, birds, pollinators, and also raises concerns about human health (Chiu *et al.*, 2021; Cui *et al.*, 2006; Kim *et al.*, 2013; Phung *et al.*, 2012; Wang *et al.*, 2016).

The acute and chronic toxic effects of CPF include asthma, leukemia, reproductive issues (Silvia *et al.*, 2020), DNA damage (Yang *et al.*, 2019), and neural developmental toxicity (He *et al.*, 2022). Studies have demonstrated that CPF and several of its degradation products can act as inhibitors of acetylcholinesterase and butyrylcholinesterase (Amitai *et al.*, 1998; Burke *et al.*, 2017; Huang *et al.*, 2015; Worek *et al.*, 2004), as well as inhibitors of glutathione S-transferase (Tiwari and Mishra, 2023), and can act as endocrine disruptors (Lasagna *et al.*, 2022; Ubaid ur Rahman *et al.*, 2021).

Apart from many experimental data, several theoretical research studies have captured our interest, employing techniques like docking studies and molecular dynamics (MD) to clarify the underlying mechanism of CPF's inhibition of reproductive and developmental enzymes. For instance, Hazarika *et al.* studied the interactions of CPF and its main degradation products with progesterone (Hazarika *et al.*, 2020) and androgen receptors (Hazarika *et al.*, 2022), where these hormones are important for the pregnancy regulation in females or the reproductive development in males. Tiwari *et al.* also claimed that among CPF and its degradation products, 3,5,6-trichloro-2-pyridinol exhibits the highest potency as an inhibitor of glutathione S-transferases, which is a crucial human enzyme involved in hormone synthesis, intracellular transport, and protection against oxidative stress (Tiwari and Mishra, 2023). Notably, Da Silva *et al.* reported a combined experimental and *in silico* study on the interactions between CPF and cockroach acetylcholinesterase (AChE) enzymes, as well as the reactivation of AChE structures by pralidoxime, a well-known antidote for organophosphate toxicants (da Silva *et al.*, 2018).

Although many researches have been conducted on the neural developmental toxicity of CPF and similar organophosphate pesticides, this work is unique where computational methods have been utilized to clarify the molecular interactions between these toxicants and cholinesterase enzymes.

The oxidation of CPF experimentally is a complex process influenced by various factors and conditions such as pH, temperature (Weber *et al.*, 2020), catalytic or photocatalytic activity (Teymourinia *et al.*, 2023), and microbial degradation (Huang *et al.*, 2021; Malakootian *et al.*, 2020; Nandhini *et al.*, 2021). Depending on these conditions and the sensitivity of spectroscopic instrumentation, several principal degradation products of CPF have been identified. While

unstable intermediates like chlorpyrifos-oxon and desethyl chlorpyrifos are easily formed through oxidation, CPF hydrolysis under alkaline conditions (Huang *et al.*, 2021; Malakootian *et al.*, 2020; Nandhini *et al.*, 2021) or catalyse by metal nanoparticles (Bootharaju and Pradeep, 2012; Teymourinia *et al.*, 2023) yields 3,5,6-trichloro-2-pyridinol and diethylthiophosphate. Methylation of 3,5,6-trichloro-2-pyridinol can result in trichloromethoxypyridine. Alternatively, pyridinol products from dechlorination are often observed under irradiation (Nandhini *et al.*, 2021; Teymourinia *et al.*, 2023).

In particular, Munoz *et al.* reported the degradation process of chlorpyrifos-methyl (Muñoz *et al.*, 2011), chlorpyrifos, and chlorpyrifos-oxon (Muñoz *et al.*, 2014) under atmospheric conditions exposed to natural sunlight. They determined the oxidation rate constants (*k*) to be 4.1 ± 0.4, 9.1 ± 2.1, and $1.7 \pm 0.9 \times 10^{-11}$ cm^3 $molecule^{-1}$ s^{-1} at 300 ± 5 K for chlorpyrifos-methyl, chlorpyrifos, and chlorpyrifos-oxon, respectively.

Given its high reactivity, $HO^{\bullet}$ radical has been greatly used in advanced oxidation processes (AOPs) for the removal of organic pollutants, particularly pesticides (Malakootian *et al.*, 2020) or pharmaceuticals (Sun *et al.*, 2023; Yao *et al.*, 2022). Several theoretical studies on the mechanisms and kinetics of $HO^{\bullet}$-initiated degradation of organophosphorus pesticides were reported for dimethoate (Shi *et al.*, 2018) and phosmet (K. Al Rawas *et al.*, 2023). Additionally, the degradation of CPF in the gas phase has been studied through theoretical approach (Zhou *et al.*, 2010). Accordingly, the H-abstraction from the -CH_2- moieties, the $HO^{\bullet}$-addition to the P atom and the C atoms bond with chlorine, and to the N atom of the pyridyl ring were determined as energetically favourable pathways. The dominant products were chlorpyrifos-oxon, trichloropyridinol, diethylthiophosphate, and SO_2. While the study considered the steric impacts of the attacked positions, it did not investigate the reaction kinetics, thereby missing information regarding the degradation rate and the individual contribution of each pathway to the overall reaction.

In this chapter, a complete quantum mechanical study of the $HO^{\bullet}$-induced degradation of CPF was performed (***Figure IV-2***), covering various aspects from mechanisms and kinetics to the ecotoxicity and cholinesterase inhibition of the most toxic degradation products. Initially, the degradation of CPF was examined in both gas and aqueous phases, exploring conventional mechanisms such as H-, S-, Cl-, and CH_3-abstraction, $HO^{\bullet}$-addition, and single electron transfer. Thermodynamic and kinetic parameters of these reactions were analysed to identify the dominant reactions and determine the branching ratio of the potential pathways. Moreover, attempts were made to oxidize the primary radical products further using other oxidizing agents, resulting in primary neutral products. Then, the acute and chronic toxicity of these products, as well as CPF itself, were evaluated across various aquatic organisms, including fish, daphnia, and green algae. Lastly, through docking and molecular dynamics, the binding sites and inhibitory activity of CPF and its degradation products on typical neural acetylcholinesterase (AChE) and butyrylcholinesterase (BChE) enzymes were predicted at the molecular level.

IV.2. Computational methods

Calculations are done as described in **Chapter II**.

Docking simulation was performed with the Autodock4 program (Morris *et al.*, 2009). PDBQT files were prepared using Autodock Tool 1.5.7. AChE (PDB ID 4EY7) and BChE (PDB ID 1P0M) were taken from RCSBPDB website (www.rscb.org). Missing residues in 1P0M were repaired using the Builder option in PyMol (The PyMOL Molecular Graphics System) and refined using ModLoop (Fiser *et al.*, 2000; Fiser and Sali, 2003). The Lamarkarian Genetic Algorithm method was applied for docking; other parameters were kept as default. The docking score (kJ mol^{-1}) was analysed, and protein-ligand interaction was visualized with Discovery Studio 2021. The degradation products with the highest docking score were selected for further study in molecular dynamics. Molecular dynamics (MD) simulations of the complexes were performed with AMBER f99SB-ILDN force field (Lindorff-Larsen *et al.*, 2010) and water model TIP3P (Jorgensen *et al.*, 1983) implemented in the GROMACS 2023 package (Abraham *et al.*, 2023). GAFF2 force field parameters with AM1-BCC charge method for ligands were prepared using Antechamber (Wang *et al.*, 2006, 2004) and ACPYPE (Sousa da Silva and Vranken, 2012). The studied complex was positioned in a cubic box at a distance of 1.2 nm from the solute to the box surface, and the system was neutralized using Na^+ and Cl^- as counterions. All simulation was performed at 300 K and 1 atm. The V-rescale (Bussi *et al.*, 2007) and Parrinello-Rahman (Parrinello and Rahman, 1981) algorithms were used to keep temperature and pressure constant. Equilibration of the system was carried out in two phases, *i.e.*, NVT (50000 steps, 2 fs/step) and NPT (250000 steps, 2 fs/step). The cutoff scheme using Verlet for short-range van der Waals cutoff (1.2 nm) and the Particle Mesh Ewald for long-range electrostatic (1.2 nm) were adopted. Finally, MD simulations were conducted employing a leap-frog integrator over a time scale of 100 ns and a time step of 2 fs. Root mean square deviation (RMSD), root mean square fluctuation (RMSF), and H-bond interactions were analysed.

IV.3. Results and discussion

IV.3.1. Structure and electronic properties of CPF

CPF predominantly exists in its neutral form (> 95.96%) in water, particularly in acidic conditions (pH > 1). Hence, in this study only the neutral form of the CPF molecule was taken into consideration for all reactions. Initially, various conformations of CPF were generated using the MSTor program, after which optimization procedures were carried out individually in both the gas phase or water. Subsequently, the most stable conformation within each phase was chosen for further calculations.

The optimized geometry and electronic structures of CPF in both the gas phase and water, are represented in ***Figure IV-1***. Although the geometrical structures in the two phases are different, the electronic properties are similar. In terms of frontier orbitals, the HOMO is primarily situated on the thiophosphate groups, while the LUMOs are positioned on the pyridyl ring and

the adjacent chlorine atoms. Additionally, the ESP maps reveal highly negative charges on the sulfur atom and positive charges on the hydrogen and chlorine atoms.

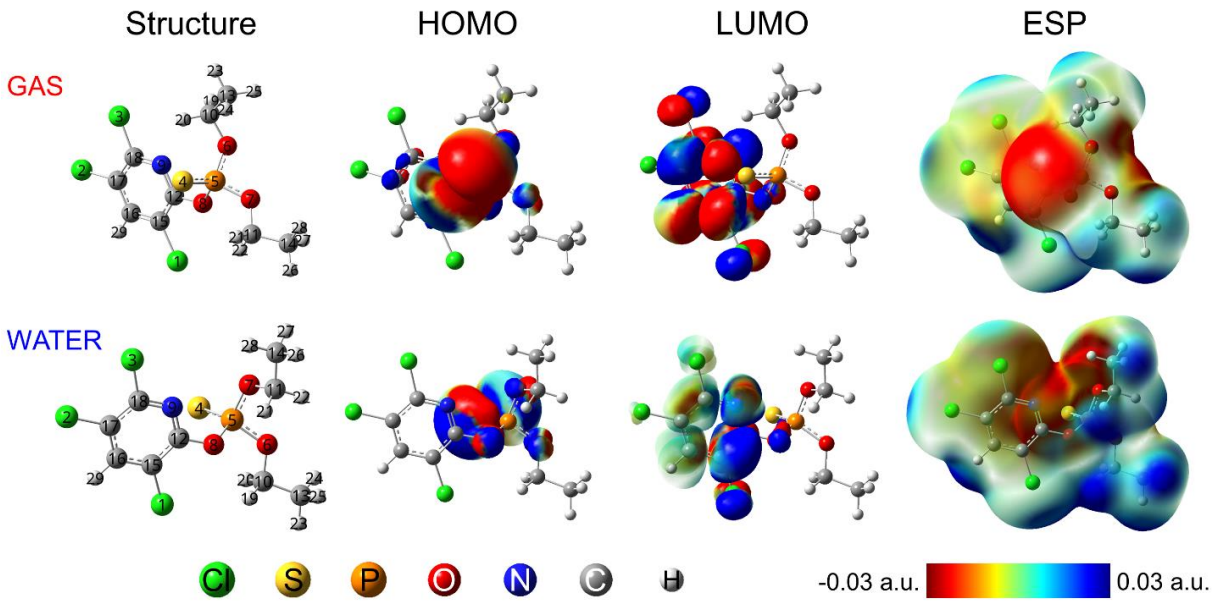

Figure IV-1*: optimized geometry of the most stable conformer of CPF, its HOMO, LUMO, and ESP maps in the gas phase and water.*

IV.3.2. Oxidation reaction mechanisms

In the degradation process of CPF initiated by HO$^{\bullet}$, the molecule undergoes abstraction, addition, and single electron transfer (SET) reactions, as elaborated in ***Figure IV-2***. Initially, eleven H-abstractions, along with three chlorine-, one sulfur-, and two methyl-abstractions, are examined. Regarding RAF reactions, seven HO$^{\bullet}$-additions are explored, including P-, N-positions, and five other C-positions of the ring. Lastly, the SET reaction is considered.

Figures IV-3 and ***IV-4*** present the ZPE-corrected enthalpy profiles of reactions at 0 K along the reaction coordinates in gas and water, respectively. The optimized geometry of transition states for all examined reactions in the gas phase is illustrated in ***Figure IV-5***, while corresponding results in water are provided in ***Figure IV-6***.

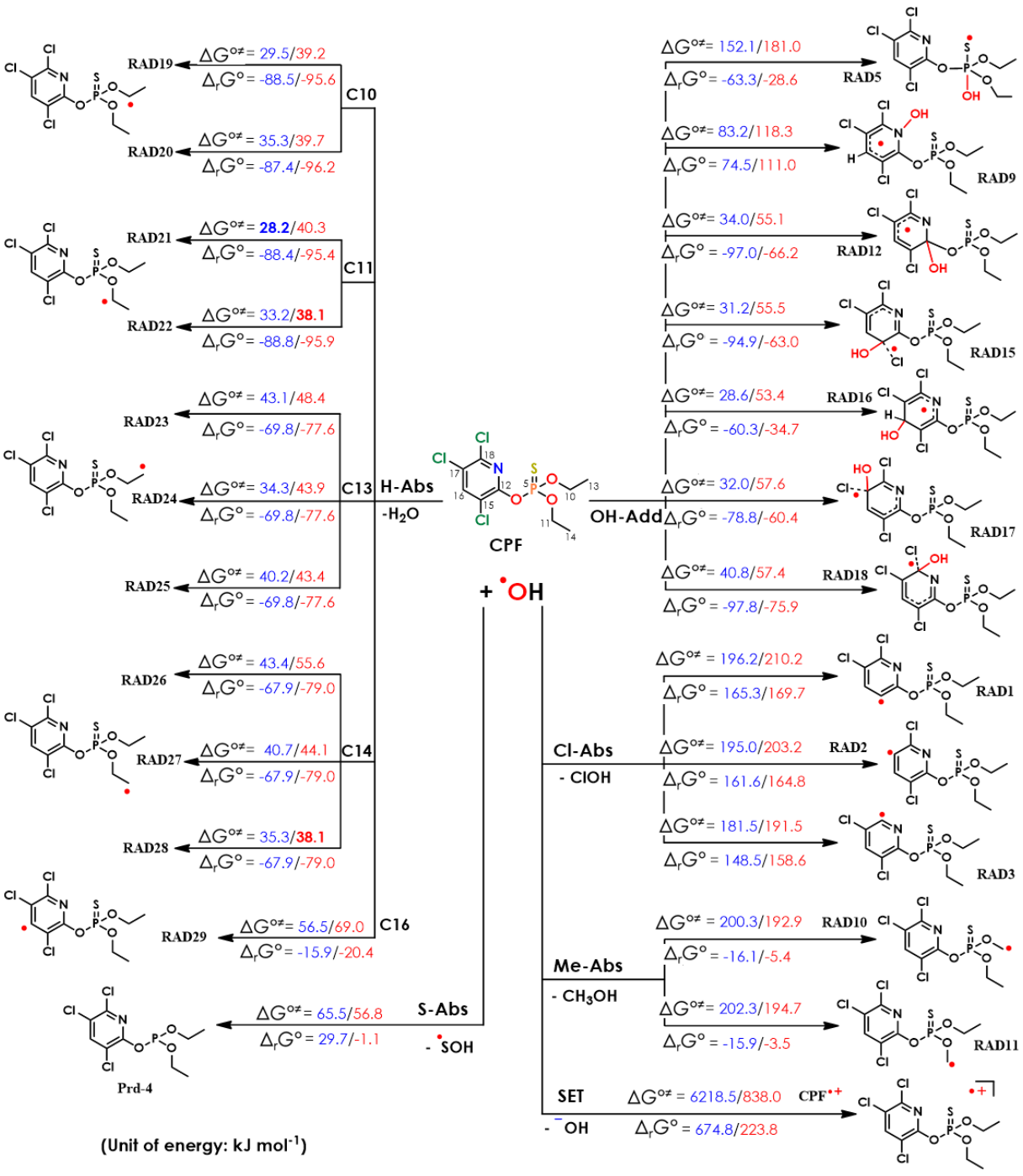

***Figure IV-2**: HO•-initiated degradation pathways of CPF in the gas phase and water. Standard Gibbs free reaction energies ($\Delta_rG°$) and standard Gibbs free activation energies ($\Delta G^{\circ\neq}$) at 298 K are written in blue and red for the gas and aqueous phases, respectively.*

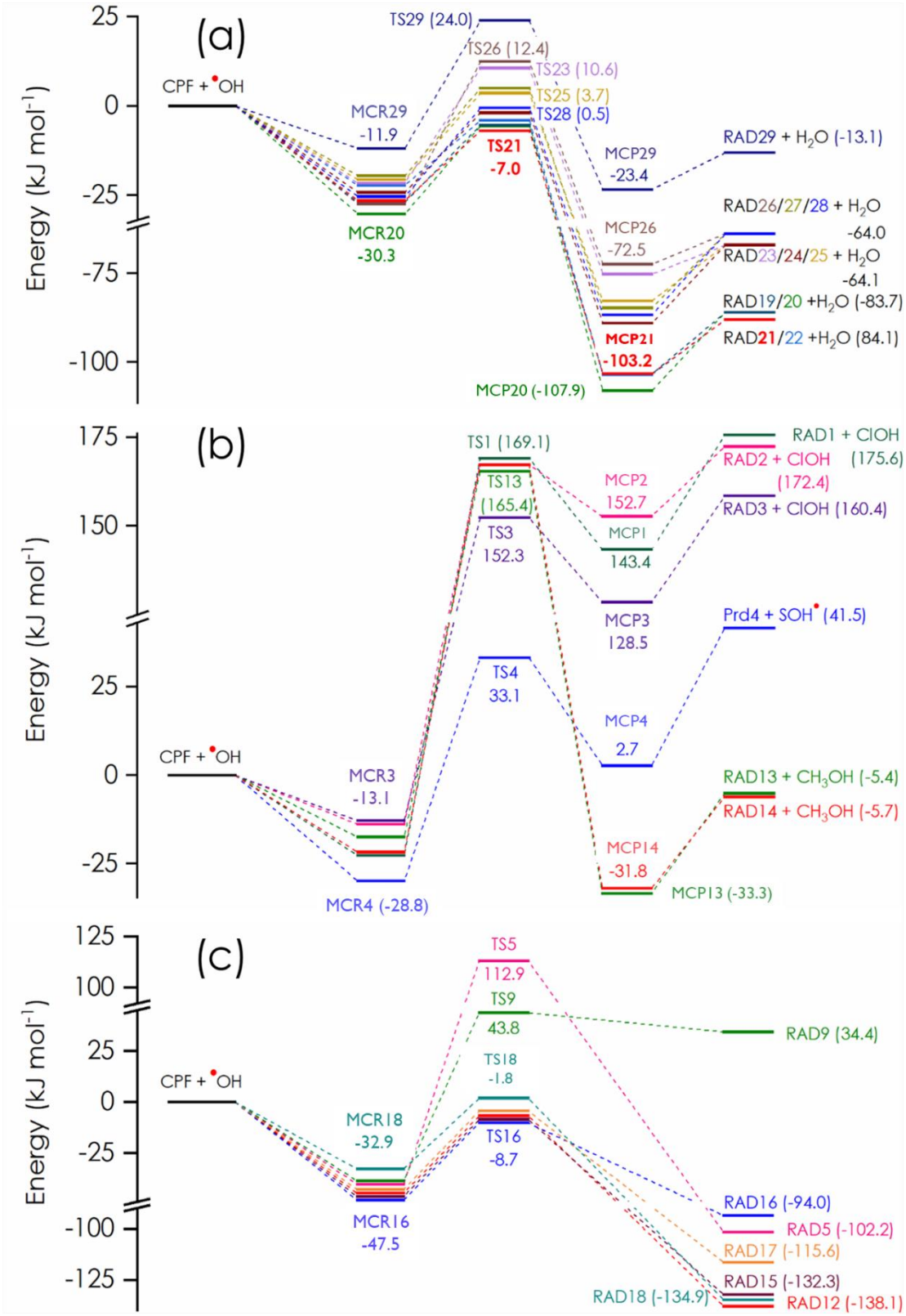

***Figure IV-3**: ZPE-corrected standard reaction enthalpy at 0 K ($\Delta_r H°_{0K}$) profile for (a) H-abstraction reaction (b) Cl-, S- and CH_3-abstraction reaction, and (c) RAF reaction between CPF (neutral) and HO• radical in gas phase; calculation performed at M06-2X/6-311++G(3df,3pd).*

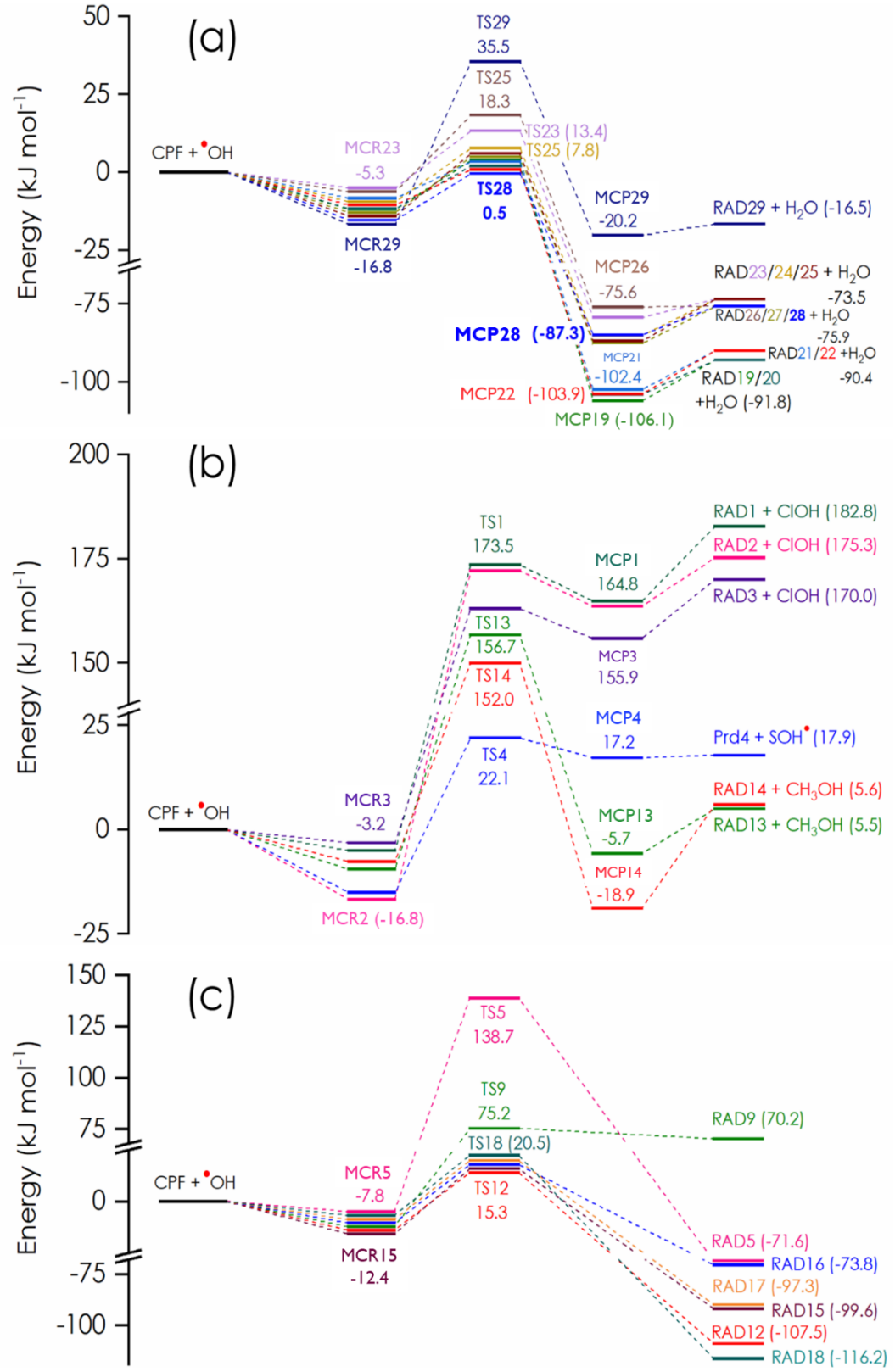

***Figure IV-4**: ZPE-corrected standard reaction enthalpy profile at 0 K ($\Delta_r H°_{0K}$) for (a) H-abstraction reaction (b) Cl-, S- and CH_3-abstraction reaction, and (c) RAF reaction between CPF (neutral) and HO• radical in water; calculation performed at M06-2X/6-311++G(3df,3pd).*

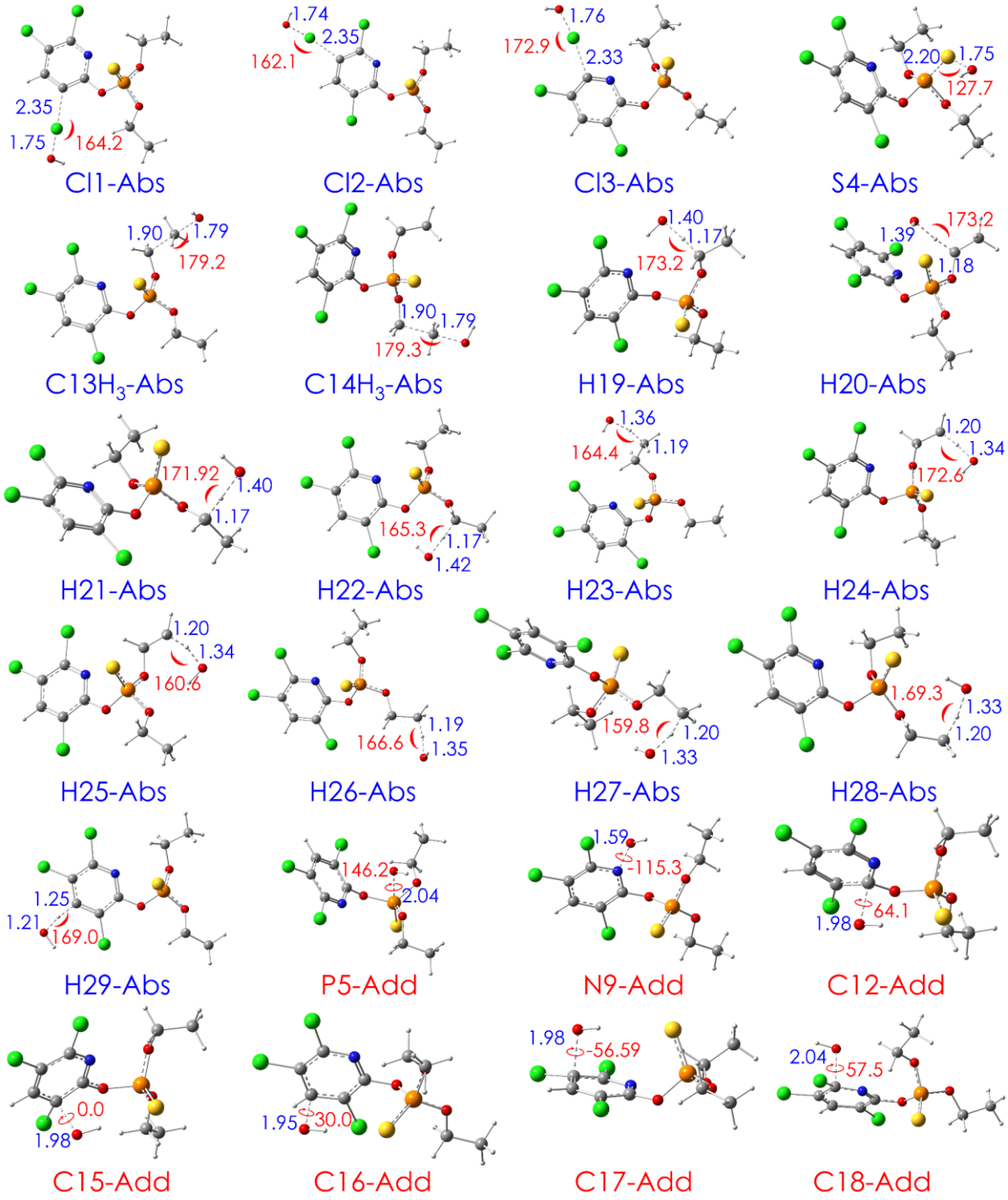

***Figure IV-5**: optimized geometries of TS structures of all reactions in gas phase; calculation performed at M06-2X/6-311++G(3df,3pd).*

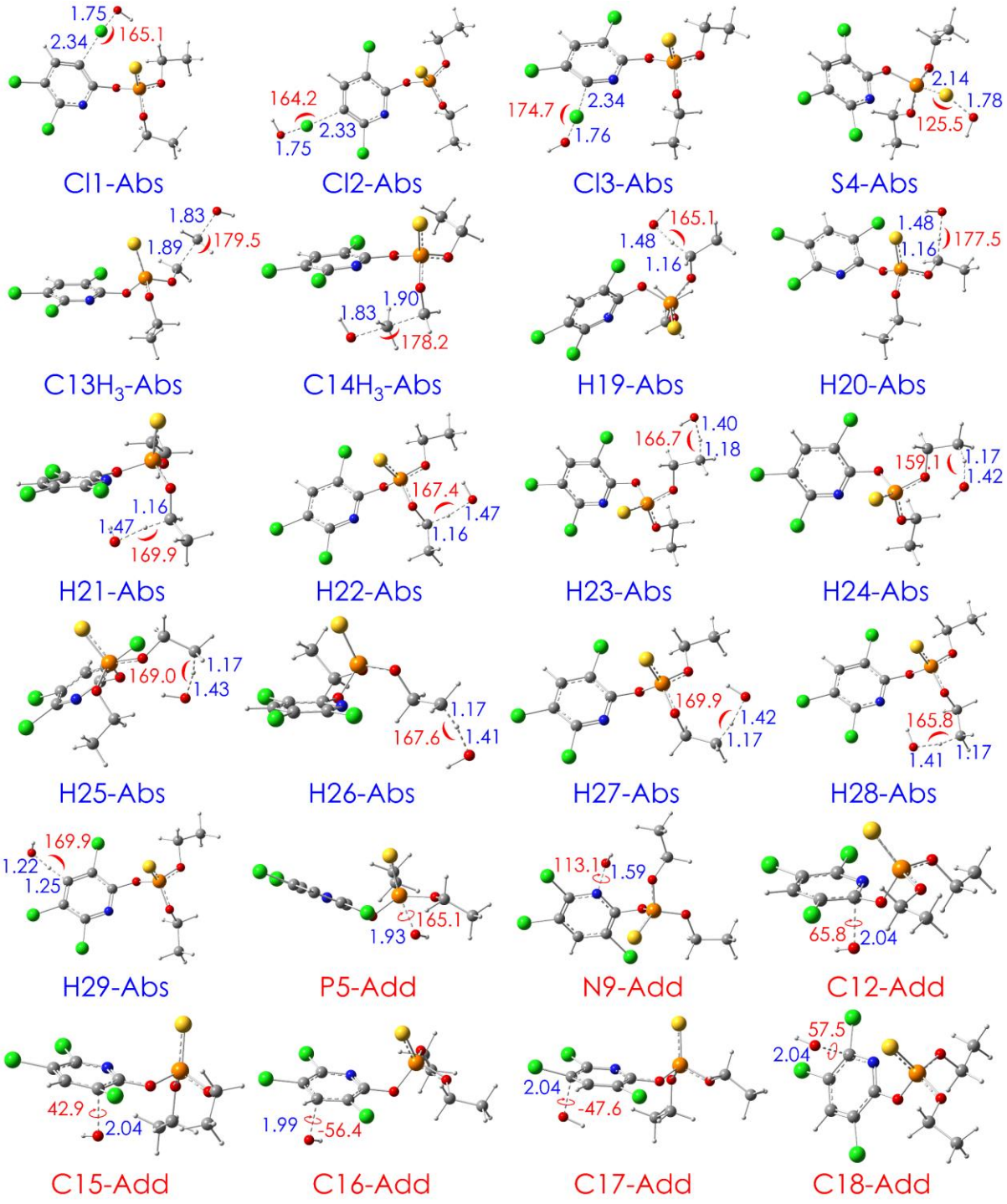

***Figure IV-6**: optimized geometries of TS structures of all reactions in water; calculation performed at M06-2X/6-311++G(3df,3pd).*

IV.3.2.1. Formal hydrogen transfer (FHT) reactions

Based on the results in ***Figure IV-2*** and ***Figure IV-3a***, it can be observed that all H-abstractions (H-Abs) in the gas phase are characterized by being exothermic, spontaneous, and exergonic, with highly negative $\Delta_r G°_{298k}$ and $\Delta_r H°_{0K}$ values. Among these, the H-Abs reactions involving methylene groups, specifically H19-H22, exhibit the lowest gaseous $\Delta_r G°$ values at 298 K, reaching -88 kJ mol^{-1}, whereas the highest $\Delta_r G°$ value is found for H29 of C16 (-15.9 kJ mol^{-1}). The $\Delta G°^{\neq}$ in the gas phase varies from 28.2 to 56.5 kJ mol^{-1} at 298 K.

As expected, the highest $\Delta G°^{\neq}$ value is associated with H29 (of C16), while the smallest $\Delta G°^{\neq}$ is observed for H19 (of C10) and H21 (of C11) at 298 K. Therefore, the H-Abs reactions at H19 and H21 emerge as the most favourable in the gas phase. It's worth noting that the lowest $\Delta G°^{\neq}$ values align with the structures of the lowest-energy TSs, which are stabilized by hydrogen bonding. For example, the TS H21-Abs is stabilized by the hydrogen bonding interaction C10-H20···N, and TS-H19-Abs involves the N···H-O interaction (refer to ***Figure IV-5***). The result is consistent with the previously reported pathways (Zhou *et al.*, 2010).

In water, similar results are observed, but the reactions are even more exergonic. The $\Delta_r G°$ values appeared to be lower by 4-12 kJ mol^{-1} at all positions compared to the gas phase. Notably, the lowest $\Delta_r G°$ values are also obtained on H-atoms of C10 and C11, *i.e.*, H20 (-96.2 kJ mol^{-1}) and H22 (-95.9 kJ mol^{-1}), while the highest $\Delta_r G°$ is still negative and is found on H29 (of C16) at -20.4 kJ mol-1. Conversely, the $\Delta G°^{\neq}$ in water is slightly higher compared to that in the gas phase, ranging from 38.1 kJ mol^{-1} (for H22 and H28) to 69.0 kJ mol^{-1} (for H29).

So, the lower $\Delta_r G°$ and higher $\Delta G°^{\neq}$ values in the aqueous phase compared to the values in the gas phase can be attributed to the increased higher stability of reactant complexes in water (McKee, 2003). Thus, the FHT reactions at H22 and H28 are the most favourable in the aqueous medium, and similar hydrogen bonding observed in their respective TS structures (***Figure IV-6***). Across both phases, the H-abstraction reactions generally more favoured in the order -CH_2- > -CH_3- > pyridyl ring.

IV.3.2.2. Cl-, S- and Me-abstractions

Figures IV-3b and ***IV-4b*** present the ZPE-corrected standard reaction enthalpy at 0 K ($\Delta_r H°_{0K}$) profile for Cl-, S-, and CH_3-abstraction reactions between CPF and HO$^{\bullet}$ in the gas phase and water. Together with the results in ***Figure IV-2***, it becomes apparent that these reactions are endothermic, non-spontaneous, and exergonic.

Initially, the S-abstraction reaction yields the neutral phosphite Prd-4 and releases the HOS$^{\bullet}$ radical. This reaction is unfavourable in the gas phase, with $\Delta_r G°$ of 29.7 kJ mol^{-1} and $\Delta G°^{\neq}$ as high as 65.5 kJ mol^{-1} at 298 K. In the aqueous medium, although the $\Delta_r G°$ is slightly negative (-1.1 kJ mol^{-1}), a very high $\Delta G°^{\neq}$ of 56.8 kJ mol^{-1} is still present as an obstacle. A similar HO$^{\bullet}$-addition to the S position was previously discussed by Munoz *et al.* However, in the presence of O_2, the proposed product underwent transformation into chlorpyrifos-oxon and HOSO (Muñoz *et al.*, 2014).

Then, considering the reactions involving three Cl atoms, very high $\Delta G^{\circ\neq}$ values (196.2, 195.4, and 181.5 kJ mol^{-1}) as well as highly positive $\Delta_r G^\circ$ values (165.3, 161.6, and 148.5 kJ mol^{-1}) made the Cl-abstractions in the gas phase unfavourable and endergonic. In the aqueous phase, even higher $\Delta_r G^\circ$ and $\Delta G^{\circ\neq}$ values, approximately 4 to 10 kJ mol^{-1} at 298 K, are observed. These mechanisms are not spontaneous and are endergonic in both phases.

In the final attempt, we tried to extract CH_3 groups. Similar results were obtained for CH_3-abstraction at the C13 and C14 positions. Despite the reaction exhibiting a negative $\Delta_r G^\circ$ (-16.1 and -15.9 kJ mol^{-1}), very high $\Delta G^{\circ\neq}$ values (200.3 and 202.3 kJ mol^{-1}) made the CH_3-abstraction unfavourable in the gas phase. In water, only a slightly lower $\Delta G^{\circ\neq}$ values 192.8 and 194.7 kJ mol^{-1} were observed (around 10 kJ mol^{-1} difference from the ones in gas phase) at 298 K.

IV.3.2.3. Radical adduct formation (RAF) reactions

The reactions involving the addition of HO$^\bullet$ to CPF were studied for all five C-, N-, and P-positions. ***Figures IV-3c*** and ***IV-4c*** represent the ZPE-corrected standard reaction enthalpy at 0 K ($\Delta_r H^\circ_{0K}$) profile for RAF reactions between CPF and HO$^\bullet$ in the gas phase and water. Based on the results presented in ***Figures IV-2, IV-3c*** and ***IV-4c,*** it becomes evident that addition to the N-position is endothermic and non-spontaneous in both mediums. For the N-adduct reaction, both $\Delta_r G^\circ$ and $\Delta G^{\circ\neq}$ were found to be highly positive, where $\Delta_r G^\circ$ values were 74.5 and 111.0 kJ mol^{-1} and $\Delta G^{\circ\neq}$ were 83.2 and 118.3 kJ mol^{-1} at 298 K in gas and water, respectively.

For the P-addition, $\Delta_r G^\circ$ obtained are negative (-63.3/-28.6 kJ mol^{-1} for gas/water) at 298 K, however, $\Delta G^{\circ\neq}$ values were very high (152.1/181.0 kJ mol^{-1} for gas/water) making this reaction unfavourable. On the other hand, all HO$^\bullet$-additions to C-atoms are spontaneous, exhibiting negative $\Delta_r G^\circ$ varying from -60.3 to -97.8 kJ mol^{-1} in the gas phase and from -28.6 to -75.9 kJ mol^{-1} in water. The most negative $\Delta_r G^\circ$ values were obtained at the C-atom bonded with chlorine *i.e.,* C18 (-97.8/-75.9 kJ mol^{-1} for gas/water). However, the smallest $\Delta G^{\circ\neq}$ values are observed at C16 in both the gas phase and water, being 28.6 and 53.4 kJ mol^{-1}, respectively. Hence, the most favourable RAF reaction is the addition to C16.

IV.3.2.4. Single electron transfer (SET) reaction

As CPF is in the neutral form, the SET reaction proves unfavourable in the gas phase, where our calculations show high $\Delta_r G^\circ$ value (675 kJ mol^{-1}) and very high $\Delta G^{\circ\neq}$ (6218.5 kJ mol^{-1}) at 298 K in the gas phase. Likewise, the calculations yield notably high $\Delta G^{\circ\neq}$ (838 kJ mol^{-1}) and $\Delta_r G^\circ$ (224 kJ mol^{-1}) values in water, indicating the unfavourable nature of SET in aqueous medium as well.

IV.3.3. Reaction kinetics

The kinetic parameters, including the diffusion rate constant (k_D, M^{-1} s^{-1}), thermal rate constant (k_T, M^{-1} s^{-1}), the apparent diffusion-corrected rate constant (k_{app}, M^{-1} s^{-1}), and the branching ratio (Γ, %) of all reactions in gas and water at 298 K, are resumed in ***Table IV-1***. The temperature-dependent rate constants within the studied range are summarized in ***Table IV-2***.

It is observed that the overall rate constant in the gas phase (1.65×10^{10} M^{-1} s^{-1}) is 35 times higher than that in water (4.76×10^{8} M^{-1} s^{-1}). Notably, the FHT reaction is predominant in both mediums. In the gas phase, the highest rate constants are determined for methylene group abstraction, *i.e.*, H21 (6.24×10^{9} M^{-1} s^{-1}) and H19 (3.21×10^{9} M^{-1} s^{-1}), with Γ values of 37.9 and 19.5%, respectively.

In water, the rate constant for the FHT reaction is nearly 50 times lower compared to the gas phase. The highest rate constants are observed for H28 (1.28×10^{8} M^{-1} s^{-1}) and H22 (1.07×10^{8} M^{-1} s^{-1}), contributing 26.9% and 22.5% to the overall reaction, respectively. Regarding the RAF reaction, the addition at C16 in the gas phase occurs with a rate constant of 2.24×10^{9} M^{-1} s^{-1}, representing 13.6% of the overall reaction. However, in water, the rate constants for the RAF reaction to C-positions decrease significantly to 10^{4} M^{-1} s^{-1}, thereby nullifying the contribution of RAF reaction to the degradation of CPF.

Reactions that are characterized by unfavourable thermodynamic parameters (mentioned in the previous section) *i.e.*, positive $\Delta_r G°$ values and/or exceedingly high barriers ($\Delta G°^{\neq}$), are expected to show negligible rate constants. Indeed, all Cl- and CH_3-abstraction reactions have negligible k_{app} within the range of 10^{-18} to 10^{-23} M^{-1} s^{-1}. While the S-abstraction demonstrates a higher rate constant of 7.85×10^{2} M^{-1} s^{-1} (in gas) and 2.65×10^{4} M^{-1} s^{-1} (in water), it remains insignificant compared to other FHT and RAF reactions. Additionally, very small k_{app} values were obtained for Add-P5 (ranging from 10^{-13} to 10^{-18} M^{-1} s^{-1} in gas and water, respectively) and for Add-N9 (ranging from 10^{-1} to 10^{-7} M^{-1} s^{-1}). The SET reaction, similarly, shows a zero-rate constant. Therefore, these reactions do not contribute to the degradation of CPF. This result agrees with previous reports (Dao *et al.*, 2023; Muñoz *et al.*, 2014; Ngo *et al.*, 2023).

***Table IV-1**: Eckart correction constant (CorrEck), the diffusion rate constant (k_D, M^{-1} s^{-1}), thermal rate constant (k_T, M^{-1} s^{-1}), apparent diffusion-corrected rate constant (k_{app}, M^{-1} s^{-1}), and branching ratio (Γ, %) of the abstraction, addition and single electron transfer reactions between CPF and $HO^{\bullet}$ in the gas phase and water at 298 K.*

	GAS			WATER				
Position	**CorrEck**	**k_T**	**Γ (%)**	**CorrEck**	**k_D**	**k_T**	**k_{app}**	**Γ (%)**
Abstraction Reactions								
Cl1	1.058	1.02×10^{-20}	0.00	1.056	4.29×10^{9}	3.45×10^{-23}	3.45×10^{-23}	0.00
Cl2	1.061	1.61×10^{-20}	0.00	1.065	4.28×10^{9}	5.69×10^{-22}	5.69×10^{-22}	0.00
Cl3	1.054	3.70×10^{-18}	0.00	1.050	4.39×10^{9}	6.57×10^{-20}	6.57×10^{-20}	0.00
S4	1.009	7.85×10^{2}	0.00	1.018	3.69×10^{9}	2.65×10^{4}	2.65×10^{4}	0.01
$C13H_3$	4.752	8.60×10^{-21}	0.00	2.838	3.94×10^{9}	1.04×10^{-19}	1.04×10^{-19}	0.00
$C14H_3$	4.950	3.94×10^{-21}	0.00	2.836	3.95×10^{9}	4.92×10^{-20}	4.92×10^{-20}	0.00
H19	**1.787**	**3.21×10^{9}**	**19.47**	2.728	2.76×10^{9}	8.69×10^{7}	8.43×10^{7}	17.70
H20	3.264	4.85×10^{8}	2.95	2.181	2.79×10^{9}	5.51×10^{7}	5.41×10^{7}	11.35
H21	**2.324**	**6.24×10^{9}**	**37.88**	2.241	2.77×10^{9}	4.51×10^{7}	4.44×10^{7}	9.32
H22	1.804	7.17×10^{8}	4.36	**2.308**	**2.76×10^{9}**	**1.12×10^{8}**	**1.07×10^{8}**	**22.53**
H23	3.027	1.99×10^{7}	0.12	2.995	2.71×10^{9}	1.65×10^{7}	1.64×10^{7}	2.43
H24	4.228	9.48×10^{8}	5.76	2.910	2.70×10^{9}	1.37×10^{7}	1.37×10^{7}	2.87
H25	4.636	9.72×10^{7}	0.59	2.766	2.73×10^{9}	1.61×10^{7}	1.60×10^{7}	3.36
H26	3.330	1.97×10^{7}	0.12	2.841	2.72×10^{9}	1.27×10^{5}	1.27×10^{5}	0.03
H27	4.723	8.02×10^{7}	0.49	2.698	2.73×10^{9}	1.17×10^{7}	1.17×10^{7}	2.45
H28	4.896	7.32×10^{8}	4.45	**2.723**	**2.72×10^{9}**	**1.34×10^{8}**	**1.28×10^{8}**	**26.90**
H29	23.93	6.94×10^{5}	0.00	62.312	2.60×10^{9}	1.17×10^{4}	1.17×10^{4}	0.00
Addition Reactions								
P5	2.51	8.61×10^{-13}	0.00	1.06	2.16×10^{9}	3.03×10^{-18}	3.03×10^{-18}	0.00
N9	1.42	5.68×10^{-1}	0.000	1.35	2.15×10^{9}	3.88×10^{-7}	3.88×10^{-7}	0.00
C12	1.83	3.11×10^{8}	1.89	1.43	2.10×10^{9}	4.93×10^{4}	4.93×10^{4}	0.01
C15	1.52	7.90×10^{8}	4.48	1.28	2.16×10^{9}	3.72×10^{4}	3.72×10^{4}	0.01
C16	1.52	2.24×10^{9}	13.64	1.45	2.16×10^{9}	9.70×10^{4}	9.70×10^{4}	0.02
C17	1.48	5.67×10^{8}	3.45	1.27	1.69×10^{9}	1.61×10^{4}	1.61×10^{4}	0.00
C18	1.47	1.61×10^{7}	0.04	1.43	2.04×10^{9}	1.89×10^{4}	1.89×10^{4}	0.00
SET Reaction								
	-	~0	0.00	-	-	~0	~0	0.00
Total								
Total		1.65×10^{10}	100.00				4.76×10^{8}	100.00

***Table IV-2**: apparent rate constants (k, in M^{-1} s^{-1}) of all oxidation reactions in (a) gas (253-323 K) and (b) water (283-323 K). (the most favourable pathways are in bold).*

(a) GAS													
T (K)	**Cl1-Abs**	**Cl2-Abs**	**Cl3-Abs**	**S4-Abs**	**C13H3-Abs**	**C14H3-Abs**	**S4-Abs**	**H19-Abs**	**H20-Abs**	**H21-Abs**	**H22-Abs**	**H23-Abs**	**H24-Abs**	**SET**
253	4.34×10^{-26}	7.87×10^{-26}	5.21×10^{-23}	6.46×10^{1}	1.55×10^{-25}	6.73×10^{-26}	6.46×10^{1}	**5.76×10^{9}**	1.17×10^{9}	**1.31×10^{10}**	1.17×10^{9}	1.32×10^{7}	1.88×10^{9}	~0
258	2.12×10^{-25}	3.77×10^{-25}	2.18×10^{-22}	8.88×10^{1}	6.02×10^{-25}	2.61×10^{-25}	8.88×10^{1}	**5.31×10^{9}**	1.04×10^{9}	**1.19×10^{10}**	1.09×10^{9}	1.38×10^{7}	1.70×10^{9}	~0
263	9.72×10^{-25}	1.70×10^{-24}	8.63×10^{-22}	1.21×10^{2}	2.25×10^{-24}	9.82×10^{-25}	1.21×10^{2}	**4.92×10^{9}**	9.24×10^{8}	**1.08×10^{10}**	1.02×10^{9}	1.44×10^{7}	1.56×10^{9}	~0
268	4.22×10^{-24}	7.27×10^{-24}	3.25×10^{-21}	1.62×10^{2}	8.12×10^{-24}	3.56×10^{-24}	1.62×10^{2}	**4.57×10^{9}**	8.29×10^{8}	**9.83×10^{9}**	9.63×10^{8}	1.50×10^{7}	1.43×10^{9}	~0
273	1.74×10^{-23}	2.94×10^{-23}	1.17×10^{-20}	2.16×10^{2}	2.83×10^{-23}	1.25×10^{-23}	2.16×10^{2}	**4.27×10^{9}**	7.48×10^{8}	**9.02×10^{9}**	9.10×10^{8}	1.57×10^{7}	1.32×10^{9}	~0
278	6.81×10^{-23}	1.14×10^{-22}	4.01×10^{-20}	2.84×10^{2}	9.49×10^{-23}	4.22×10^{-23}	2.84×10^{2}	**4.01×10^{9}**	6.79×10^{8}	**8.31×10^{9}**	8.62×10^{8}	1.64×10^{7}	1.22×10^{9}	~0
283	2.54×10^{-22}	4.18×10^{-22}	1.32×10^{-19}	3.71×10^{2}	3.08×10^{-22}	1.38×10^{-22}	3.71×10^{2}	**3.77×10^{9}**	6.20×10^{8}	**7.69×10^{9}**	8.20×10^{8}	1.72×10^{7}	1.14×10^{9}	~0
288	9.08×10^{-22}	1.47×10^{-21}	4.16×10^{-19}	4.80×10^{2}	9.65×10^{-22}	4.35×10^{-22}	4.80×10^{2}	**3.56×10^{9}**	5.69×10^{8}	**7.15×10^{9}**	7.82×10^{8}	1.81×10^{7}	1.07×10^{9}	~0
293	3.10×10^{-21}	4.96×10^{-21}	1.26×10^{-18}	6.16×10^{2}	2.93×10^{-21}	1.33×10^{-21}	6.16×10^{2}	**3.37×10^{9}**	5.24×10^{8}	**6.66×10^{9}**	7.48×10^{8}	1.89×10^{7}	1.00×10^{9}	~0
298	1.02×10^{-20}	1.61×10^{-20}	3.70×10^{-18}	7.85×10^{2}	8.60×10^{-21}	3.94×10^{-21}	7.85×10^{2}	**3.21×10^{9}**	4.85×10^{8}	**6.24×10^{9}**	7.17×10^{8}	1.99×10^{7}	9.48×10^{8}	~0
303	3.22×10^{-20}	5.01×10^{-20}	1.05×10^{-17}	9.92×10^{2}	2.45×10^{-20}	1.13×10^{-20}	9.92×10^{2}	**3.05×10^{9}**	4.51×10^{8}	**5.86×10^{9}**	6.90×10^{8}	2.08×10^{7}	8.98×10^{8}	~0
308	9.81×10^{-20}	1.51×10^{-19}	2.87×10^{-17}	1.24×10^{3}	6.77×10^{-20}	3.14×10^{-20}	1.24×10^{3}	**2.92×10^{9}**	4.21×10^{8}	**5.52×10^{9}**	6.64×10^{8}	2.18×10^{7}	8.53×10^{8}	~0
313	2.88×10^{-19}	4.37×10^{-19}	7.60×10^{-17}	1.55×10^{3}	1.82×10^{-19}	8.50×10^{-20}	1.55×10^{3}	**2.79×10^{9}**	3.94×10^{8}	**5.21×10^{9}**	6.42×10^{8}	2.29×10^{7}	8.13×10^{8}	~0
318	8.20×10^{-19}	1.23×10^{-18}	1.95×10^{-16}	1.92×10^{3}	4.74×10^{-19}	2.24×10^{-19}	1.92×10^{3}	**2.68×10^{9}**	3.70×10^{8}	**4.94×10^{9}**	6.21×10^{8}	2.40×10^{7}	7.78×10^{8}	~0
323	2.26×10^{-18}	3.35×10^{-18}	4.88×10^{-16}	2.36×10^{3}	1.21×10^{-18}	5.72×10^{-19}	2.36×10^{3}	**2.58×10^{9}**	3.49×10^{8}	**4.69×10^{9}**	6.02×10^{8}	2.52×10^{7}	7.45×10^{8}	~0

T (K)	**H25-Abs**	**H26-Abs**	**H27-Abs**	**H28-Abs**	**H29-Abs**	**N9-Add**	**C12-Add**	**C15-Add**	**C16-Add**	**C17-Add**	**C18-Add**	**P5-Add**	**Overall**
253	1.36×10^{8}	1.19×10^{7}	1.02×10^{8}	1.43×10^{9}	4.09×10^{5}	8.42×10^{-3}	6.55×10^{8}	1.69×10^{9}	4.84×10^{9}	8.73×10^{8}	5.39×10^{6}	4.34×10^{-16}	3.29×10^{10}
258	1.29×10^{8}	1.25×10^{7}	9.81×10^{7}	1.30×10^{9}	4.29×10^{5}	1.26×10^{-2}	5.92×10^{8}	1.52×10^{9}	4.37×10^{9}	8.22×10^{8}	5.52×10^{6}	1.13×10^{-15}	2.99×10^{10}
263	1.23×10^{8}	1.32×10^{7}	9.45×10^{7}	1.19×10^{9}	4.51×10^{5}	1.84×10^{-2}	5.37×10^{8}	1.38×10^{9}	3.96×10^{9}	7.77×10^{8}	5.65×10^{6}	2.87×10^{-15}	2.73×10^{10}
268	1.18×10^{8}	1.39×10^{7}	9.14×10^{7}	1.09×10^{9}	4.77×10^{5}	2.67×10^{-2}	4.91×10^{8}	1.26×10^{9}	3.61×10^{9}	7.37×10^{8}	5.80×10^{6}	7.04×10^{-15}	2.51×10^{10}
273	1.13×10^{8}	1.47×10^{7}	8.87×10^{7}	1.01×10^{9}	5.05×10^{5}	3.83×10^{-2}	4.50×10^{8}	1.16×10^{9}	3.30×10^{9}	7.01×10^{8}	5.95×10^{6}	1.68×10^{-14}	2.31×10^{10}
278	1.09×10^{8}	1.55×10^{7}	8.64×10^{7}	9.37×10^{8}	5.36×10^{5}	5.41×10^{-2}	4.15×10^{8}	1.06×10^{9}	3.04×10^{9}	6.69×10^{8}	6.10×10^{6}	3.88×10^{-14}	2.14×10^{10}
283	1.05×10^{8}	1.64×10^{7}	8.45×10^{7}	8.75×10^{8}	5.70×10^{5}	7.56×10^{-2}	3.84×10^{8}	9.82×10^{8}	2.80×10^{9}	6.40×10^{8}	6.25×10^{6}	8.75×10^{-14}	2.00×10^{10}
288	1.02×10^{8}	1.73×10^{7}	8.28×10^{7}	8.21×10^{8}	6.08×10^{5}	1.05×10^{-1}	3.56×10^{8}	9.10×10^{8}	2.59×10^{9}	6.13×10^{8}	6.42×10^{6}	1.92×10^{-13}	1.86×10^{10}
293	9.96×10^{7}	1.83×10^{7}	8.14×10^{7}	7.74×10^{8}	6.49×10^{5}	1.43×10^{-1}	3.32×10^{8}	8.47×10^{8}	2.41×10^{9}	5.89×10^{8}	6.58×10^{6}	4.12×10^{-13}	1.75×10^{10}
298	9.72×10^{7}	1.94×10^{7}	8.02×10^{7}	7.32×10^{8}	6.94×10^{5}	1.94×10^{-1}	3.11×10^{8}	7.90×10^{8}	2.24×10^{9}	5.67×10^{8}	6.75×10^{6}	8.61×10^{-13}	1.65×10^{10}
303	9.52×10^{7}	2.05×10^{7}	7.92×10^{7}	6.95×10^{8}	7.43×10^{5}	2.60×10^{-1}	2.92×10^{8}	7.40×10^{8}	2.10×10^{9}	5.47×10^{8}	6.93×10^{6}	1.76×10^{-12}	1.55×10^{10}
308	9.34×10^{7}	2.17×10^{7}	7.84×10^{7}	6.62×10^{8}	7.97×10^{5}	3.46×10^{-1}	2.74×10^{8}	6.94×10^{8}	1.97×10^{9}	5.29×10^{8}	7.11×10^{6}	3.52×10^{-12}	1.47×10^{10}
313	9.19×10^{7}	2.30×10^{7}	7.77×10^{7}	6.33×10^{8}	8.55×10^{5}	4.56×10^{-1}	2.59×10^{8}	6.54×10^{8}	1.85×10^{9}	5.12×10^{8}	7.29×10^{6}	6.91×10^{-12}	1.40×10^{10}
318	9.05×10^{7}	2.43×10^{7}	7.72×10^{7}	6.07×10^{8}	9.18×10^{5}	5.97×10^{-1}	2.45×10^{8}	6.17×10^{8}	1.74×10^{9}	4.97×10^{8}	7.48×10^{6}	1.33×10^{-11}	1.33×10^{10}
323	8.94×10^{7}	2.57×10^{7}	7.68×10^{7}	5.83×10^{8}	9.86×10^{5}	7.74×10^{-1}	2.33×10^{8}	5.84×10^{8}	1.65×10^{9}	4.83×10^{8}	7.67×10^{6}	2.50×10^{-11}	1.27×10^{10}

(b) WATER														
T (K)	**Cl1-Abs**	**Cl2-Abs**	**Cl3-Abs**	**S4-Abs**	**$C13H_3$-Abs**	**$C14H_3$-Abs**	**S4-Abs**	**H19-Abs**	**H20-Abs**	**H21-Abs**	**H22-Abs**	**H23-Abs**	**H24-Abs**	**SET**
283	8.13×10^{-25}	1.35×10^{-23}	1.93×10^{-21}	1.60×10^{4}	4.03×10^{-21}	2.18×10^{-21}	8.07×10^{-5}	8.11×10^{7}	5.38×10^{7}	4.31×10^{7}	$\mathbf{1.10\times10^{8}}$	1.32×10^{7}	1.26×10^{7}	1.35×10^{-38}
288	2.96×10^{-24}	4.90×10^{-23}	6.51×10^{-21}	1.90×10^{4}	1.23×10^{-20}	6.38×10^{-21}	1.31×10^{-4}	8.22×10^{7}	5.39×10^{7}	4.35×10^{7}	$\mathbf{1.09\times10^{8}}$	1.42×10^{7}	1.30×10^{7}	1.10×10^{-37}
293	1.03×10^{-23}	1.70×10^{-22}	2.11×10^{-20}	2.25×10^{4}	3.64×10^{-20}	1.80×10^{-20}	2.11×10^{-4}	8.32×10^{7}	5.40×10^{7}	4.40×10^{7}	$\mathbf{1.08\times10^{8}}$	1.52×10^{7}	1.33×10^{7}	8.36×10^{-37}
298	3.45×10^{-23}	5.69×10^{-22}	6.57×10^{-20}	2.65×10^{4}	1.04×10^{-19}	4.92×10^{-20}	3.33×10^{-4}	8.43×10^{7}	5.41×10^{7}	4.44×10^{7}	$\mathbf{1.07\times10^{8}}$	1.64×10^{7}	1.37×10^{7}	5.93×10^{-36}
303	1.11×10^{-22}	1.83×10^{-21}	1.97×10^{-19}	3.10×10^{4}	2.87×10^{-19}	1.30×10^{-19}	5.18×10^{-4}	8.54×10^{7}	5.42×10^{7}	4.49×10^{7}	$\mathbf{1.07\times10^{8}}$	1.76×10^{7}	1.41×10^{7}	3.94×10^{-35}
308	3.44×10^{-22}	5.66×10^{-21}	5.72×10^{-19}	3.62×10^{4}	7.70×10^{-19}	3.36×10^{-19}	7.96×10^{-4}	8.65×10^{7}	5.44×10^{7}	4.54×10^{7}	$\mathbf{1.06\times10^{8}}$	1.88×10^{7}	1.45×10^{7}	2.46×10^{-34}
313	1.03×10^{-21}	1.69×10^{-20}	1.60×10^{-18}	4.20×10^{4}	2.00×10^{-18}	8.39×10^{-19}	1.21×10^{-3}	8.77×10^{7}	5.46×10^{7}	4.59×10^{7}	$\mathbf{1.05\times10^{8}}$	2.01×10^{7}	1.49×10^{7}	1.45×10^{-33}
318	2.98×10^{-21}	4.88×10^{-20}	4.35×10^{-18}	4.85×10^{4}	5.06×10^{-18}	2.04×10^{-18}	1.81×10^{-3}	8.89×10^{7}	5.48×10^{7}	4.65×10^{7}	$\mathbf{1.05\times10^{8}}$	2.15×10^{7}	1.53×10^{7}	8.10×10^{-33}
323	8.33×10^{-21}	1.36×10^{-19}	1.15×10^{-17}	5.59×10^{4}	1.25×10^{-17}	4.84×10^{-18}	2.67×10^{-3}	9.01×10^{7}	5.51×10^{7}	4.70×10^{7}	$\mathbf{1.04\times10^{8}}$	2.30×10^{7}	1.57×10^{7}	4.29×10^{-32}

T (K)	**H25-Abs**	**H26-Abs**	**H27-Abs**	**H28-Abs**	**H29-Abs**	**N9-Add**	**C12-Add**	**C15-Add**	**C16-Add**	**C17-Add**	**C18-Add**	**P5-Add**	**Overall**
283	1.61×10^{7}	9.54×10^{4}	1.18×10^{7}	$\mathbf{1.35\times10^{8}}$	9.16×10^{3}	8.08×10^{-8}	3.63×10^{4}	2.63×10^{4}	6.92×10^{4}	1.11×10^{4}	1.24×10^{4}	1.60×10^{-19}	4.76×10^{8}
288	1.61×10^{7}	1.05×10^{5}	1.17×10^{7}	$\mathbf{1.32\times10^{8}}$	9.92×10^{3}	1.39×10^{-7}	4.03×10^{4}	2.96×10^{4}	7.77×10^{4}	1.26×10^{4}	1.43×10^{4}	4.42×10^{-19}	4.76×10^{8}
293	1.60×10^{7}	1.16×10^{5}	1.17×10^{7}	$\mathbf{1.30\times10^{8}}$	1.08×10^{4}	2.34×10^{-7}	4.46×10^{4}	3.32×10^{4}	8.70×10^{4}	1.42×10^{4}	1.65×10^{4}	1.18×10^{-18}	4.76×10^{8}
298	1.60×10^{7}	1.27×10^{5}	1.17×10^{7}	$\mathbf{1.28\times10^{8}}$	1.17×10^{4}	3.88×10^{-7}	4.93×10^{4}	3.72×10^{4}	9.70×10^{4}	1.61×10^{4}	1.89×10^{4}	3.03×10^{-18}	4.76×10^{8}
303	1.60×10^{7}	1.40×10^{5}	1.17×10^{7}	$\mathbf{1.26\times10^{8}}$	1.28×10^{4}	6.33×10^{-7}	5.43×10^{4}	4.15×10^{4}	1.08×10^{5}	1.81×10^{4}	2.15×10^{4}	7.57×10^{-18}	4.77×10^{8}
308	1.60×10^{7}	1.53×10^{5}	1.17×10^{7}	$\mathbf{1.24\times10^{8}}$	1.40×10^{4}	1.02×10^{-6}	5.96×10^{4}	4.61×10^{4}	1.20×10^{5}	2.02×10^{4}	2.45×10^{4}	1.84×10^{-17}	4.78×10^{8}
313	1.61×10^{7}	1.68×10^{5}	1.17×10^{7}	$\mathbf{1.22\times10^{8}}$	1.54×10^{4}	1.61×10^{-6}	6.54×10^{4}	5.12×10^{4}	1.33×10^{5}	2.26×10^{4}	2.78×10^{4}	4.33×10^{-17}	4.79×10^{8}
318	1.61×10^{7}	1.83×10^{5}	1.17×10^{7}	$\mathbf{1.21\times10^{8}}$	1.69×10^{4}	2.51×10^{-6}	7.15×10^{4}	5.66×10^{4}	1.46×10^{5}	2.52×10^{4}	3.14×10^{4}	9.95×10^{-17}	4.81×10^{8}
323	1.62×10^{7}	2.00×10^{5}	1.18×10^{7}	$\mathbf{1.19\times10^{8}}$	1.86×10^{4}	3.87×10^{-6}	7.80×10^{4}	6.25×10^{4}	1.61×10^{5}	2.80×10^{4}	3.53×10^{4}	2.23×10^{-16}	4.83×10^{8}

Figure IV-7 presents the temperature-dependent apparent rate constants and the branching ratio Γ of the significant reactions in both gas (253-323 K) and water (283-323 K). In the gas phase (***Figure IV-7a***), all the rate constants decrease as the temperature rises. Notably, for critical reactions like H21-Abs, H19-Abs, and C16-Add, rate constants decrease by approximately fivefold over the 253-323 K temperature range.

The decline in the rate constant of the FHT reactions as temperature rises in the gas phase is linked to the destabilization of pre-reactive complexes at higher temperatures. In the RAF reactions, the potential back-decomposition of the energy-rich HO-aromatic adduct to initial reactants, generally involving a higher barrier than decomposition through C-H bond cleavage, might lead to reactions that are less competitive compared to the FHT reactions.

Both experimental and theoretical studies have reported these phenomena (Perry *et al.*, 1977; Uc *et al.*, 2008). Regarding the branching ratio, the proportions of H21-Abs and C16-Add channels decreased from 40 to 37% and from 15 to 13% at higher temperatures, respectively, while the H19-Abs channel saw a slight increase from 17.5 to 20% as the temperature increased.

Interestingly, FHT reactions become dominant in water. The rate constant of the other irrelevant reactions, such as addition reactions at C atoms of the pyridine ring (about 10^{3}-10^{4} M^{-1} s^{-1}), P-Add (10^{-20}-10^{-16} M^{-1} s^{-1}), N-add (10^{-8}-10^{-6} M^{-1} s^{-1}), and others, are not shown in ***Figure IV-7b*** due to its negligible contribution to the total reaction. Within the 283-323 K temperature range, the most predominant reactions are determined at H28-Abs (28-26%), H22-Abs (23-22%), and H19-Abs (17-19%) (***Figure IV-7b***). For the main channels, the rate constant decreases from 1.21×10^{8} to 1.07×10^{8} M^{-1} s^{-1} (H22) and from 1.55×10^{8} to 1.22×10^{8} M^{-1} s^{-1} (H28).

However, for other channels such as H19, H21, H23, H24, and H26, there is an upward trend with increasing temperature. This rising trend could be attributed to the increasing Eckart correction rate constant (k+Eck), which is sufficient to tolerate the decreasing equilibrium constant between the isolated reactants and the MRC (K_{eq}). This phenomenon occurs because of the changes in the ratios of K_{eq}, Eckart tunnelling-corrected rate constant (k+Eck), and thermal rate constant (k_T) at two extreme temperatures, 283 K and 323 K (***Table IV-3***). These findings align with our previous observations concerning metazachlor and phosmet insecticide (Dao *et al.*, 2023; K. Al Rawas *et al.*, 2023).

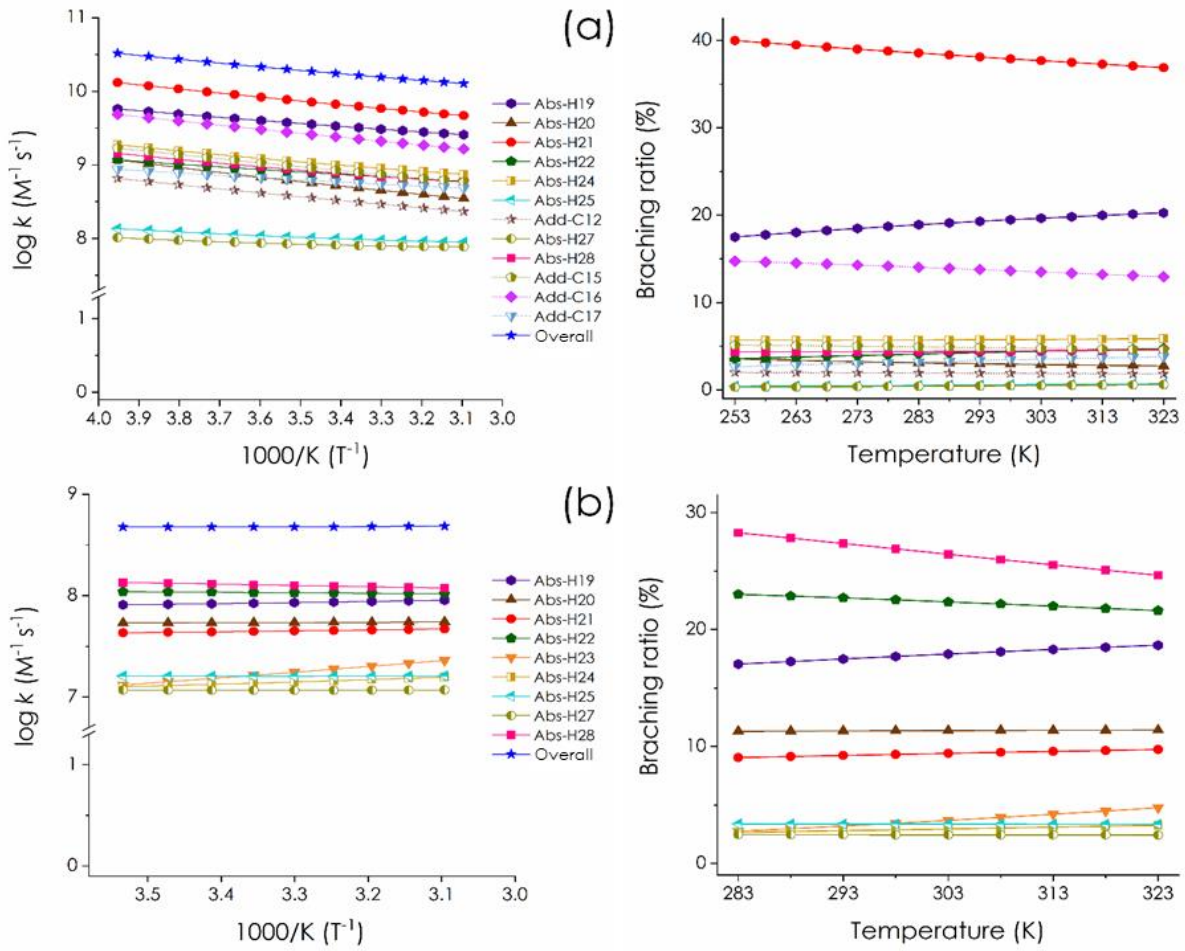

***Figure IV-7**: temperature-dependent apparent rate constants (log k) and branching ratio (Γ, %) of main reactions in (a) the gas phase in the range of 253-323 K and (b) water in the range of 283-323 K.*

***Table IV-3**: the ratios of the equilibration constant K_{eq}, Eckart-corrected rate constant (k+Eck) and thermal rate constant (k_T) at 283 and 323 K of the H-Abs reaction in water.*

FHT channel	K_{eq}(283K)/K_{eq}(323K)	*k*+Eck(283K)/*k*+Eck(323K)	k_T(283K)/k_T(323K)
H19	1.64	0.57	0.93
H20	1.72	0.58	1.00
H21	1.49	0.62	0.93
H22	1.74	0.63	1.09
H23	1.18	0.48	0.57
H24	1.62	0.5	0.81
H25	1.92	0.52	1.00
H26	1.25	0.38	0.48
H27	1.86	0.54	1.00
H28	2.11	0.57	1.19
H29	2.27	0.22	0.49

IV.3.4. Lifetime of CPF in the presence of HO• radicals

The lifetime of CPF in the presence of HO• radicals was also examined across the temperature range of 283-323 K, and with different concentrations of HO• (***Table IV-4***). In the gas phase, [HO•] is fixed as 2.59×10^{-15} M (Prinn *et al.*, 2005), while a lower concentration (10^{-18} to 10^{-15} M) can exist in water as reported in the literature (Burns *et al.*, 2012; Collins and Kimball, 1949). As a result, CPF may be easily decomposed in the gas phase within a short time range 1.93×10^{4} to 3.04×10^{4} s (5 to 8 hours), based on the temperature. On the contrary, its persistence in natural water is much longer, ranging from 2.07×10^{6} to 2.10×10^{9} s, which corresponds from 24 days to 66 years. It is assumed that CPF is more persistent in the natural water environment than in the gas phase.

Table IV-4*: the lifetime τ (s) of CPF in the gas phase and natural water as a function of HO• concentrations and temperature (283-323 K).*

T (K)	**283**	**288**	**293**	**298**	**303**	**308**	**313**	**318**	**323**
GAS									
$k_{overall}$, M^{-1} s^{-1}	2.00×10^{10}	1.86×10^{10}	1.75×10^{10}	1.65×10^{10}	1.55×10^{10}	1.47×10^{10}	1.40×10^{10}	1.33×10^{10}	1.27×10^{10}
[HO•], M					**τ_{gas}, s**				
2.59×10^{-15}	1.93×10^{4}	2.07×10^{4}	2.21×10^{4}	2.34×10^{4}	2.48×10^{4}	2.62×10^{4}	2.76×10^{4}	2.90×10^{4}	3.04×10^{4}
WATER									
$k_{overall}$, M^{-1} s^{-1}	4.76×10^{8}	4.76×10^{8}	4.76×10^{8}	4.76×10^{8}	4.77×10^{8}	4.78×10^{8}	4.79×10^{8}	4.81×10^{8}	4.83×10^{8}
[HO•], M					**τ_{w}, s**				
1×10^{-15}	2.10×10^{6}	2.10×10^{6}	2.10×10^{6}	2.10×10^{6}	2.10×10^{6}	2.09×10^{6}	2.09×10^{6}	2.08×10^{6}	2.07×10^{6}
1×10^{-16}	2.10×10^{7}	2.10×10^{7}	2.10×10^{7}	2.10×10^{7}	2.10×10^{7}	2.09×10^{7}	2.09×10^{7}	2.08×10^{7}	2.07×10^{7}
1×10^{-17}	2.10×10^{8}	2.10×10^{8}	2.10×10^{8}	2.10×10^{8}	2.10×10^{8}	2.09×10^{8}	2.09×10^{8}	2.08×10^{8}	2.07×10^{8}
1×10^{-18}	2.10×10^{9}	2.10×10^{9}	2.10×10^{9}	2.10×10^{9}	2.10×10^{9}	2.09×10^{9}	2.09×10^{9}	2.08×10^{9}	2.07×10^{9}

IV.3.5. Further reactions of main-radical products with other oxidizing agents

The primary radical products resulting from the degradation of CPF by HO• were identified earlier, as the H-abstraction radical products indicated as RAD19 and RAD21 in the gas phase and RAD22 and RAD28 in water. Here, we elaborate the reactions of these radicals when exposed to other oxidizing agents like triplet oxygen ($^3O_2$) and radicals such as HO•, •NO, and •NO_2. After observing that the results for the reactions occurring in both gas (***Figure IV-8*****)** and water (***Figure IV-9***) phases are similar, we chose to discuss the reactions in water as an illustrative example.

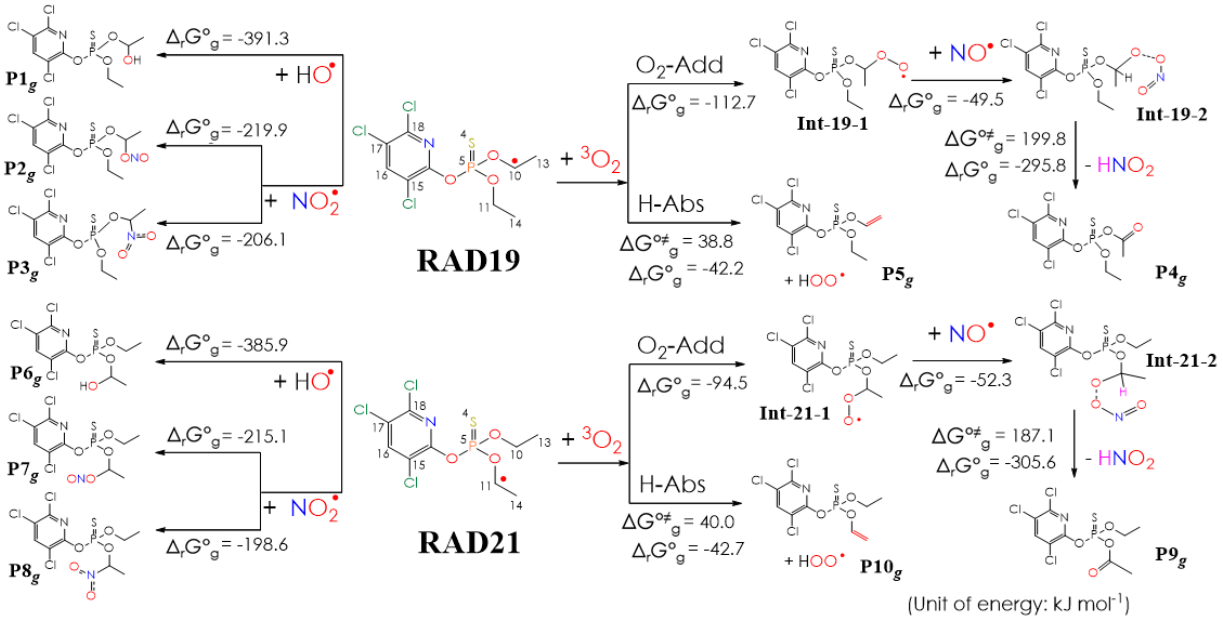

***Figure IV-8**: standard Gibbs free reaction energies ($\Delta_rG°$) and standard Gibbs free activation energy ($\Delta G°^{\neq}$) calculated for further reactions of main radical products with other oxidizing agents in gas phase (subscript g for gas) at 298 K.*

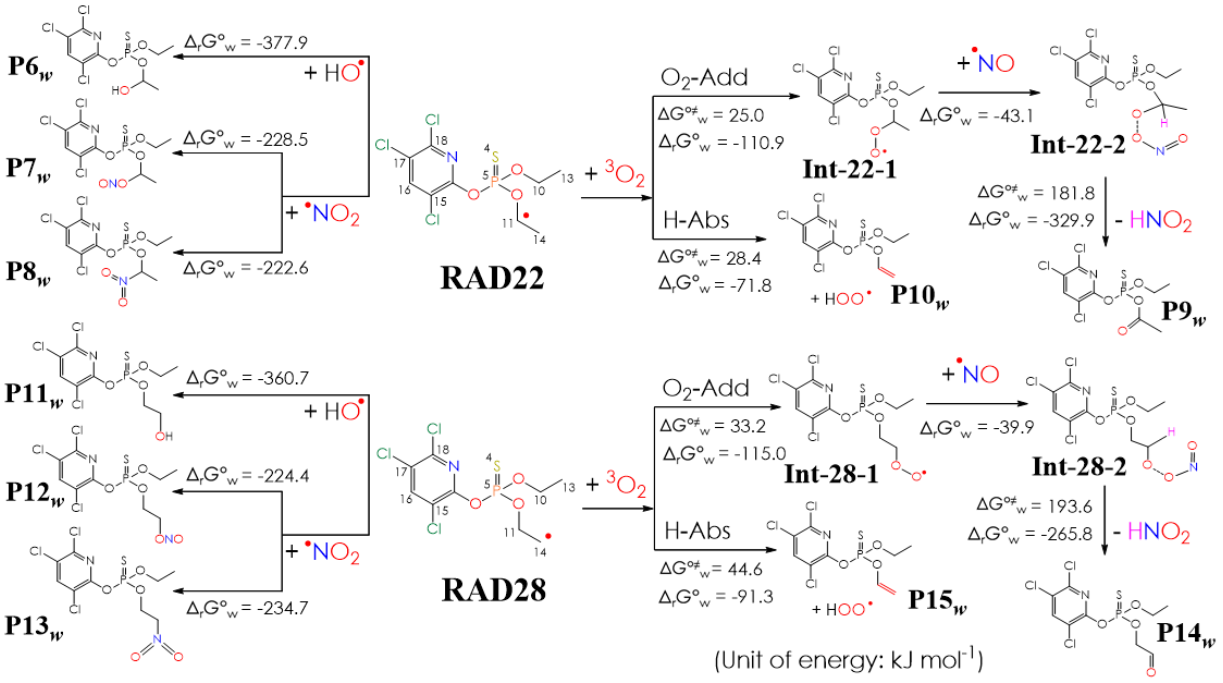

***Figure IV-9**: standard Gibbs free reaction energies ($\Delta_rG°$) and standard Gibbs free activation energy ($\Delta G°^{\neq}$) of subsequent reactions of RAD22 and RAD28 with other oxidizing agents in water (subscript w for water) at 298 K.*

The subsequent addition of HO$^{\bullet}$ at C11 of RAD22 or C14 of RAD28, generate two alcohol derivatives, **P6**$_w$ and **P11**$_w$, with very low $\Delta_r G°$ values of -377.9 and -360.7 kJ mol^{-1}, respectively. Regarding $^{\bullet}NO_2$-addition, this reaction can proceed in two directions: O-addition or N-addition, yielding **P7**$_w$ and **P8**$_w$ when reacting with RAD22, and **P12**$_w$ and **P13**$_w$ when reacting with RAD28.

The $\Delta_r G°$ values for these products are much higher compared to those of the HO$^{\bullet}$-addition products, ranging from -222.6 to -234.7 kJ mol^{-1}. Similarly, the reaction between $^3O_2$ and either RAD22 or RAD28 can proceed through two pathways. In the first pathway, $^3O_2$ addition to C11 of RAD22 yields a new radical, **Int-22-1**, followed by $^{\bullet}$NO addition to generate intermediate **Int-22-2**, which subsequently transforms into **P9**$_w$ and HNO_2. In the second pathway, the H-abstraction of RAD22 by $^3O_2$ leads to the formation of **P10**$_w$ and HOO$^{\bullet}$. Similar reactions for RAD28 at C14 form **P14**$_w$ and **P15**$_w$.

It can be observed that all reactions involving other oxidizing agents have highly negative $\Delta_r G°$ values, indicating that all reactions are spontaneous and favourable. The $\Delta G°^{\neq}$ values, which are determined for the reactions between a molecule and a radical, range from 28.4 to 44. kJ mol^{-1} for the H-abstraction pathways, and from 25.0 to 33.2 kJ mol^{-1} for the O_2-addition pathways. However, for the final step leading to the formation of **P9**$_w$ and **P14**$_w$ (HNO_2 dissociation), a considerably higher $\Delta G°^{\neq}$ (181.8 - 193.6 kJ mol^{-1}) is observed, suggesting that these steps may occur at a slower rate.

IV.3.6. Ecotoxicity, bioaccumulation, developmental toxicity, and mutagenicity

Table IV-5 represents the aquatic toxicity and the bioconcentration factor (BCF), bioaccumulation factor (BAF), developmental toxicity, and mutagenicity of CPF and its degradation products formed in water. The acute and chronic toxicity levels were estimated for fish, daphnia, and green algae. CPF shows an acute toxicity levels of 0.47 and 0.35 mg L^{-1} for fish and daphnia, and 0.86 mg L^{-1} for green algae, indicating highly toxic levels. In addition, the chronic toxicity of CPF shows that it is very toxic to fish and daphnia (ChV 0.06 and 0.08 mg L^{-1}) and toxic to green algae (ChV 0.43 mg L^{-1}). The products of the NO$^{\bullet}$-addition reaction, *i.e.*, **P7**$_w$ and **P12**$_w$, are also very toxic to all studied species. Despite having the lowest $\Delta_r G°$, **P6**$_w$ and **P11**$_w$ products of the HO$^{\bullet}$-addition reaction are less toxic to fish and green algae and only toxic to daphnia (LC_{50} from 6.65 to 7.69 mg L^{-1}). Moreover, the other products are considered toxic to almost all species.

***Table IV-5**: aquatic acute and chronic toxicity, bioconcentration (BCF, L/kg wet-wt), bioaccumulation (BAF, L/kg wet-wt), developmental toxicity, and mutagenicity of CPF and its degradation products **P6$_w$-P15$_w$**. Acute and chronic toxicities (mg L^{-1}) are coloured green, yellow, and red for harmful, toxic, and very toxic properties.*

Compounds		**CPF**	**P6$_w$**	**P7$_w$**	**P8$_w$**	**P9$_w$**	**P10$_w$**	**P11$_w$**	**P12$_w$**	**P13$_w$**	**P14$_w$**	**P15$_w$**
Log K_{ow}		5.108	3.570	5.084	4.165	3.667	4.972	3.643	5.157	4.239	3.619	4.972
Acute toxicity[a]	Fish (LC_{50})	0.47	11.72	0.72	3.69	9.54	0.61	10.07	0.64	3.17	3.74	0.61
	Daphnia (LC_{50})	0.35	7.69	0.12	2.56	6.32	0.46	6.65	0.11	2.21	2.92	0.46
	Green Algae (EC_{50})	0.86	10.43	0.05	4.36	8.89	1.06	9.28	0.04	3.88	2.06	1.06
Chronic toxicity[b]	Fish (ChV)	0.06	1.36	0.01	0.46	1.12	0.08	1.18	0.01	0.40	0.24	0.08
	Daphnia (ChV)	0.08	1.12	0.01	0.44	0.95	0.10	0.99	0.01	0.38	0.04	0.10
	Green Algae (ChV)	0.43	3.77	0.02	1.78	3.28	0.51	3.41	0.02	1.61	1.05	0.51
BCF (L/kg wet-wt)		1090	58.5	1050	260	122	886	65.4	1170	291	113	886
BAF (L/kg wet-wt)		2340	113	429	205	140	871	122	447	217	184	871
Developmental toxicity		0.59	0.84	0.70	0.69	0.72	0.63	0.72	0.67	0.57	0.65	0.63
Mutagenicity		-0.10	-0.07	-0.07	-0.07	-0.08	-0.10	-0.09	-0.08	-0.03	-0.09	-0.10

[a] Criteria set by the European Union (described in Annex VI of Directive 67/548/EEC); [b] criteria set by the Chinese hazard evaluation guidelines for new chemical substances (HJ/T 154-2004)

Next, the BCF is calculated by the ratio of the pesticide residue in an organism's tissue over the pesticide contaminant in the environment. Conversely, the BAF represents the ratio of the pesticide tissue concentrations relative to the environmental pesticide concentrations. As a result, all BCF and BAF values exceed 1, signifying that the pesticide concentration within the organism surpasses that of the environment, leading to a greater accumulation of the pesticide within the organism compared to that in the environment.

Chlorpyrifos, **P7$_w$**, and **P12$_w$** showed the highest BCF values ranging from 1050 to 1170 L/kg wet-wet, whereas, and as expected, the lowest BCF values are found for **P6$_w$** and **P11$_w$**, of 58.5 and 65.4 L/kg wet-wt respectively. Moreover, chlorpyrifos has much higher BAF value (2340 L/kg wet-wt) than its degradation products, with several hundred L/kg wet-wt values. Fortunately, the BAF values of all these products range from 871 to 113 L/kg wet-wt, which are lower than the bioaccumulative threshold. The developmental toxicity values (from 0.57 to 0.84) indicate that CPF and its degradation products are considered potential developmental toxicants. However, the mutagenicity values (from -0.03 to -0.10) estimate that all studied compounds are non-mutagenic.

IV.3.7. Cholinesterase inhibition

Neurotoxicity of CPF and its degradants are studied *via* cholinesterase inhibition activities towards two human's origin enzyme structures, acetylcholinesterases AChE (PDB ID: 4EY7) and butyrylcholinesterase BChE (PDB ID 1P0M). Molecular interaction between CPF and its degradation products in water, **P6$_w$-P15$_w$**, with AChE and BChE, are first investigated by

docking study. Binding energy, inhibition constant, and the essential H-bond interactions are resumed in ***Table IV-6***.

Table IV-6*: binding energy (kJ mol^{-1}) between the CPF and its degradation products to AChE and BChE enzymes, calculated by Autodock4, along with its key residues interacting (conventional and unconventional H-bonds).*

Protein	**Cpd**	**E binding (kJ mol^{-1})**	**K_i (298.15 K)**	**H-bonding**
AChE	CPF	-30.25	4.99 µM	ASP74, TYR124, PRO88
	P6w	-31.88	2.62 µM	ASP74, TYR124, TRP86, PRO88, GLY121
	P7w	**-37.78**	241.61 nM	ASP74, TYR124, TYR337, THR83, PRO88, GLY121
	P8w	-31.84	2.66 µM	GLY121, GLY122, ALA204
	P9w	-33.22	1.51 µM	TYR124, TYR337, THR83, TRP86, PRO88
	P10w	-31.76	2.74 µM	SER293, PHE295, ARG296, TYR341
	P11w	-30.33	4.86 µM	GLY122, TYR124, SER203, TRP86, GLY121
	P12w	**-35.86**	526.07 nM	SER293, PHE295, TYR124
	P13w	-32.97	1.68 µM	GLY121, GLY122, TYR124, ALA204, PRO88
	P14w	-30.63	4.33 µM	TYR124, TYR337, TRP86, PRO88, PHE338
	P15w	-31.05	3.65 µM	TYR124, TYR337, TYR341
BChE	CPF	-30.21	5.10 µM	GLY117, SER198
	P6w	-31.92	2.56 µM	TYR128, GLU197, SER198, GLY439
	P7w	-33.81	1.19 µM	GLY121, SER198, HIS438, GLY439
	P8w	**-34.94**	759.30 nM	GLU197, SER198
	P9w	-31.42	3.11 µM	GLY117, SER198, GLU197, GLY439
	P10w	-30.25	5.03 µM	SER198, GLY439
	P11w	-29.12	7.92 µM	TYR128, HIS438, GLY439
	P12w	-30.96	3.74 µM	ASN70, ASN83, THR120
	P13w	**-34.48**	907.82 nM	TYR128, SER198, THR120, HIS438
	P14w	-29.92	5.77 µM	SER198, GLY115, TYR128, GLY439
	P15w	-30.75	4.10 µM	SER198, GLY439
AChE	**E20 redock**	**-47.40**	4.97 nM	PHE295

As one can see, the binding energy of the degradant products is all higher than that of CPF. Unsurprisingly, the $^{\bullet}NO_2$-addition primary products form the most stable complexes with the studied cholinesterase enzymes. The highest binding energy in the case of acetylcholinesterase is found for N-addition products, **P7**$_w$, and **P12**$_w$, while for BChE, O-addition products, **P8**$_w$ and **P13**$_w$ form the most stable complexes. The binding scores are estimated at -37.78, -34.94, -35.86, and -34.48 kJ mol^{-1} for **P7**$_w$, **P8**$_w$, **P12**$_w$, and **P13**$_w$, respectively. In the best cases, the inhibition constant is lowered to 241 (**P7**$_w$) or 526 nM (**P12**$_w$). To further study the ligand-protein interactions and the stability of the complexes, we conducted the molecular dynamic (MD) simulation for the best docking cases, specifically **P7**$_w$ and **P12**$_w$ with AChE and **P8**$_w$ and **P13**$_w$ with BChE. The time evolution of electrostatic and van-der-Waals (vdW) interactions of all studied complexes are presented in ***Figure IV-10***.

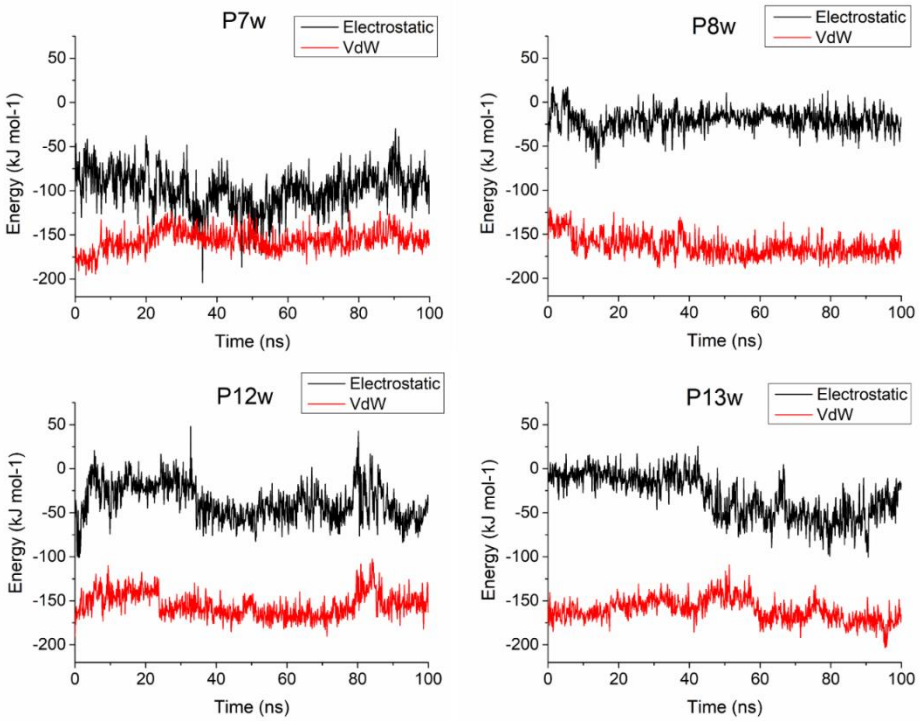

***Figure IV-10**: electrostatic and van-der-Waals (vdW) interaction energies of the studied complexes in a 100 ns time-frame.*

The root means square fluctuation (RMSF) of the residues in protein structures is displayed in ***Figure IV-11***. The root means square deviation (RMSD) analysis of the ligand and the backbone in each complex is presented in ***Figure IV-12***, indicating that the protein structures, as well as the complexes, are stabilized over a 100 ns time scale. We obtain the most stable complex with **P7**$_w$ (***Figure IV-10***), similar to docking results. The vdW energy is about -150 kJ mol^{-1} in all systems, while the electrostatic in **P7**$_w$ is significantly lower than the others. Indeed, the non-bonded interaction between **P7**$_w$ and AChE enzyme is stabilized by both electrostatic and vdW interaction, with values of -99.97 ± 20.76 and -156.65 ± 11.47 kJ mol^{-1}, respectively. This result also indicates that the vdW interaction is more important than the electrostatic one in the binding mechanism.

However, similar results are found for **P8**$_w$, **P12**$_w$, and **P13**$_w$, with less contribution of electrostatic interaction. Side-chain contacts between **P7**$_w$ and AChE are mainly found with TYR72, TRP86, GLY122, TYR124, SER125, GLY126, PHE 338, and TYR341 residues. Furthermore, the stable conformation of the complex also relies on strong interaction between the ligand and the protein, *i.e.*, hydrogen bonding. We observe a stable number of three H-bonds over the 100 ns time frame for **P7**$_w$ (***Figure IV-13***), which are mainly formed between the O atoms of **P7**$_w$ and the H of TYR124 (54.4%, which is the number of hydrogen bond/number of the snapshot), ARG296 (31.6%), and PHE295 (13.9%) residues. A similar type of H-bonds is observed with **P12**$_w$, although the number of H-bonds reduces to 2. In the case of BChE, O and N atoms of **P13**$_w$ and **P8**$_w$ can form contacts with H atoms of THR120 and

SER287 residues. However, considering the number of H-bonds and the non-bonded energies of the complexes, we can conclude that **P8$_w$**, **P12$_w$**, and **P13$_w$** are much less stable than **P7$_w$**. Therefore, the **P7$_w$** might be the riskiest degradant as an acetylcholinesterase inhibitor. Finally, the stereo view of **P7$_w$** in the active pocket of the AChE enzyme, taken from the snapshot at 92.3 ns, is given in ***Figure IV-14*** for illustration.

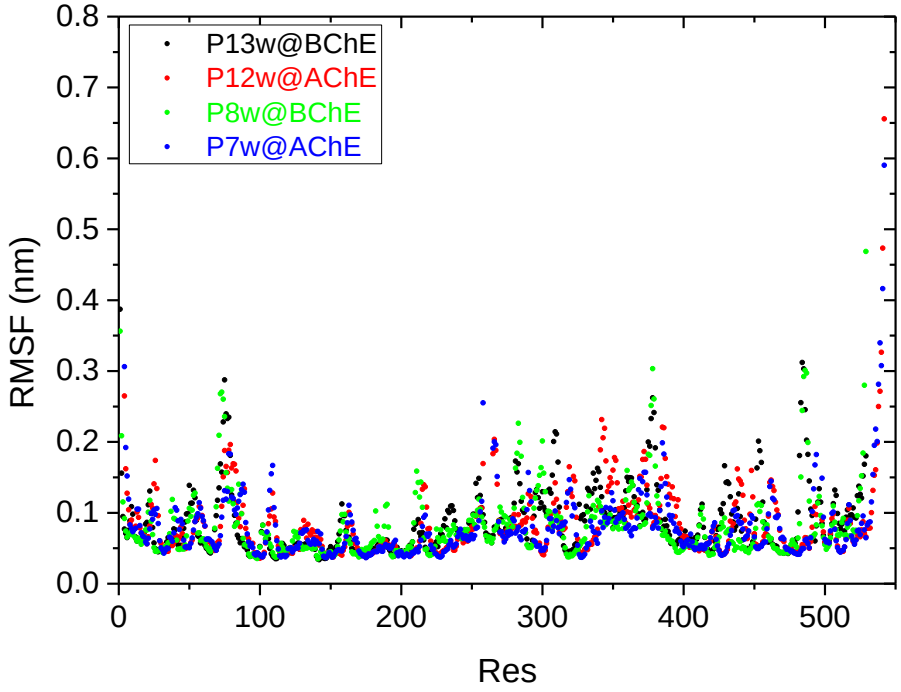

***Figure IV-11**: root mean square fluctuation (RMSF) of residues in studied cholinesterase enzymes during the MD simulation.*

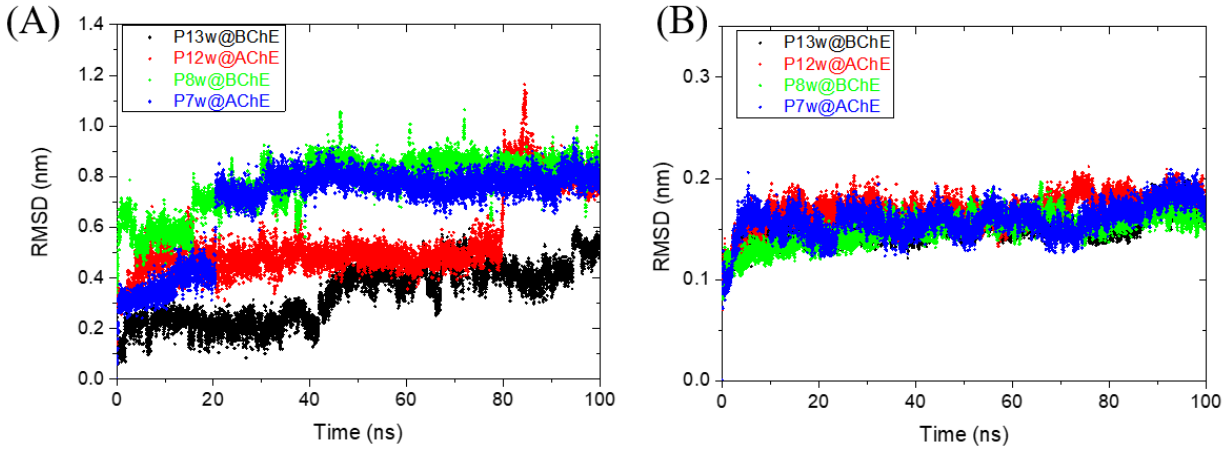

***Figure IV-12**: root mean square deviation (RMSD, nm) of (A) the ligand, and (B) the backbone of the complexes over a 100 ns time frame.*

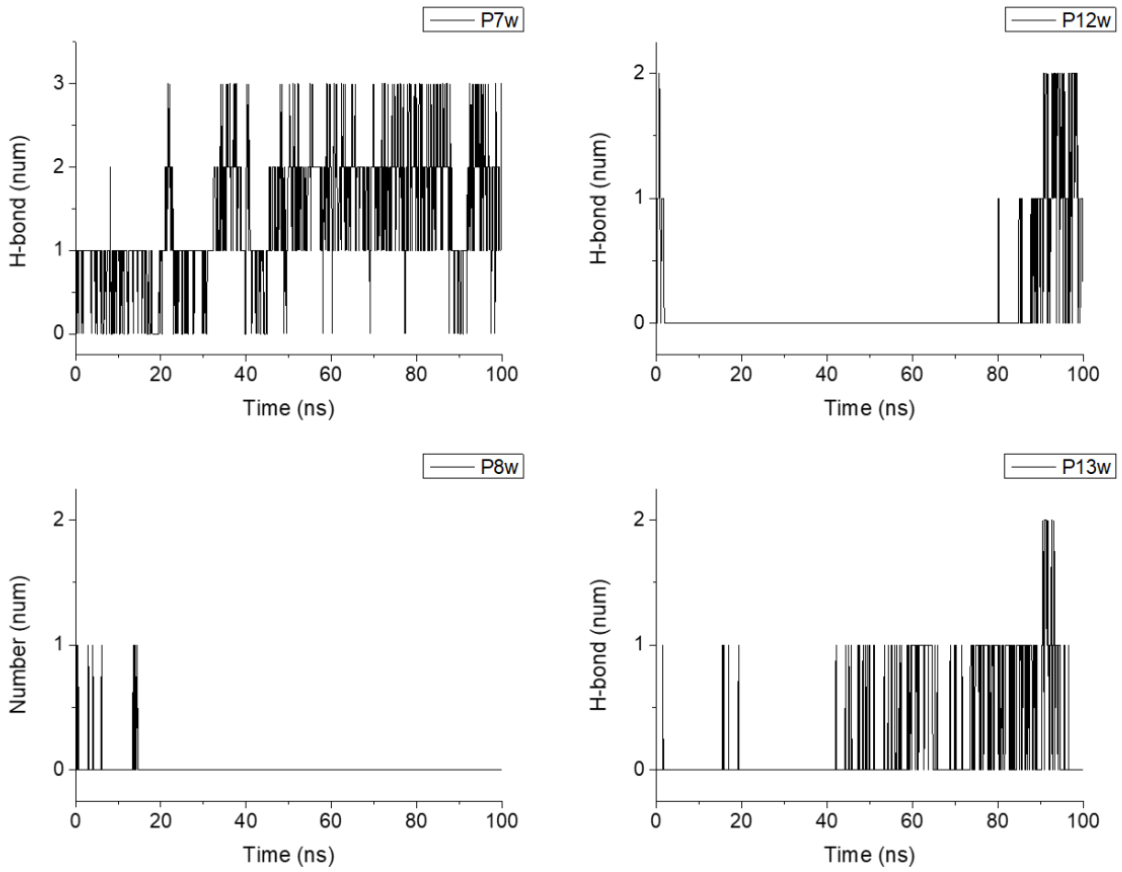

***Figure IV-13**: number of H-bonds between the cholinesterases and corresponding degradants.*

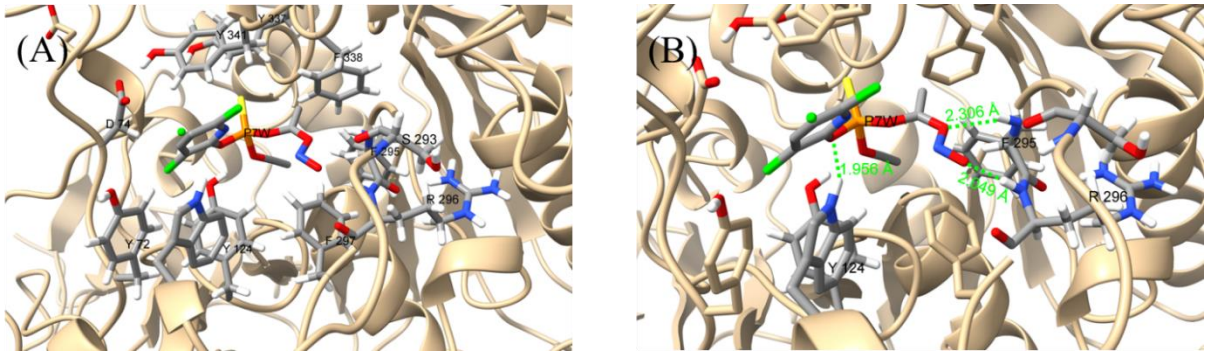

***Figure IV-14**: stereo view of the complex of $P7_w$ in the active pocket of AChE at 92.3 ns snapshot with (A) important side-chain contacts, and (B) H-bond interactions.*

IV.4. Conclusions

In summary, a theoretical study was made on the oxidation of chlorpyrifos pesticide initiated by $HO^{\bullet}$ radicals in the gas phase and water, covering various aspects such as thermodynamics, mechanisms, kinetics, ecotoxicity, and cholinesterase inhibition of the degradation products.

The oxidation of CPF by $HO^{\bullet}$ involves conventional mechanisms such as H-, S-, Cl-, and CH_3-abstraction, $HO^{\bullet}$-addition, and single electron transfer.

The most favourable H-abstraction pathways were observed at the methyl groups (H19 and H21 in gas, and H28 and H22 in water), with overall rate constant of reactions at 298 K being 1.65×10^{10} and 4.76×10^{8} M^{-1} s^{-1} in the gas phase and water, respectively. Moreover, the apparent rate constant decreases five times when the temperature raised from 253 to 323 K in the gas phase, while almost no change was observed in water within the 283-323 K range.

CPF has a lifetime of approximately 5-8 hours (283-323 K) in the gas phase, but it could stably exist in natural water for up to 66 years at low temperatures and low [$HO^{\bullet}$].

The further reactions of the main channel products with other oxidizing agents (*i.e.*, $^3O_2$, $HO^{\bullet}$, $^{\bullet}NO$, $^{\bullet}NO_2$) lead to primary possible neutral products **P1$_g$-P10$_g$** (in the gas phase) and **P6$_w$-P15$_w$** (in water). The ecotoxicity of CPF and its degradation products **P6$_w$-P15$_w$** was studied toward fish, daphnia, and green algae. According to the acute and chronic toxicity values, the most toxic products were **P7$_w$** and **P12$_w$** and the parent CPF molecule.

Finally, docking and molecular dynamics studies suggest that **P7$_w$** is the most potent acetylcholinesterase inhibitor; H-bonds are found between H atoms of TYR124, ARG296, and PHE295 (AChE) and O atoms of **P7$_w$**.

The results of this work proved that the theoretical study is a valuable approach in which it can provide a detailed understanding of the mechanisms and the kinetics of the degradation process of CPF in the environments that contain $HO^{\bullet}$ radicals. Understanding this oxidation process is helpful in devising effective strategies for removing pesticides in wastewater treatment conditions of AOPs. Additionally, it serves as an important tool for studying the toxicity of the degradation by-products, especially those that may go undetected due to limitations in detection capabilities of the existing instruments.

IV.5. References

Abraham, M., Alekseenko, A., Bergh, C., Blau, C., Briand, E., Doijade, M., Fleischmann, S., Gapsys, V., Garg, G., Gorelov, S., Gouaillardet, G., Gray, A., Irrgang, M.E., Jalalypour, F., Jordan, J., Junghans, C., Kanduri, P., Keller, S., Kutzner, C., Lemkul, J.A., Lundborg, M., Merz, P., Miletić, V., Morozov, D., Páll, S., Schulz, R., Shirts, M., Shvetsov, A., Soproni, B., Spoel, D. van der, Turner, P., Uphoff, C., Villa, A., Wingbermühle, S., Zhmurov, A., Bauer, P., Hess, B., Lindahl, E., 2023. GROMACS 2023 Manual. https://doi.org/10.5281/zenodo.7588711

Amitai, G., Moorad, D., Adani, R., Doctor, B.P., 1998. Inhibition of acetylcholinesterase and butyrylcholinesterase by chlorpyrifos-oxon. Biochemical Pharmacology 56, 293–299. https://doi.org/10.1016/s0006-2952(98)00035-5

Bootharaju, M.S., Pradeep, T., 2012. Understanding the Degradation Pathway of the Pesticide, Chlorpyrifos by Noble Metal Nanoparticles. Langmuir 28, 2671–2679. https://doi.org/10.1021/la2050515

Burke, R.D., Todd, S.W., Lumsden, E., Mullins, R.J., Mamczarz, J., Fawcett, W.P., Gullapalli, R.P., Randall, W.R., Pereira, E.F.R., Albuquerque, E.X., 2017. Developmental neurotoxicity of the organophosphorus insecticide chlorpyrifos: from clinical findings to preclinical models and potential mechanisms. Journal of Neurochemistry 142, 162–177. https://doi.org/10.1111/jnc.14077

Burns, J.M., Cooper, W.J., Ferry, J.L., King, D.W., DiMento, B.P., McNeill, K., Miller, C.J., Miller, W.L., Peake, B.M., Rusak, S.A., Rose, A.L., Waite, T.D., 2012. Methods for reactive oxygen species (ROS) detection in aqueous environments. Aquatic Sciences 74, 683–734. https://doi.org/10.1007/s00027-012-0251-x

Bussi, G., Donadio, D., Parrinello, M., 2007. Canonical sampling through velocity rescaling. Journal of Chemical Physics 126, 014101. https://doi.org/10.1063/1.2408420

Chiu, K.-C., Sisca, F., Ying, J.-H., Tsai, W.-J., Hsieh, W.-S., Chen, P.-C., Liu, C.-Y., 2021. Prenatal chlorpyrifos exposure in association with PPARγ H3K4me3 and DNA methylation levels and child development. Environmental Pollution 274, 116511. https://doi.org/10.1016/j.envpol.2021.116511

Collins, F.C., Kimball, G.E., 1949. Diffusion-controlled reaction rates. Journal of Colloid Science 4, 425–437. https://doi.org/10.1016/0095-8522(49)90023-9

Cui, Y., Guo, J., Xu, B., Chen, Z., 2006. Binding of chlorpyrifos and cypermethrin to blood proteins. Pesticide Biochemistry and Physiology 85, 110–114. https://doi.org/10.1016/j.pestbp.2005.11.004

da Silva, F.D., Nogara, P.A., Braga, M.M., Piccoli, B.C., Rocha, J.B.T., 2018. Molecular docking analysis of acetylcholinesterase corroborates the protective effect of pralidoxime against chlorpyrifos-induced behavioral and neurochemical impairments in *Nauphoeta cinerea*. Computational Toxicology 8, 25–33. https://doi.org/10.1016/j.comtox.2018.07.003

Dao, D.Q., Taamalli, S., Louis, F., Kdouh, D., Srour, Z., Ngo, T.C., Truong, D.H., Fèvre-Nollet, V., Ribaucour, M., El Bakali, A., Černušák, I., 2023. Hydroxyl radical-initiated decomposition of metazachlor herbicide in the gaseous and aqueous phases: Mechanism, kinetics, and toxicity evaluation. Chemosphere 312, 137234. https://doi.org/10.1016/j.chemosphere.2022.137234

Fiser, A., Do, R.K., Sali, A., 2000. Modeling of loops in protein structures. Protein Sci 9, 1753–1773. https://doi.org/10.1110/ps.9.9.1753

Fiser, A., Sali, A., 2003. ModLoop: automated modeling of loops in protein structures. Bioinformatics 19, 2500–2501. https://doi.org/10.1093/bioinformatics/btg362

Giesy, J.P., Solomon, K.R. (Eds.), 2014. Ecological Risk Assessment for Chlorpyrifos in Terrestrial and Aquatic Systems in the United States, Reviews of Environmental Contamination and Toxicology. Springer International Publishing, Cham. https://doi.org/10.1007/978-3-319-03865-0

Hazarika, J., Ganguly, M., Borgohain, G., Sarma, S., Bhuyan, P., Mahanta, R., 2022. Disruption of androgen receptor signaling by chlorpyrifos (CPF) and its environmental degradation products: a structural insight. Journal of Biomolecular Structure and Dynamics 40, 6027–6038. https://doi.org/10.1080/07391102.2021.1875885

Hazarika, J., Ganguly, M., Mahanta, R., 2020. A computational insight into the molecular interactions of chlorpyrifos and its degradation products with the human progesterone

receptor leading to endocrine disruption. Journal of Applied Toxicology 40, 434–443. https://doi.org/10.1002/jat.3916
He, X., Tu, Y., Song, Y., Yang, G., You, M., 2022. The relationship between pesticide exposure during critical neurodevelopment and autism spectrum disorder: A narrative review. Environmental Research 203, 111902. https://doi.org/10.1016/j.envres.2021.111902
Huang, M., Yu, J., Li, B., Deng, C., Wang, L., Wu, W., Dong, L., Zhang, F., Fan, M., 2015. Intergrowth and coexistence effects of TiO2–SnO2 nanocomposite with excellent photocatalytic activity. Journal of Alloys and Compounds 629. https://doi.org/10.1016/j.jallcom.2014.11.225
Huang, Y., Zhang, W., Pang, S., Chen, J., Bhatt, P., Mishra, S., Chen, S., 2021. Insights into the microbial degradation and catalytic mechanisms of chlorpyrifos. Environmental Research 194, 110660. https://doi.org/10.1016/j.envres.2020.110660
Jorgensen, W.L., Chandrasekhar, J., Madura, J.D., Impey, R.W., Klein, M.L., 1983. Comparison of simple potential functions for simulating liquid water. The Journal of Chemical Physics 79, 926–935. https://doi.org/10.1063/1.445869
Kim, H.-H., Lim, Y.-W., Yang, J.-Y., Shin, D.-C., Ham, H.-S., Choi, B.-S., Lee, J.-Y., 2013. Health risk assessment of exposure to chlorpyrifos and dichlorvos in children at childcare facilities. Science of the Total Environment 444, 441–450. https://doi.org/10.1016/j.scitotenv.2012.11.102
Lasagna, M., Ventura, C., Hielpos, M.S., Mardirosian, M.N., Martín, G., Miret, N., Randi, A., Núñez, M., Cocca, C., 2022. Endocrine disruptor chlorpyrifos promotes migration, invasion, and stemness phenotype in 3D cultures of breast cancer cells and induces a wide range of pathways involved in cancer progression. Environmental Research 204, 111989. https://doi.org/10.1016/j.envres.2021.111989
Lindorff-Larsen, K., Piana, S., Palmo, K., Maragakis, P., Klepeis, J.L., Dror, R.O., Shaw, D.E., 2010. Improved side-chain torsion potentials for the Amber ff99SB protein force field. Proteins 78, 1950–1958. https://doi.org/10.1002/prot.22711
Malakootian, M., Shahesmaeili, A., Faraji, M., Amiri, H., Silva Martinez, S., 2020. Advanced oxidation processes for the removal of organophosphorus pesticides in aqueous matrices: A systematic review and meta-analysis. Process Safety and Environmental Protection 134, 292–307. https://doi.org/10.1016/j.psep.2019.12.004
McKee, M.L., 2003. Comparison of Gas-Phase and Solution-Phase Reactions of Dimethyl Sulfide and 2-(Methylthio)ethanol with Hydroxyl Radical. Journal of Physical Chemistry A 107, 6819–6827. https://doi.org/10.1021/jp034704h
Morris, G.M., Huey, R., Lindstrom, W., Sanner, M.F., Belew, R.K., Goodsell, D.S., Olson, A.J., 2009. AutoDock4 and AutoDockTools4: Automated Docking with Selective Receptor Flexibility. Journal Computional Chemistry 30, 2785–2791. https://doi.org/10.1002/jcc.21256
Muñoz, A., Ródenas, M., Borrás, E., Vázquez, M., Vera, T., 2014. The gas-phase degradation of chlorpyrifos and chlorpyrifos-oxon towards OH radical under atmospheric conditions. Chemosphere 111, 522–528. https://doi.org/10.1016/j.chemosphere.2014.04.087
Muñoz, A., Vera, T., Sidebottom, H., Mellouki, A., Borrás, E., Ródenas, M., Clemente, E., Vázquez, M., 2011. Studies on the Atmospheric Degradation of Chlorpyrifos-Methyl. Environmental Science & Technology 45, 1880–1886. https://doi.org/10.1021/es103572j
Nandhini, A.R., Harshiny, M., Gummadi, S.N., 2021. Chlorpyrifos in environment and food: a critical review of detection methods and degradation pathways. Environmental Science: Processes Impacts 23, 1255–1277. https://doi.org/10.1039/D1EM00178G

Ngo, T.C., Taamalli, S., Srour, Z., Fèvre-Nollet, V., El Bakali, A., Louis, F., Černuśák, I., Dao, D.Q., 2023. Theoretical insights into the oxidation of quinmerac herbicide initiated by HO• radical in aqueous media: Mechanism, kinetics, and ecotoxicity. Journal of Environmental Chemical Engineering 11, 109941. https://doi.org/10.1016/j.jece.2023.109941

Parrinello, M., Rahman, A., 1981. Polymorphic transitions in single crystals: A new molecular dynamics method. Journal of Applied Physics 52, 7182–7190. https://doi.org/10.1063/1.328693

Perry, R.A., Atkinson, R., Pitts, J.N.Jr., 1977. Kinetics and mechanism of the gas phase reaction of hydroxyl radicals with aromatic hydrocarbons over the temperature range 296-473 K. Journal of Physical Chemistry 81, 296–304. https://doi.org/10.1021/j100519a004

Phung, D.T., Connell, D., Miller, G., Hodge, M., Patel, R., Cheng, R., Abeyewardene, M., Chu, C., 2012. Biological monitoring of chlorpyrifos exposure to rice farmers in Vietnam. Chemosphere 87, 294–300. https://doi.org/10.1016/j.chemosphere.2011.11.075

The PyMOL Molecular Graphics System, V.S., LLC. URL https://www.pymol.org/

K. Al. Rawas, H., Al. Mawla, R., Pham, T.Y.N., Truong, D.H., Nguyen, T.L.A., Taamalli, S., Ribaucour, M., Bakali, A.E., Černušák, I., Dao, D.Q., Louis, F., 2023. New insight into environmental oxidation of phosmet insecticide initiated by HO˙ radicals in gas and water – a theoretical study. Environmental Science: Processes Impacts 25, 2042–2056. https://doi.org/10.1039/D3EM00325F

Shi, X., Zhang, R., Li, Y., Zhang, Q., Xu, X., Wang, W., 2018. Mechanism theoretical study on OH-initiated atmospheric oxidation degradation of dimethoate. Journal of Molecular Structure 1163, 61–67. https://doi.org/10.1016/j.molstruc.2018.02.104

Silvia, S.C., Magnarelli, G., Rovedatti, M.G., 2020. Evaluation of endocrine disruption and gestational disorders in women residing in areas with intensive pesticide application: An exploratory study. Environmental Toxicology and Pharmacology 73, 103280. https://doi.org/10.1016/j.etap.2019.103280

Sousa da Silva, A.W., Vranken, W.F., 2012. ACPYPE - AnteChamber PYthon Parser interfacE. BMC Research Notes 5, 367. https://doi.org/10.1186/1756-0500-5-367

Sun, Y., Li, M., Hadizadeh, M.H., Liu, L., Xu, F., 2023. Theoretical insights into the degradation mechanisms, kinetics and eco-toxicity of oxcarbazepine initiated by OH radicals in aqueous environments. Journal of Environmental Sciences 129, 189–201. https://doi.org/10.1016/j.jes.2022.08.022

Teymourinia, H., Alshamsi, H.A., Al-nayili, A., Gholami, M., 2023. Photocatalytic degradation of chlorpyrifos using Ag nanoparticles-doped g-C3N5 decorated with dendritic CdS. Chemosphere 344, 140325. https://doi.org/10.1016/j.chemosphere.2023.140325

Tiwari, N., Mishra, A., 2023. Computational perspectives on Chlorpyrifos and its degradants as human glutathione S-transferases inhibitors: DFT calculations, molecular docking study and MD simulations. Computational Toxicology 26, 100264. https://doi.org/10.1016/j.comtox.2023.100264

Ubaid ur Rahman, H., Asghar, W., Nazir, W., Sandhu, M.A., Ahmed, A., Khalid, N., 2021. A comprehensive review on chlorpyrifos toxicity with special reference to endocrine disruption: Evidence of mechanisms, exposures and mitigation strategies. Science of The Total Environment 755, 142649. https://doi.org/10.1016/j.scitotenv.2020.142649

Uc, V.H., Alvarez-Idaboy, J.R., Galano, A., Vivier-Bunge, A., 2008. Theoretical Explanation of Nonexponential OH Decay in Reactions with Benzene and Toluene under Pseudo-First-Order Conditions. Journal of Physical Chemistry A 112, 7608–7615. https://doi.org/10.1021/jp8026258

Wang, J., Wang, W., Kollman, P.A., Case, D.A., 2006. Automatic atom type and bond type perception in molecular mechanical calculations. Journal of Molecular Graphics and Modelling 25, 247–260. https://doi.org/10.1016/j.jmgm.2005.12.005

Wang, J., Wolf, R.M., Caldwell, J.W., Kollman, P.A., Case, D.A., 2004. Development and testing of a general amber force field. Journal of Computational Chemistry 25, 1157–1174. https://doi.org/10.1002/jcc.20035

Wang, L., Liu, Z., Zhang, J., Wu, Y., Sun, H., 2016. Chlorpyrifos exposure in farmers and urban adults: Metabolic characteristic, exposure estimation, and potential effect of oxidative damage. Environmental Research 149, 164–170. https://doi.org/10.1016/j.envres.2016.05.011

Weber, N.H., Stockenhuber, S.P., Benhelal, E., Grimison, C.C., Lucas, J.A., Mackie, J.C., Stockenhuber, M., Kennedy, E.M., 2020. Products and mechanism of thermal decomposition of chlorpyrifos under inert and oxidative conditions. Environmental Science: Processes Impacts 22, 2084–2094. https://doi.org/10.1039/D0EM00295J

Worek, F., Thiermann, H., Szinicz, L., Eyer, P., 2004. Kinetic analysis of interactions between human acetylcholinesterase, structurally different organophosphorus compounds and oximes. Biochemical Pharmacology 68, 2237–2248. https://doi.org/10.1016/j.bcp.2004.07.038

Yang, B., Qin, C., Hu, X., Xia, K., Lu, C., Gudda, F.O., Ma, Z., Gao, Y., 2019. Enzymatic degradation of extracellular DNA exposed to chlorpyrifos and chlorpyrifos-methyl in an aqueous system. Environment International 132, 105087. https://doi.org/10.1016/j.envint.2019.105087

Yao, J., Tang, Y., Zhang, Y., Ruan, M., Wu, W., Sun, J., 2022. New theoretical investigation of mechanism, kinetics, and toxicity in the degradation of dimetridazole and ornidazole by hydroxyl radicals in aqueous phase. Journal of Hazardous Materials 422, 126930. https://doi.org/10.1016/j.jhazmat.2021.126930

Zhou, Q., Sun, X., Gao, R., Zhang, Q., Wang, W., 2010. Mechanism study on OH-initiated atmospheric degradation of the organophosphorus pesticide chlorpyrifos. Journal of Molecular Structure: THEOCHEM 952, 8–15. https://doi.org/10.1016/j.theochem.2010.03.023

Chapter V. Fenpyrazamine

V.1. Introduction

Our ability to produce food in sufficient quantities and of satisfactory quality, crucial for the rapidly expanding and discerning population, is significantly hindered by crop fungi. Pesticides, particularly fungicides, have become an indispensable and effective solution to this pressing issue. Synthetic fungicides have been used to protect crops in most countries worldwide for over 100 years, where controlling fungal diseases leads to improved crop yields and higher incomes for farmers (Gulkowska *et al.*, 2014).

Fungicides, which could be natural or manufactured, are agents that act to protect plants against fungi and eliminate fungal infections. Together with herbicides, insecticides, and plant growth regulators, they form a battery of agrochemicals called pesticides. They are available to protect crops and preserves their yield, measured in the quantity or quality of products.

The term "fungicide" refers to compounds that control a huge scope of organisms, including true fungi (*e.g.*, Ascomycota and Basidiomycota), Oomycota (*e.g.*, Phytophthora and Pythium), and the Plasmodiophora. However, fungicides do not contain chemicals that control bacteria, viruses, and nematodes, which are controlled by antibiotics, insecticides, and genetic methods.

Since the discovery of different pesticide types, many factors have ensured their continued use and growth in the pesticide industries. These factors encompass a growing global population, rising incomes, and direct advantages for both growers (*e.g.*, reduced labour costs, improved yields, and increased profits) and consumers (*e.g.*, enhanced consistency in food quality, a wider range of produce and lower prices) (Oliver and Hewitt, 2014).

Fungicide utilization has grown significantly in the last decades and is routinely applied throughout the plant growing season. Several treatments may be used each season depending on the crop type and its conditions (Reilly *et al.*, 2012).

However, the intensive application of fungicides has presented additional issues, such as the development of resistance and potential hazards to farmers and nearby residents during the application process. There are also risks to consumers through residues in food and adverse impacts on the environment, including accumulation in soils, contamination of natural waters, and detrimental effects on non-target organisms (Dehne *et al.*, 2011).

Within the agricultural industry, diseases like gray mold (*Botrytis cinerea*) and stem rot (*Sclerotinia sclerotiorum*) pose significant threats to the yield and productivity of fruit trees and vegetables. Effectively controlling these diseases becomes crucial. Various fungicides, including benomyl, have been formulated to control gray mold. However, since gray mold has a short lifecycle coupled with prolific spore production, it is difficult to control and is classified as a phytopathological fungus prone to developing resistance to fungicides (Leroux *et al.*, 2002).

Novel fungicides were in demand to meet the need for gray mold control. One such innovation is fenpyrazamine (FPA), a fungicide that was discovered and developed by Sumitomo Chemical Co., Ltd. Fenpyrazamine ($C_{17}H_{21}N_3O_2S$), or S-allyl 5-amino-2,3-dihydro-2-isopropyl-3-oxo-4-(o-tolyl)pyrazole-1-carbothioate (***Figure V-1***), is a fungicidal compound that belongs to the pyrazole fungicides chemical family.

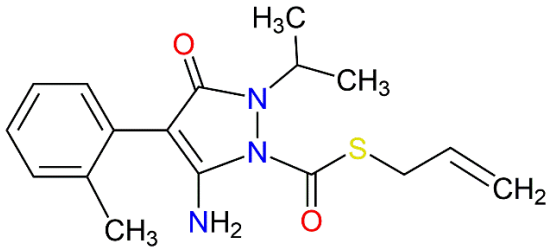

***Figure V-1**: structure of fenpyrazamine (FPA).*

Distinguished by its aminopyrazolinone structure, this fungicide stands out as a unique example not found among agricultural chemicals. It has a low vapor pressure of 2.89×10^{-8} Pa at 25°C, indicating that it is not highly volatile and thus has a limited potential to evaporate into the atmosphere under standard environmental conditions. Moreover, its solubility in water is 20.4 mg/L at 20°C.

Fenpyrazamine demonstrates notably strong effectiveness against gray mold, stem rot, and brown rot affecting fruits and vegetables. Sumitomo Chemical Co., Ltd. registered fenpyrazamine fungicide in Korea and acquired EU registration. The product was introduced as "PROLECTUS®" in Italy in October 2012 and as "Pixio® DF" in Japan in January 2014. Following that, Sumitomo Chemical Co., Ltd. obtained registration for fenpyrazamine and introduced the fungicide in several EU countries and Australia (Kimura *et al.*, 2017).

Fenpyrazamine has been registered in more than 30 countries, including the European Union (EU), the USA, Chile, Japan, and Korea. These registrations cover a range of crops, including almonds, grapes, lettuce, tomato, zucchini, cucumber, blueberry, cranberry, strawberry, pistachio, ginseng, and ornaments (APVMA, 2015).

Fenpyrazamine's effectiveness against fungi was evaluated, demonstrating potent inhibition of germ tube elongation and inducing morphological alterations in *Botrytis cinerea* germ tubes. Furthermore, it exhibited significant preventive efficacy, achieving 100% control against gray mold at a low concentration, just 1/16 of the registered concentration (250 mg a.i./L) for cucumber gray mold in Japan. Fenpyrazamine's target enzyme is 3-keto reductase in the ergosterol biosynthetic pathway. The fungicide also displayed high efficacy in field trials against pathogenic *Sclerotiniaceae* like *Botrytis* spp., *Sclerotinia* spp., and *Monilinia* spp., indicating its practical applicability (Kimura *et al.*, 2017).

According to the World Health Organization, the acceptable daily intake for fenpyrazamine was established to be 0-0.3 mg/kg body weight, which represents an International Estimated Daily Intake of 0-2% of the upper bound of the ADI. An International Estimated Short-Term Intake was calculated for fenpyrazamine for which an Acute Reference Dose was established to be 0.8 mg/kg body weight. Moreover, an estimated maximum dietary burden test was conducted, and 2.38 mg/kg of fenpyrazamine residue in grape pomace was found (FAO, 2017). In addition, fenpyrazamine was tested and found to be non-carcinogenic in rats with an acute oral LD_{50} > 2000 mg/kg and acute inhalation LD_{50} > 4.84 mg/L (Tanaka *et al.*, 2012).

Like other organic compounds, fenpyrazamine could decompose and react with other species in the environment. Therefore, it is essential to understand the decomposition and oxidation processes of the fenpyrazamine fungicide under environmental conditions to better assess its lifetime, toxicology and impact on human health and the environment. Facing this task, several research approaches have been investigated, in which quantum chemistry has become one of the indispensable pillars allowing a better understanding of the mechanisms and kinetics of fungicide degradation.

Using molecular simulations and density functional theory (DFT) calculations, several theoretical studies have been reported on the reaction mechanisms and the kinetics of $HO^{\bullet}$-initiated oxidation of pesticides like dimethoate (Shi *et al.*, 2018), metazachlor (Dao *et al.*, 2023), quinmerac (Ngo *et al.*, 2023), phosmet (K. Al Rawas *et al.*, 2023), and chlorpyrifos (Truong *et al.*, 2024).

No literature data exists on the environmental degradation of fenpyrazamine (FPA) and its potential degradation products. Hence, this study aims to investigate the degradation mechanisms of FPA induced by $HO^{\bullet}$ through three distinct reaction pathways: formal hydrogen transfer (FHT), radical adduct formation (RAF), and single electron transfer (SET). The thermodynamics, mechanisms, kinetics of reactions, and the lifetime of FPA will be examined in the aqueous phase at various temperatures ranging from 283 to 323 K, covering the temperature range of water in environmental settings and water treatment processes. Additionally, the ecotoxicity of FPA and its degradation products will be assessed in the aquatic environment, highlighting their impact on aquatic organisms.

V.2. Results and discussion

V.2.1. Structure and electronic properties of fenpyrazamine

First, a conformational analysis was made using the MSTor software to find the most stable conformer of FPA. The ConfGen module of this program allows the generation of Gaussian input files for a set of conformational structures by rotating around specified bonds in an input structure. The 5 torsions 4 initial dihedral angles (0°, 90°, 180°, and 270°) of the FPA molecule lead to 372 initial structures. The geometry optimizations at the M06-2X/6-31+G(d,p) level of theory found 15 conformers, where the most stable conformation was chosen to study the potential energy surfaces of FPA towards $HO^{\bullet}$ radicals. The optimized structure of the most stable conformer of FPA in the aqueous phase is shown in ***Figure V-2***. To know more about the electronic properties of FPA molecules, its Fukui indices, highest occupied molecular orbital (HOMO), lowest unoccupied molecular orbital (LUMO), and the electrostatic potential (ESP) maps were investigated and shown in ***Figures V-3*** and ***V-4***.

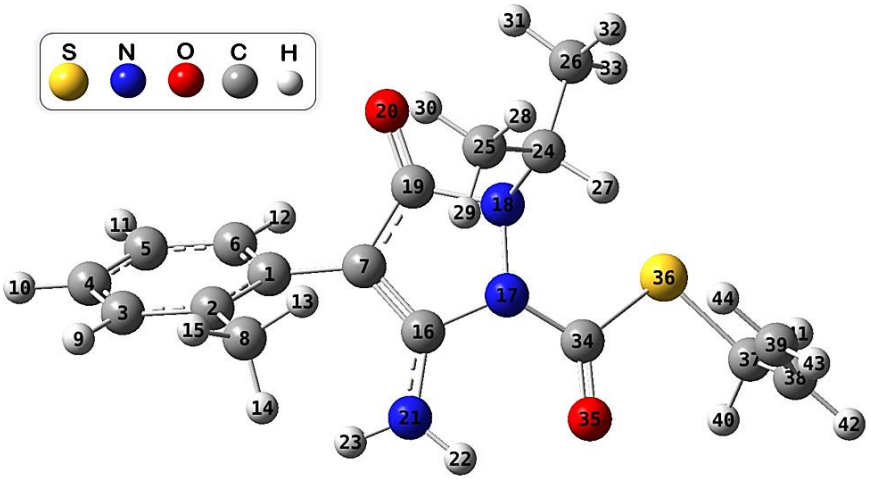

***Figure V-2**: optimized structure of the most stable conformer of FPA.*

From the ESP map, the region of high electron density (in red colour) is located at the C=O group and the O atom (O20), while that of the low electron density is located at the C-C bond related to the S atom, and at the N-H bonds. Moreover, it could be seen that the HOMO is primarily situated at the rings, whereas the LUMO is located at the pyrazole ring, and the C=O group bonded to the S atom. This information enables the prediction of molecular regions with a high tendency to donate electrons and those that tend to accept them in single electron transfer reactions with external radicals. The results of the calculated Fukui indices (f^0) for radical attack show that the NH_2, the pyrazole ring, and the C=O groups may be favourable sites for the radical reaction.

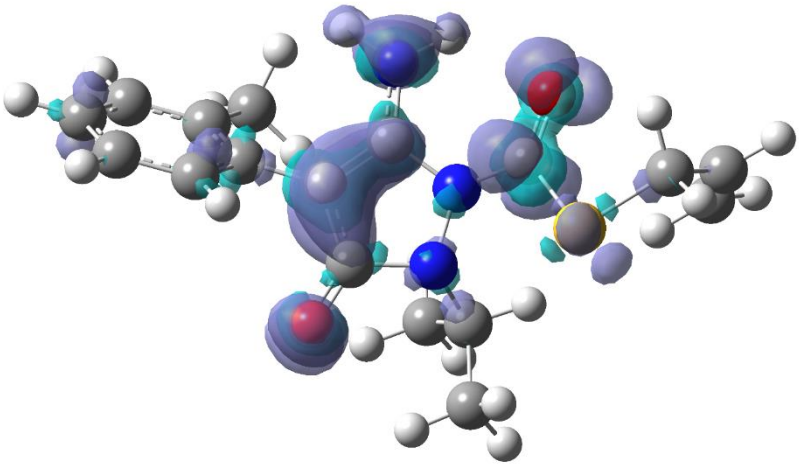

***Figure V-3**: plot of Fukui function for radical attack (f^0) describing the possible main reactive sites of FPA.*

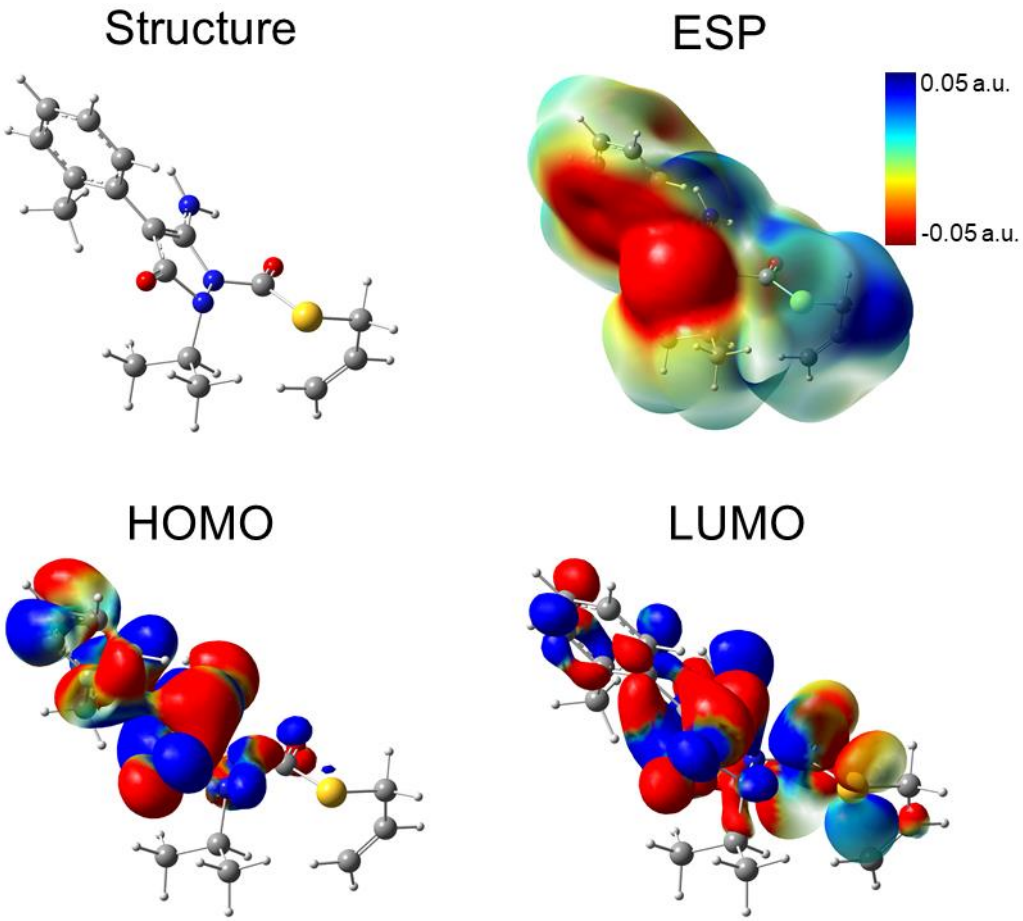

Figure V-4*: representation of the HOMO, LUMO, and ESP maps of FPA molecule.*

To identify in which state fenpyrazamine exists in the environment, its pKa and molar fraction were calculated. The pKa value (*i.e.*, 3.42) was obtained based on the calculated Gibbs free energies of both protonated (at N17, N18, N21, O20, and O35 positions) and deprotonated forms of FPA (Rebollar-Zepeda and Galano, 2016), where the protonation was most favourable at O20 atom.

The results show that FPA predominantly exists in its protonated form in an acidic medium (pH < 3.4), while it predominantly exists in the neutral form when pH > 3.4 (***Figure V-5***). In the pH range from 6 to 8, which reproduces the environmental condition of almost all surface water and underground water, FPA exists totally in the neutral form. Thus, according to the main purpose of this work, which is to evaluate the environmental degradation of the organic contaminant, we will only consider the neutral form of FPA molecule in all reactions.

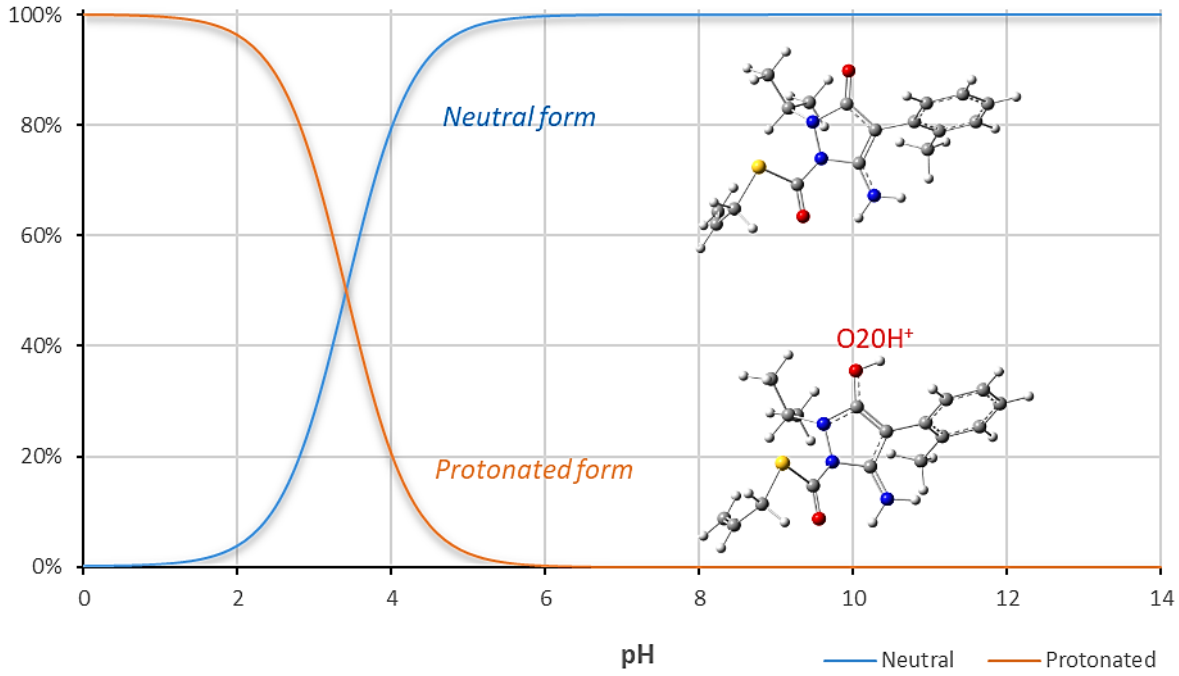

***Figure V-5**: plot of the molar fraction (%) of the neutral or protonated forms of FPA as a function of the pH in the aqueous phase.*

V.2.2. Oxidation reaction mechanisms

The degradation process of fenpyrazamine by HO• radicals in the environment involves 21 formal H-abstractions (FHT), 12 HO•-additions at the unsaturated atoms (RAF), and a single electron transfer (SET) reaction. ZPE and SOC corrections were considered in all energy calculations. The computational details were resumed in **Chapter II**.

V.2.2.1. Formal hydrogen transfer (FHT) reactions

The results of the H-abstraction reaction (***Figure V-6***) reveal that all the pathways are exergonic and spontaneous, with negative values of their standard Gibbs free reaction energy ($\Delta_r G°$) at 298 K. These values range from -144.56 kJ mol^{-1} (at H41 of the methylene group) to -35.58 kJ mol^{-1} (at H10 of the benzyl ring). In addition, the Gibbs free activation energy ($\Delta G°^{\neq}$) was found to be lowest between 25.65 and 35.55 kJ mol^{-1}, at H13 and H15 of the methyl group (of C8), H40 of the methylene group (of C37 adjacent to the S atom), and H31 of the methyl group (of C26), respectively. It is noteworthy that H31 is stabilised by a hydrogen bond with the oxygen atom O20. However, as expected, the highest $\Delta G°^{\neq}$ value of 84.03 kJ mol^{-1} was seen at H23 of the amino group of N21. This may be due to several factors like steric hindrance and the electron-withdrawing effect of the nitrogen atom rich in electron densities. These factors may make the H-abstraction from this group more challenging than from C-H bonds of the methyl (-CH_3) groups or the methylene (-CH_2-) ones. Furthermore, all the FHT reaction pathways are exothermic, as indicated by their negative standard reaction enthalpy at 0 K ($\Delta_r H°_{0K}$) (***Table V-***

1). These values vary from -141.59 (at H41) to -34.61 kJ mol^{-1} (at H11). The lowest energy barrier (E_0) at the TS at 0 K was found at H13 (-10.87 kJ mol^{-1}) and H15 (-10.86 kJ mol^{-1}).

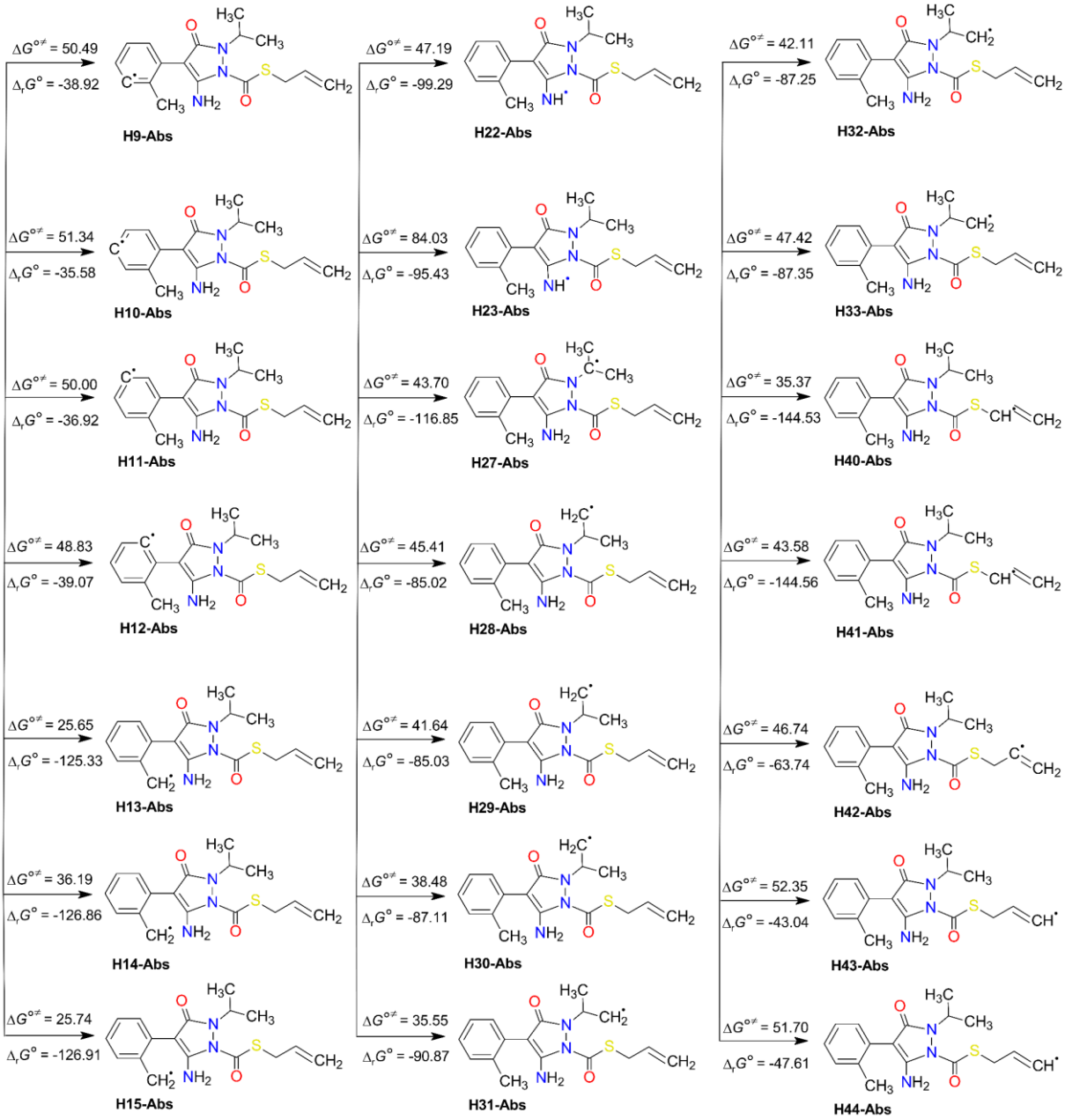

Figure V-6*: H-abstraction degradation pathways of FPA (with water product). Standard Gibbs free reaction energies ($\Delta_r G°$) and standard Gibbs free activation energies ($\Delta G^{\circ\neq}$) at 298 K. Units are in kJ* mol^{-1}.

This indicates that the FHT pathways at the methyl groups (H13/H15 and H30/H31) and the methylene group (H40/H41) are the predominant reactions, with H15 the most favourable. From a thermodynamics point of view, we can conclude that FHT reactions are generally

favoured in the order -CH_3- > -CH_2- > benzyl ring > -NH_2. This finding will be validated later in the reaction kinetics section.

***Table V-1**: standard enthalpy ($\Delta H°_{0K}$) for MCR and MCP, adiabatic energy barrier (E_0) for TS, and standard reaction enthalpy ($\Delta_r H°_{0K}$) for products (P) at 0 K of the FHT reactions, in addition to their standard activation enthalpy ($\Delta H°^{\neq}_{298K}$) and standard reaction enthalpy ($\Delta_r H°_{298K}$) at 298 K. Units are in kJ mol^{-1}.*

Positions	MCR	TS	MCP	P	$\Delta H°^{\neq}_{298K}$	$\Delta_r H°_{298K}$
H9	-17.99	15.00	-43.81	-36.58	11.93	-36.06
H10	-26.54	17.14	-39.29	-35.82	14.51	-35.13
H11	-26.53	16.64	-38.63	-34.61	14.18	-34.09
H12	-24.97	13.50	-46.26	-36.24	10.69	-35.59
H13	-19.67	-10.87	-145.27	-125.17	-15.15	-125.20
H14	-17.98	-0.12	-136.73	-125.65	-3.73	-125.49
H15	-19.65	-10.86	-144.79	-125.67	-15.15	-125.49
H22	-21.39	12.72	-103.97	-94.46	8.56	-94.65
H23	-3.61	50.18	-98.77	-92.50	46.23	-93.16
H27	-12.54	6.54	-109.70	-109.29	2.99	-107.23
H28	-14.71	10.06	-87.11	-79.85	6.15	-77.65
H29	-12.02	3.96	-92.53	-79.85	0.11	-77.64
H30	-19.66	-1.50	-99.19	-82.72	-6.38	-80.51
H31	-22.20	-1.99	-102.02	-85.34	-6.35	-83.21
H32	-14.71	8.39	-94.00	-83.46	5.01	-81.82
H33	-20.19	7.96	-97.65	-83.50	2.77	-81.84
H40	-19.80	-0.78	-153.40	-141.58	-4.56	-140.99
H41	-14.51	8.23	-147.88	-141.59	5.07	-140.99
H42	-19.81	12.34	-64.25	-59.80	9.29	-58.61
H43	-14.11	17.87	-45.81	-40.08	14.97	-39.29
H44	-19.82	14.83	-59.17	-44.85	11.83	-44.03

V.2.2.2. Radical adduct formation (RAF) reactions

RAF reaction in fenpyrazamine occurs by HO$^{\bullet}$-addition on 12 unsaturated carbon atoms, forming 12 radical-adduct products. These C atoms include C1-C6 of the benzyl ring, C7/C16/C19 of the pyrazole ring, C34 of the carbonyl group, and C38/C39 of the vinyl group. The results of the calculated standard Gibbs free reaction energies ($\Delta_r G°$) and standard Gibbs free activation energies ($\Delta G°^{\neq}$) at 298 K of this reaction are presented in ***Figure V-7***.

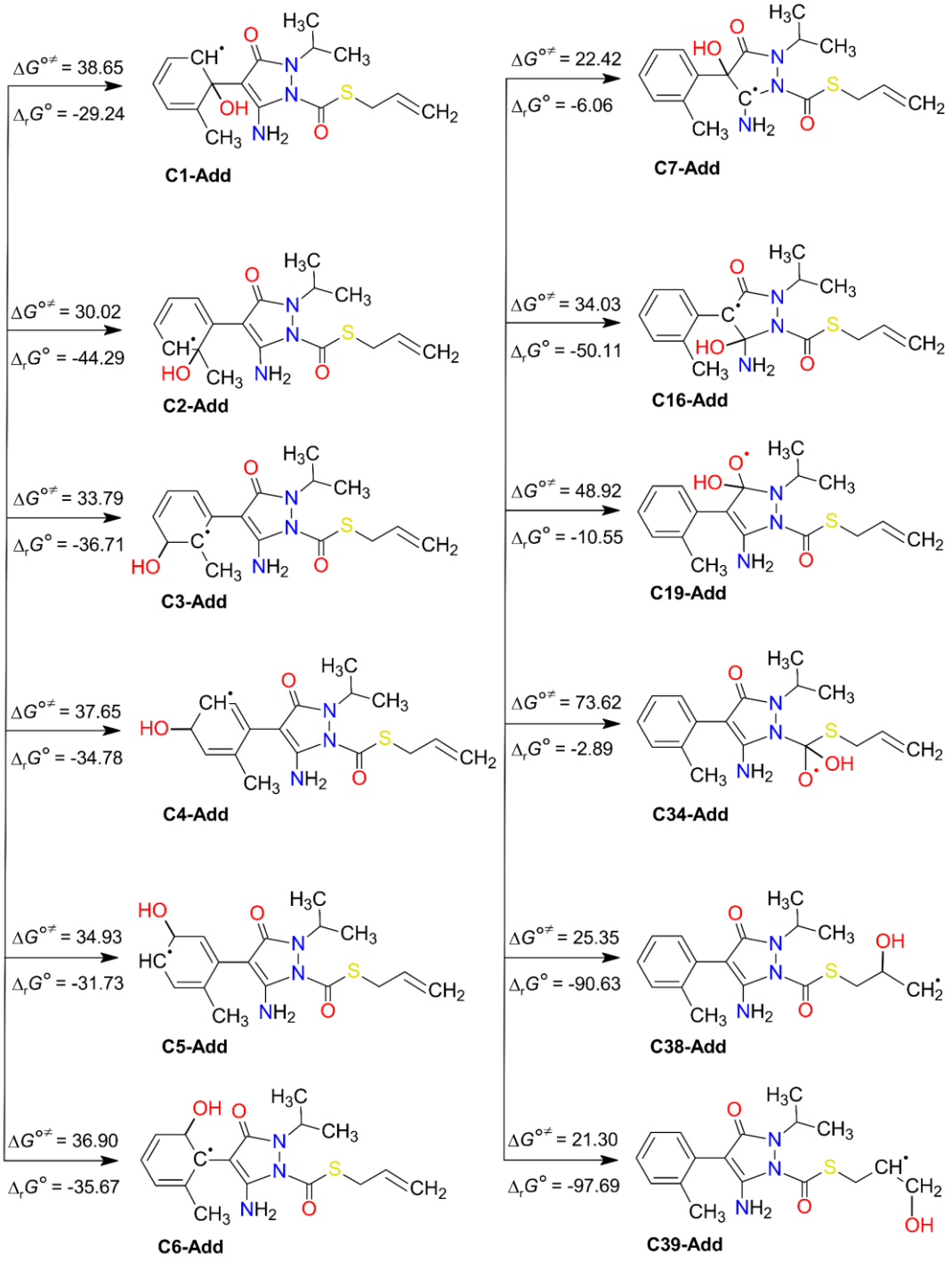

***Figure V-7**: HO•-addition degradation pathways of FPA. Standard Gibbs free reaction energies ($\Delta_r G°$) and standard Gibbs free activation energies ($\Delta G^{\circ\neq}$) at 298 K. Units are in kJ mol^{-1}.*

The results show that the HO•-addition reactions at all the concerned positions were exergonic and spontaneous, with negative values of their standard Gibbs free reaction energy ($\Delta_r G°$), ranging from -97.69 (at C39) to -2.89 kJ mol^{-1} (at C34). The same trend was seen from the value

of the standard Gibbs free activation energy ($\Delta G°^{\neq}$), which was also lowest at C39 (21.30 kJ mol^{-1}) and highest at C34 (73.62 kJ mol^{-1}). Moreover, all the RAF reaction pathways are exothermic, as indicated by the negative standard reaction enthalpy ($\Delta_r H°_{0K}$) obtained at 0 K (***Table V-2***). The relative values of $\Delta_r H°_{0K}$ vary from -135.40 (at C39) to -32.21 kJ mol^{-1} (at C19).

These findings indicate that HO$^{\bullet}$-addition on C39 is the most favourable thermodynamic pathway due to the lack of steric hindrance. In addition, by comparing the energy barriers (E_0) at the TS at 0 K (***Table V-2***), it is observed that the lowest values are at C2, C7, C38, and C39, which suggest that these pathways are also feasible.

Table V-2*: standard enthalpy ($\Delta H°_{0K}$) for MCR and MCP, adiabatic energy barrier (E_0) for TS, and standard reaction enthalpy ($\Delta_r H°_{0K}$) for products (P) at 0 K of the RAF reactions, in addition to their standard activation enthalpy ($\Delta H°^{\neq}_{298K}$) and standard reaction enthalpy ($\Delta_r H°_{298K}$) at 298 K. Units are in kJ mol^{-1}.*

Positions	MCR	TS	P	$\Delta H°^{\neq}_{298K}$	$\Delta_r H°_{298K}$
C1	-17.93	-1.21	-66.36	-5.89	-70.74
C2	-20.13	-10.24	-85.26	-14.94	-91.04
C3	-20.13	-3.17	-74.29	-6.66	-78.53
C4	-20.12	0.66	-73.41	-3.09	-78.16
C5	-26.54	0.35	-68.88	-2.67	-72.90
C6	-26.55	-2.81	-76.66	-7.99	-82.62
C7	-22.43	-18.31	-48.91	-23.41	-54.29
C16	-24.96	-7.87	-89.99	-13.49	-95.38
C19	-25.02	6.05	-32.21	0.02	-38.38
C34	-22.83	32.79	-43.11	27.61	-48.45
C38	-14.11	-9.83	-128.50	-13.56	-132.79
C39	-19.81	-14.64	-135.40	-18.93	-140.60

V.2.2.3. Single electron transfer (SET) reaction

The transfer process of one electron from FPA to the HO$^{\bullet}$ radical was also calculated. At 298 K, the values of $\Delta G°^{\neq}$ and $\Delta_r G°$ obtained were 26.47 and 26.53 kJ mol^{-1}, respectively (***Figure V-8***). These values are relatively low, which means that the SET reaction between FPA and HO$^{\bullet}$ is essential, and it will be considered for further calculations.

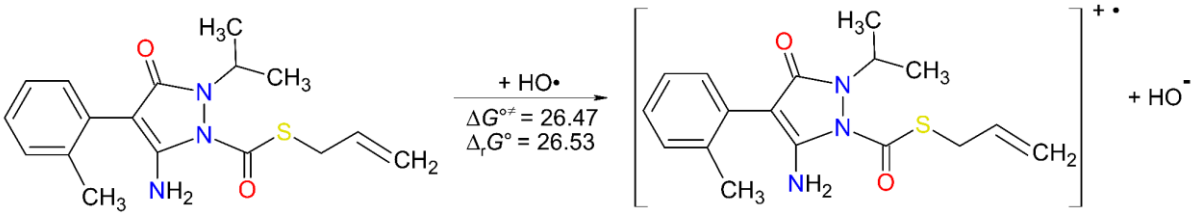

***Figure V-8**: standard Gibbs free reaction energy ($\Delta_r G°$) and standard Gibbs free activation energy ($\Delta G^{\circ\neq}$) at 298 K for the SET reaction. Units are in kJ mol^{-1}.*

V.2.3. Reaction kinetics of fenpyrazamine oxidation

The kinetics of the FHT, RAF, and SET reactions were studied to better understand the oxidation pathways of fenpyrazamine by HO• radicals. This was done by calculating the rate constants of each reaction channel over a temperature range of 283-323 K. The results for the rate constant (k) and the branching ratio (Γ, %) for all reactions are presented in ***Figure V-9***, and Tables ***V-3*** and ***V-4***.

As can be seen in Tables ***V-3*** and ***V-4***, the total rate constant of the FHT reactions at 298 K being 6.09×10^{9} M^{-1} s^{-1},less than that of RAF reactions being 8.21×10^{9} M^{-1} s^{-1}, indicates that the RAF reaction is more predominant. The rate constant of the FHT reaction pathway varies from 3.24 (at H23) and 8.57×10^{5} (at H43) to 2.45×10^{9} M^{-1} s^{-1} (at H15), while those of the RAF reaction range from 4.34×10^{1} (at C34) to 2.28×10^{9} M^{-1} s^{-1} (at C39). The most favourable pathways in the FHT and RAF reactions can be seen from the branching ratio values illustrated in Figures ***V-9b*** and ***9d***, respectively.

Regarding the influence of temperature, the degradation of FPA by HO• has an overall rate constant value ranging from 1.21×10^{10} to 2.56×10^{10} M^{-1} s^{-1} as the temperature changes from 283 to 323 K. The total rate constant of the H-abstraction reactions varied from 4.73×10^{9} to 8.22×10^{9} M^{-1} s^{-1}, with their total branching ratio values ranging between 39.00 and 32.07% of the overall branching ratio. Meanwhile, the total rate constants of HO•-addition reactions varied from 6.12×10^{9} to 1.18×10^{10} M^{-1} s^{-1}, representing 50.55 to 45.95%. Moreover, the rate constant values of the SET reaction were observed to be between 1.27×10^{9} to 5.63×10^{9} M^{-1} s^{-1} (2.35×10^{9} at 298 K), representing 10.45 to 21.98% of the overall reaction, which is notably high.

As expected, among the H-abstraction reactions, the highest branching ratios were observed at H15 of the methyl group (increasing from 14.06%, reaching 14.73%, then decreasing to 14.01% with T) indicating the predominant pathway, and at H13 of the same group (increasing from 11.96%, reaching 12.74%, then decreasing to 12.43%). These are followed by H40 abstraction of the methylene group (3.76 to 1.69%) and H31 of the methyl group (3.44 to 1.42%).

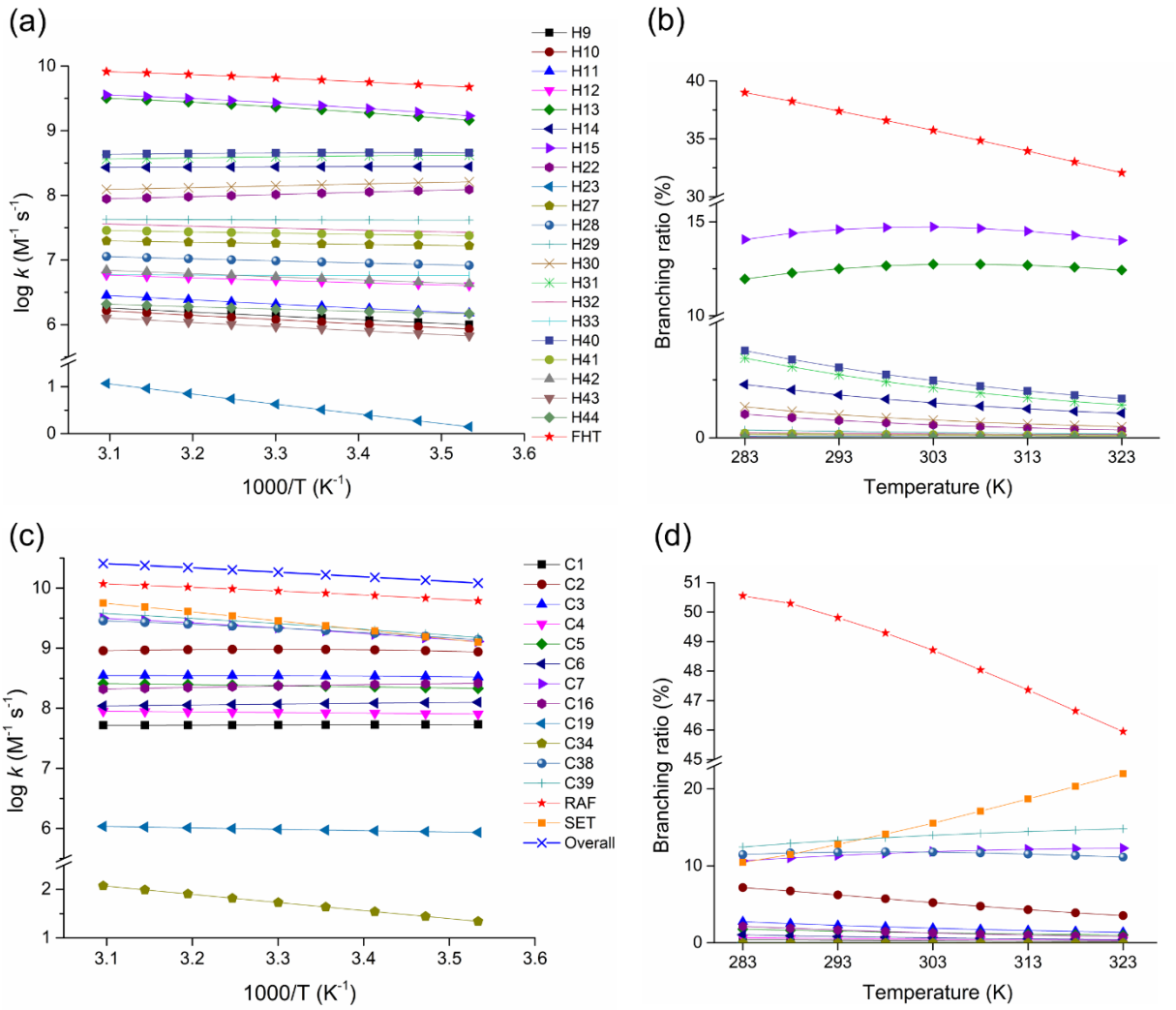

***Figure V-9**: rate constant (log k) and branching ratio (Γ, %) values for the FHT (a, b) and the RAF and SET (c, d) reactions in the temperature range of 283-323 K.*

All the FHT channels show an incline in the rate constant values with the increasing temperature, except the channels H14, H22, H30, H31, and H40, which show a slight decline. This phenomenon is probably due to the destabilization of pre-reactive complexes at higher temperatures. Moreover, it could be due to the reduced tunnelling effect at higher temperatures, which decreases the reaction rate.

Concerning the RAF reactions, the highest rate constant value was recognized at the C39 position of the vinyl group, increasing from 1.51×10^{9} to 3.80×10^{9} M^{-1} s^{-1} corresponding to 12.45 to 14.82% of the overall reaction, indicating the most favourable $HO^{\bullet}$-addition site. The addition at C38 of the same group follows this channel with a rate constant increasing from 1.39×10^{9} to 2.85×10^{9} M^{-1} s^{-1}, and the addition at C7 of the pyrazole ring with a rate constant of 1.29×10^{9} to 3.15×10^{9} M^{-1} s^{-1}. In contrast, all the $HO^{\bullet}$-addition reaction pathways (except C34) have a decreasing trend in the rate constant values as a function of temperature.

***Table V-3**: apparent rate constants (k, in M^{-1} s^{-1}) of all oxidation reactions, with the total FHT, RAF, SET, and the overall rate constants in the temperature range of 283-323 K. (the most favourable pathways are in bold).*

T (K)	H9-Abs	H10-Abs	H11-Abs	H12-Abs	H13-Abs	H14-Abs	H15-Abs	H22-Abs	H23-Abs	H27-Abs	H28-Abs	H29-Abs
283	1.00×10^{6}	8.54×10^{5}	1.50×10^{6}	4.03×10^{6}	$\mathbf{1.45\times10^{9}}$	2.79×10^{8}	$\mathbf{1.70\times10^{9}}$	1.23×10^{8}	1.40	1.66×10^{7}	8.26×10^{6}	4.14×10^{7}
288	1.08×10^{6}	9.29×10^{5}	1.63×10^{6}	4.21×10^{6}	$\mathbf{1.66\times10^{9}}$	2.79×10^{8}	$\mathbf{1.95\times10^{9}}$	1.18×10^{8}	1.86	1.70×10^{7}	8.59×10^{6}	4.14×10^{7}
293	1.17×10^{6}	1.01×10^{6}	1.77×10^{6}	4.40×10^{6}	$\mathbf{1.88\times10^{9}}$	2.79×10^{8}	$\mathbf{2.20\times10^{9}}$	1.13×10^{8}	2.47	1.73×10^{7}	8.93×10^{6}	4.15×10^{7}
298	1.26×10^{6}	1.10×10^{6}	1.92×10^{6}	4.61×10^{6}	$\mathbf{2.11\times10^{9}}$	2.78×10^{8}	$\mathbf{2.45\times10^{9}}$	1.08×10^{8}	3.24	1.77×10^{7}	9.29×10^{6}	4.16×10^{7}
303	1.36×10^{6}	1.19×10^{6}	2.07×10^{6}	4.83×10^{6}	$\mathbf{2.34\times10^{9}}$	2.77×10^{8}	$\mathbf{2.70\times10^{9}}$	1.03×10^{8}	4.24	1.81×10^{7}	9.67×10^{6}	4.17×10^{7}
308	1.46×10^{6}	1.29×10^{6}	2.25×10^{6}	5.06×10^{6}	$\mathbf{2.56\times10^{9}}$	2.75×10^{8}	$\mathbf{2.94\times10^{9}}$	9.88×10^{7}	5.52	1.84×10^{7}	1.01×10^{7}	4.18×10^{7}
313	1.57×10^{6}	1.40×10^{6}	2.43×10^{6}	5.31×10^{6}	$\mathbf{2.78\times10^{9}}$	2.74×10^{8}	$\mathbf{3.18\times10^{9}}$	9.49×10^{7}	7.14	1.89×10^{7}	1.05×10^{7}	4.20×10^{7}
318	1.69×10^{6}	1.52×10^{6}	2.62×10^{6}	5.57×10^{6}	$\mathbf{2.99\times10^{9}}$	2.72×10^{8}	$\mathbf{3.39\times10^{9}}$	9.14×10^{7}	9.18	1.93×10^{7}	1.09×10^{7}	4.22×10^{7}
323	1.81×10^{6}	1.64×10^{6}	2.83×10^{6}	5.85×10^{6}	$\mathbf{3.18\times10^{9}}$	2.70×10^{8}	$\mathbf{3.59\times10^{9}}$	8.83×10^{7}	1.17×10^{1}	1.97×10^{7}	1.13×10^{7}	4.25×10^{7}

T (K)	H30-Abs	H31-Abs	H32-Abs	H33-Abs	H40-Abs	H41-Abs	H42-Abs	H43-Abs	H44-Abs	C1-Add	C2-Add	C3-Add
283	1.62×10^{8}	$\mathbf{4.17\times10^{8}}$	2.67×10^{7}	5.77×10^{6}	$\mathbf{4.55\times10^{8}}$	2.38×10^{7}	4.28×10^{6}	6.70×10^{5}	1.47×10^{6}	5.38×10^{7}	8.70×10^{8}	3.32×10^{8}
288	1.56×10^{8}	$\mathbf{4.14\times10^{8}}$	2.77×10^{7}	5.76×10^{6}	$\mathbf{4.58\times10^{8}}$	2.43×10^{7}	4.55×10^{6}	7.28×10^{5}	1.53×10^{6}	5.36×10^{7}	9.10×10^{8}	3.38×10^{8}
293	1.51×10^{8}	$\mathbf{4.09\times10^{8}}$	2.88×10^{7}	5.76×10^{6}	$\mathbf{4.58\times10^{8}}$	2.48×10^{7}	4.85×10^{6}	7.90×10^{5}	1.59×10^{6}	5.34×10^{7}	9.37×10^{8}	3.43×10^{8}
298	1.45×10^{8}	$\mathbf{4.03\times10^{8}}$	3.00×10^{7}	5.77×10^{6}	$\mathbf{4.55\times10^{8}}$	2.54×10^{7}	5.15×10^{6}	8.57×10^{5}	1.66×10^{6}	5.32×10^{7}	9.53×10^{8}	3.46×10^{8}
303	1.40×10^{8}	$\mathbf{3.96\times10^{8}}$	3.11×10^{7}	5.78×10^{6}	$\mathbf{4.52\times10^{8}}$	2.60×10^{7}	5.48×10^{6}	9.29×10^{5}	1.73×10^{6}	5.29×10^{7}	9.58×10^{8}	3.48×10^{8}
308	1.36×10^{8}	$\mathbf{3.88\times10^{8}}$	3.23×10^{7}	5.81×10^{6}	$\mathbf{4.48\times10^{8}}$	2.66×10^{7}	5.82×10^{6}	1.01×10^{6}	1.81×10^{6}	5.27×10^{7}	9.54×10^{8}	3.49×10^{8}
313	1.31×10^{8}	$\mathbf{3.79\times10^{8}}$	3.35×10^{7}	5.84×10^{6}	$\mathbf{4.43\times10^{8}}$	2.73×10^{7}	6.18×10^{6}	1.09×10^{6}	1.89×10^{6}	5.25×10^{7}	9.43×10^{8}	3.50×10^{8}
318	1.27×10^{8}	$\mathbf{3.71\times10^{8}}$	3.48×10^{7}	5.88×10^{6}	$\mathbf{4.38\times10^{8}}$	2.80×10^{7}	6.55×10^{6}	1.18×10^{6}	1.98×10^{6}	5.23×10^{7}	9.27×10^{8}	3.51×10^{8}
323	1.23×10^{8}	$\mathbf{3.63\times10^{8}}$	3.61×10^{7}	5.93×10^{6}	$\mathbf{4.32\times10^{8}}$	2.87×10^{7}	6.94×10^{6}	1.27×10^{6}	2.08×10^{6}	5.21×10^{7}	9.07×10^{8}	3.51×10^{8}

T (K)	C4-Add	C5-Add	C6-Add	C7-Add	C16-Add	C19-Add	C34-Add	C38-Add	C39-Add	FHT	RAF	SET	Overall
283	8.04×10^{7}	2.14×10^{8}	1.26×10^{8}	$\mathbf{1.29\times10^{9}}$	2.60×10^{8}	8.62×10^{5}	2.19×10^{1}	$\mathbf{1.39\times10^{9}}$	$\mathbf{1.51\times10^{9}}$	4.73×10^{9}	6.12×10^{9}	1.27×10^{9}	1.21×10^{10}
288	8.16×10^{7}	2.21×10^{8}	1.24×10^{8}	$\mathbf{1.49\times10^{9}}$	2.55×10^{8}	8.89×10^{5}	2.77×10^{1}	$\mathbf{1.58\times10^{9}}$	$\mathbf{1.75\times10^{9}}$	5.17×10^{9}	6.80×10^{9}	1.55×10^{9}	1.35×10^{10}
293	8.28×10^{7}	2.27×10^{8}	1.22×10^{8}	$\mathbf{1.71\times10^{9}}$	2.49×10^{8}	9.16×10^{5}	3.48×10^{1}	$\mathbf{1.77\times10^{9}}$	$\mathbf{2.00\times10^{9}}$	5.63×10^{9}	7.50×10^{9}	1.93×10^{9}	1.51×10^{10}
298	8.40×10^{7}	2.33×10^{8}	1.20×10^{8}	$\mathbf{1.94\times10^{9}}$	2.43×10^{8}	9.44×10^{5}	4.34×10^{1}	$\mathbf{1.97\times10^{9}}$	$\mathbf{2.28\times10^{9}}$	6.09×10^{9}	8.21×10^{9}	2.35×10^{9}	1.67×10^{10}
303	8.51×10^{7}	2.38×10^{8}	1.18×10^{8}	$\mathbf{2.17\times10^{9}}$	2.36×10^{8}	9.71×10^{5}	5.37×10^{1}	$\mathbf{2.16\times10^{9}}$	$\mathbf{2.56\times10^{9}}$	6.55×10^{9}	8.93×10^{9}	2.85×10^{9}	1.83×10^{10}
308	8.62×10^{7}	2.44×10^{8}	1.15×10^{8}	$\mathbf{2.42\times10^{9}}$	2.29×10^{8}	1.00×10^{6}	6.60×10^{1}	$\mathbf{2.35\times10^{9}}$	$\mathbf{2.86\times10^{9}}$	7.00×10^{9}	9.66×10^{9}	3.44×10^{9}	2.01×10^{10}
313	8.72×10^{7}	2.49×10^{8}	1.13×10^{8}	$\mathbf{2.66\times10^{9}}$	2.22×10^{8}	1.03×10^{6}	8.07×10^{1}	$\mathbf{2.53\times10^{9}}$	$\mathbf{3.17\times10^{9}}$	7.44×10^{9}	1.04×10^{10}	4.09×10^{9}	2.19×10^{10}
318	8.83×10^{7}	2.54×10^{8}	1.11×10^{8}	$\mathbf{2.91\times10^{9}}$	2.15×10^{8}	1.06×10^{6}	9.81×10^{1}	$\mathbf{2.70\times10^{9}}$	$\mathbf{3.48\times10^{9}}$	7.84×10^{9}	1.11×10^{10}	4.83×10^{9}	2.38×10^{10}
323	8.94×10^{7}	2.59×10^{8}	1.09×10^{8}	$\mathbf{3.15\times10^{9}}$	2.08×10^{8}	1.09×10^{6}	1.19×10^{2}	$\mathbf{2.85\times10^{9}}$	$\mathbf{3.80\times10^{9}}$	8.22×10^{9}	1.18×10^{10}	5.63×10^{9}	2.56×10^{10}

***Table V-4**: branching ratio (Γ, %) of all oxidation reactions, with the total FHT, RAF, SET, and the overall branching ratio at the temperature range of 283-323 K. (the most favourable pathways are in bold).*

T (K)	H9-Abs	H10-Abs	H11-Abs	H12-Abs	H13-Abs	H14-Abs	H15-Abs	H22-Abs	H23-Abs	H27-Abs	H28-Abs	H29-Abs
283	0.01	0.01	0.01	0.03	**11.96**	2.30	**14.06**	1.02	0.00	0.14	0.07	0.34
288	0.01	0.01	0.01	0.03	**12.28**	2.07	**14.39**	0.87	0.00	0.13	0.06	0.31
293	0.01	0.01	0.01	0.03	**12.50**	1.85	**14.59**	0.75	0.00	0.12	0.06	0.28
298	0.01	0.01	0.01	0.03	**12.66**	1.67	**14.70**	0.65	0.00	0.11	0.06	0.25
303	0.01	0.01	0.01	0.03	**12.74**	1.51	**14.73**	0.56	0.00	0.10	0.05	0.23
308	0.01	0.01	0.01	0.03	**12.74**	1.37	**14.65**	0.49	0.00	0.09	0.05	0.21
313	0.01	0.01	0.01	0.02	**12.69**	1.25	**14.50**	0.43	0.00	0.09	0.05	0.19
318	0.01	0.01	0.01	0.02	**12.58**	1.14	**14.28**	0.38	0.00	0.08	0.05	0.18
323	0.01	0.01	0.01	0.02	**12.43**	1.06	**14.01**	0.34	0.00	0.08	0.04	0.17

T (K)	H30-Abs	H31-Abs	H32-Abs	H33-Abs	H40-Abs	H41-Abs	H42-Abs	H43-Abs	H44-Abs	C1-Add	C2-Add	C3-Add
283	1.34	**3.44**	0.22	0.05	**3.76**	0.20	0.04	0.01	0.01	0.44	7.18	2.74
288	1.15	**3.06**	0.21	0.04	**3.38**	0.18	0.03	0.01	0.01	0.40	6.73	2.50
293	1.00	**2.72**	0.19	0.04	**3.04**	0.16	0.03	0.01	0.01	0.35	6.22	2.27
298	0.87	**2.42**	0.18	0.03	**2.73**	0.15	0.03	0.01	0.01	0.32	5.72	2.08
303	0.77	**2.16**	0.17	0.03	**2.47**	0.14	0.03	0.01	0.01	0.29	5.22	1.90
308	0.67	**1.93**	0.16	0.03	**2.23**	0.13	0.03	0.01	0.01	0.26	4.75	1.74
313	0.60	**1.73**	0.15	0.03	**2.02**	0.12	0.03	0.00	0.01	0.24	4.31	1.60
318	0.54	**1.56**	0.15	0.02	**1.84**	0.12	0.03	0.00	0.01	0.22	3.90	1.48
323	0.48	**1.42**	0.14	0.02	**1.69**	0.11	0.03	0.00	0.01	0.20	3.54	1.37

T (K)	C4-Add	C5-Add	C6-Add	C7-Add	C16-Add	C19-Add	C34-Add	C38-Add	C39-Add	FHT	RAF	SET	Overall
283	0.66	1.77	1.04	**10.65**	2.15	0.01	0.00	**11.47**	**12.45**	39.00	50.55	10.45	100.00
288	0.60	1.63	0.92	**11.03**	1.89	0.01	0.00	**11.68**	**12.91**	38.24	50.29	11.47	100.00
293	0.55	1.51	0.81	**11.35**	1.66	0.01	0.00	**11.78**	**13.30**	37.39	49.81	12.80	100.00
298	0.50	1.40	0.72	**11.62**	1.46	0.01	0.00	**11.82**	**13.66**	36.58	49.29	14.13	100.00
303	0.46	1.30	0.64	**11.85**	1.29	0.01	0.00	**11.79**	**13.97**	35.74	48.71	15.54	100.00
308	0.43	1.21	0.57	**12.02**	1.14	0.00	0.00	**11.68**	**14.23**	34.85	48.04	17.12	100.00
313	0.40	1.14	0.52	**12.15**	1.01	0.00	0.00	**11.54**	**14.46**	33.95	47.36	18.69	100.00
318	0.37	1.07	0.47	**12.24**	0.90	0.00	0.00	**11.35**	**14.65**	33.01	46.65	20.34	100.00
323	0.35	1.01	0.43	**12.29**	0.81	0.00	0.00	**11.14**	**14.82**	32.07	45.95	21.98	100.00

V.2.4. The lifetime of fenpyrazamine in the presence of HO• radicals

To ascertain how long fenpyrazamine persists in the environment when subjected to HO• radicals, its lifetime (τ) was computed over the 283-323 K temperature range at different concentrations of HO• in natural waters (*i.e.*, from 10^{-15} to 10^{-18} M) (Burns *et al.*, 2012).

The results presented in ***Table V-5*** show that at low temperature (*i.e.*, 283 K) and low HO• concentration (*i.e.*, 10^{-18} M), the lifetime of FPA was 8.3×10^{7} s (2.62 years). As the temperature increases to 323 K, the lifetime decreases to 3.9×10^{7} s (1.24 years). Moreover, at 323 K, increasing the [HO•] from 10^{-18} to 10^{-15} M leads to a decrease in the lifetime to 3.9×10^{4} s (10.84 hours). In addition, at 298 K, the lifetime varies between 16.67 hours to 1.90 years.

It can be seen that higher temperatures and concentrations of HO• increase the degradation process of FPA, hence decreasing its lifetime.

Table V-5*: the lifetime (τ, s) of FPA calculated in a temperature range of 283-323 K, based on [HO•] in the natural waters.*

T (K)	**283**	**288**	**293**	**298**	**303**	**308**	**313**	**318**	**323**
$k_{overall}$, M^{-1} s^{-1}	1.21×10^{10}	1.35×10^{10}	1.51×10^{10}	1.67×10^{10}	1.83×10^{10}	2.01×10^{10}	2.19×10^{10}	2.38×10^{10}	2.56×10^{10}
[HO•], M					**τ, s**				
1×10^{-15}	8.3×10^{4}	7.4×10^{4}	6.6×10^{4}	6×10^{4}	5.5×10^{4}	5×10^{4}	4.6×10^{4}	4.2×10^{4}	3.9×10^{4}
1×10^{-16}	8.3×10^{5}	7.4×10^{5}	6.6×10^{5}	6×10^{5}	5.5×10^{5}	5×10^{5}	4.6×10^{5}	4.2×10^{5}	3.9×10^{5}
1×10^{-17}	8.3×10^{6}	7.4×10^{6}	6.6×10^{6}	6×10^{6}	5.5×10^{6}	5×10^{6}	4.6×10^{6}	4.2×10^{6}	3.910^{6}
1×10^{-18}	8.3×10^{7}	7.4×10^{7}	6.6×10^{7}	6×10^{7}	5.5×10^{7}	5×10^{7}	4.6×10^{7}	4.2×10^{7}	3.9×10^{7}

V.2.5. Further oxidation reactions of the main-radical product

H15-Abs was the main radical product arising from the abstraction of H15 hydrogen species of fenpyrazamine by HO•. The further oxidation of this radical product was studied towards different oxidizing agents in aquatic environments like $^{3}O_2$, HO•, •NO, and •NO_2 at 298 K, and the results are presented in ***Figure V-10***.

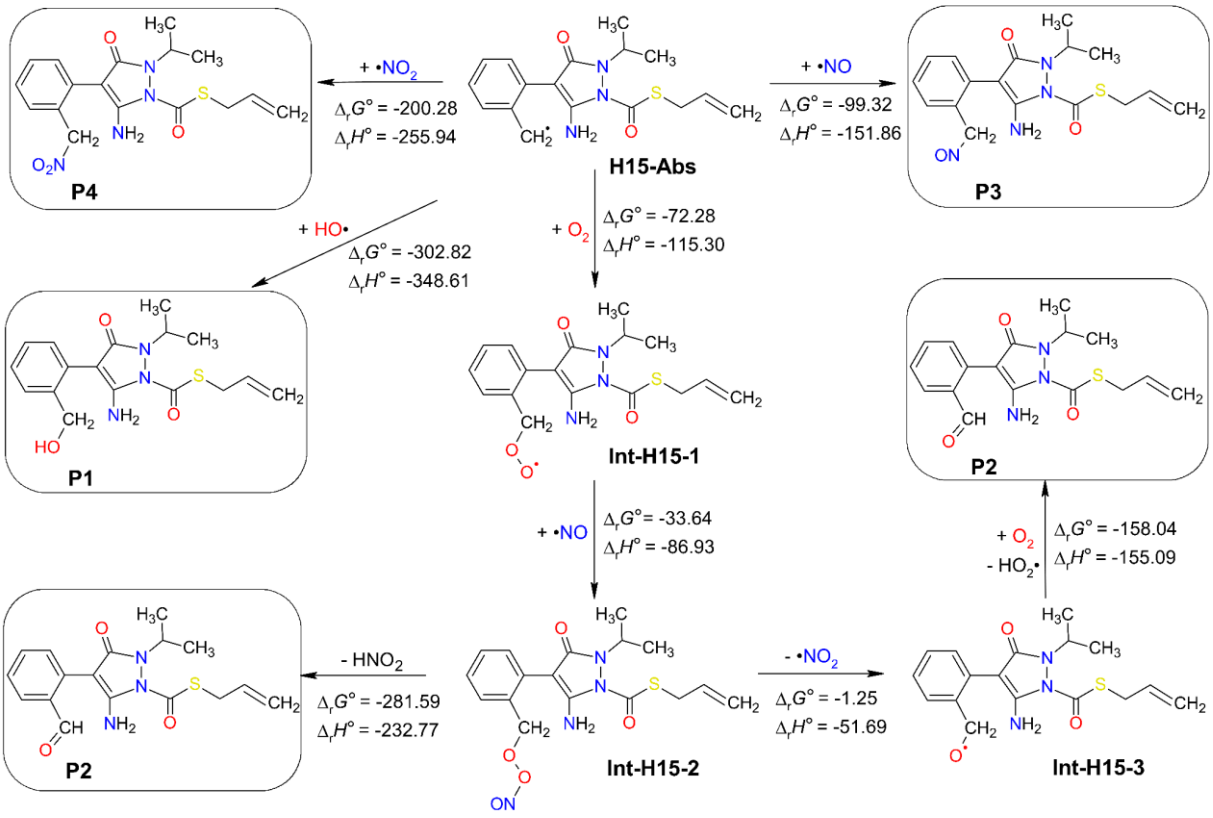

***Figure V-10**: standard Gibbs free reaction energy ($\Delta_rG°$) and standard reaction enthalpy ($\Delta_rH°$) calculated for the further reactions of H15-Abs with $^3O_2$, HO•, •NO, and •NO$_2$ at 298 K. Units are in kJ mol^{-1}.*

All the subsequent reactions are exergonic, spontaneous, and exothermic, indicated by their highly negative $\Delta_rG°$ and $\Delta_rH°$ values. The direct addition of HO• at C8 of the H15-Abs radical seems to be the most feasible reaction with the lowest $\Delta_rG°$ value of -302.82 kJ mol^{-1}, generating the neutral product **P1**. In the same way, $^3O_2$ can attack C8 to form **Int-H15-1** intermediate with $\Delta_rG°$ value of -72.28 kJ mol^{-1}. This intermediate can react with •NO at the O position to form **Int-H15-2** intermediate**,** which then undergoes O–O bond cleavage forming •NO$_2$ that abstract a hydrogen from C8 producing HNO$_2$ and the neutral product **P2**. In another pathway, the dissociation of •NO$_2$ from **Int-H15-2** can form another intermediate **Int-H15-3**, which in turn reacts with $^3O_2$ to produce HO$_2$• and **P2**.

Moreover, the direct reaction of H15-Abs with •NO and •NO$_2$ can yield the products **P3** and **P4** with $\Delta_rG°$ values of -99.32 and -200.28 kJ mol^{-1}, respectively.

On the other hand, C39-Add was the main radical product obtained from the HO•-addition at C39 of FPA, forming a radical at C38. Similarly, the essential further oxidation of C39-Add was also studied, and the results are shown in ***Figure V-11***.

The addition of HO• at C38 of C39-Add radical produces **P5** with the lowest $\Delta_rG°$ value of -344.92 kJ mol^{-1}, indicating the most feasible reaction. The reaction C39-Add radical with $^3O_2$ generates the intermediate **Int-C39-1** with $\Delta_rG°$ value of -100.10 kJ mol^{-1}. **Int-C39-1** reacts with •NO to form a second intermediate **Int-C39-2**, which subsequently transforms into HNO$_2$

and the neutral product **P6** after the cleavage of O–O bond and the abstraction of hydrogen from C38 by $^{\bullet}NO_2$. In a second pathway, **P6** can be produced by the reaction of $^3O_2$ with **Int-C39-3** (product of **Int-C39-2** after the $^{\bullet}NO_2$ dissociation). Furthermore, the neutral products **P7** and **P8** can be generated from the reaction of C39-Add with $^{\bullet}NO$ and $^{\bullet}NO_2$, with $\Delta_rG°$ values of -122.53 and -219.57 kJ mol^{-1}, respectively.

By comparing between H15-Abs and C39-Add radical products, it is observed that the further degradation reactions of C39-Add have lower $\Delta_rG°$ values than those of H15-Abs. This shows the preference for the radical attack at C38 as previously proved in the kinetics section. Moreover, the highly negative $\Delta_rG°$ values indicate that these reactions are spontaneous and favourable, and may occur at a high rate.

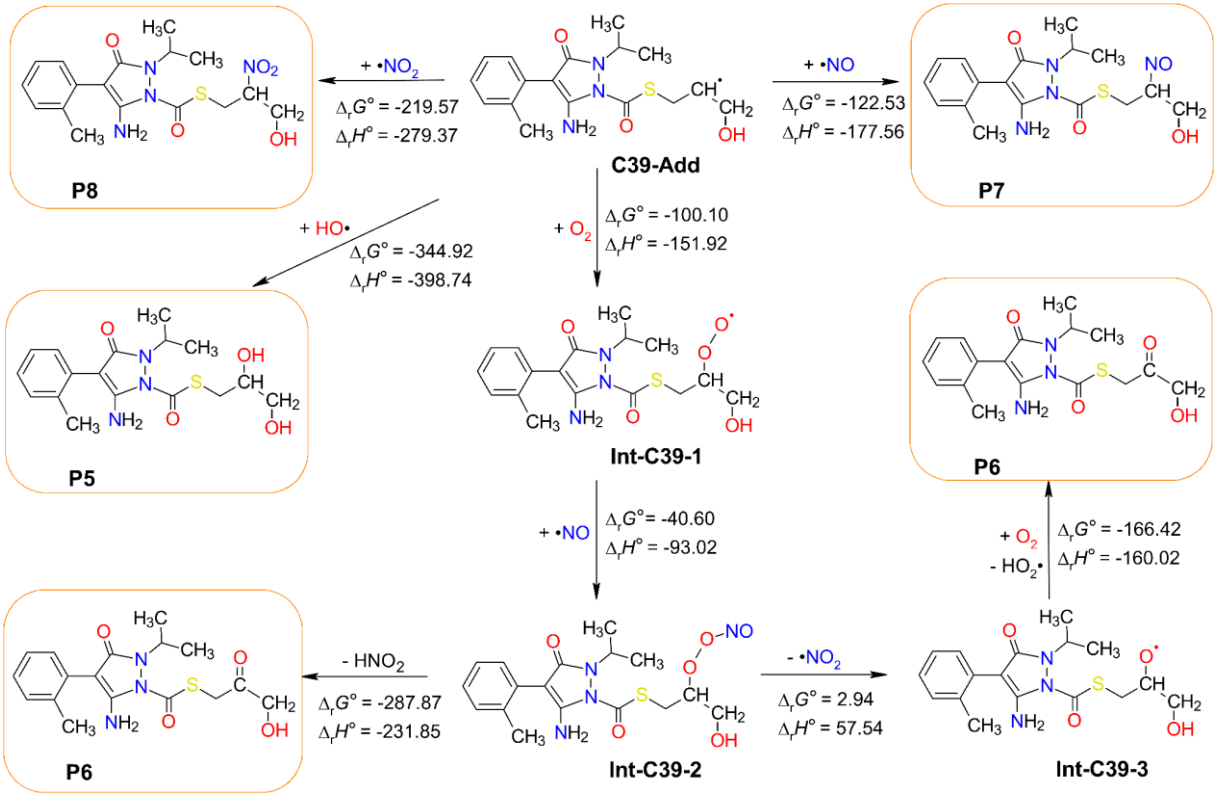

***Figure V-11**: standard Gibbs free reaction energy ($\Delta_rG°$) and standard reaction enthalpy ($\Delta_rH°$) calculated for the further reactions of C39-Add with $^3O_2$, HO$^{\bullet}$, $^{\bullet}NO$, and $^{\bullet}NO_2$ at 298 K. Units are in kJ mol^{-1}.*

V.2.6. Ecotoxicity, bioaccumulation, developmental toxicity, and mutagenicity

The toxicity estimation of FPA and its essential degradation products was studied towards some aquatic species (*e.g.*, fish, daphnia, and green algae) present in the ecosystem, in addition to their BAF, BCF, developmental toxicity, and mutagenicity values. The results are presented in ***Table V-6***.

***Table V-6**: aquatic acute (LC_{50} and EC_{50}) and chronic (ChV) toxicity, BCF (L/kg wet-wt), BAF (L/kg wet-wt), developmental toxicity, and mutagenicity of FPA and its degradation products **P1-P8**. Acute and chronic toxicities (mg/L) are coloured green, orange, and yellow for not harmful, harmful, and toxic properties.*

Compounds		FPA	P1	P2	P3	P4	P5	P6	P7	P8
Log K_{ow}		1.808	0.343	0.978	1.622	0.939	-0.652	-0.652	-0.639	-0.463
Acute toxicity	Fish (LC_{50})	85.1	818.0	64.7	122.6	360.0	3880	3860	3960	3150
	Daphnia (LC_{50})	9.9	80.4	65.1	14.0	37.9	340	338	347	282
	Green Algae (EC_{50})	8.6	97.1	34.2	12.6	40.0	516	513	526	409
Chronic toxicity	Fish (ChV)	5.3	85.7	15.3	8.2	30.5	578	575	587	438
	Daphnia (ChV)	0.8	5.5	0.6	1.1	2.8	20.7	20.6	21.2	17.5
	Green Algae (ChV)	2.8	28.1	11.4	4.0	12.1	137	136	140	111
BCF (L/kg wet-wt)		7.25	3.16	3.16	5.46	3.16	3.16	3.16	3.16	3.16
BAF (L/kg wet-wt)		7.45	1.08	1.87	4.78	1.66	0.91	0.91	0.91	0.91
Developmental toxicity		1.09	N/A	N/A	N/A	N/A	N/A	N/A	N/A	N/A
Mutagenicity		0.21	N/A	N/A	N/A	N/A	N/A	N/A	N/A	N/A

It is observed that FPA and its degradation products are less toxic and less harmful to aquatic species compared to the previously studied phosmet and chlorpyrifos pesticides. The acute toxicity values of FPA were found to be 85.1, 9.9, and 8.6 mg/L for fish, daphnia, and green algae, respectively. This means that FPA is harmful to fish and toxic to daphnia and green algae. The values of the chronic toxicity of FPA were 5.3, 0.8, and 2.8 mg/L, which means it's harmful to fish and green algae but toxic to daphnia.

Concerning the by-products, the data show higher values of LC_{50} and ChV than those of FPA, which means they are less harmful than the main FPA compound. The products **P1**, **P3**, and **P4** do not cause acute toxicity to fish; **P1**, **P2**, and **P4** do not cause chronic toxicity to fish and green algae. Moreover, LC_{50} and ChV values of the products **P5**, **P6**, **P7**, and **P8** show that they are not harmful, and their negative partition coefficient (Log K_{ow}) values indicate that they are hydrophilic and have high water solubilities.

All the BCF and BAF values of FPA and its degradation products indicate that they are non-bioaccumulative. The BCF and BAF values of FPA were revealed to be 7.25 and 7.45 L/kg wet-wt, respectively, which are higher than those of its by-products, varying from 3.16 to 5.46 L/kg wet-wt for BCF and from 0.91 to 4.78 L/kg wet-wt for BAF.

Fenpyrazamine is considered a developmental toxicant due to its developmental toxicity value of 1.09, whereas it is non-mutagenic with a mutagenicity value of 0.21. On the other hand, no data was found for the developmental toxicity and mutagenicity of the products **P1**-**P8**.

V.3. Conclusions

Fenpyrazamine (FPA) is a new fungicide that has shown strong effectiveness against gray mold, stem rot, and brown rot, which affect fruits and vegetables. The degradation process of FPA induced by $HO^{\bullet}$ was studied in the aqueous phase by DFT calculations at a temperature range of 283-323 K. Three reaction mechanisms were considered: H-abstraction (FHT), $HO^{\bullet}$-addition (RAF), and single electron transfer (SET).

Over the temperature range 283-323 K, it is noteworthy that the decreasing order of the three studied reaction mechanisms is as follows: RAF > FHT > SET. At 298 K, very close total rate constants were obtained for the FHT and RAF reactions (*i.e.*, 6.09×10^{9} and 8.21×10^{9} M^{-1} s^{-1}, respectively), while that of SET reaction was 2.35×10^{9} M^{-1} s^{-1}, and 1.67×10^{10} M^{-1} s^{-1} for the overall rate constant.

The abstraction of H15 (H15-Abs) of the methyl group was observed to be the most favourable abstraction pathway, followed by H13 of the same group (H13-Abs), H40 of the methylene group (H40-Abs), and H31 of the methyl group (H13-Abs). Furthermore, the preferred site for the $HO^{\bullet}$-addition was observed at C38/C39 of the vinyl group (C38-Add and C39-Add) and C7 of the pyrazole ring (C7-Add), where C39-Add showed the most favourable pathway.

The lifetime of FPA in natural waters may vary from 10.84 hours to 2.62 years depending on the temperature (283-323 K) and on the concentration of $HO^{\bullet}$ radical (10^{-15} to 10^{-18} M).

The subsequent reactions of the main radical product from the FHT reaction (H15-Abs) and that from the RAF reaction (C39-Add) were studied towards different oxidizing agents in aquatic environments like $^{3}O_2$, $HO^{\bullet}$, $^{\bullet}NO$, and $^{\bullet}NO_2$ at 298 K, leading to 8 possible products **P1**, **P2**, **P3**, **P4**, **P5**, **P6**, **P7**, and **P8**.

The toxicity estimation of FPA revealed that it is not bioaccumulative and mutagenic, but it is considered a developmental toxicant, harmful to fish, and toxic to daphnia and green algae. However, the degradation products are less dangerous than the FPA itself.

V.4. References

APVMA, 2015. Australian Pesticides and Veterinary Medicines Authority, Data guidelines. https://www.apvma.gov.au/registrations-and-permits/data-guidelines (accessed 6.25.24).

Burns, J.M., Cooper, W.J., Ferry, J.L., King, D.W., DiMento, B.P., McNeill, K., Miller, C.J., Miller, W.L., Peake, B.M., Rusak, S.A., Rose, A.L., Waite, T.D., 2012. Methods for reactive oxygen species (ROS) detection in aqueous environments. Aquatic Sciences 74, 683–734. https://doi.org/10.1007/s00027-012-0251-x

Dao, D.Q., Taamalli, S., Louis, F., Kdouh, D., Srour, Z., Ngo, T.C., Truong, D.H., Fèvre-Nollet, V., Ribaucour, M., El Bakali, A., Černušák, I., 2023. Hydroxyl radical-initiated decomposition of metazachlor herbicide in the gaseous and aqueous phases: Mechanism, kinetics, and toxicity evaluation. Chemosphere 312, 137234. https://doi.org/10.1016/j.chemosphere.2022.137234

Dehne, H.-W., Deising, H.B., Gisi, U., Kuck, K.H., Russell, P.E., Lyr, H., 2011. Modern fungicides and antifungal compounds VI. DPG Spectrum Phytomedizin. Proceedings of the 16th International Reinhardsbrunn Symposium, April 25 - 29, 2010, Friedrichroda, Germany.

FAO, 2017. Pesticide residues in food. Joint FAO/WHO meeting on pesticide residues. https://www.fao.org/fileadmin/templates/agphome/documents/Pests_Pesticides/JMPR/Report2017/web_2017_JMPR_Report_Final.pdf (accessed 6.25.24).

Gulkowska, A., Buerge, I.J., Poiger, T., 2014. Online solid phase extraction LC–MS/MS method for the analysis of succinate dehydrogenase inhibitor fungicides and its applicability to surface water samples. Analytical and Bioanalytical Chemistry 406, 6419–6427. https://doi.org/10.1007/s00216-014-8073-4

K. Al Rawas, H., Mawla, R.A., Pham, T.Y.N., Truong, D.H., Nguyen, T.L.A., Taamalli, S., Ribaucour, M., Bakali, A.E., Černušák, I., Dao, D.Q., Louis, F., 2023. New insight into environmental oxidation of phosmet insecticide initiated by HO˙ radicals in gas and water – a theoretical study. Environmental Science: Processes Impacts 25, 2042–2056. https://doi.org/10.1039/D3EM00325F

Kimura, N., Hashizume, M., Kusaba, T., Tanaka, S., 2017. Development of the novel fungicide fenpyrazamine. Journal of Pesticide Science 42, 137–143. https://doi.org/10.1584/jpestics.J17-01

Klavarioti, M., Mantzavinos, D., Kassinos, D., 2009. Removal of residual pharmaceuticals from aqueous systems by advanced oxidation processes. Environment International 35, 402–417. https://doi.org/10.1016/j.envint.2008.07.009

Leroux, P., Fritz, R., Debieu, D., Albertini, C., Lanen, C., Bach, J., Gredt, M., Chapeland, F., 2002. Mechanisms of resistance to fungicides in field strains of Botrytis cinerea. Pest Management Science 58, 876–888. https://doi.org/10.1002/ps.566

Ngo, T.C., Taamalli, S., Srour, Z., Fèvre-Nollet, V., El Bakali, A., Louis, F., Černuśák, I., Dao, D.Q., 2023. Theoretical insights into the oxidation of quinmerac herbicide initiated by HO• radical in aqueous media: Mechanism, kinetics, and ecotoxicity. Journal of Environmental Chemical Engineering 11, 109941. https://doi.org/10.1016/j.jece.2023.109941

Oliver, R.P., Hewitt, H.G., 2014. Fungicides in Crop Protection, 2nd Edition. CABI.

Rebollar-Zepeda, A.M., Galano, A., 2016. Quantum mechanical based approaches for predicting pKa values of carboxylic acids: evaluating the performance of different strategies. RSC Advances 6, 112057–112064. https://doi.org/10.1039/C6RA16221E

Reilly, T.J., Smalling, K.L., Orlando, J.L., Kuivila, K.M., 2012. Occurrence of boscalid and other selected fungicides in surface water and groundwater in three targeted use areas in the United States. Chemosphere 89, 228–234. https://doi.org/10.1016/j.chemosphere.2012.04.023

Shi, X., Zhang, R., Li, Y., Zhang, Q., Xu, X., Wang, W., 2018. Mechanism theoretical study on OH-initiated atmospheric oxidation degradation of dimethoate. Journal of Molecular Structure 1163, 61–67. https://doi.org/10.1016/j.molstruc.2018.02.104

Tanaka, S., Ishikawa, R., Armengaud, P., Senechal, Y., 2012. General characteristics of fenpyrazamine, a novel fungicidal compound for controlling gray mold. AFPP – 10th international conference on plant diseases tours – 3, 4 and 5 December 2012.

Truong, D.H., Nguyen, T.L.A., Alharzali, N., Al Rawas, H.K., Taamalli, S., Ribaucour, M., Nguyen, H.L., El Bakali, A., Ngo, T.C., Černušák, I., Louis, F., Dao, D.Q., 2024. Theoretical insights into the HO•-induced oxidation of chlorpyrifos pesticide: Mechanism, kinetics, ecotoxicity, and cholinesterase inhibition of degradants. Chemosphere 350, 141085. https://doi.org/10.1016/j.chemosphere.2023.141085

General conclusions and perspectives

Pesticides are widely used in agriculture to protect crops from pests, diseases, and weeds. While pesticides play a crucial role in modern agriculture by protecting crops and ensuring food security, their use comes with significant human health and environmental risks. Balancing the benefits and drawbacks requires stringent regulatory frameworks, the promotion of sustainable practices, and ongoing research into safer and more effective pest control alternatives.

The aim of this thesis is to contribute to the ongoing research on pesticides, by studying their degradation in the atmosphere induced by atmospheric oxidants such as O_2, O_3, $HO^{\bullet}$, $^{\bullet}NO$, and $^{\bullet}NO_2$, where no literature data exists.

The atmospheric degradation of three pesticides, phosmet insecticide, chlorpyrifos insecticide, and fenpyrazamine fungicide, by hydroxyl radical were theoretically studied in this thesis. The DFT method was applied for performing the calculations of the electronic structures at the M06-2X/6-311++G(3df,3pd)//M06-2X/6-31+G(d,p) level of theory. This level of theory was very accurate in computing the thermokinetics data.

Three different reaction pathways were considered: H-abstractions, $HO^{\bullet}$-additions on the unsaturated atoms, and single electron transfer reactions. The results of the thermodynamics study showed that the majority of the FHT and RAF reactions pathways were exothermic, exergonic and spontaneous. The most favourable H-abstraction pathways were observed at the methyl and the methylene groups in the three pesticides. The most favourable $HO^{\bullet}$-addition pathway varied between the three pesticides, where it was at the P-atom in phosmet, at the C-atom of the aromatic ring in CPF, and at the vinyl group in FPA.

The SET reactions were non-spontaneous and negligible in the gas phase, but notably more significant in the aqueous phase. However, they were considered in phosmet and FPA, but negligible in CPF.

The results of the kinetic calculations show that phosmet at 298 K has an overall rate constant of 2.05×10^{10} M^{-1} s^{-1} in the gas phase, and 1.36×10^{9} M^{-1} s^{-1} in the aqueous phase. In CPF, the overall rate constant appeared to be 1.65×10^{10} and 4.76×10^{8} M^{-1} s^{-1} in the gas and aqueous phases, respectively, while that of FPA was 1.67×10^{10} M^{-1} s^{-1}, indicating that phosmet tends to degrade faster than CPF in both phases, while FPA degrade faster the in aqueous phase. Furthermore, the RAF reaction was more important than the FHT reaction in phosmet and FPA, while the opposite was observed in CPF at 298 K.

The lifetime of the three pesticides in both gas and aqueous phases varied depending on the temperature and on the concentration of $HO^{\bullet}$ radical. Phosmet has an atmospheric lifetime of approximately 6 hours in the gas phase, an up to 26.52 years in the aqueous phase. CPF has a lifetime of approximately 5-8 hours in the gas phase, but it could exist in natural water for up to 66 years. In contrast, FPA appeared to be less persistent with lifetime vary from 10.84 hours to 2.62 years in natural waters.

Finally, the ecotoxicity of these pesticides and their degradation by-products were estimated in the aquatic environment to understand their impact on aquatic species. CPF and its degradation products was very toxic to aquatic species, while phosmet was less toxic, and FPA showed the least toxicity.

The results of this thesis were valorised in:

- ✓ 5 oral communications: 2 seminars, and 3 international conferences.
- ✓ 17 posters: national and international conferences and events.
- ✓ 3 publications:

1) **K. Al Rawas, H.**, *et al.* A theoretical study on the environmental oxidation of fenpyrazamine fungicide initiated by hydroxyl radical. **2024**. (*Submitted*)
2) Truong, D.H., Nguyen, T.L.A., Alharzali, N., **K. Al Rawas**, **H.**, *et al.* Theoretical insights into the $HO^{\bullet}$-induced oxidation of chlorpyrifos pesticide: Mechanism, kinetics, ecotoxicity, and cholinesterase inhibition of degradants. *Chemosphere*, **2024**, 350, p.141085. https://doi.org/10.1016/j.chemosphere.2023.141085
3) **K. Al Rawas, H.**, AlMawla, R., Pham, T.Y.N., Truong, D.H., Nguyen, T.L.A., Taamalli, S., Ribaucour, M., Bakali, A.E., Černušák, I., Dao, D.Q., Louis, F. New insight into environmental oxidation of phosmet insecticide initiated by $HO^{\bullet}$ radicals in gas and water – a theoretical study. *Environmental Science: Processes & Impacts*, **2023**, 25, pp.2042 - 2056. https://doi.org/10.1039/D3EM00325F

The work in this thesis was part of the ongoing research project on chlorophenols pesticides held in collaboration with the group of Pr. Ivan Černušák at Comenius University in Bratislava, Slovakia. The project included the degradation of tetrachlorophenol (TeCP) and pentachlorophenol (PCP) pesticides by $HO^{\bullet}$ radicals, and the results were valorised in 2 oral communications, 9 posters in national and international conferences and events, and one submitted article (July, 2024):

- ✓ Alharzali, N., Černušák, I., **K. Al Rawas, H.**, Taamalli, S., El Bakali, A., Louis, F., Dao, D.Q. Is high-level calculation necessary for assessing the atmospheric reactivity of pentachlorophenol with hydroxyl radical? DFT vs. Ab-initio calculations. *Journal of Physical Chemistry*, **2024**. (*Submitted*)

This PhD thesis has addressed and contributed to a deeper understanding of the degradation of pesticides using molecular simulations. It has successfully achieved its primary objectives, including the thermochemical, kinetics, environmental fate and ecotoxicity study of the pesticide's oxidation by hydroxyl radical. Furthermore, it described and elaborated a full methodology that could be used for future research on the degradation process of other pesticides, or other emerging contaminants such as plastics, tire wear additives, and PFAS.

Appendix

Electronic structure calculations for molecular systems containing 2-4 atoms

The abstraction reaction occurring between HO• and the studied pesticide's molecules involves H-, Cl-, and S-abstraction, forming the by-products H_2O, HOCl, and HOS• respectively. On the other side, the degradation reactions of the studied pesticides and their by-products were treated towards other species such as •NO, •NO_2, O_2 in the aqueous phase. These reactions produce some secondary products such as HNO_2, HO_2•.The structures of all these species and products were optimized at the M06-2X/6-31+G(d,p) level of theory in both gas and aqueous phases, and are presented in ***Figure A-1***. The values of the distances between atoms are in Angstrom, Å. The obtained values of the bonds length and the angles shows a very slight difference in comparison with the experimental values. For example, in the gas phase, the bond length between H and O was shorter by 0.006 Å in HO• and H_2O, and the angle is smaller by 0.1 degree compared to the experimental one. In HOCl, the angle was smaller by 1.6 degree in the experiment, while the bond length between O and Cl is the same. This indicates the efficiency of the used level of theory.

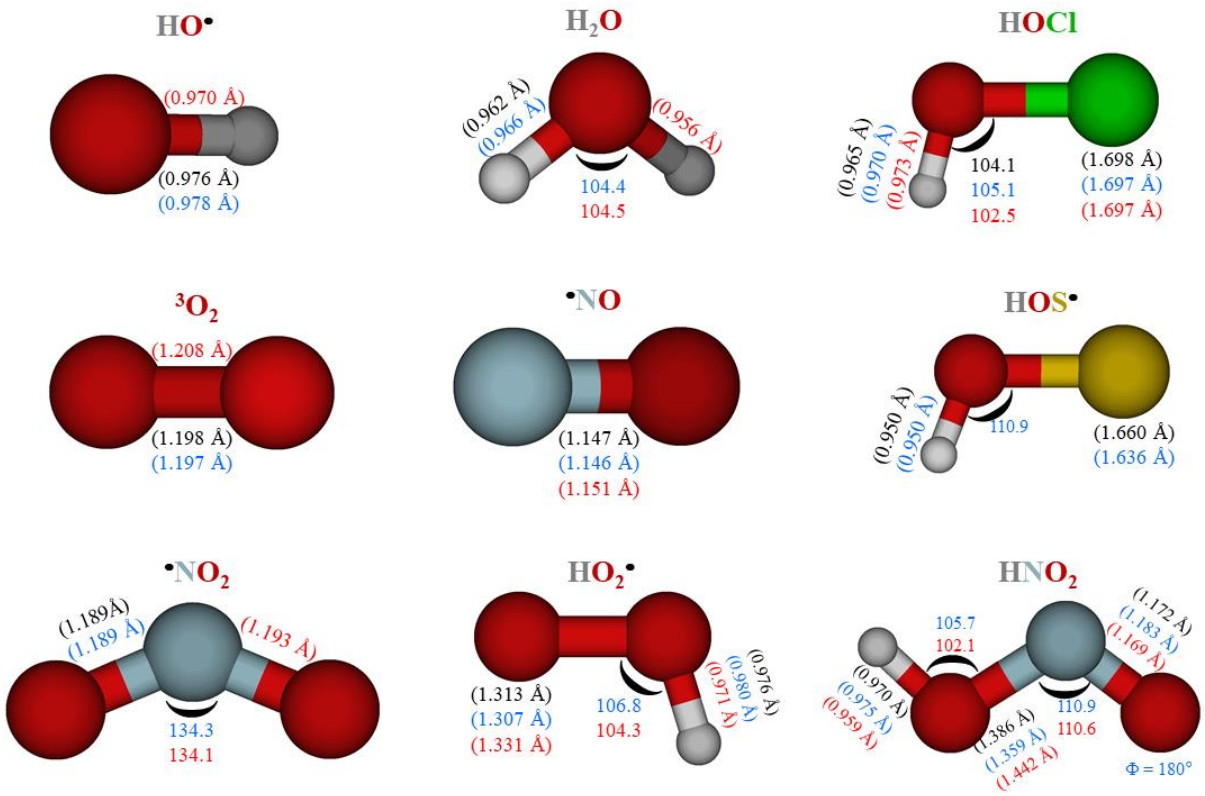

Figure A-1*: the optimized structures and the bond length and angles between atoms of HO•, •NO, •NO_2, O_2, H_2O, HNO_2, HO_2•, HOCl, and HOS• calculated at the M06-2X/6-31+G(d,p) level of theory in the gas phase (in black) and aqueous phase (in blue), compared with the experimental data (gas phase) from (NIST CCCBDB) (in red).*

The symmetry number, point group, electronic state, zero-point energy (ZPE), standard molar entropy ($S°_{298K}$), rotational constants, and the scaled vibrational frequencies (ω_i) of these different species, at the M06-2X/6-31+G(d,p) level of theory in both gas and aqueous phases, are summarized in ***Table A-1***.

The homonuclear diatomic molecules (*i.e.*, O_2) having $D_{\infty h}$ point group are linear and highly symmetric, and have a center of inversion. They are characterized by an infinite rotational axis along the z-axis (C_∞), coupled with reflection symmetry across multiple planes (σ_h).

Heteronuclear diatomic molecules having $C_{\infty v}$ point group (*i.e.*, $HO^\bullet$, and $^\bullet NO$), are linear and less symmetric, and have no center of inversion. They have an infinite number of coincident rotation axes, all the way up to C_∞, combined with vertical mirror planes (σ_v) that bisect the molecule.

Species with C_{2v} symmetry group (*i.e.*, H_2O, and $^\bullet NO_2$) are characterized by a C_2 rotational axis, along with two perpendicular mirror planes (σ_v) passing through the axis. They possess a principal axis of rotation and two perpendicular mirror planes that intersect at the central atom.

Species with C_1 symmetry group (*i.e.*, $HOS^\bullet$) are characterized by the absence of any symmetry elements other than the identity (E). They lack any specific symmetry operations, resulting in a unique orientation and arrangement of atoms.

Species with C_s point group (*i.e.*, HNO_2, $HO_2^\bullet$ and HOCl) are characterized by a single mirror plane (σ) that bisects the molecule. This symmetry group is associated with molecules possessing a center of inversion and a unique axis of rotation.

Regarding the electronic state of these molecules, the $^2\Pi$ electronic state, for example, refers to a molecular electronic state characterized by two quantum numbers: the spin multiplicity ($2S+1 = 2$), where S is the total electron spin, and the total orbital angular momentum quantum number (Π), where $L = 1$. Moreover, the $^2A_1$ electronic state refers to a molecular electronic state characterized by two quantum numbers: the spin multiplicity (2) and the symmetry label (A_1).

By comparing with the experimental data, the M06-2X/6-311+G(d,p) demonstrates an excellent efficiency in reproducing the vibrational frequencies of $HO^\bullet$, with 1% change. For H_2O in the gas phase, an acceptable estimation was observed with a difference of less than 1% in the first vibrational frequency, 6% in the second and 6% in the third one. These three modes belong to the symmetric bend, symmetric and asymmetric stretching of O-H bonds, respectively.

However, M06-2X/6-311+G(d,p) overestimates the first vibrational mode of HOCl showing the stretching of O-Cl bond by approximately 4% greater than the experimental value. This also affected the ZPE which shows a value greater by 1.23 kJ mol^{-1} than the experimental one. Moreover, this method also overestimates the vibrational frequency of $^\bullet NO$ by 9%.

***Table A-1**: geometric parameters, zero-point energy (ZPE), standard molar entropy ($S°_{298K}$), rotational constants, and scaled vibrational frequencies of $HO^{\bullet}$, $^{\bullet}NO$, $^{\bullet}NO_2$, O_2, H_2O, HOCl, HNO_2, $HO_2^{\bullet}$, HOCl, and $HOS^{\bullet}$, calculated at the M06-2X/6-31+G(d,p) level of theory in the gas phase (in black) and aqueous phase (in blue), compared with the experimental data (gas phase) from (NIST CCCBDB) if available (in red).*

Species	Symmetry number	Point group	Electronic state	ZPE (kJ mol^{-1})	$S°_{298K}$ (J mol^{-1} K^{-1})	Rotational constants (GHz)	Scaled vibrational frequencies (cm^{-1})
$HO^{\bullet}$	1	$C_{\infty v}$	$^2\Pi$	21.53	183.60	559.96	3781
				21.30	183.64	556.92	3741
				21.35	183.74	566.93	3738
$^{\bullet}NO$	1	$C_{\infty v}$	$^2\Pi$	11.90	210.64	51.46	2090
				11.86	210.64	51.50	2083
				11.22	210.76	50.12	1904
$^{\bullet}NO_2$	2	C_{2v}	$^2A_1$	23.10	239.91	245.28, 13.14, 12.48	245, 13, 12
				22.59	239.96	243.30, 13.17, 12.49	765, 1481, 1722
				22.05	240.17	239.87, 13.00, 12.30	757, 1358, 1666
O_2	2	$D_{\infty h}$	$^3\Sigma_g$	10.09	204.94	44.02	1772
				10.10	204.93	44.94	1774
				9.31	205.15	43.10	1580
H_2O	2	C_{2v}	$^1A_1$	54.05	188.72	844.46, 424.67, 282.57	1599, 3884, 4009
				53.23	188.87	813.62, 428.34, 280.61	1574, 3838, 3935
				53.88	188.84	835.73, 435.06, 278.36	1595, 3657, 3756
HNO_2	1	C_s	$^1A'$	52.76	247.66	96.24, 13.00, 11.45	583, 707, 934, 1345, 1861, 3837
				52.49	246.92	97.32, 13.16, 11.59	642, 732, 951, 1348, 1792, 3754
				50.74	249.11	92.90, 12.52, 11.02	
$HO_2^{\bullet}$	1	C_s	$^2A''$	36.55	228.67	625.02, 34.47, 32.67	1264, 1457, 3697
				36.57	228.58	626.80, 34.68, 32.86	1298, 1456, 3668
				35.44	229.10	610.27, 33.52, 31.67	
HOCl	1	C_s	$^1A'$	34.56	236.30	620.52, 15.03, 14.68	772, 1248, 3857
				34.36	236.28	620.23, 15.03, 14.67	774, 1274, 3796
				33.33	236.50	613.48, 15.12, 14.72	743, 1276, 3794
$HOS^{\bullet}$	1	C_1	^2A	33.55	240.10	661.04, 16.46, 16.06	889, 1171, 3832
				33.23	240.06	664.12, 16.49, 16.09	884, 1187, 3765